A RATIONAL DESIGN APPROACH FOR THE CRYOPRESERVATION OF NATURAL AND ENGINEERED TISSUES

A Dissertation
Presented to
The Academic Faculty

by

Indra Neil Mukherjee

In Partial Fulfillment
of the Requirements for the Degree
Doctor of Philosophy in the
School of Chemical & Biomolecular Engineering

Georgia Institute of Technology
April 2008

A RATIONAL DESIGN APPROACH FOR THE CRYOPRESERVATION OF NATURAL AND ENGINEERED TISSUES

Approved by:

Dr. Athanassios Sambanis, Advisor
School of Chemical & Biomolecular Engineering
Georgia Institute of Technology

Dr. Mark R. Prausnitz
School of Chemical & Biomolecular Engineering
Georgia Institute of Technology

Dr. Robert C. Long, Jr.
Department of Radiology, School of Medicine
Emory University

Dr. Ying C. Song
Department of Surgery and Institute of Molecular Medicine and Genetics
Medical College of Georgia

Dr. Peter J. Ludovice
School of Chemical & Biomolecular Engineering
Georgia Institute of Technology

Date Approved: November 19, 2007

To my family: Ma, Baba and Shawmeet

"It is not the critic who counts: not the man who points out how the strong man stumbles or where the doer of deeds could have done better. The credit belongs to the man who is actually in the arena, whose face is marred by dust and sweat and blood, who strives valiantly, who errs and comes up short again and again, because there is no effort without error or shortcoming, but who knows the great enthusiasms, the great devotions, who spends himself for a worthy cause; who, at the best, knows, in the end, the triumph of high achievement, and who, at the worst, if he fails, at least he fails while daring greatly, so that his place shall never be with those cold and timid souls who knew neither victory nor defeat."

- Theodore Roosevelt, 1910

ACKNOWLEDGEMENTS

I would like to acknowledge those that have contributed enormously to my professional and personal development while at Georgia Tech. Firstly, I would like to express my appreciation and gratitude to my thesis advisor, Dr. Athanassios Sambanis, for his unwavering guidance and support. He provided a perfect balance of mentorship and independence - giving me the freedom to investigate and cultivate my own research interests. I have learned a lot from Dr. Sambanis – he has been a great advisor and mentor. I would like to thank Dr. Ying Song for all of his encouragement, expertise and contributions in shaping this project. My immense appreciation also extends to Dr. Bob Long for patiently teaching me so much about MR and his tremendous help with the cartilage NMR experiments. I would also like to thank Drs. Song and Long for allowing me to do experiments in their laboratories. In addition, I would like to thank Drs. Prausnitz and Ludovice for their critical feedback and commitment to this work.

I am fortunate to have worked with a great group of people in the Sambanis Lab on a daily basis. When I first entered the lab, Tony Tang and Shing-Yi Cheng, and Thein Tun were kind enough to teach me lab and tissue culture techniques. Throughout the years, many thanks to Jeff Gross, Heather Bara, Angie Gulino, Hajira Ahmad, Alison Stucky, Fernie Goh, Jayeun Sung and Yang Li for all of their support and helpful discussions. I would like to particularly thank Yang for all of his tremendous help with experiments and modeling work.

Technical assistance is greatly appreciated by Johnafel Crowe for training on the confocal microscope, flow cytometer, and Coulter counter; Chris Wilson for showing me

mechanical testing and rheometery. I would like to thank all the people in Dr. Athanasios Mantalaris' Biological Systems Engineering Lab at Imperial College for their help and for teaching me about stem cells while I was visiting their lab - particularly Jay Cha, Mark Placzek, Yu-Shik Hwang, and Maya Lim. To this end, I would like to thank Dr. Robert Nerem for giving me the opportunity to work at Imperial College.

I would like to extend my appreciation to so many people for making life outside the lab so fun and memorable – Jose, Ashwini, Preeti, Suchitra, Jun, Mike, Jason, Don, Chris W, Chris L, Sarah, John, Mary, Adam, Cindy, Chen, Derek and so many others.

The immutable love and support of my family has been a source of great strength throughout my life. My Mom, Dad and brother have always encouraged and motivated me to do my best for which I will always be grateful. I would like to thank the Gupta family – Ram Uncle, Meera Auntie and Abhishek- for all of their encouragement, support and best wishes. Finally, I would like to thank Nimisha for all the love and everlasting support she has give me. The determination and enthusiasm you apply and exhibit in your daily life has been truly inspirational to me. I am very blessed to have you in my life now and forever.

This work was supported by funding from the NIH (R01DK073991), NSF (Georgia Tech/Emory Center for the Engineering for Living Tissues (GTEC) an ERC Program (EEC-9731643); Student and Teacher Enhancement Program (STEP) Fellowship; International Research Education in Engineering (IREE) Fellowship) and Department of Education CD4 GAANN Fellowship.

TABLE OF CONTENTS

	Page
ACKNOWLEDGEMENTS	iv
LIST OF TABLES	x
LIST OF FIGURES	xi
SUMMARY	xv
CHAPTER 1 INTRODUCTION	1
CHAPTER 2 BACKGROUND	6
2.1 Cryopreservation	6
2.1.1 Basic Steps and Operating Parameters	6
2.1.1.1 Cooling and Warming	6
2.1.1.2 Cryoprotectants	7
2.1.1.3 Conventional Freezing and Vitrification	8
2.1.2 Cell Suspensions, Tissues and Organs	10
2.1.3 Mathematical Modeling	12
2.1.4 Cell Death Due to Cryopreservation	15
2.2 Diabetes Mellitus and Treatment Options	19
2.2.1 Tissue Engineered Pancreatic Substitute	21
2.2.2 Pancreatic Substitute Construct Composition	22
2.2.3 Insulin-secreting Insulinoma Cells	23
2.2.4 Cryopreservation of Encapsulated Cell Systems	24
2.3 Embryonic Stem Cells (ESCs)	25
2.3.1 ESCs	25
2.3.2 ESC Preservation and Encapsulation	25
2.3.2.1 ESC Cryopreservation	25
2.3.2.2 ESC Encapsulation	27
2.4 Articular Cartilage	28
2.4.1 Articular Cartilage Composition, Structure and Function	28
2.4.2 Articular Cartilage Defects and Treatments	29
2.5 Preservation of Chondrocytes and Cartilage	30
CHAPTER 3 EFFECTS OF CRYOPRESERVATION ON CELL VIABILITY AND INSULIN SECRETION IN A MODEL TISSUE ENGINEERED PANCREATIC SUBSTITUTE	32
3.1 Abstract	32
3.2 Introduction	33
3.3 Materials and Methods	35
3.3.1 Cell and Cell Culture	35
3.3.2 Fabrication of Beads	36

3.3.3 Vitrification and Conventional Freezing Protocols 36
3.3.4 Cryosubstitution, Histology 37
3.3.5 Cell Viability Measurement 38
3.3.6 Static Insulin Secretion Protocol 38
3.3.7 Statistical Analysis 39
3.4 Results 39
3.5 Discussion 43

CHAPTER 4 CRYOPROTECTANT DELIVERY AND REMOVAL FROM MURINE INSULINOMAS AT VITRIFICATION-RELEVANT CONCENTRATIONS 46
4.1 Abstract 46
4.2 Introduction 47
4.3 Materials and Methods 49
4.3.1 Cell and Cell Culture 49
4.3.2 Measuring Cell Volume Changes and Membrane Permeabilties 49
4.3.3 Determination of Osmotically-inactive Cell Volume (V_b) 50
4.3.4 Cell Osmotic Tolerance 50
4.3.5 Analytical Techniques 51
4.3.6 Cryoprotectant Addition-Removal Simulations and Experiments 51
4.3.7 Effects of Cryoprotectant Exposure on Cell Viability 52
4.3.8 Mathematical Modeling and Calculations 53
4.3.8.1 Membrane Permeability Parameters 53
4.3.8.2 Activation Energy 54
4.3.9 Statistical Analysis 55
4.4 Results 55
4.4.1 βTC-tet Cell Membrane Permeability Characteristics 55
4.4.2 βTC-tet Cell Osmotic Tolerance 58
4.4.3 Simulation and Experimental Results CPA Addition and Removal 59
4.4.4 Effects of CPA Exposure on Insulinomas 62
4.5 Discussion 62

CHAPTER 5 CRYOPRESERVATION PROTOCOL DESIGN AND IMPLEMENTATION: A CELL ENCAPSULATED SYSTEM STUDY 68
5.1 Abstract 68
5.2 Introduction 69
5.3 Materials and Methods 71
5.3.1 Cell and Cell Culture 71
5.3.2 Fabrication of Beads 71
5.3.3 Mathematical Modeling and Calculations 72
5.3.3.1 CPA Transport across Cell Membrane 72
5.3.3.2 CPA Transport through Matrix 73
5.3.3.3 CPA Transport through Matrix and Across Cell Membrane 75
5.3.4 Thermal Characterization of Vitrification Solutions 78
5.3.5 Vitrification and Conventional Freezing 78
5.3.6 Mechanical Testing 82

5.3.7 Cell Viability Measurements 83
5.3.8 Statistical Analysis 84
5.4 Results 85
5.4.1 CPA Transport 85
5.4.2 Vitrification Solution Thermal Analysis 85
5.4.3 CPA Transport Modeling and Cryopreservation Experiments 85
5.4.4 Mechanical Testing 92
5.5 Discussion 96

CHAPTER 6 CRYOPRESERVATION OF ENCAPSULATED MURINE AND HUMAN EMBROYONIC STEM CELLS FOR BIOPROCESS ENGINEERING 100
6.1 Abstract 100
6.2 Introduction 101
6.3 Materials and Methods 104
6.3.1 Cell Culture 104
6.3.2 EB Formation 105
6.3.3 Cell Encapsulation 105
6.3.4 RNA Extraction and RT-PCR 106
6.3.5 Cryopreservation 107
6.3.6 Viability and Encapsulated Cell Growth Kinetics 108
6.3.7 Effects of CPA Solutions on Cryopreservation of Cell Suspensions 109
6.4 Results 109
6.4.1 Effect of CPA Solutions on Cryopreservation of Cell Suspensions 109
6.4.2 Growth Kinetics and Cryopreservation 109
6.4.3 EB Formation after Cryopreservation 113
6.4.4 Gene Expression from Cryopreserved Encapsulated Cells 113
6.4.5 Cryopreservation with 2-step cooling/warming 115
6.4.6 Encapsulation and Cryopreservation of hESCs 118
6.5 Discussion 120

CHAPTER 7 CRYOPROTECTANT TRANSPORT THROUGH ARTICULAR CARTILAGE FOR LONG-TERM STORAGE: EXPERIMENTAL AND MODELING STUDIES 123
7.1 Summary 123
7.2 Introduction 124
7.3 Materials and Methods 127
7.3.1 Chemicals 127
7.3.2 Tissue Isolation 127
7.3.3 Magnetic Resonance (MR) Imaging Setup, Acquisition and Analysis 127
7.3.4 MR Spectroscopy Setup, Acquisition and Analysis 130
7.3.5 Mathematical Modeling and Calculations 131
7.3.6 CPA Transport Across Cell Membrane 132
7.3.7 CPA Transport through Cartilage Extracellular Matrix 133
7.3.8 Determination of the Effective Diffusivities through Cartilage Matrix 135

7.3.8.1 Bulk Solution Diffusivity Calculations 136
7.3.8.2 CPA Transport through Matrix and Across Cell Membrane 137
7.4 Results
7.4.1 ^{1}H NMR Imaging and Spectroscopy 138
7.4.2 Simulations of Cell Volume Change and Intracellular Solute Concentrations 143
7.5 Discussion 145

CHAPTER 8 CONCLUSIONS AND FUTURE DIRECTIONS 152
8.1 Conclusion 152
8.2 Future Directions 155
8.2.1 Mathematical Model 155
8.2.2 Encapsulated Insulinomas 156
8.2.3 Encapsulated Murine Embryonic Stem Cells 158
8.2.4 Articular Cartilage 158

APPENDIX I ALGINATE-ENCAPSULATED CELLS 160
A1.1 Apoptosis after Cryopreservation of Cell Suspensions 160
A1.2 Examining the Role of Stress Proteins after Cryopreservation 164
A1.3 ^{13}C NMR Metabolic Study using PCA Extraction 166
A1.4 NMR T2 Microimaging of Cryopreserved Cell-Free Alginate Beads 168
A1.5 FITC Dextran PLL Permeability Studies 169
A1.6 CPA Addition-Removal Data for Encapsulated Insulinomas 171

APPENDIX II ARTICULAR CARTILAGE 172
A2.1 Heat Transport Measurements and Calculations 172
A2.2 Mechanical Testing after Cryopreservation 177
A3.3 Chondron/Chondrocyte Isolation 180

APPENDIX III MISCELLANEOUS
A3.1 DSC Runs with VS55 and DP6 181

REFERENCES 184

LIST OF TABLES

Page

Table 2.1: Examples of CPA addition-removal protocols for vitrification 14

Table 4.1: Water and solute membrane permeabilities of βTC-tet cells 57

Table 5.1: Optimized and sub-optimal cryopreservation protocols used for vitrification of encapsulated βTC-tet cells 80

Table 5.2: CPA diffusivities through alginate-encapsulated, inactivated βTC-tet cells 87

Table 5.3: Values of model parameters used in this study 87

Table 5.4: Pairwise comparisons between vitrification and conventionally frozen groups for each day of culture 94

Table 6.1: Primer information and PCR conditions 106

Table 7.1: Values of model parameters used 134

Table 7.2: T1 and T2 values of 6.9 M DMSO in bulk solution and in cartilage equilibrated with this solution 139

Table 7.3A: Diffusivities through cartilage relative to bulk solution diffusivities (D_{eff}/D_o) for each component in a multi-solute vitrification solution and of DMSO in a single solute solution. 143

Table 7.3B: Effective diffusivities of CPAs through articular cartilage from the literature 147

Table A.2.1 Thermal properties of CPA solutions 176

Table A.3.1 Thermal data for various vitrification solutions 183

LIST OF FIGURES

Page

Figure 2.1 A. Temperature – solute concentration profile during conventional freezing; B. Temperature – solute concentration profile during vitrification 9

Figure 2.2 Shrink – swell behavior of βTC- tet cells 14

Figure 2.3 A. Mitochondrial apoptosis mediated pathway; B. Membrane-mediated cell surface receptor-initiated apoptosis pathway 18

Figure 3.1 Morphology of frozen and vitrified beads at –90°C. Freeze substitution of controlled-rate frozen beads shows considerable ice formation throughout the construct (A). Freeze substitution of vitrified beads shows the absence of ice in the construct (B). Light microscopy sections were stained with toluidine blue 40

Figure 3.2 Histology of fresh and rewarmed vitrified and frozen beads 41

Figure 3.3 Cell viability (normalized to initial cell number) of cryopreserved groups using alamarBlue® 42

Figure 3.4 Static insulin secretion rates from fresh, vitrified (VS55 and PEG400) and frozen beads exposed to a square wave of glucose concentration 43

Figure 4.1 Boyle-van't Hoff plot for βTC-tet cells 55

Figure 4.2 Representative plot of normalized voltage pulses vs. time generated by a Coulter Counter upon the abrupt addition at t=0 of βTC-tet cells to a 10% dimethyl sulfoxide solution at 22°C 56

Figure 4.3 Osmotic tolerances for βTC-tet cells 58

Figure 4.4 Simulated volume response of βTC-tet cells during addition and removal of A. 2.5 M DMSO, B. 2.5 M 1,2 propanediol (PD), C. 3.0 M DMSO, D. 3.0 M PD, E. 3.0 M DMSO+3.0 M PD 60

Figure 4.5 Viability of βTC-tet cells, measured by alamarBlue® and normalized to isotonic values 61

Figure 4.6 Normalized cell viability of βTC-tet cells, measured by alamarBlue®, after exposure to various concentrations of DMSO (black bars), PD (gray bars) and a cocktail of 3.0 M DMSO + 3.0 M PD (white bar) 63

Figure 5.1 A. Typical ^{1}H NMR spectrum of CPA and acetonitrile used to determine CPA concentrations with a calibration curve (inset); representative data and modeling for

B. diffusion-in and C. diffusion-out of 2 M PD at 22°C from alginate beads containing inactivated βTC-tet cells 86

Figure 5.2 DSC thermograms during warming at 5°C/min of vitrification solutions. A. 3 M DMSO + 3 M PD + 0.3 M sucrose; B. 5.5 M PD + 1 M sucrose; T_g=glass transition temperature; T_d=devitrification temperature; n/o=not observed 88

Figure 5.3 Simulated cell volume excursions and intracellular CPA concentrations at the center of 0.5 mm beads for two vitrification solutions 89

Figure 5.4 Normalized cell viability of alginate encapsulated βTC-tet cells in vitrification solutions after CPA cytotoxicity testing 91

Figure 5.5 Normalized cell viability, measured by alamarBlue®, of alginate-encapsulated βTC-tet cells after cryopreservation using optimized and intentionally sub-optimal protocols 93

Figure 5.6 Confocal micrographs of cryopreserved-thawed alginate encapsulated βTC-tet cells at Day 1 and 4 post-preservation using the LIVE/DEAD™ assay 95

Figure 5.7 A. Schematic of bead mechanical testing setup; B. Typical force vs. dimensionless approach profile for compressing alginate beads; C.Young's moduli of fresh and cryopreserved alginate beads using compressive mechanical testing 96

Figure 6.1 Effects of various DMSO-based cryoprotectant solutions on murine embryonic stem cell (mESC) survival 110

Figure 6.2 A. Photomicrographs of alginate-encapsulated mESCs over time; B. Cell growth kinetics of alginate-encapsulated mESCs 111

Figure 6.3 A. Cell growth kinetics of cryopreserved alginate-encapsulated mESCs over time; B. Viability using live-dead kit three days post thaw; C. Photomicrographs of alginate-encapsulated mESCs after thawing 112

Figure 6.4 Photomicrographs of embryoid body formation over time 113

Figure 6.5 Gene expression via RT-PCR for fresh and frozen-thawed mESCs 114

Figure 6.6 Multiphoton microscopy images of frozen-thawed encapsulated mESCs using LIVE/DEAD™ assay 116

Figure 6.7 A. Photomicrographs of frozen-thawed encapsulated mESCs stored at -80°C and LN_2; B. Fluorescent pictures of frozen-thawed beads using LIVE/DEAD™ assay; C. Cell viability of cryopreserved beads 118

Figure 6.8 A. Single hESC colony encapsulated in an alginate bead; B. Micrographs of single encapsulated hESC colony before and after cryopreservation; C. Viability of hESC colony with LIVE/DEAD™ assay 119

Figure 7.1 Schematic of NMR sample holder for articular cartilage 128

Figure 7.2 ^{1}H NMR Imaging of DMSO diffusion in cartilage. A. Time series montage of ^{1}H NMR images; B. Imaging signal intensity averaged over the acquisition plane normalized to the signal intensity in the surrounding solution 139

Figure 7.3 A. ^{1}H NMR spectrum of half strength VS55 cocktail at 200MHz in a 1x1x1 mm^{3} volume of interest (VOI) in articular cartilage positioned in the center after CPA equilibration; B. ^{1}H NMR spectra of half strength VS55 cocktail in the bulk at 200MHz in a 1x1x1 mm^{3} VOI 141

Figure 7.4 Representative concentration profiles of permeating half strength VS55 into articular cartilage 142

Figure 7.5 Simulated normalized cell volume and total intracellular CPA osmolality of chondrocytes at the periphery (solid lines) and the center (dashed lines) of a 5 mm diameter by 2 mm thick cartilage plug exposed to stepwise addition and removal of VS55 vitrification cocktail 144

Figure 7.6 Simulated concentration profiles of VS55 components in the matrix in a 5 mm diameter by 2 mm thick cartilage plug 146

A.1.1 A. Confocal micrographs of control and apoptotic cells using early, middle and late stage markers; B. Typical flow cytograms of control CPA-treated and froze-thawed BTC-tet cells; C. Apoptotic activity (%) of βTC-tet cells relative to fresh controls 161

A.1.2 Western blot of heat shock proteins over time from βTC-tet cells 165

A.1.3 ^{13}C NMR spectrum from freshly encapsulated βTC-tet cells after incubation in uniformly labeled C13-glucose for 4 hrs 167

A.1.4 A: T2 NMR micro-images of fresh and frozen-thawed, cell-free 2% alginate beads; B. Light micrograph of frozen-thawed cell-free alginate bead; 169

A.1.5 Confocal micrographs of fresh and frozen-thawed APA beads after 4 minutes of exposure to 19 and 148.3kDa FITC-dextrans 170

A.1.6 Addition-removal of low and high concentrations of single and multi-solute CPAs for alginate encapsulated βTC-tet cells 171

A.2.1 A: Cartilage temperature measurement setup; B. Temperature profiles of CPA solutions and articular cartilage equilibrated in solution measured by hypodermic thermocouple during cooling 173

A. 2.2 A: Dynamic shear and B: dynamic compressive moduli, of cryopreserved 4mm porcine articular cartilage 179

A.2.3 Micrographs of chondron and chondrocyte after isolation from bovine articular cartilage 180

A.3.1 DSC heat flow thermogram of VS55 during warming 181

A.3.2 DSC heat flow thermogram of DP6 during warming 182

SUMMARY

Key to the success of natural and engineered tissues becoming clinically available until needed is their long-term storage at low temperatures. This can be implemented by means of freezing or vitrification. In the former process, samples are cooled at a controlled rate in conjunction with low concentrations of cryoprotectants (CPAs). This leads to ice formation in the extracellular space and often an amorphous glass intracellularly. Although safe and commonplace for cell suspensions, this approach is problematic for tissues due to the deleterious effects of ice to cells and the extracellular matrix. To this end, vitrification offers an attractive approach for tissue banking by forming an amorphous glass both intra- and extracellularly avoiding ice formation. Generally, high concentrations of cryoprotectants (CPAs) are used in conjunction with high cooling and warming rates to achieve this. However, hurdles associated with applying this technique include the ability to adequately deliver and remove CPAs due to cellular osmotic and cytotoxic effects as well as achieving adequate cooling and warming rates throughout the tissue to avoid ice formation. The aim of this work was to account for these factors in designing cryopreservation protocols for native and engineered tissues that had intrinsically different characteristics, including tissue size and extracellular matrix properties. The tissues investigated were two types of three-dimensional, cell encapsulated systems consisting of murine insulinomas and murine embryonic stem cells, and native articular cartilage.

Each tissue system was compartmentalized into cellular and extracellular components; each compartment was characterized individually, and then combined to

describe the entire tissue system. Cell membrane permeabilities for murine insulinomas for water and different CPAs were determined using an electronic particle counter; chondrocyte values were taken from literature. CPA transport through the extracellular matrices of 2 mm alginate hydrogel microbeads and 8 mm diameter x 5-10 mm thickness articular cartilage disks were measured using magnetic resonance spectroscopy and imaging. While NMR was used as an offline assay tool to measure CPA concentrations through the alginate beads, CPA transport through articular cartilage was measured using a novel approach of localized magnetic resonance spectroscopy. Alginate beads were found to have fast CPA equilibration times, on the order of 10 minutes at a given CPA concentration, whereas articular cartilage took on the order of 4-5 hours. The CPA transport parameters from the two compartments were coupled in a mathematical model to determine cell volume excursions and intracellular CPA concentrations to changing bulk solution CPA conditions for a 3-D geometry. To apply this method to high concentrations of CPAs used in vitrification, the model incorporated stepwise addition and removal and CPA osmotic non-idealities as a function of concentration.

Simulations of multi-step addition and removal of vitrification-relevant CPA concentrations taking into account cells at different positions within the tissue, suggested a total time of 15 minutes for alginate-encapsulated cells and 2 hours for articular cartilage of clinically-relevant thickness (5 mm diameter x 3 mm thickness). To validate the approach, optimized vs. intentionally sub-optimal protocols were compared for a bioartificial pancreatic substitute based on alginate-encapsulated murine insulinoma cells using two different vitrification solutions. In addition to assessing viability though metabolic function of the cells post-thaw, the mechanical strength of the alginate matrix

was evaluated by determining Young's modulus using compression mechanical testing. Vitrification of the beads resulted in higher cellular viability compared to a conventionally frozen control. Young's moduli measurements indicated similar values for vitrified and conventionally frozen groups compared to fresh controls.

Studies with a second cell-encapsulated system consisting of encapsulated murine embryonic stem cells were also performed. In these, cryopreservation conditions were not systematically optimized, only protocols deemed appropriate on the basis of experimentation with other similar systems were used. Although slow freezing is routinely used to store murine embryonic stem cell suspensions, a similar protocol used on the encapsulated cells resulted in extensive cell death and structural damage of the beads. Although viable cell number in frozen-thawed beads returned to fresh control levels after three days and gene expression levels of pluripotency and germ layer markers after embryoid body formation were present in frozen-thawed groups, the structural damage incurred by the beads was deemed not acceptable. A two-step freezing protocol had better results with higher cell viabilities and retention of bead structural integrity post-thaw. However, further studies are needed to analyze gene expression levels when this protocol is employed.

In conclusion, this thesis has established a systematic methodology to design cryopreservation protocols using experimental measurements and a mathematical model for tissues. Future studies could include expanding upon the developed model to incorporate heat transfer in the tissue during cooling/warming and looking at apoptotic cell death due to cryopreservation and employing strategies to minimize them. Though there is still much to be done to develop successful cryopreservation protocols for

engineered and natural tissues, this thesis provides a quantitative framework towards addressing long-term storage strategies.

CHAPTER 1

INTRODUCTION

Long-term storage of natural and engineered tissues is essential for off-the-shelf availability, quality and sterility control, storage and distribution. Cryopreservation, or storage of biologics at cryogenic temperatures, offers a promising approach. Two main methods used in the field of cryopreservation are conventional freezing and vitrification. Conventional freezing generally involves cooling at a prescribed rate (such as with a controlled rate freezer) in the presence of low concentration cryoprotectants (CPAs) down to -80°C, followed by plunging into liquid nitrogen. In this way, ice forms in the extracellular milieu and either ice crystallizes or a glass forms intracellularly depending on the applied cooling rate and intracellular solute and water composition. Vitrification refers to the amorphous, glass-like solidification of the entire system in the presence of high CPA concentrations, with no ice formation upon cooling and/or warming. In contrast to conventional freezing, vitrification promotes glass formation both intra- and extracellularly.

Cell suspensions are routinely cryopreserved by conventional freezing with post-thaw viabilities greater than 90% [3]. However, conventional freezing has shown little or limited success with tissues or organs. This is, in part, due to the damaging effects of ice to cells and the extracellular environment [4-6]. Alternatively, ice-free cryopreservation would alleviate this limitation and could be used to potentially preserve biological materials with sensitive cells and complex matrix properties. One current challenge, however, in applying this approach is the use of high CPA concentrations necessary to

avoid ice formation. Associated critical issues with this are cellular osmotic and/or chemical toxicity. Though excessive osmotic excursions can be irreversibly damaging [7], this is mitigated by maintaining the cells within their osmotic excursion tolerances by stepwise CPA delivery and removal. CPA cytotoxicity can be reduced by minimizing exposure times and operating at lower temperatures. Extending these considerations from cell suspensions to tissues involves increased length scales and presence of an extracellular matrix effect on CPA transport times. Due to the intrinsic differences among tissues, including tissue size, extracellular matrix composition and cell type, cryopreservation protocols would need to be customized.

In this thesis three tissues were investigated, two with high matrix permeabilities and one with low matrix permeability. It was hypothesized that most other commonly cryopreserved tissues would lie within the parameters important to these contrasting tissue systems. The first studied tissue system stems from our lab's interest in cell-based therapies for Type I diabetes. It was a model tissue engineered pancreatic substitute based on insulin-secreting (murine insulinoma cell line) cells sequestered in an alginate-based biomaterial. This microbead construct has been extensively characterized *in vitro* and *in vivo* by our lab as well as other investigators [8-15]; it is composed of 2% calcium alginate and beads are approximately 500-650 μm in diameter. Based on these small length scales and highly aqueous environment, small molecular weight (MW) solutes diffuse and equilibrate quickly throughout the tissue [15, 16]. The second tissue system investigated, closely related to the pancreatic substitute in construct design, was alginate-encapsulated embryonic stem cells (ESCs). This system would be suitable for ESC expansion, embryoid body (EB) formation and tissue-specific terminal differentiation, as

well as allow automation and optimization as a bioprocess [17, 18]. The encapsulation material consisted of 1.1% calcium alginate and beads were approximately 2 mm in diameter. The third tissue system studied was articular cartilage. Successful cryopreservation of articular cartilage would, at least partially, alleviate limited availability of fresh allograft tissue needed for effective treatment of focal articular defects [19-22]. Moreover, long-term storage of cartilage grafts would be beneficial to avoid extracellular matrix degradation and loss of chondrocyte viability while necessary lab tests are conducted for contamination. Cryopreservation of articular cartilage is currently limited to chondrocyte suspensions and thin cartilage slices [5, 23-25]. The extracellular matrix of articular cartilage has a much lower permeability to small MW solutes than the alginate microbead systems [26], making CPA equilibration at large length scales slow, and challenging to cryopreserve at clinically-relevant length scales (5 mm diameter, 2-3 mm in thickness).

The overall objective of this thesis was to explore and generate a quantitative framework for the rational design of cryopreservation protocols, and to identify key design features that enable the cryopreservation of i) three-dimensional, cell encapsulated systems, and ii) articular cartilage. Taking a hierarchical approach, each tissue system was compartmentalized into cellular and extracellular components; each compartment was characterized individually, and then combined to describe the entire tissue system. These studies were accomplished by conducting the following aims: 1) determine cell membrane permeabilities, osmotic tolerance limits and cryoprotectant toxicity; and experimentally assess the effects of cryopreservation within this domain of conditions on cell viability and function; 2) determine heat and cryoprotectant transport properties

through the extracellular milieu of 3-D engineered (hydrogel-based encapsulated cells) and natural (articular cartilage) tissues; then combine the information obtained at the cell and matrix level to create a cryopreservation model for the entire tissue system; 3) implement the developed cryopreservation protocols on the system of encapsulated insulin-secreting cells and characterize their effects at both the cell and biomaterial levels.

This thesis is separated into five distinct studies presented in CHAPTERS 3-7, grouped based on the tissue investigated and not necessarily in the order in which they were performed. Most of these chapters represent a modified version of a manuscript either already published (CHAPTERS 3 and 4), in preparation for submission (CHAPTER 5), or under review for publication (CHAPTER 7). Additional background material, discussing topics described earlier in greater detail, is presented in CHAPTER 2. Conclusions and recommended future work are described in CHAPTER 8 and preliminary studies and results are presented in the APPENDIX.

Initially, in proof of concept studies, baseline vitrification protocols were applied to encapsulated insulinoma cells and their results are presented in CHAPTER 3. To optimize vitrification protocols, a systematic procedure was then developed. Membrane permeabilities to CPAs and water were measured (CHAPTER 4) and these were combined with CPA effective diffusivities through the matrix measured by off-line assays (CHAPTER 5) in a 3-D model of encapsulated insulin-secreting cells (CHAPTER 5). To validate the approach, optimized vs. intentionally sub-optimal protocols were compared (CHAPTER 5). Experiments with the second construct of encapsulated embryonic stem cells (CHAPTER 6) were, by necessity, few, due to the limited

availability of cells and cryopreservation-related equipment available at Imperial College London, where these studies were peformed. In these, cryopreservation conditions were not systematically optimized, only protocols deemed appropriate on the basis of experimentation with other similar systems were used. With cartilage cryopreservation, the third tissue investigated, a key issue is the lower CPA diffusivity through the matrix. So, in experiments with cartilage, emphasis was placed on developing magnetic resonance (MR) imaging and localized spectroscopy techniques for measuring the diffusivities of single and multiple high concentration CPAs in the tissue (CHAPTER 7). With cartilage, too, proposed CPA addition-removal protocols were developed by constructing and analyzing a mathematical model of CPA diffusion through the matrix and CPA and water transport through the chondrocyte membranes.

Overall, this thesis provides a systematic, rational design framework for cryopreserving three-dimensional tissues based on experimentally measured parameters. With most current cryopreservation protocols being empirically based, the approach developed in this thesis narrows the domain of conditions within which to explore cryopreservation conditions for the successful long-term storage of tissues.

CHAPTER 2

BACKGROUND

2.1 Cryopreservation

The need for long-term storage is a critical issue for the preservation of natural tissues, organs as well as tissue engineered products. Cryopreservation may offer a solution by preservation at cryogenic temperatures. Conventional approaches to cryopreservation have provided success to preserving cell suspensions and thin tissues [27]; however, such procedures can not necessarily be extended to preserve larger tissues, organs and engineered tissue due principally to the deleterious effect of extracellular ice formation that would disrupt and damage the tissues' highly extensive and organized structure. It is essential that function as well as structure be retained post-cryopreservation.

2.1.1 Basic steps and operating parameters

The cryopreservation of cells and tissues includes several critical steps: a) cryoprotectant (CPA) addition at a suprazero temperature; b) cooling at a prescribed rate down to a subzero temperature; c) storage below the glass transition temperature (T_g) of the system; d) thawing; e) CPA removal at a suprazero temperature followed by cell culturing. The manipulated parameters include cooling and thawing rates, CPA composition (components and concentrations), and temperature of CPA addition and removal.

2.1.1.1 Cooling and Warming

The cooling rate is a critical parameter in the overall outcome of cell survival. For each cell type there exits an optimal cooling rate to ensure maximum survival.

During slow cooling, as the extracellular environment crystallizes, a chemical potential imbalance between the intra- and extracellular spaces drives water out of the cells and results in cell dehydration. This leads to intracellular solute concentration build up which can become toxic known as 'solution effects'. If, on the other hand, the cooling rate is too fast, there is no time for intracellular water efflux after the extracellular environment has formed ice and this results in damaging intracellular ice formation (IIF) [28].

Warming is also important to ensure proper post-thaw survival. Generally the warming rate implemented is dependent on the cooling rate used. The most common way for warming is exposure to room temperature or a 37°C water bath to achieve fast warming allowing cells to spend less time in cytotoxic CPA concentrations and minimizing time for recrystallization. With both cooling and warming, heat transport issues are critical, especially in tissues characterized by large length scales, to achieve homogenous and uniform rates.

2.1.1.2 Cryoprotectants

In 1949 Polge et al discovered that the use of certain solutes (e.g., glycerol) allowed mammalian cells to be successfully frozen and thawed [29]. Since then other solutes have also been found to protect cells during cooling. Generally, cryoprotective chemicals, low in molecular weight, can be divided into two categories: a) permeating CPAs such as dimethyl sulfoxide (DMSO), 1,2 propanediol (PG), 1,2 ethylene glycol (EG) and 1,4 butanediol (BD), which can pass through the cell membrane; and b) non-permeating CPAs such as sugars (sucrose, mannitol) and hydroxyethyl starch that can not go through the cell membrane.

CPAs generally serve a protective role in cryopreservation by lowering potentially lethal concentrations of intracellular electrolytes. However, high concentrations of CPAs, used in vitrification, can be toxic to cells. This is a function of exposure and removal times of the CPAs as well as temperature. Toxicity can be reduced by lowering the temperature, reducing the CPA loading and unloading times, or using CPA cocktails [30]. In addition to cytotoxic considerations, osmotically induced changes in cell volume due to CPA addition and removal can also cause damage to cells if in excess. This issue will be discussed in more detail in the Mathematical Modeling section. Therefore, it is important to account for toxic and osmotic effects of CPAs on cells when designing cryopreservation protocols.

2.1.1.3 Conventional freezing and vitrification

Conventional freezing and vitrification are two main approaches to cryopreservation of biological materials. In the former process, as the system is controlled rate cooled (typically 0.1 – 1°C/min) in the presence of low concentration CPAs (1-2 M), extracellular ice forms first (the intracellular compartment is supercooled). As a result of this created osmotic imbalance, the intracellular solute concentrations in the unfrozen phase build up to a point that it can vitrify, or form an amorphous liquid (glass). A glassy state can be achieved intracellulary while the extracellular space is still comprised of ice [31]. This is schematically depicted in Figure 2.1A which shows that as the solute is cooled from step 1, the temperature-solute concentration profile follows the liquidus curve, step 2, and finally the solution concentration builds up sufficiently as it is cooled quickly to form a glass (step 3). The vitrification process is characterized by the formation of a glassy state

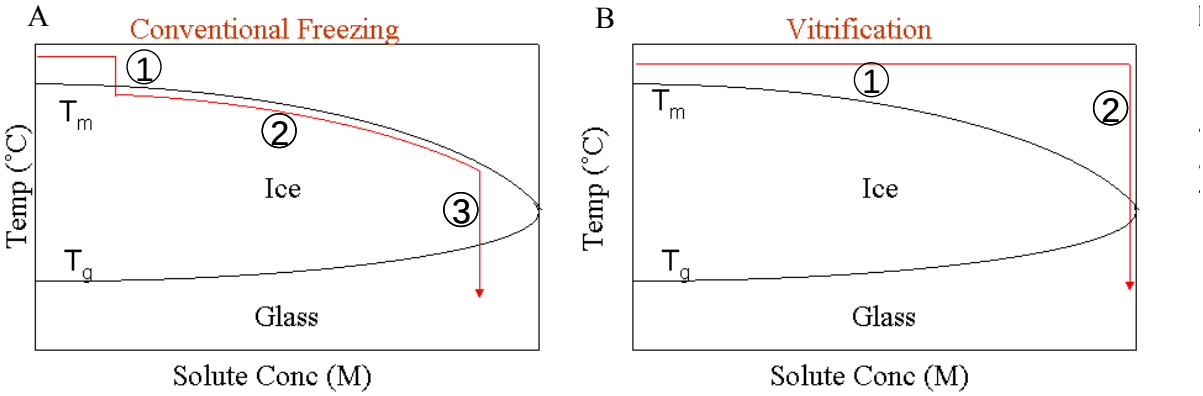

Figure 2.1 A. Temperature-solute concentration profile during conventional freezing; B. Temperature-solute concentration profile during vitrification

throughout the system, both intra- and extracellularly in attempts to avoid ice crystallization throughout. This is achieved by using high cooling rate in conjunction with high concentrations of CPAs (typically greater than 45 % w/w) as qualitatively indicated in Figure 2.1B [32-34]. As it is cooled below the glass transition temperature (T_g), high concentration CPAs become sufficiently viscous (greater than 10^{15} poise) to suppress ice crystallization and form an amorphous liquid glass where translational and rotational molecular motions essentially cease (at relevant time scales) [35]. The glass transition is associated with abrupt physical changes such as heat capacity, mechanical properties and reflective index. As discussed above, the warming rate is equally as important as the cooling rate. Adequate warming rates are necessary to avoid ice formation during warming that may arise from devitrification and recrystallization. Ice formed during thawing is just as deleterious as if formed during cooling. Devitrification refers to the process of crystallization upon warming of a glass (i.e., transition from glassy to crystalline state). This is different from recrystallization which refers to the

growth of smaller ice crystals (initially created during glass formation) upon warming [36].

2.1.2 Critical cryopreservation issues with cell suspensions, tissues and organs

Although cryopreservation has proven effective in shipping and storing isolated cells, multicellular systems still remain challenging. Over the years, cryobiologists have investigated the mechanisms of cryoinjury to cells during freezing and thawing and have developed methods to preserve numerous cell-types at very high recovery rates [3]. The methods center on preventing intracellular ice formation as well as minimizing changes in the remaining liquid phase that is not frozen. Maintaining high cell viability through freezing and thawing in cryopreservation protocols require the use of cryoprotective agents that are generally applied to cell suspensions or small cell aggregates in simple tissues. However, extending such protocols to more complex tissues and organs having definite structure has proven problematic, primarily due to the harmful formation of ice in multicellular structures [4, 5, 37, 38]. Tissue engineered constructs would be associated with similar problems. The presence of extracellular ice, though generally not harmful for cell suspensions, poses a major hazard for multicellular tissues. There has been evidence to suggest the damaging role of ice in tissue cryopreservation [4, 6]. Limiting the amount and size of ice formation during cryopreservation would avoid the inherent problems of extracellular ice formation from freezing. Based on this, many cryobiologists believe that the only way to successfully preserve complex tissues and organs is through ice-free cryopreservation approaches such as vitrification. Indeed previous studies have demonstrated improved preservation using vitrification over conventional freezing methods. This includes venous allografts, articular cartilage, heart valves, embryos and

islets [31, 37, 39-41]. Preliminary work in our lab with tissue engineered pancreatic substitutes has also supported this [42, 43].

Due to larger length scales in tissues and especially organs, heat and mass transport become limiting for successful cryopreservation. Issues in heat transfer include non-uniform cooling which can cause crystallization, and non-homogenous warming which can cause devitrification and recrystallization. Cooling problems contribute to stresses that may cause fractures [44-46] which provide nucleating sites for devitrification upon warming [47]. In order to address warming issues, electromagnetic techniques such as microwave warming have been used to achieve faster warming rates [48]. However, this approach suffers from non-uniformity as well as thermal runaway causing heat-denaturation of tissue. Mass transfer limitations for tissues and organs include long exposure times necessary to achieve adequate CPA equilibration for 3-D tissues with low CPA diffusivites, such as in articular cartilage [26]. Although diffusion and perfusion-based CPA delivery have been implemented, CPA cytotoxicity after a prolonged time remains a critical issue.

Another key issue with tissues and organs is cell population heterogeneity. Most tissues and organs contain multiple cell types with each cell type having its own optimal cooling rates and individual biophysical characteristics [3]. Due to this mixed cell population, preservation by conventional freezing would be challenging. The use of high concentrations of CPAs for ice-free preservation, on the other hand, would not suffer from these limitations as adequate CPA equilibration of the system would be sufficient for vitrification conditions. Though CPA delivery and removal times would need to be

carefully considered and designed, a conservative approach could still ensure maximal delivery with minimal cytotoxicity.

2.1.3 Mathematical modeling

At equilibrium, the chemical potential of the intracellular solution is equal to that of the extracellular solution. Due to the fact that the cell membrane is semi-permeable, water will move in or out of the cell in response to changes in the extracellular solution concentrations. During freezing, the extracellular solution becomes increasingly concentrated as the unfrozen water fraction diminishes. Water therefore leaves the cell until the chemical gradient is negated and osmotic equilibrium is reestablished. The equilibrium cell volume is a function of the extracellular solute concentration, expressed by the Boyle-van't Hoff equation [7]:

$$V = \pi_e^o (V_o - b)\frac{1}{\pi_e} + b \ , \qquad (1)$$

where π_e is the extracellular osmolality of the solution <osmolal>, b is the osmotically inactive cell volume <μm^3> and V_o and π_e^o are the isotonic cell volume <μm^3> and isotonic extracellular osmolality <osmolal>, respectively. Generally expressed as a Boyle-van't Hoff (BVH) plot, the relative cell volume, V/V_o, is expressed as a function of inverse osmolality. Extrapolation of this line to infinite osmolality (zero on the abscissa) has been used to estimate the osmotically inactive cell volume [49, 50]. When cells are exposed to an increased concentration of an effectively impermeant solute the cell will shrink to a volume defined by the BVH plot.

The rate of movement of water across the cell membrane is limited by the permeability properties of the membrane, namely water permeability, L_p , and solute permeability, P_s. The rate of change of the cell volume is dependent on the osmotic gradient across the membrane as well as the permeability of the membrane. When a cell is exposed to a hypertonic solution of a permeating solute, there is an initial abrupt shrinkage caused by water efflux determined by L_p, followed by a slower return to normal volume as the solute permeates at a rate determined by P_s (generally referred to as shrink/swell behavior) [7]. The fluxes of water and of the ith solute through the cell membrane are described by the following equations [51].

$$\frac{dV_w}{dt} = -L_p ART(M^e - M^i) \tag{2}$$

$$\frac{dN_i}{dt} = P_{si} A(M_i^e - M_i^i) \tag{3}$$

In the above equations, V_w (μm^3) is the volume of water inside the cell; L_p ($\mu m/sec \bullet atm$) is the water permeability; A (μm^2) is the surface area of the cell; R (($\mu m^3 \bullet atm$)/(mol•K)) is the universal gas constant; T (K) is the absolute temperature; M^e and M^i (osmoles/μm^3) are the total external and internal osmotic concentrations, respectively; M_i^e and M_i^i (osmoles/μm^3) are the external and internal osmotic concentrations, respectively of the ith solute; N_i (osmoles) is the intracellular amount of the ith solute; and P_{si} ($\mu m/s$) is the ith solute permeability.

When a cell is exposed to a CPA solution, initially water will leave the cell, (generally water efflux is higher than CPA influx) causing the cell to shrink (Figure 2.2). Though the cell volume will return to its isotonic state as the CPA solution permeates the

cell membrane and reaches equilibrium, excessive volume excursions can be harmful to the cells [52]. To address this issue, CPAs at high concentrations are usually loaded and removed in a stepwise fashion to reduce sharp fluctuations in cell volume. Additionally in stepwise dilution, sucrose, an impermeant solute, is often added to the extracellular solution to counteract the water influx that occurs during removal of permeant solutes from the extracellular solution [53, 54]. Examples of CPA addition and removal protocols for vitrification are listed in Table 2.1.

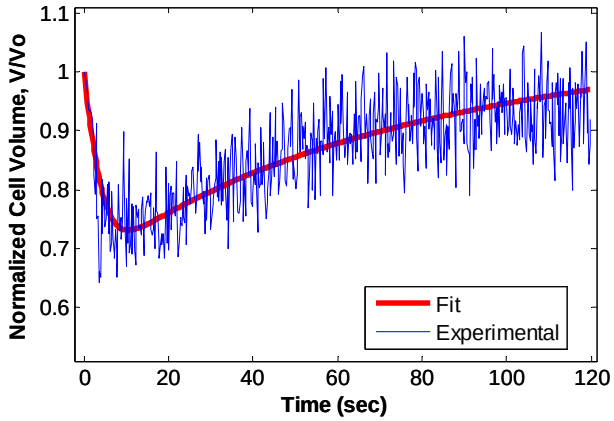

Figure 2.2 Shrink-swell behavior of βTC-tet cells in response to the abrupt addition of 10% dimethyl sulfoxide solution at t=0 at 22°C measured by an electronic particle counter (experimental). The solid line is a model fit of the data to determine membrane permeabilites [1]

Table 2.1: Examples of CPA Addition-Removal Protocols for Vitrification

Full Strength CPA	Addition Steps	Removal Steps	Carrier Solution	Cell type	Reference
7.2 M Ethylene Glycol (EG) + 0.6 M Sucrose	1) 1.775 M EG for 40 s 2) 3.55 M EG for 30 s 3) Full strength for 1 min	4) 0.4 M sucrose for 2-3 mins 5) 0.25 M sucrose for 2-3 mins 6) 0.125 M sucrose for 3-6 mins	10 mg/mL human serum albumin (HAS) in removal solutions	Human oocytes	[55]
5.5 M EG + 1 M sucrose	1) 1.5 M EG for 2.5 mins 2) Full strength for 20 sec	3) 1 M sucrose for 2.5 mins 4) 0.50 M sucrose for 2.5 mins 5) 0.25 M sucrose for 2.5 mins	DPBS + 10% FBS	Human oocytes	[56]

Table 2.1 (continued)

		6) 0.125 M sucrose for 2.5 mins 7) 0.0 M sucrose for 2.5 mins			
15% EG + (15% DMSO or 15% PD) + 0.5 M sucrose	1) 1.33 M EG + (1.06 M DMSO or 1.03 M PD) for 5 mins 2)Full strength for 1 min	3) 1.0 M sucrose for 1 min 4) 0.5 M sucrose for 3 mins 5) 0.0 M sucrose for 5mins	DPBS + 1 mg/mL glucose + 0.11 mg/mL sodium pyruvate + 20% FBS	Bovine oocytes	[57]
2.26 M DMSO + 2.84 M EG + 0.65 M sucrose + Ficoll	1) 1.13 M DMSO + 1.42 M EG for 1.0 min 2) full strength for 20 sec	3) 0.25 M sucrose for 1 min 4) 0.15 M sucrose for 2 mins 6) 0.0 M sucrose for 5 mins	G-MOPS + 12 mg/mL HAS	Mouse oocytes	[58]

2.1.4. Cell death due to cryopreservation

Much of the early improvements and optimization in the field of cryopreservation have centered on biophysical parameters, as described previously, such as cryoprotectant composition (type and concentration), cooling/warming rates, intra- and extracellular ice formation, osmotic excursions and membrane water and solute transport. However, post-thaw survival varies among protocols and cell types used, often ranging from 10-90% [59, 60]. Although post-thaw survival is often evaluated within hours of thawing, some studies have found concomitant cell death much later [61, 62]. Cell death as a result of cryopreservation generally falls into three groups: ice-related rupture, necrosis and apoptosis.

The first type of damage can be described by a mechanical or physical (e.g. osmotic imbalance) cell rupture where the nucleation and propagation of intra- and/or extracellular ice causes damage to intracellular organelles and cell plasma membrane. Ice-related cell damage has been studied extensively [7, 28, 63, 64] and efforts to prevent

or minimize it (such as vitrification) have been explored [34]. Necrosis, a common form of cell death following stress, is characterized by a rapid, energy-independent process in which the cell responds to insult by swelling, random DNA fragmentation by endonucleases, compromised cell membrane integrity, and finally cell lysis in which the contents of the cell are released. Because of this, an immunological response usually follows in an *in vivo* setting. The last form of death as a result of cryopreservation is gene-regulated cell death, or apoptosis.

Apoptosis, or programmed cell death, is ordered, energy-dependent, and has distinct morphological hallmarks including cell shrinkage, chromatin condensation, non-random DNA fragmentation, compartmentalization of intracellular components, intact cell membrane (until the end of apoptosis) and cellular fragmentation [65]. This cascade of events consists of the initiation, execution and termination phase and is induced by factors including UV radiation, nutrient stress, growth factor deprivation, ischemia and cryopreservation [2, 62]. Initiator pathways can be divided into nuclear, membrane and mitochondrial-mediated.

Stress-inducing agents can directly affect the nucleus to initiate apoptosis thereby damaging DNA. Damaged DNA is either repaired by the cell or leads to apoptotic cell death. A transcription factor, p53, regulates DNA repair by signaling the cell to go into cell cycle arrest (G_o phase) while the DNA is being repaired. DNA damage results in an upregulation of p53, inducing transcription of pro-apoptotic genes such as Bax and by activating endonucleases to cleave damaged DNA.

Another route of apoptosis initiation is via membrane-mediated cell surface receptors which signal specific transduction pathways for cell death (Figure 2.2). The

protein receptors belong to the Tumor Necrosis Factor (TNF) superfamily and include Fas and TRAIL [66]. Apoptosis is initiated through ligand binding to the receptor or by self-dimerization of the receptor. In the case of the Fas receptor, Fas ligand (FasL) binds to the receptor or the Fas receptor self-dimerizes; in either case, this causes recruitment of FADD (Fas-associated death domain protein) adaptor protein which promotes binding of pro-caspase-8 or -10. Binding of this complex causes autocatalysis and activation of these pro-caspases into their active form, caspase-8 and -10, which then activate caspase -3 and -7, signaling the execution phase of apoptosis.

Mitochondria are susceptible to stresses that can initiate an apoptotic cascade after cryopreservation-induced insult causing a change in mitochondrial permeability transition pore activity. Regulated and prevented by the Bcl-2 family of proteins, antagonists include Bax, Bad that heterodimerize with Bcl-2 to inhibit its action. This leads to the release of cytochrome c into the cytosol which heterodimerizes with cytosolic APAF-1 to activate caspase-9 via proteolytic activation of pro-caspase 9. Caspase-9 activation leads to caspase-3 and -7 catalysis, which then activate endonucleases that cleave DNA and results in cell death [67].

Recently, a molecular basis of cryopreservation-induced delayed onset cell death (CIDOCD) has been implicated in contributing to cell death mainly via apoptosis [61, 68]. Despite using similar cryopreservation protocols, Baust et al measured lower cell viabilites 24 hours post-thaw compared to other reports that assessed survival 1-6 hours later for cell types including MDCK, human fibroblasts and human renal cells [69]. The authors attribute this discrepancy in reported values to CIDOCD and suggest evaluating viability 24 hours post-thaw to allow the

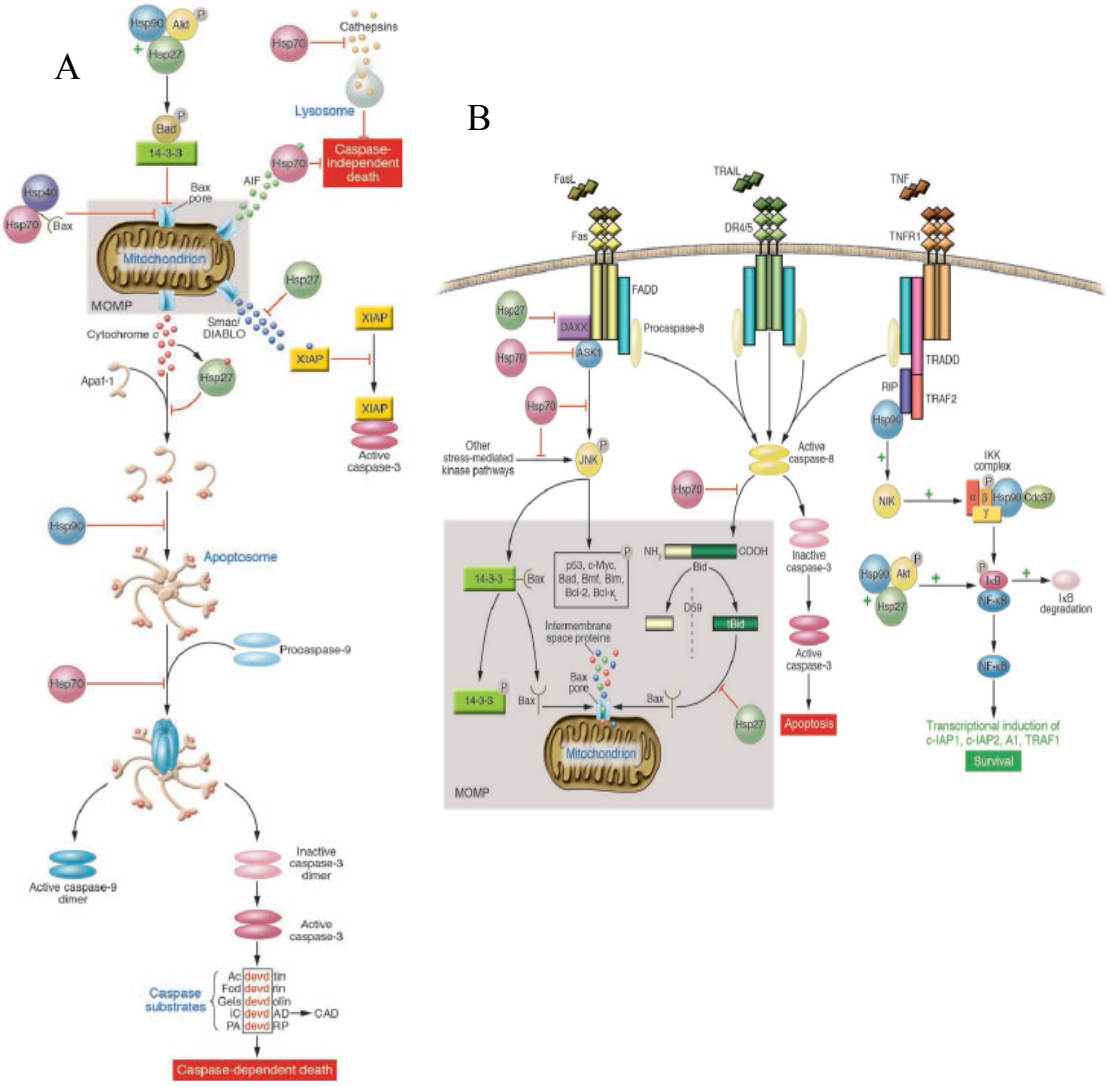

Figure 2.3 A. Mitochondrial-mediated apoptosis pathway. B. Membrane-mediated cell surface receptor-initiated apoptosis pathway [2]

system to reach "survival equilibrium" following the peak of CIDOCD and prior to cell proliferation [61, 62]. Initiation of apoptosis post-cryopreservation has been shown for membrane-mediated Fas-receptor initiation through caspase-8 activation for human fibroblasts [70] and activation of caspase-9 for spermatozoa [67]. Executioner caspases, such as caspsase-3, are activated post-thaw and their inhibition can reduce cryopreservation associated cell death [71-75]. Yagi et al demonstrated that mitochondrial injury, measured by mitochondrial membrane potential, is reduced by caspase inhibition for primary porcine hepatocytes [74]. In addition to using caspase inhibitors, Sarkar et al used cytokine combination treatment (IL-2, IL-4, IL-7) to rescue $CD4^+$ T-cells from cryopreservation-mediated cell death [75]. All these studies suggest that programmed cell death following cryopreservation is important to characterize and study, and strategies to minimize its effects can greatly increase cell survival post-thaw.

2.2 Diabetes mellitus and treatment options

Diabetes mellitus is becoming a worldwide epidemic, currently affecting more than 170 million people worldwide according to the World Health Organization (WHO) with numbers predicted to double within the next two decades. In the United States alone, there are approximately 18.2 million people afflicted with Type 1 or Type 2 diabetes, costing over $132 billion dollars in direct and indirect costs. Type 1 diabetes, comprising 10% of the diabetic population, is an autoimmune disease in which the body's own immune system attacks and kills the insulin-producing cells (β-cells) located in the islets of Langerhans of the pancreas. This renders the patient unable to produce insulin, leaving blood glucose levels to fluctuate outside the physiologically normal range. As a

result, the patient is dependent on exogenous sources of insulin for glucose regulation. The current treatment of insulin-dependent diabetes involves monitoring blood glucose levels and daily bolus insulin injections or by subcutaneous or intraperitoneal insulin delivery via pumps. Type 2 makes up the majority of diabetics, and it is characterized by the ineffectiveness of insulin produced or insulin resistance. Its causes are both genetic and environmental, associated with increased age, unhealthy diet and sedentary lifestyle. Treatment includes proper diet, exercise and drugs (such as sulfonylureas). A subpopulation of Type 2 diabetics may eventually rely upon insulin injections to maintain normoglycemia and thereby fall into the same category of insulin-dependent diabetics as Type 1.

Despite glycemic control by daily insulin injection therapy, the relatively poor regulation of insulin delivery leads to numerous complications. Complications may include retinopathy, neuropathy, nephropathy and microvessel damage. The Diabetes Control and Complications Trial of 1993 concluded that tight glycemic regulation delays and reduces diabetic-related complications [76]. Bolus insulin injections do not provide the physiologically tight glycemic control offered by the native pancreas and so alternative approaches are needed.

Cell-based therapies are an attractive approach to address insulin-dependent diabetes due to the cells' innate machinery for regulated insulin release in response to physiologic changes in glucose levels. Based on this motivation, islet transplantation has become a potential approach, especially since the promising results of the Edmonton Protocol. This study showed that cadaveric human islet transplantation via intraportal vein delivery of islets without the use of glucocorticoid-based immunosuppression can

result in long-term insulin independence, via intraportal vein delivery of islets [77]. However, the use of long-term immunosuppression and availability of donor tissue makes this therapy, although promising, limited.

2.2.1 Tissue Engineered Pancreatic Substitute

Tissue engineering holds the potential to alleviate some of the stresses of tissue and organ shortages for replacement therapy of insulin-dependent diabetes [12]. Moreover, it has the potential to provide a more physiologic, less invasive and potentially less costly treatment for type I diabetes. The potential market for pancreas replacement products is expected to be a rapidly growing target segment over 1999-2010, expanding at a 6.8% compound annual rate due to increases in the incidence of diabetes. Based on 1999 patient populations and pricing estimates, the potential U.S. market for the tissue engineered bioartificial pancreas is approximately $2.5 billion [78].

Currently there exist several designs for a tissue engineered pancreatic substitute. Typically, these constructs utilize insulin-secreting cells surrounded by a semi-permeable membrane. This membrane allows for the passage of nutrients and metabolites (such as glucose and insulin), but excludes larger antibodies and immune cells of the host. Cell encapsulated construct designs include vascular devices, diffusion chambers and the most common, microcapsules. The advantages of the microcapsules include a high surface area to volume ratio and also ease of handling. A major disadvantage includes difficulty in retrieval post-transplantation. Typically, the size of these beads range from hundreds of microns to about one millimeter. The most prevalent type is comprised of an alginate gel coated with poly-L-lysine (PLL) with an outermost layer of alginate, which is

commonly referred to as an alginate-poly-l-lysine-alginate (APA) bead. This is based on the encapsulation system of Lim and Sun [79].

2.2.2 Pancreatic Substitute Construct Composition: Alginate and poly-L-lysine membrane

Alginate is a common term for the family of unbranched polymers (block-copolymers) of 1,4-linked β-D-mannuronic acid (M) and α-Lguluronic acid (G) residues that vary in proportion, sequence and molecular weight depending on the type and source of alginate. The gelation of alginate occurs when divalent or multivalent cations, typically Ca^{2+}, interact ionically with blocks of G residues between two different chains resulting in a three-dimensional network [80]. The strength of this network depends on the overall fraction of G residues, in particular the frequency and length of contiguous G blocks, and the ion concentration at the time of gelation [81]. The physical properties of alginate gels vary depending on their chemical composition; for example, a high G alginate is characterized by a stiffer and more porous gel whereas high M content alginates are softer and less porous [82, 83]. Tanaka et. al. found that the diffusion coefficients of solutes under $2x10^4$ molecular weight into and out of alginate beads agree with those in a free water system [16].

The alginate gel is usually coated with poly-L-lysine as it provides structural support to the bead as well as it acts as an immune barrier. The poly-L-lysine membrane can be adjusted to have a molecular weight cutoff of 45-60kDa [15], thus allowing small solutes to pass through (such as glucose, insulin and dissolved oxygen) while excluding larger molecules, such as antibodies, and whole cells, such as macrophages.

2.2.3 Insulin-secreting insulinoma cells

In the development of a tissue engineered pancreatic substitute, cell sourcing is a major issue. The use of human or porcine primary pancreatic cells is associated with limited availability, including difficulty in cell amplification with also a loss of phenotype with culturing time [84]. Hence, researchers have tried to find more phenotypically stable cell lines that can also be easily amplified. Examples include engineered non-β-cells, stem cells and transformed β-cells [85].

Efrat et al. have developed continuous murine β cell lines (βTC), derived from insulinomas arising in transgenic mice that express the simian virus 40 (SV40) T antigen (Tag) in β cells under control of the insulin promoter [86]. They can easily proliferate under normal culturing conditions and retain their phenotype over a range of passages. An obstacle to the use of transformed β-cell lines in transplantation is their uncontrolled proliferation. To address this drawback, Efrat et al. used the tetracycline conditional gene expression system to regulate Tag activity in β cells from transgenic mice. A βTC line developed from these mice, βTC-tet, is strictly dependent on Tag expression for its proliferation. In the absence of tetracycline, the Tag transgene is expressed and maintains the cells in continuous proliferation. In the presence of tetracycline, Tag expression is tightly shut off, leading to a complete arrest of cell replication. The regulation is reversible, allowing resumed cell growth upon removal of tetracycline. This system offers an efficient way for cell expansion in culture and for regulation of cell numbers after transplantation [87]. The ability to easily amplify these cells in culture as well as control their proliferation with tetracycline makes these glucose-responsive insulin producing cells an attractive cell source for a pancreatic substitute.

2.2.4 Cryopreservation of encapsulated cell systems

Despite the advantages and applications of encapsulated cell systems, there have been limited studies on the ability to cryopreserve such systems for long-term storage. Due to the soft, hydrogel composition of these systems, they are particularly susceptible to freezing injury. Results in the field have been mixed, with reports of varying cell viabilities and extent of matrix damage post-thaw [42, 88-97]. Most published studies have used slow cooling with 5-20% DMSO. In one study the necessary incubation time in DMSO was found to be 5 hours [98] for optimal cell survival. This is surprising as studies in our lab found DMSO to diffuse in alginate beads in a few minutes (see CHAPTER 5). A detailed study by Heng et al varied cooling rates, CPA type and composition and the use of non-permeating CPAs (sucrose, ficoll) for cryopreserving African green monkey kidney cells encapsulated in alginate microbeads [91]. They found slow cooling with a range of DMSO and ethylene glycol (EG) concentrations resulted in a high post-thaw cell viability of 80-85%, with ~60% of the microcapsules remaining intact when 2.8 M DMSO and 2.7 M EG were used. The presence of 0.25 M sucrose significantly improved post-thaw cell viability upon slow cooling with 2.8 M DMSO, though it had no effect on microcapsule integrity. Rapid cooling with 3.5 or 4.5 M DMSO resulted in <10% cell viability with retention of bead integrity. Studies in our lab have shown vitrification to be a promising approach for long-term storage of alginate microcapsules, retaining cell viability, function and capsule integrity. Ice formation due to slow freezing and low concentrations of DMSO caused cryodamage [42, 43]. Kuleshova et al. have published a few studies on vitrification of encapsulated hepatocytes [92, 96]. In the first study, they used 40% (w/w) EG and 0.6 M sucrose to vitrify

collagen-encapsulated hepatocytes. This method was a modification of a cryopreservation protocol used for embryos and oocytes [91]. The second paper utilized the same CPA solution to successfully vitrify M- and G- collagen-encapsulated hepatocytes in cryostraws. With this method, however, scale-up would be a critical issue to address as cryostraws only allow volumes of 250 μL to be preserved.

2.3 Embryonic Stem Cells (ESCs)

2.3.1 Embryonic Stem Cells

Embryonic stem cells hold great promise for cell-based therapies, tissue engineering and basic science research due to their self-renewal potential and ability to differentiate into any cell type [99-102]. ESCs are isolated from pluripotent cells of the developing blastocyst, and when implanted *in vivo,* they have been shown to differentiate into bone, cartilage, muscle and epithelium [103].

2.3.2 Embryonic Stem Cell Preservation and Encapsulation

2.3.2.1 ESC Cryopreservation

Cryopreservation of murine embryonic stem cells (mESCs) has been successfully achieved and well established, similar to methods used to cryopreserve commonly used cell lines [104]. This usually includes the use of low concentration cryoprotectants (1-2 M), such as dimethyl sulfoxide (DMSO) and ethylene glycol (EG), which are added to the single cell suspension and cooled in a cryovial at a slow cooling rate (1 to 5°C/min) down to -80°C and then plunged into liquid nitrogen. Samples are thawed rapidly in a 37°C water bath, CPA is then removed typically in a single-step by dilution in culture

media and after centrifugation the cells are returned to culture flasks. This typically results in over 80% cell survival and the cells remain undifferentiated [104]. Unfortunately, human embryonic stem cells (hESCs) that are cryopreserved with this slow cooling, rapid thaw approach suffer from low viability and spontaneous cell differentiation. It is believed that intimate physical contact and cell-cell signaling are essential for hESC survival and pluripotency [105-108]. Due to this need for cell-cell association, it is thought that successful cryopreservation of hESCs would be as cell colonies, not single cell suspensions such as for mESCs [106]. Challenges with cryopreservation of cell aggregates include ensuring adequate CPA equilibration throughout the cell cluster, while minimizing CPA cytotoxicity for the outermost cells; and ice formation that may occur during freezing that can damage the gap junctions and other cell-cell interactions that are required for normal hESC function. Indeed studies employing slow cooling for cryopreservation of hESCs colonies have resulted in very poor post-thaw survival, with studies reporting 10-20% viability, with often times the cells becoming differentiated [107, 109-112]

Due to the damaging effects of ice formation, vitrification, or ice-free cryopreservation, is an attractive approach for long-term storage of hESCs. Using a combination of high concentration cryoprotectants and rapid cooling and thawing rates, ice crystallization can be avoided and instead water achieves an amorphous glass. Studies applying vitrification have reported higher hESC survival, greater than 75%, than conventional slow freezing [111-113]. Moreover, these studies demonstrated that a large proportion of post-thawed cells remained undifferentiated, though colony size and growth were reduced compared to fresh controls.

2.3.2.2 ESC Encapsulation

In addition to vitrification, cell entrapment in gels may offer protection during cryopreservation that might otherwise be absent to naked cells. Hepatocytes that were cryopreserved in alginate hydrogels or sandwiched in between collagen had higher viabilities and metabolic function post-cryopreservation than their cell suspension counterparts [93, 114, 115]. In addition, adherent hESC colonies on tissue culture plates were coated in Matrigel and slowly cooled. Cryopreserving adherent hESC colonies directly on culture plates led to improved viability and less cell differentiation than hESC colonies cryopreserved as a cell suspension ($3x10^5$ viable cells/plate vs. $0.2x10^5$ viable cells/plate) [116].

The use of entrapped ESCs in 3-D alginate beads is an attractive system that can potentially promote ESC expansion, embryoid body (EB) formation and terminal differentiation. This would be valuable for tissue engineering applications, such as skeletal engineering, for the formation of bone. Using bioreactors, this system would allow for automation and optimization of a bioprocess to yield adequate cell numbers for clinical therapies [17, 18]. For example, batches of encapsulated ESCs could be expanded up to a specific cell density and then cryopreserved. After thawing, they would be driven towards EB formation and down a specific tissue lineage. Alternatively, the beads could be cryopreserved further downstream in the bioprocess, after expansion and EB formation, and then driven towards terminal differentiation after thawing. These strategies are currently being explored.by colleagues at Imperial College.

2.4 Articular Cartilage

2.4.1 Articular Cartilage Composition, Structure and Function

Articular cartilage (AC) is a dense, hydrated soft tissue that lines the articulating surfaces of joints. On a wet weight basis, it is composed of 70-85% interstitial fluid, 10-20% collagen, and the remainder is glycoproteins, lipids and proteins [117]. Its primary physiologic function is mechanical, providing a remarkably low friction bearing surface, and serving to distribute joint loads over a larger area [117]. The biochemical composition and structure of the extracellular matrix allow it to perform these functions, and damage of the structure due to disease or trauma can significantly impair the tissue's mechanical function. Adult articular cartilage generally contains chondrocytes, composing 5-10% of the total tissue volume [118].

The primary collagen in articular cartilage is collagen type II, which forms a fibrillar network with a well defined ultrastructural organization. Small amounts of other collagens such as types VI, IX, X, XI, XII and XIV are also found in articular cartilage [119, 120]. The collagen's network provides the majority of the tissue's mechanical strength due to collagen's high tensile stiffness. Within the tissue, negatively charged macromolecules interact with the positively charged, ionic interstitial fluid, leading to a substantial osmotic swelling pressure [117]. Within the tissue, the matrix constituents are organized in a specific zonal order [121]. Relative to tissue wet weight, the collagen content is greatest at the surface and decreases with depth, the proteoglycan content is lowest at the surface and greatest in the middle, and the water content is greatest at the surface and decreases with depth [122]. The unique composition and organization of the zones in articular cartilage allow it to perform its distinct biomechanical role.

2.4.2 Articular Cartilage Defects and Treatment

Compression forces or shear stress on the articular surface can lead to cartilage damage. This results in subsequent loss of normally functioning cartilage causing pain and swelling. During healing, chondrocytes respond to injury by secreting matrix macromolecules but often do not reach the damaged site due to the dense extracellular matrix inhibiting transport. Due to the avascularity of cartilage, healing is slow and minimal. Clinicians have explored several treatment options for patients with articular cartilage defects. Therapeutic interventions without active biologics may involve lavage and arthroscopy, and microfracturing and drilling [123]. A commercialized technology by Genzyme Biosurgery (Carticel™) involves harvesting healthy cartilage from the patient and expanding chondrocytes in cell culture. After expansion the chondrocytes are returned to the surgeon for implantation where a periosteal flap is taken from the tibia and placed over the cartilage defect, and the chondrocytes are injected into the defect beneath the periosteal flap. Another treatment option could potentially involve taking cartilage plugs that have been stored in liquid nitrogen and use it to repair the injury site. Clinical application of cryopreserved allogeneic osteochondral grafts would not have regulatory hurdles as the tissue would not have been altered in any way. Because cartilage is avascular implanted cryopreserved-thawed allogeneic cartilage would not suffer immune rejection from the recipient's body.

2.4.3 Preservation of Chondrocytes and Cartilage

Isolated chondrocytes can be preserved using conventional cryopreservation methods involving freezing; however, currently there is no satisfactory method to consistently preserve cartilage tissue [23, 24]. Studies using various animal articular cartilage models [21, 22, 124, 125] and human cartilage biopsies [126] have revealed less than 20% chondrocyte viability following conventional cryopreservation procedures employing either DMSO or glycerol as cryoprotectants. Ohlendorf et al. [22] used a bovine articular cartilage osteochondral plug model to study a clinical cryopreservation protocol, which employed slow cooling and 8% DMSO as the cryoprotectant. They observed loss of viability in all chondrocytes except those in the most superficial layer at the articular surface. Using ovine cartilage, Muldrew et al. [124] found viable cells post-cryopreservation close to the articular surface and deep at the bone/cartilage interface, whereas the middle layer was devoid of viable cells. The reason for lack of cell survival deeper than the superficial layers of articular cartilage is most likely multifactorial, but seems to be related principally to mass and heat transfer considerations [27]. Typically employed concentrations of DMSO (8-20%) may not penetrate adequately to limit intracellular ice formation, resulting in cell death and lysis and the release of intracellular enzymes that may further damage the neighboring matrix [26]. Extracellular ice may not directly damage the cells, but it does damage the matrix resulting in inferior biomechanical properties. Recent studies by Pegg and co-workers indicate that ice forms preferentially within the chondron instead of the surrounding acellular matrix [23].

To avoid ice formation and consequent tissue damage, a limited number of studies have investigated vitrification as a means for preservation; however, results are few and

varied. Studer and co-workers [127] were able to vitrify 150 μm thick segments of bovine articular cartilage by freezing at high pressures, and Jomha et al [128] partially vitrified porcine articular cartilage using high concentration of DMSO and rapid cooling. Song and co-workers [25] were able to successfully vitrify rabbit articular cartilage plugs using a baseline protocol utilizing VS55, a vitrification solution. In this latter study, preserved and fresh control plugs were implanted in the tibial plateau of allogeneic recipients, and the plugs were examined histochemically upon explantation. Fresh and vitrified explants had essentially the same histology, whereas conventionally frozen grafts were devoid of chondrocytes and only fibroblast-like cells were observed. More recently, Pegg et al. [129] developed a liquidus-tracking method, which prevented the crystallization of ice during vitrification of ovine articular cartilage and did not require rapid warming. Cartilage preserved this way incorporated sulfate into newly synthesized glycosaminoglycans (sGAG) at approximately 70% of the rate of fresh control cartilage. Due to mass and heat transport limitations, despite success with small dimension AC, cryopreservation of clinically relevant sized plugs remains a challenge.

CHAPTER 3

EFFECTS OF CRYOPRESERVATION ON CELL VIABILITY AND INSULIN SECRETION IN A MODEL TISSUE ENGINEERED PANCREATIC SUBSTITUTE[1]

3.1 Abstract

The use of encapsulated insulin-secreting cells constitutes a promising approach towards the treatment of insulin-dependent diabetes. However, long- term storage for off-the-shelf availability still remains an issue which can be addressed by cryopreservation. This study investigated cryopreservation of a model tissue engineered pancreatic substitute by two ice–free cryopreservation (vitrification) solutions (designated VS55 and PEG400) in comparison to a conventional freezing protocol. The model substitute consisted of insulin-secreting mouse insulinoma βTC3 cells entrapped in calcium alginate/poly-L-lysine/alginate (APA) beads. Cell viability and static insulin secretion from the thawed cryopreserved groups were characterized and compared against fresh controls. Cell viability tests using alamarBlue® showed that, as compared to the fresh groups, the VS55 had the highest viability ($p<0.05$), followed by both the PEG400 ($p<0.001$) and the frozen groups ($p<0.001$). In response to a square wave of glucose, the static insulin secretion data showed that the VS55 and PEG400 groups had similar induction levels against the fresh group, whereas the frozen group had the poorest secretion rate. Cryosubstitution of capsules showed ice formation in the frozen group but no ice in the

---

[1] Modification of a paper published in **Cell Transplantation**, 14(7): 449-456 (2005).

vitrified groups. Microscopic observations revealed holes and/or tears within beads subjected to freezing, whereas no such abnormalities were detected in the vitrified samples. Overall, vitrification was found to be a promising preservation procedure for this encapsulated cell system.

3.2 Introduction

The use of encapsulated insulin-secreting, glucose-responsive cells constitutes a promising approach towards treatment of insulin-dependent diabetes by offering a more effective and less invasive alternative to insulin injections. Studies using both small and large diabetic animal models [79, 130-133] have shown restoration of normoglycemia for various periods of time following the implantation of encapsulated allogeneic or xenogeneic cells. In spite of these advances in the field, there remain several critical issues to be addressed, including long-term storage of encapsulated cell systems. Indeed, it is anticipated that encapsulated cells will be fabricated at a centralized location, and long-term preservation would be essential for off-the-shelf availability of the product.

One possible route to address this is through cryopreservation. Pioneering work done by Polge and others found that chemicals such as glycerol [29] and dimethyl sulfoxide (DMSO) [63] protected biological materials during freezing and thawing. Traditional cryopreservation utilizes permeating cryoprotectants at low cooling rates or non-permeating cryoprotectants at high cooling rates to reduce ice formation [27]. However, when cryoprotectants are used in high concentrations (6-9M) [34] in conjunction with very high cooling rates, ice formation can be avoided altogether during freezing and thawing; this is known as vitrification. Vitrification refers to the physical process by which a concentrated solution of cryoprotectants solidifies during cooling

without crystallization. The solid, called a glass, retains the normal molecular and ionic distributions of the liquid state and is therefore usually considered to be an extremely viscous supercooled liquid. Ice-free preservation is expected to be advantageous for biological systems by avoiding the harmful effects of ice formation associated with conventional freezing.

Indeed previous studies have demonstrated improved preservation using vitrification over conventional freezing methods. With regard to pancreatic tissue in particular, Jutte et al. reported successful vitrification of both mouse and human islets [134, 135]. Furthermore, Bodziony et al. [41], comparing vitrification of rat pancreatic islets to six other cryopreservation protocols, found no significant viability difference between the vitrified and the other groups; however, the vitrified group was the only one with glucose-stimulated insulin secretion comparable to the control. In other studies exemplifying the versatility of the vitrification process, venous allografts, articular cartilage and heart valves were shown to have better preservation over conventional freezing [37, 39, 136]

This study investigated cryopreservation of a model tissue engineered pancreatic substitute by two vitrification solutions, a baseline VS55 solution and one incorporating 400 molecular weight polyethylene glycol, in comparison to a conventional freezing protocol. The model substitute consisted of insulin-secreting mouse insulinoma βTC3 cells entrapped in calcium alginate/poly-L-lysine/alginate (APA) beads, which has been shown to be a functional, scaleable pancreatic substitute [10, 15, 137]. Cell viability and insulin secretion properties post-vitrification and post-freezing were characterized and compared against controls. Overall, vitrification was found to be a promising

preservation procedure for this encapsulated cell system with the potential to be applicable to other tissue substitutes as well.

3.3 Materials and Methods

APA-encapsulated βTC3 cells were prepared at Georgia Institute of Technology (Georgia Tech) and shipped to Organ Recovery Systems, Inc. (ORS) by overnight express at ambient temperature in T-flasks filled with supplemented DMEM. At ORS, encapsulated cells were cryopreserved (vitrified and frozen), and specimens were also subjected to histology and cryosubstitution. Cell viability in thawed and non-preserved beads was assessed with alamarBlue®. Specimens were also subjected to static insulin secretion tests; samples from these insulin secretion tests were shipped to Georgia Tech on dry ice overnight for analysis by radioimmunoassay. Tests performed to evaluate an appropriate method for shipping encapsulated cells between the two places found that delivery in media-filled T-flasks at ambient temperature retained high cell viability (77-89%).

3.3.1 Cell and Cell Culture

βTC3 cells were obtained from the laboratory of Dr. Shimon Efrat, Albert Einstein College of Medicine, Bronx, NY [86]. Monolayer cultures were initiated from frozen stocks and cultured in T-flasks in complete growth medium consisting of Dulbecco's Modified Eagle's Medium (DMEM) (Fisher Scientific, Fairlawn, NJ) supplemented with 1% glutamine (Sigma Chemical Co, St. Louis, MO), 15% heat-inactivated horse serum (Sigma), 2.5% fetal bovine serum (Hyclone, Logan, UT) and 1% penicillin/streptomycin (Fisher Scientific). Cultures were incubated in a 37°C, 5% CO_2,

humidified incubator. Cells were split at ratios of 1:5 when confluent and used between passage numbers of 38 and 44.

3.3.2 Fabrication of beads

βTC3 cells were entrapped in calcium alginate/poly-L-lysine (PLL) /alginate (APA) beads using previously published protocols [10, 13], briefly as follows: cells were detached from monolayer cultures by trypsinization (0.05% Trypsin-EDTA, Mediatech Cellgro, Herndon, VA) and suspended at a density of $3x10^7$ cells/mL alginate in a filter-sterilized solution of 2.0% sodium alginate (ISP Alginates, Inc, San Diego, CA) in 0.85% aqueous NaCl. The suspension was added in dropwise fashion into an 1.1% $CaCl_2$ bath, forming beads of gel containing entrapped cells; beads were then coated with poly-L-lysine and finally with an outer layer of 0.20% alginate. The beads were made with an electrostatic droplet generator (Nisco Engineering AG, Zurich, Switzerland) and ranged from 500-650μm in diameter. Beads were incubated with culture media in T-flasks placed on an orbital shaker in a 37°C, 5% CO_2, humidified incubator.

3.3.3 Vitrification and Conventional Freezing Protocols

VS55 was used as the base line vitrification solution composed of 3.1 M DMSO, 2.2 M 1,2 propanediol and 3.1 M formamide [7]. It has been reported that combinations of low concentrations of cryoprotective agents (CPA) with 400 molecular weight PEG are extremely effective at controlling ice formation [31]. This vitrification solution (noted as PEG400) consisted of 5M propanediol, 1M DMSO and 12% PEG 400. The times needed for loading and unloading the vitrification solutions were derived based on CPA permeation studies, which showed that the time to equilibrium in APA beads is of the order of 2-3 minutes (data not shown). After addition of the final vitrification solution,

encapsulated constructs were cooled rapidly (43°C/min) to -100°C, followed by slow cooling (3°C/min) to -135°C, and finally stored in a freezer at -135°C for a minimum of 24 hours. These samples were either warmed for further study, or cryosubstituted to determine the location and distribution of ice, if any, within the constructs. A thermocouple was inserted into a separate dummy sample of the same vitrification solution without any beads, and its output was monitored via a digital thermometer. Vitrified samples were rewarmed in two stages: first, a slower warming to -100°C (30°C/min) and then rapid warming to melting (225°C/min). The slower warming rate was achieved by moving the sample to the top of the -135°C freezer. The fast warming rate was generated by placing the glass vial in a mixture of 30% DMSO/water at room temperature [37].

Conventional cryopreservation was used as the frozen control [38]. Briefly, samples were initially immersed for 20 min in DMEM containing 10%DMSO-10% fetal calf serum at 4°C. Samples were then cooled at a controlled rate of 1.0°C/min to -80°C and finally transferred to liquid nitrogen for storage. Thawing was accomplished by immersing the containers in a water bath controlled at 37°C until all ice had visibly disappeared, whereupon the containers were transferred to an ice bath for elution of the DMSO. This was achieved in sequential steps in which the samples were transferred to DMEM containing 0.5M, 0.25M and finally 0.0M mannitol as an osmotic buffer.

3.3.4 Cryosubstitution, Histology

Cryosubstitution is a technique in which tissue is preserved at subzero temperatures using organic solvents to dissolve ice [138]. In this way the profile of any ice domains can be revealed in the frozen or vitrified samples. Cryosubstitution of the

cryopreserved beads took place at -90° C using a substitution solution of methanol and osmium tetroxide. Vials containing samples and substitution mixture were placed in a heat sink to maintain the temperature of the mixture constant. The substitution solution was changed three times over a five-day period, then the heat sink and samples were transferred to -20°C for 24 hours. Following that, the temperature was changed to 4°C for two hours and finally to room temperature. Beads were transferred to 100% acetone followed by the addition of Araldite resin, embedded, polymerized and sectioned for examination under a light microscope.

3.3.5 Cell viability measurement

The alamarBlue® (BioSource International, Inc.) assay was used to assess the cell viability of the APA beads pre- and post- cryopreservation. For these experiments, 100 μL of beads, 100 μL alamarBlue® and 1 mL DMEM were placed into a 24- well plate (3 wells for each bead type). Controls were also used in which 100 μl alamarBlue® and 1 mL DMEM were put into the wells. After proper mixing, the 24- well plate was placed into a 37˚C/5% CO_2 incubator for 3 hours. Following incubation, 100 μL of medium from each well, including controls, were placed into a 96-well microtiter plate for reading. The plate was read with a Spectra Max Gemini Plate Reader using an excitation wavelength of 544 nm and an emission wavelength of 590 nm. All readings were normalized to initial cell number.

3.3.6 Static Insulin Secretion Protocol

Insulin secretion tests were performed on APA Beads with βTC3 cells before and after several methods of cryopreservation to evaluate their insulin secretion in response to a square wave of glucose. For each experiment, approximately 0.5 mL beads and 12 mL

of medium were placed in a flask on an orbital shaker in a 37°C/5% CO_2 incubator. Beads were exposed for two hours to glucose-free (basal) DMEM medium with sampling at hours 1 and 2 (with rinsing and replacement of basal medium at each hour), followed by exposure to 8 mM of glucose-supplemented medium for 2 hours with sampling at hours 3 and 4 (with rinsing and replacement of glucose-supplemented medium at each hour), and finally 2 hours of exposure to basal medium with sampling at hours 5 and 6 (with rinsing and replacement of basal medium). To account for small variations in cell number per bead and volume of beads in each experiment, the highest secretion rate of each set of cultures studied in parallel was set equal to 1 and the other secretion rates were normalized relative to that value. Insulin concentrations were measured by radioimmunoassay (Linco Research, St. Charles, MO) following the manufacturer's protocol.

3.3.7 Statistical Analysis

Statistical analyses were done using one-way ANOVA with Tukey's multiple comparison test with a sample size consisting of replicate experiments of n=5 for fresh, VS55 and frozen groups and n=4 for PEG400 group. All results with a value of $p<0.05$ were considered statistically significant.

3.4 Results

APA-encapsulated βTC3 cells were cryopreserved using two vitrification and one conventional freezing protocols. Capsules were assessed post-preservation to evaluate bead morphology and structure, cell viability, and insulin secretion in response to glucose.

Cryosubstitution fixation and staining of sections show the appearance of the APA beads after freezing (Figure 3.1A) or vitrified storage (Figure 3.1B). Light microscopy of toluidine blue-stained bead cross-sections illustrates extensive ice crystal formation in frozen beads (Figure 3.1A), but no ice formation in vitrified samples (Figure 3.1B).

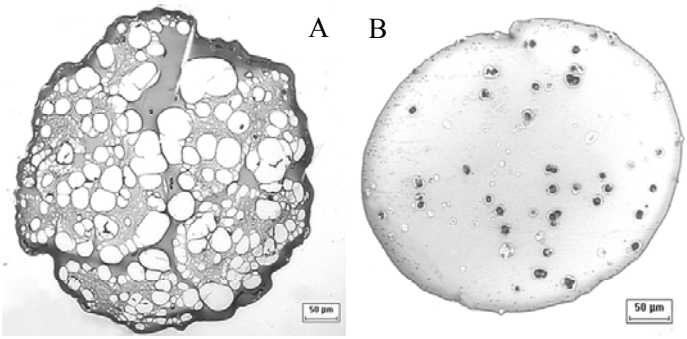

Figure 3.1 Morphology of frozen and vitrified beads at –90°C. Freeze substitution of controlled-rate frozen beads shows considerable ice formation throughout the construct (A). Freeze substitution of vitrified beads shows the absence of ice in the construct (B). Light microscopy sections were stained with toluidine blue; scale bars represent 50µm.

Histological sections of fresh, frozen, and vitrified samples were compared by light microscopy (Figure 3.2). There were extensive fractures (tears) and vacuolation in the constructs of frozen specimens (Figures 3.2 B, C). On the other hand, there were no observable fractures and vacuolation was lower in the vitrified specimens (Figures 3.2 D, E).

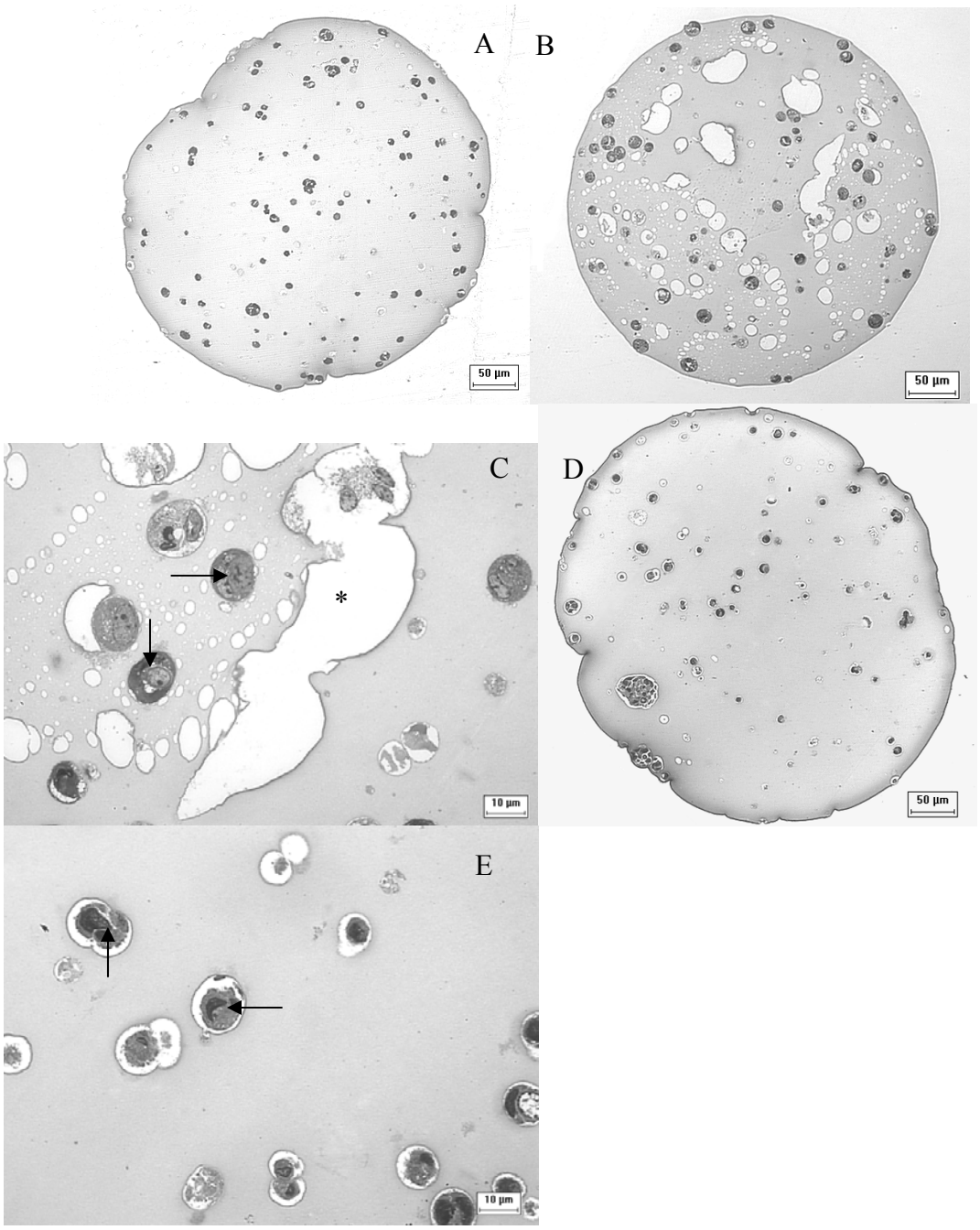

Figure 3.2 Histology of fresh and rewarmed vitrified and frozen beads. Low magnification of APA-encapsulated βTC3 cells shortly after preparation (A). Controlled-rate frozen and re-warmed APA beads with βTC3 cells (B) indicate tears throughout the construct. At higher magnification, tears (asterisk) are clearly visible throughout the construct (C). Vitrified APA beads with βTC3 cells, which have been re-warmed (D, E), show a construct free of tears compared to the controlled-rate frozen beads. Arrows indicate βTC3 cells (C,E). The sections were stained with toluidine blue; in figures A,B,D scale bars represent 50µm; in figures C,E scale bars represent 10µm.

Cell viability in beads was measured by alamarBlue®, a metabolic indicator that is reduced in proliferating cells. As compared to the fresh group, all cryopreserved groups had lower viabilities (VS55: $p<0.05$; PEG400 and frozen groups: $p<0.001$) (Figure 3.3). The VS55 group had a higher viability than either the PEG400 or the frozen group ($P<0.001$), whereas the viabilities of the latter two were statistically the same ($p>0.05$).

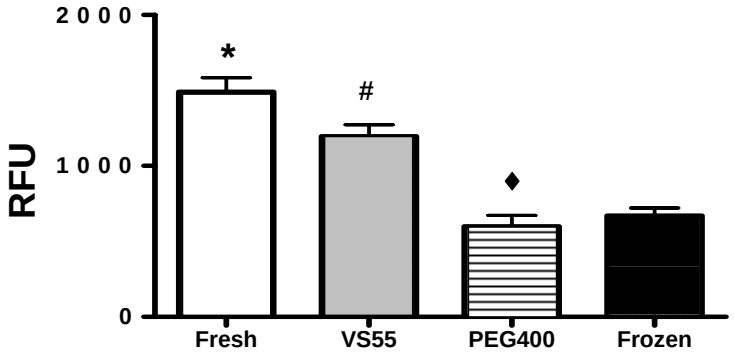

Figure 3.3 Cell viability (normalized to initial cell number) of cryopreserved groups using alamarBlue®. ***** fresh vs. VS55, $p<0.05$, fresh vs. PEG400, $p<0.001$, and fresh vs. frozen, $p<0.001$; # VS55 vs. PEG400, $p<0.001$, VS55 vs. frozen, $p<0.001$; ♦ PEG400 vs. frozen, $p> 0.05$; data are presented as mean ± SEM.

The static insulin secretion data showed that, as compared to the fresh group, the VS55 group displayed similar secretion dynamics. The PEG400 group exhibited a somewhat lower induced insulin secretion rate, but the difference was not statistically significant. The frozen group had the poorest secretion rate, and indeed at 3rd and 4th hours during glucose induction, the frozen group exhibited significantly lower secretion relative to the other groups (Figure 4). These results suggest that cryopreservation using the VS55, possibly also PEG400 protocols could prove to be a successful means of preservation, as their insulin secretion rates closely mirrored those of the control group.

Freezing using the conventional protocol implemented in this study was a poor candidate for cryopreserving the encapsulated cell system, as both the cell viability and induced secretion rate of frozen beads were significantly lower than those of the fresh group.

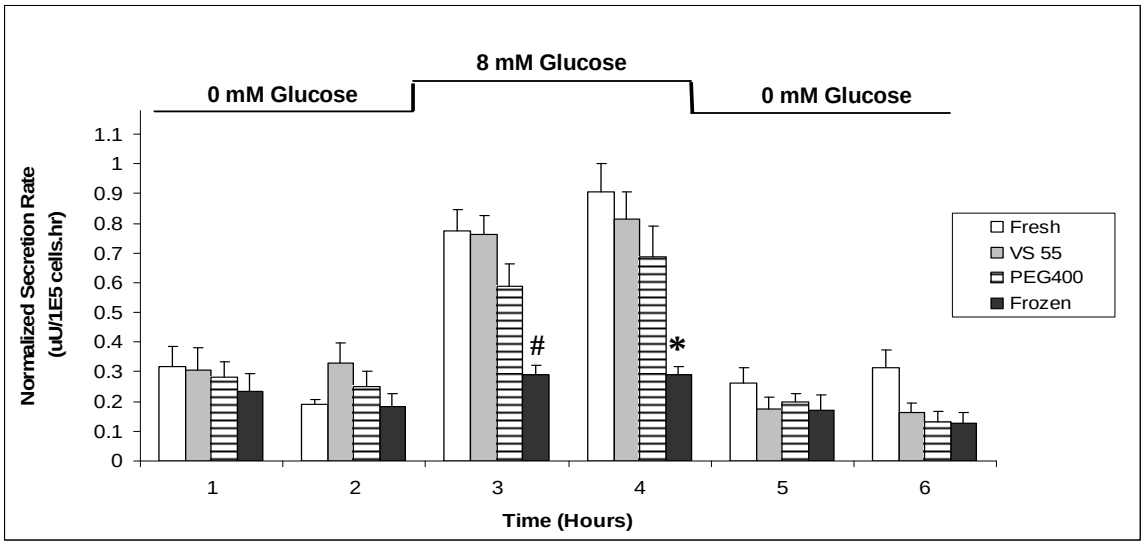

Figure 3.4 Static insulin secretion rates from fresh, vitrified (VS55 and PEG400) and frozen beads exposed to a square wave of glucose concentration. # indicate fresh vs. frozen, $p<0.001$;VS55 vs frozen, $p<0.001$; PEG400 vs frozen, $p<0.05$; * indicate fresh vs. frozen, $p<0.001$; VS 55 vs frozen, $p<0.01$; PEG400 vs frozen, $p<0.05$; data are presented as mean ± SEM; n=3.

3.5 Discussion

The presence of extracellular ice, although generally not harmful for cell suspensions, poses a significant challenge in the preservation of multicellular tissues and organs [4, 6, 27]. Mass and heat transport limitations imposed by the three-dimensional architecture of tissues, as well as their naturally high organization and complexity, influence their response to freezing. Limiting the amount and size of ice crystals formed during cryopreservation would avoid the inherent problems of extracellular ice, which include mechanical damage to cells and matrix of the tissue. Hence, vitrification may

offer a possible solution. With regard to tissue substitutes, vitrification has shown promise in preserving a tissue engineered blood vessel [139]. In this study, a model pancreatic substitute consisting of APA-entrapped βTC3 cells performed better after ice-free preservation than after conventional freezing

Having cells in hydrogels is advantageous, since diffusivities of small molecules in hydrogels are comparable to those in water and higher than those in tissues [15, 140-143]. βTC3 cells in APA beads initially are homogeneously distributed as single units. However, over time they remodel forming cell clusters which, depending on the type of alginate used, are either randomly dispersed in the matrix or are localized at the periphery of beads [13]. Diffusivities within clusters are expected to be similar to those in tissues. Thus, preservation of constructs incorporating single cells would be preferable to constructs incorporating cell clusters, as the necessary exposure times to cytotoxic CPAs would be lower for architectures incorporating single cells, thereby increasing chances for cell survival.

Indeed, preservation of cell aggregates poses significant challenges, as evidenced by work reported with islets. The findings of Bodziony et al. [42] concluded that vitrification was the most favorable among cryopreservation protocols tested on islets, as evaluated by their functional and morphological integrity post-preservation. However, different results are reported in other studies with pancreatic islets. Langer et al. [144] found conventional methods of cryopreservation to be superior to vitrification with respect to islet viability after thawing, though functional studies were not included in that study. Jutte et al. [134] compared a vitrification protocol to a conventional cryopreservation method regarding glucose-induced insulin release from thawed islets

and found both methods to give comparable results. Overall, the literature shows mixed results regarding cryopreservation of islets; however, vitrification of islets indeed appears significantly more challenging than vitrification of APA-encapsulated βTC3 cells.

Although this study showed the retention of cell viability and function after vitrification for the encapsulated cell constructs, as well as minimal damage to the calcium alginate matrix, it did not address the effects of cryopreservation on the beads' poly-L-lysine immunoprotective membrane. In order to be successful, the desired cryopreservation method should not compromise the morphological and functional integrity of the materials, in addition to maintaining cell viability and function. Furthermore, the design of cryopreservation protocols must account for cytotoxic effects of CPAs, especially at high concentrations [145], by evaluating the optimal CPA concentrations and exposure and elution times. This work is currently under way in our laboratory.

CHAPTER 4

CRYOPROTECTANT DELIVERY AND REMOVAL FROM MURINE INSULINOMAS AT VITRIFICATION-RELEVANT CONCENTRATIONS [2]

4.1 Abstract

Development of optimal cryopreservation protocols requires delivery and removal of cryoprotective agents (CPAs) in such a way that negative osmotic and cytotoxic effects on cells are minimized. This is especially true for vitrification, where high CPA concentrations are employed. In this study, we report on the determination of cell membrane permeability parameters for water (L_p) and solute (P_s), and on the design and experimental verification of CPA addition and removal protocols at vitrification-relevant concentrations for a murine insulinoma cell line, βTC-tet cells. Using membrane permeability values and osmotic tolerance limits, mathematical modeling and computer simulations were used to design CPA addition and removal protocols at high concentrations. The cytotoxic effects of CPAs were also evaluated. Cells were able to tolerate the addition and removal of 2.5 M dimethyl sulfoxide (DMSO) and 2.5 M 1,2 propanediol (PD) in single steps, but required multi-step addition and removal with 3.0 M DMSO, 3.0 M PD, and a vitrification-relevant concentration of 3.0 M DMSO+3.0M PD. Cytotoxicity studies revealed that βTC-tet cells were able to tolerate the presence of single component 6.0 M DMSO and 6.0 M PD and to a lesser extent 3.0 M DMSO+3.0 M PD. These results determine the time and concentration domain of CPA exposure that

---

[2] Modification of a paper published in **Cryobiology,** 55(1): 10-18 (2007).

cells can tolerate and are essential for designing cryopreservation protocols for free cells as well as cells in engineered tissues.

4.2 Introduction

The need for long-term storage is a critical issue for the preservation of cells, natural and engineered tissues and possibly organs. Cryopreservation may offer a clinically relevant solution by preservation at cryogenic temperatures allowing for off-the-shelf availability, sterility testing, and quality control monitoring.

Development of effective protocols for the cryopreservation of tissue engineered substitutes requires knowledge of fundamental biophysical characteristics of the cellular component. Permeating cryoprotective agents (CPAs) help protect cells from injury by lowering lethal concentrations of intracellular electrolytes and decreasing the amount of extracellular ice formed [146]. However, CPAs may cause cell damage due to rapid volume excursions upon exposure of cells to CPA solutions, as well as by chemical cytotoxicity, especially at high concentrations, as used in vitrification protocols. For a certain CPA concentration step change, cellular volume excursions are determined by the water (L_p, cm/s•atm) and solute (P_s, cm/s) permeabilities. When a cell is exposed to a hypertonic solution of a permeating solute, there is an initial abrupt shrinkage caused by water efflux determined by L_p, followed by a slower return to normal volume as the solute permeates at a rate determined by P_s, which is generally referred to as shrink/swell behavior [7]. To prevent large osmotically induced changes in cell volume and high water fluxes through the cell membrane which can cause damage to cells [52], CPAs are generally loaded and removed in a stepwise manner. Chemical toxicity can also be reduced by lowering the temperature or reducing the CPA loading and unloading times.

Proper design of CPA loading and unloading procedures is thus essential to obtain the benefits of CPA function in cryopreservation while minimizing negative effects on cells.

Our laboratory is interested in tissue engineering a pancreatic substitute for treatment of insulin-dependent diabetes. A promising construct for laboratory and preclinical studies consists of glucose-responsive, insulin-secreting βTC-tet mouse insulinomas [87] encapsulated in a calcium alginate/ poly-L-lysine/ alginate (APA) matrix [10, 15]. The ability to easily amplify these cells in culture as well as control their proliferation by tetracycline makes βTC-tet cells an attractive cell source for a pancreatic substitute. We have previously shown that a baseline vitrification protocol better preserves an encapsulated cell system relative to conventional freezing, in terms of both cell viability and function, as well as biomaterial structure [42, 43]. However, to optimize cryopreservation protocols and minimize cell damage, a thorough characterization is required of the osmotic and cytotoxic effects of cryoprotectants used in the cryopreservation process.

In this study, we report on the determination of cell membrane permeability parameters and on the design and experimental implementation of CPA addition and removal protocols at vitrification-relevant concentrations that avoid the occurrence of damaging osmotic excursions. Besides osmotic considerations, use of CPAs at high concentrations may impose cytotoxic effects, and this is also addressed with the same cell line. With the capability to deliver high concentrations of CPAs, the proposed addition and removal protocols can be used to vitrify systems incorporating βTC-tet mouse insulinomas.

4.3 Materials and Methods

4.3.1 Cell and cell culture

βTC-tet cells were obtained from the laboratory of Dr. Shimon Efrat, Albert Einstein College of Medicine, Bronx, NY [87]. Monolayer cultures were initiated from frozen stocks and cultured in T-flasks in complete growth medium consisting of Dulbecco's Modified Eagle's Medium (DMEM) (Fisher Scientific, Fairlawn, NJ) supplemented with 1% glutamine (Sigma Chemical Co, St. Louis, MO), 10% fetal bovine serum (KSE Scientific, Durham, NC) and 1% penicillin/streptomycin (Fisher Scientific). Cultures were incubated in a 37°C, 5% CO_2, humidified incubator. Cells were split at a ratio of 1:5 when confluent and used between passage numbers of 33 and 40.

4.3.2 Measuring cell volume changes and membrane permeability

Cell volumes were measured with a Beckman Coulter™ Multisizer™ 3 Coulter Counter® (Beckman Coulter, Fullerton, CA, USA) using a 100 μm aperture and calibrated with 10μm latex beads (Beckman Coulter, Inc). To measure cell volume responses to cryoprotectants, approximately $3x10^6$ βTC-tet cells in 150-300 μL PBS were abruptly added to 90 mL of well-mixed 10% v/v solutions (1.4 M) of dimethyl sulfoxide (DMSO) (Sigma, St. Louis, MO) and 1,2 propanediol (PD) (Sigma). Collected average pulse height data were converted to cell volumes by the Coulter Counter® software using its built-in digital pulse processor. Cell volumes were normalized to the isotonic cell volume and plotted as a function of time. Measurements were carried out at 4, 22 and 37°C. CPA and water fluxes through the cell membrane were described mathematically by equations (1) and (2) presented in the Mathematical Modeling and Calculations

section. Equation solutions were fitted to experimental data to obtain the CPA and water membrane permeability parameters.

4.3.3 Determination of osmotically- inactive volume (V_b) for βTC-tet cells

βTC-tet cells initially in isotonic (~0.272 Osm) saline were added to microcentrifuge tubes containing saline solutions ranging from 0.201 to 1.00 Osm at 22°C. The osmolarity of the solutions was measured with a freezing point osmometer (Advanced Micro- Osmometer, Advanced Instruments, Inc, Norwood, MA). Following equilibration, cell volumes were measured with the Beckman Coulter™ Multisizer™ 3 Coulter Counter®. Cell volumes were normalized to the isotonic cell volume and plotted against the reciprocal of osmolality. The osmotically inactive volume (V_b) was calculated by fitting a straight line to the data and extrapolating it to infinite concentration [49, 50].

4.3.4 Cell osmotic tolerance

Osmotic tolerance limits of βTC-tet cells were determined by assessing cell viability following their equilibration with anisosmotic NaCl solutions ranging from 0.137-5.341 Osm (using an osmometer, as described above) at 2-4°C (using an ice bath) and 22°C (room temperature). Equilibration times were determined based on measured water permeability (L_p) values and ranged from several seconds to ten minutes, depending on the osmolality of the solutions. A fixed volume of cell suspension was added to each of several microcentrifuge tubes containing the test solutions. After the necessary equilibration period, the cells were removed from the test solution by centrifugation at 100 x g for 5 minutes, returned to isotonic saline, and assessed for cell viability. Experimental results were normalized to iso-osmotic saline controls treated in

an identical fashion. Additionally, tests showed that centrifugation and resuspension in isotonic saline solution did not affect cell viability (data not shown).

4.3.5 Analytical techniques

Cell viability was measured by trypan blue (Sigma, St. Louis, MO) and alamarBlue® (BioSource International, Inc., Camarillo, CA). The trypan blue dye exclusion evaluates cell membrane integrity, as the dye is unable to cross intact plasma membranes labeling only dead cells. Cell suspensions were assayed with an automated Beckman Coulter® Vi-CELL™ (Beckman Coulter, Fullerton, CA, USA) cell viability analyzer. AlamarBlue® evaluates the mitochondrial metabolic activity of the cells. For this assay, approximately $2.5x10^6$ cells, 100 μL alamarBlue® and 1 mL DMEM, or only 100 μL alamarBlue® and 1 mL DMEM for controls, were placed in each well of a 24-well plate. After proper mixing, the 24- well plate was placed into a 37˚C/5% CO_2 incubator for 2 hours, following which 100 μL of medium from each well were transferred into a 96-well microtiter plate. The plate was read with a Spectra Max Gemini Plate Reader (Molecular Devices, Sunnyvale, CA) using an excitation wavelength of 544 nm and an emission wavelength of 590 nm.

4.3.6 Cryoprotectant addition-removal: Simulations and experiments

Membrane permeability values were used in equations (1) and (2) in the Mathematical modeling and calculations section to compute normalized cell volumes and intracellular CPA concentrations for βTC-tet cells exposed to various concentrations of DMSO and PD by themselves or in combination in solution. The CPAs were added and removed in a single step or in a stepwise fashion. During stepwise CPA removal, the

solutions contained 0.3 M mannitol as an osmotic buffer, except for the last removal step in which isotonic culture medium was used.

Modeling results were used to design experiments involving addition and removal of cryoprotectants from cells. βTC-tet cells were plated in 12-well tissue culture plates (Beckton Dickinson Labware, Franklin City, NJ) until 80% confluent. As per the computer simulations of CPA addition (4°C) and removal (22°C), cells were exposed to solutions of 2.5 M and 3.0 M DMSO and PD, as well as a cocktail of 3.0 M DMSO + 3.0 M PD in a stepwise manner (during removal, the solutions contained 0.3 M mannitol to serve as an osmotic buffer; the last removal step was isotonic culture medium). In parallel, cells were exposed to PBS in the same stepwise addition-removal manner as the corresponding experimental group. At the end of the process, cell viability was evaluated with alamarBlue®.

4.3.7 Effect of cryoprotectant exposure on cell viability

βTC-tet cells were plated in a 48-well plate in 500 μL of culture medium overnight. Before being exposed to cryoprotectant solutions, the cells were cooled by placing the plate on ice. Solutions of 2-6 M DMSO and 2-6 M PD in PBS, as well as a cocktail of 3 M DMSO and 3 M PD, were tested for their cytotoxic effects on βTC-tet cells by implementing the following procedure: CPAs were added in a stepwise manner at 4°C; cells were exposed to the final CPA concentration for 15 minutes at 4°C; and the CPAs were then removed in a stepwise manner at 22°C (removal solutions contained 0.3 M mannitol; the last removal step was isotonic culture medium). In a positive control, cells were exposed to PBS in the same stepwise addition-removal manner as the

corresponding experimental group. Following CPA removal, cell viability was measured using alamarBlue®.

4.3.8 Mathematical modeling and calculations

4.3.8.1 Membrane permeability parameters

The two-parameter model describing water and solute flux via the cell membrane is [51]:

$$\frac{dV_w}{dt} = -L_p ART(M^e - M^i) \tag{4.1}$$

$$\frac{dN_s}{dt} = P_s A(M_s^e - M_s^i) \tag{4.2}$$

where V_w (μm^3) is the volume of water inside the cell, L_p is the water permeability (cm/sec•atm), A is the surface area of the cell (μm^2), R is the universal gas constant ((μm^3•atm)/(mol•K)), T is the absolute temperature (K), M^e and M^i are the external and internal osmolality (osmolal), respectively, N_s is the number of moles of permeating solute inside the cell, P_s is the solute permeability (cm/s), and M_s^e and M_s^i are the external and internal osmolalites of the permeating CPA (osmolal), respectively. Model solutions were fit to experimental data to obtain values of the water (L_p) and solute (P_s) permeability of βTC-tet cells using a least-squares fit (Nelder-Mead Simplex direct routine) with the aid of Matlab (MathWorks, Natick, MA). Numerical integration was carried out using fourth-order Runge-Kutta. Transport across the cell membrane of the dual solute system of 3 M DMSO and 3 M PD was modeled as a single component system of the slower permeant, DMSO. An osmotic virial equation model was used to account for the non-ideality of the 6 M DMSO solution osmolality as described by Elliott et al. [147] using the quadratic form of the equation,

$$\pi = c_i + B_i c_i^{\,2} + \ldots \quad , \tag{4.3}$$

where c_i is the molal concentration of solute i (moles of solute per kilogram of solvent), B_i is the second osmotic virial coefficient, taken as 0.0843 (moles of solute per kilogram of solvent)$^{-1}$ for DMSO as per Elliott et al [147].

The inactive cell volume, V_b , was determined from the Boyle van't Hoff relationship [7],

$$V = \pi_e^o (V_o - b)\frac{1}{\pi_e} + V_b \ , \tag{4.4}$$

where π_e is the extracellular osmolality of the solution (osmolal), V_b is the osmotically inactive cell volume (μm^3) and V_o and π_e^o are the isotonic cell volume (μm^3) and isotonic extracellular osmolality (osmolal), respectively. βTC-tet cells were exposed to various anisosmotic NaCl solutions, allowed to equilibrate, and then measured for their volume using a Coulter Counter®. Extrapolation of the relative cell volume as a function of inverse osmolality to infinite osmolality (zero on the abscissa) was used to estimate the osmotically inactive cell volume.

4.3.8.2 Activation Energy (E_a)

The temperature dependence of the membrane permeability parameters, L_p and P_s, can be expressed with an associated activation energy (E_a). Assuming an Arrhenius relationship (Equation 4), the activation energy was determined by plotting ln (L_p) or ln (P_s) against inverse absolute temperature and calculating the slope of the resulting straight line.

$$L_p \ or \ P_s = A \exp(\frac{-E_a}{RT}), \tag{4.5}$$

In the above equation, A is the frequency factor based on the experimental data, R is the ideal gas constant, T is the absolute temperature and E_a is the activation energy.

4.3.9 Statistical Analysis

Statistical analyses were done using Student's t-test (for single vs. multi-step CPA addition and removal) and ANOVA (for cytotoxicity study). Comparisons were considered significant at $p<0.05$.

4.4 Results

4.4.1 βTC-tet cell membrane permeability characteristics

βTC-tet cells followed the Boyle van't Hoff relationship over the osmotic range tested, 0.201-1.00 Osm, as shown in Figure 4.1 ($R^2 = 0.9851$). The osmotically inactive volume, V_b, was found to be 0.184 by extrapolating the relative cell volume as a function of inverse osmolality to infinite osmolality.

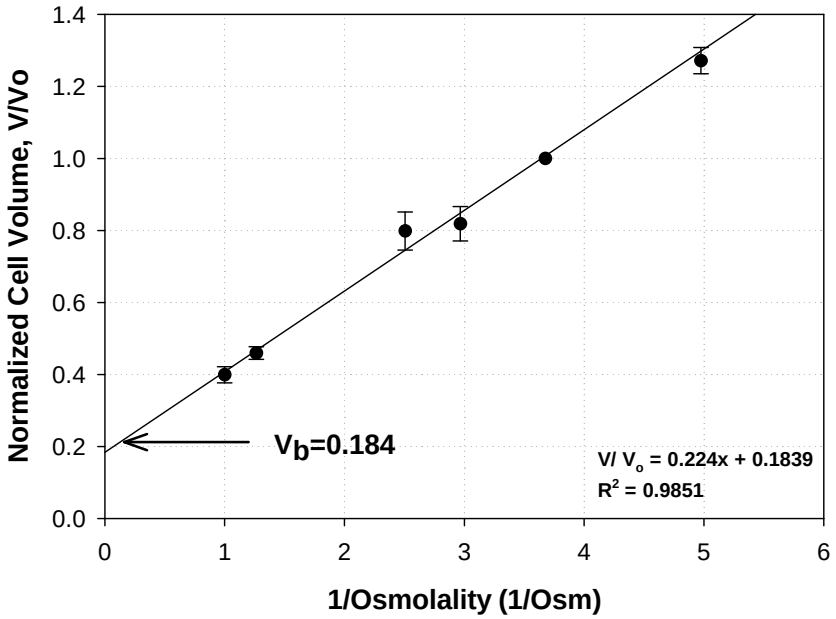

Figure 4.1 Boyle-van't Hoff plot for βTC-tet cells. The data points represent normalized volume (mean ± SE) of cells equilibrated in NaCl solutions ranging from 0.201-1.0 Osm. The osmotically inactive volume (V_b=0.184) was found by extrapolating the concentration of the extracellular solution to infinite osmolality. Solid line indicates a

best fit through the data points assuming a linear relationship. n=3 for all points except for the lowest osmolality (0.201 Osm) for which n=4.

When exposed to DMSO and PD, cells exhibited the characteristic shrink/swell behavior in response to a hypertonic solution of a permeating solute. With both CPAs, experiments were performed at 4, 22 and 35°C. A representative plot is shown in Figure 4.2 for βTC-tet cells exposed to 10% dimethyl sulfoxide at time 0 at 22°C. The figure shows raw pulse data obtained by the instrument, normalized to the initial pulse magnitude, which are proportional to the average cell volume at each particular instant of time; the two-parameter (L_p and P_s) fit through the data is also shown. The determined permeability parameters for each CPA at each temperature are summarized in Table 4.1A. PD was found to be more permeable than DMSO at all temperatures ($p<0.055$), consistent with literature [148, 149].

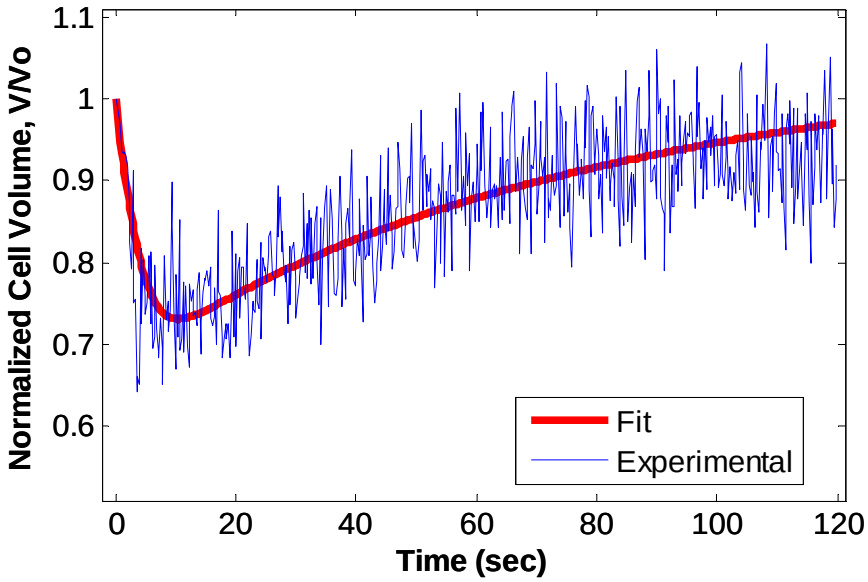

Figure 4.2 Representative plot of normalized voltage pulses vs. time generated by a Coulter Counter upon the abrupt addition at t=0 of βTC-tet cells to a 10% dimethyl sulfoxide solution at 22°C. Voltage pulses are proportional to cell volume, hence, normalized pulses represent the cell volume normalized to the volume at t=0. The solid line is the two parameter (L_p and P_s) fit through the data points.

Activation energies for L_p and P_s were calculated assuming an Arrhenius relationship (R^2>0.94 for all cases). The corresponding calculated activation energies are presented in Table 4.1B.

Table 4.1. **A**. Water (L_p) and solute (P_s) membrane permeabilities of βTC-tet cells at 4 and 22°C, mean ± SEM (standard error mean); **B.** Activation energies (E_a) for L_p and P_s for each CPA.

A

CPA / Parameter	DMSO	PD	Temp
L_p (μm/atm•s)	(6.67 ± 0.88) x 10^{-4}	(5.0 ± 0.65) x 10^{-4}	4°C
P_s (μm/s)	(4.73 ± 0.037) x 10^{-2}	(5.81 ± 0.056) x 10^{-2}	
L_p (μm/atm•s)	(3.07 ± 0.29) x 10^{-3}	(4.45 ± 0.15) x 10^{-3}	22°C
P_s (μm/s)	(1.45 ± 0.077) x 10^{-1}	(2.32 ± 0.15) x 10^{-1}	
L_p (μm/atm•s)	(1.15 ± 0.032) x 10^{-2}	(6.9 ± 0.015) x 10^{-3}	35°C
P_s (μm/s)	(6.1 ± 1.2) x 10^{-1}	(7.71 ± 0.135) x 10^{-1}	

B

Activation Energy (kcal/mol)	DMSO	PD
L_p	15.4	15.4
P_s	14.1	14.6

4.4.2 βTC-tet cells osmotic tolerance

To determine the osmotic tolerances of βTC-tet cells, cells were exposed to a range of anisosmotic NaCl solutions and assessed for viability following equilibration using the trypan blue dye exclusion method and alamarBlue®. The results from both assays correlated well with each other. The Boyle van't Hoff relationship (see Equation 4.4) was used to calculate the expected equilibrium cellular volume in each test solution. Comparing these volumes with the corresponding percent viability allowed for the determination of volume changes that the cells were able to tolerate. A cutoff value for viability was used to determine acceptable osmotic tolerances.

Cell viability as assessed by trypan blue and alamarBlue were found to be greater than 80% between 0.137-1.250 Osm (Figure 4.3). Cell viability dropped off significantly beyond this range. The corresponding volume changes calculated from the Boyle-van't Hoff plot are +80% and -50% of the equilibrium volume, respectively.

4.4.3 Simulations and Experimental Results for addition and removal of CPAs

Computer simulations (Figure 4.4) were used to model single step and stepwise CPA addition and removal to maintain cell volume excursions within osmotically tolerable limits. Experiments were then carried out using the simulated addition and removal protocols (Figure 4.5). Briefly, 2.5 M DMSO was added in 2 steps at 180 s/step and removed in 2 steps at 90s and 240s; 2.5 M PD was added in 2 steps at 100s/step and removed in 2 steps at 90s and 240s; 3.0 M DMSO was added in 3 steps at 180 s/step and removed in 3 steps at 60s, 60s and 240s; 3.0 M PD was added in 3 steps at 120 s/step and

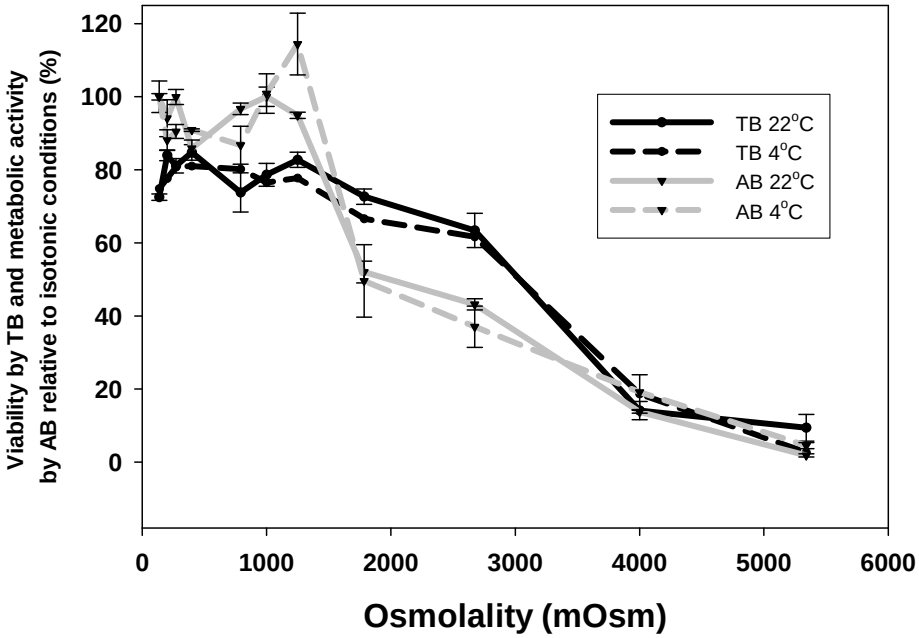

Figure 4.3 Osmotic tolerances for βTC-tet cells. βTC-tet cells were exposed to anisosmotic saline concentrations for 15 minutes at 4°C and 22°C, pelleted and then returned to isotonic saline for viability assessment using trypan blue (TB) and alamarBlue® (AB); each data point is the mean (±) standard deviation (SD) from n=5-7.

removed in 3 steps at 45s, 45s and 240s; 3.0 M DMSO + 3.0 M PD was added in 3 steps at 240s/step and removed in 3 steps at 120s/step and finally 300s. The duration of the steps was determined based on maintaining the cell volume changes to within their osmotically tolerable limits. The removal steps contained 0.3 M mannitol as an osmotic buffer but the last removal step did not contain any mannitol (i.e, isotonic, culture media).

Although membrane permeabilities and osmotic tolerances may differ between suspended and attached cells, the simulations of Figure 4, based on parameters obtained with suspended βTC-tet cells, were used to guide the addition and removal of CPAs from monolayer βTC-tet cultures. Experimental results are shown in Figure 4.5. As expected, for the lower concentrations of CPAs, single or stepwise addition and removal resulted in high viability as the volume excursions did not surpass osmotic tolerances. However, single step addition and removal of 3 M DMSO and 3 M PD resulted in lower cell

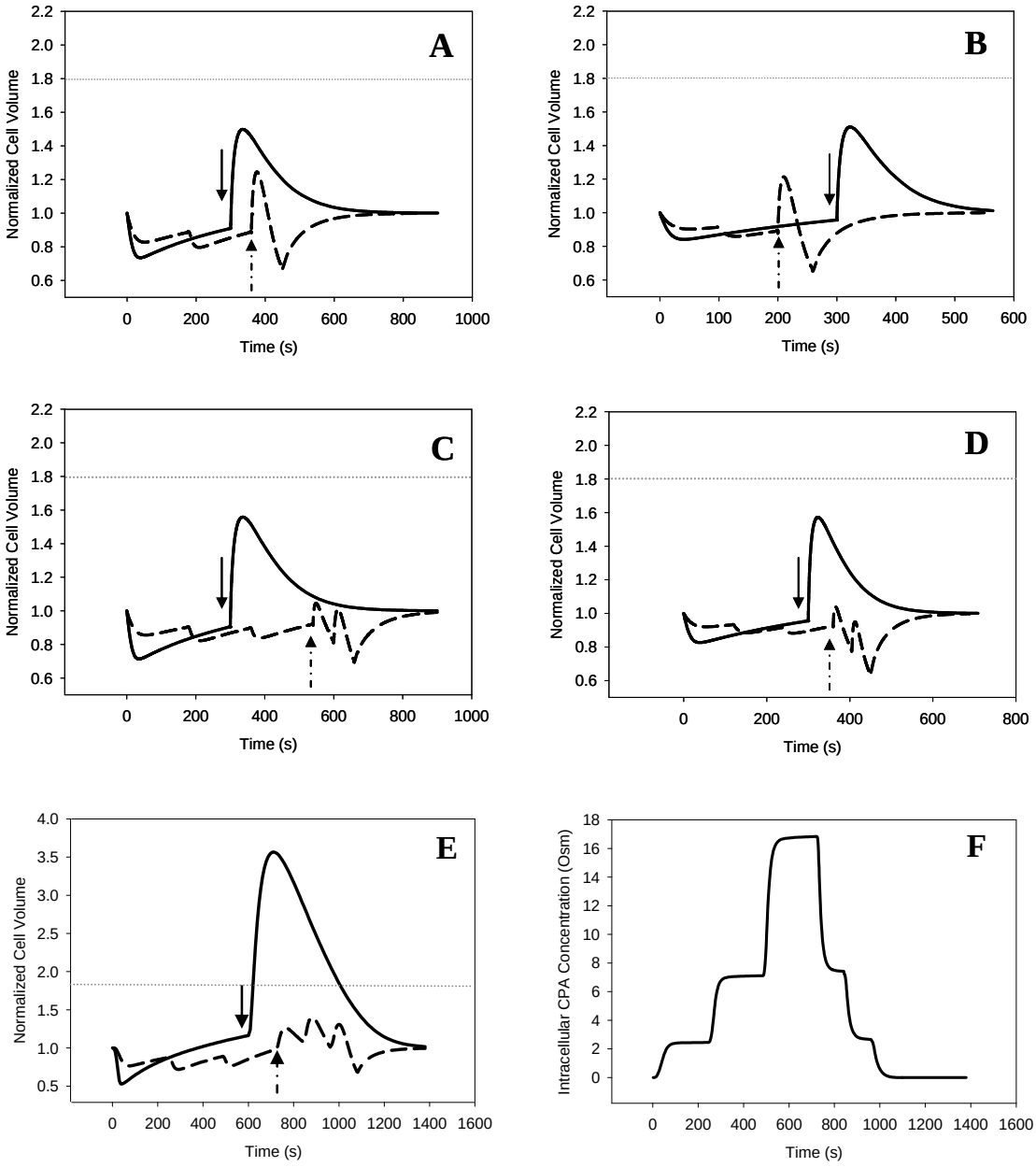

Figure 4.4 Simulated volume response of βTC-tet cells during addition and removal of (A) 2.5 M DMSO, (B) 2.5 M 1,2 propanediol (PD), (C) 3.0 M DMSO, (D) 3.0 M PD, (E) 3.0 M DMSO+3.0 M PD; solid lines indicate single step addition-removal; dashed lines indicate multi-step addition-removal; arrows indicate the demarcation between CPA addition and removal; (F) Simulated intracellular solute concentration of multi-step addition and removal of 3.0 M DMSO+3.0 M PD. The horizontal dotted lines represent the upper osmotic tolerance limits for the βTC-tet cells used in the simulations (lower limit is below volume excursions exhibited in the simulations)

viability compared to the multi-step approach. The largest difference between single and multi-step addition and removal came from the use of a vitrification-relevant cocktail of 3 M DMSO+3 M PD (Figure 4.5). The single step addition and removal of this cocktail resulted in excessive volume excursions; however, its proper stepwise addition and removal kept the cellular volume excursions within a tolerable limit and thus enabled higher cell survival. Based on computer simulations, equilibration of intracellular cryoprotectant concentrations (shown for the vitrification-relevant CPA cocktail, Figure 4F) was rapid, occurring within a few minutes; this agrees with the results of Wusteman, et al. who found equilibration of vascular endothelial cells with 6.12 M PD to occur within 2 minutes [149].

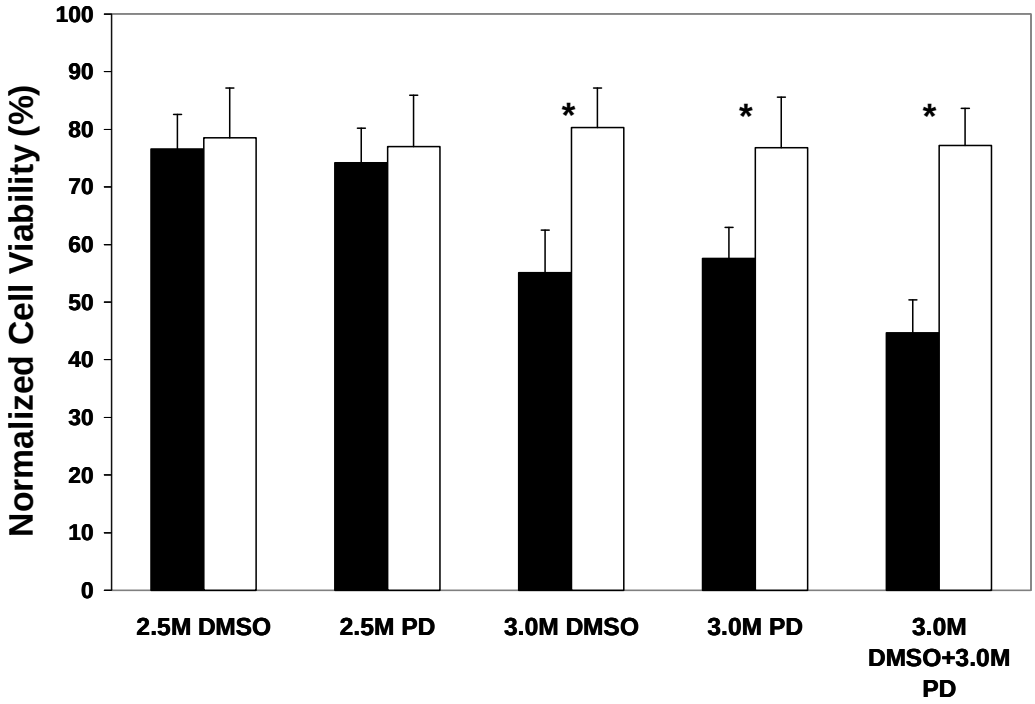

Figure 4.5. Viability of βTC-tet cells, measured by alamarBlue® and normalized to isotonic values, following single-step (filled bars) and multi-step (open bars) CPA addition and removal; each bar graph is the mean (±) SD from n=3; * indicates statistical difference between corresponding single and multi-step addition and removal with the

following p-values: 3 M DMSO single-step vs. multi-step=0.0000125; 3 M PD single-step vs. multi-step=0.000392; 3 M DMSO + 3 M PD single-step vs. multi-step=0.0000489.

4.4.4 Effects of cryoprotectant exposure on insulinomas

A concentration range of DMSO and PD were studied to determine the effects of cryoprotectant exposure on βTC-tet viability. Again, even though this experiment was conducted with βTC-tet monolayers, the simulations of Figure 4 were used to guide the stepwise addition and removal of the 4 M and 6 M concentrations of CPAs; addition and removal of the CPAs at 2 M were carried out in single steps. Cell viability decreased with increasing CPA concentration from 2 M to 4 M and from 4 M to 6 M for DMSO, and from 2 M to 4 M for PD (Figure 4.6). Interestingly, exposure to the CPA cocktail (3 M DMSO+3 M PD) resulted in a lower viability compared to 6 M PD; the latter was not statistically different from the viability in 6 M DMSO. Overall, these results indicate that under proper CPA loading and unloading, βTC-tet cells can tolerate high concentrations of DMSO, PD or a combination of the two. This type of study is useful for selecting low toxicity CPAs for the development of vitrification solutions.

4.5 Discussion

In this study, membrane permeabilities as well as osmotic and cytotoxic tolerances of murine insulinomas were determined to develop a multi-step addition and removal procedure for CPAs at vitrification-relevant concentrations. This information helps in developing optimized cryopreservation protocols for cells by themselves and incorporated in a tissue engineered pancreatic substitute.

Electronic particle counters, such as the Coulter Counter®, have been used extensively to determine water and solute permeability parameters by modeling the transient kinetic behavior of cell volume changes in response to a step change in the

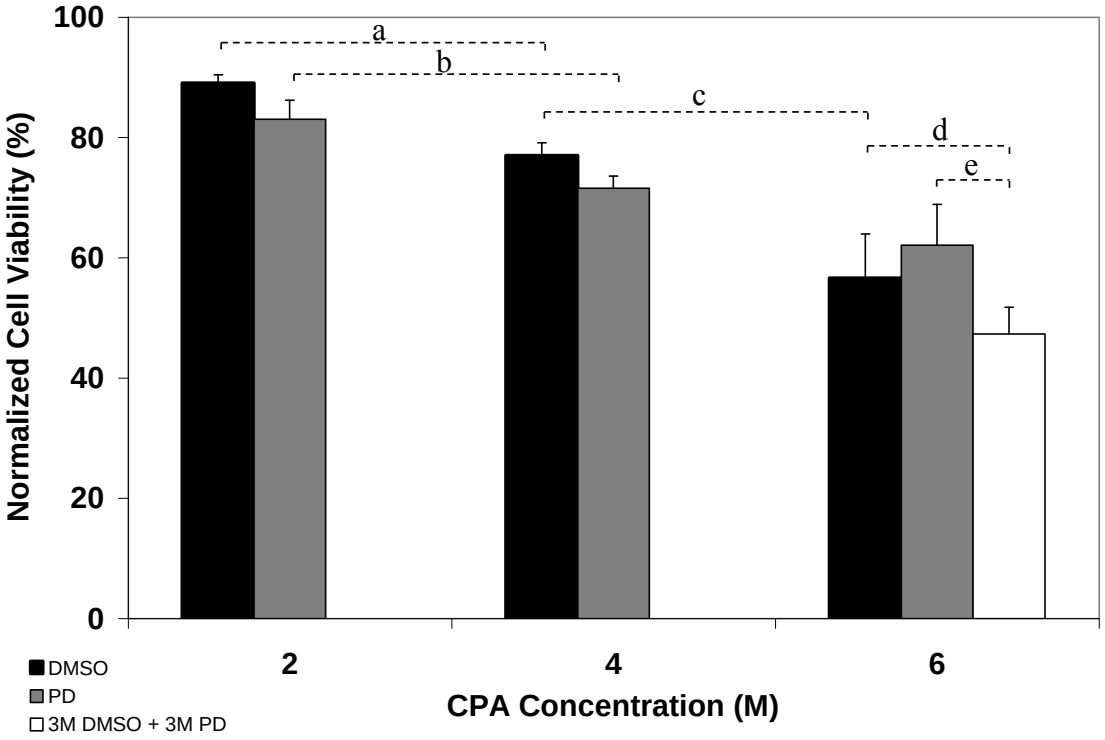

Figure 4.6 Normalized cell viability of βTC-tet cells, measured by alamarBlue®, after exposure to various concentrations of DMSO (black bars), PD (gray bars) and a cocktail of 3.0 M DMSO + 3.0 M PD (white bar); values are mean ± SD normalized to controls (using PBS only) from n=3 in each group, except with 6 M CPAs where n=5; horizontal brackets indicate comparison between groups with the following p-values: a: 0.0011; b: 0.0025; c: 0.0064; d: 0.072; e: 0.018

concentration of a permeating CPA [24, 146, 148-150]. Values of L_p and P_s in the presence of DMSO and PD at 22°C were found to be similar to reported values for other cell types, including human vascular endothelial cells [149], hamster islets [151], and human platelets [152]. As with other cells, βTC-tet cells were found to be more

permeable to PD than DMSO [146]. Besides cell type, membrane permeability parameters depend on temperature, CPA type, and possibly CPA concentration [146, 153]. To examine the effect of CPA concentration on the membrane permeability of βTC-tet cells, kinetic cell volume changes to DMSO and PD were studied at room temperature for concentration steps of 0 to 1.5 M and of 1.5 M to 3.0 M. Volume profiles measured with the Coulter Counter® were fit to the two-parameter permeability formulism, as before.

Membrane permeability parameters can depend on several factors, including temperature, initial CPA concentration and cell culturing mode and organization. The temperature dependence usually follows the Arrhenius relationship, which was also observed in this study with insulin-producing cells. Initial CPA concentration can increase or decrease the membrane permeability depending on the cell and solute type [146, 154, 155] (also preliminary data from our lab, not shown). Recent work by Elliott et. al. [147] examined the dependence of osmolality on higher CPA concentrations by investigating the effect of solution non-ideality in osmotic equilibrium modeling. In this work, osmolalites from a high (6 M) CPA concentration solution was accounted for based on their model.

Another factor that can influence membrane permeability is the organization or attachment status of the cells. Membrane permeability for human dermal fibroblasts reportedly differ by more than 20-fold between cells in suspension and in tissue engineered collagen constructs (4.34×10^{-14} m/Pa·s vs. 105×10^{-14} m/Pa·s) [156]. Using this factor of 20 for membrane permeability variability, CPA addition and removal simulations were carried out for βTC-tet cells at 3 M DMSO + 3 M PD, keeping the

addition and removal protocol the same as in the simulations of Figure 4.4. Increasing or decreasing the permeabilites together by a factor of 20 maintained the volume excursions within the osmotically tolerable limits (simulations not shown). Hence, using cell suspension-derived membrane permeabilites to design of CPA addition-removal protocols is valuable for cell monolayers, too, as done in this study. Currently, measuring membrane permeability parameters for cell monolayers remains more challenging and potentially more costly compared to cell suspensions [157]. Furthermore, cell organization may play a more significant role during cryopreservation: it has been shown that monolayers are more prone to intracellular freezing than cell suspensions due to cell-cell and cell-substrate interactions [158-160]. A recent study by Pegg [159] investigated the cryopreservation of human umbilical vascular endothelial cells as suspensions and monolayers on solid polystyrene microcarrier beads. Using the same arbitrarily designed CPA addition and removal protocol for both cell culture configurations, different cryopreservation protocols were tested by varying the cooling rate and then assessed for cell recovery post-thawing. Although cell recovery was similar between suspensions and monolayers at high cooling rates (10, 47 or 500 ^{o}C/min), it was different at slower cooling rates (0.3 and 1 ^{o}C/min), indicating that cell culturing mode plays a significant role in the cryopreservation outcome.

The activation energies for L_p for DMSO and PD were found to be similar to corresponding activation energies reported for human islets for the same CPAs [49]. Also, the activation energies for P_s for DMSO and PD were similar to values reported for human corneal keratocytes with the same CPAs [146]. In the osmotic tolerance studies, employed viability assays were based on cell membrane permeability (trypan blue

exclusion dye) and cell metabolic activity (alamarBlue®). It was found that the two methods compared well with each other. Dye exlusion methods, such as trypan blue or propidium iodide, are end-point assays that evaluate only membrane integrity, which is indicative of necrosis or late-stage apoptosis. These assays are not sensitive to cells that might recover after stress. Pegg et al. [24] also recognized this fact by utilizing a functional assay for chondrocytes by measuring the ability of the cells to incorporate inorganic $^{35}SO_4^{2-}$ into newly synthesized sulfated glycosaminoglycans. Hence, dye exclusion studies in conjunction with metabolic assays may provide more insight on cellular status than either assay alone.

Computer simulations were used to predict cell volume excursions due to changes in CPA concentrations, and CPA addition/removal procedures were designed that retained cells within the osmotically tolerated domain of conditions. Moreover, CPAs were tested for their cytotoxic effects. Although cocktails have generally been used to reduce cytotoxicity of high CPA concentrations, this is empirical and thus may not be generally applicable [161]. Indeed, the 3 M DMSO+ 3 M PD cocktail was found to be more cytotoxic towards βTC-tet cells than 6 M of each CPA alone under the experimental conditions implemented in this study (Figure 4.6). Transport across the cell membrane of the dual-solute system of DMSO and PD was modeled as a single component system of the slower permeant, DMSO. This is a reasonable approximation, since equilibration of the more rapidly permeating CPA, PD, should occur first.

This study has defined the necessary parameters to cryopreserve murine insulinomas that have been used in model tissue engineered pancreatic substitutes [10, 15]. The use of encapsulated insulin-secreting cells holds significant promise for

effectively treating insulin-dependent diabetes, by providing a highly regulated system that responds to environmental glucose cues. The development and characterization of cryopreservation protocols is an integral part of making this therapeutic modality available at a clinically-relevant scale. This includes coupling information from this study with water and cryoprotectant transport rates through the matrix to provide the necessary information to effectively cryopreserve all cells in a tissue engineered construct. Although differences may arise in the osmotic behavior of cells as free in suspension compared to those embedded in a matrix, it is anticipated that such differences will be small or negligible, as is the case for chondrons relative to free chondrocytes [162, 163].

CHAPTER 5

CRYOPRESERVATION PROTOCOL DESIGN AND IMPLEMENTATION: A CELL ENCAPSULATED SYSTEM STUDY

5.1 Abstract

Cryopreservation of hydrogel-based, encapsulated cell systems is an important step towards their clinical availability. Due to their susceptibility to ice damage during freezing, vitrification was explored, whereby ice crystallization was avoided during cooling/warming. A systematic approach was undertaken to develop cryopreservation protocols using two vitrification solutions, 3 M dimethyl sulfoxide + 3 M 1, 2 propanediol (PD) +0.3 M sucrose (DP6_0.3S) and 5.5 M PD + 1 M sucrose (55PD_1S), by utilizing a CPA transport model that coupled experimentally determined cryoprotectant (CPA) effective diffusivities through the extracellular space and cell membrane permeabilities. After determining glass transition and devitrification temperatures of the solutions by differential scanning calorimetry, encapsulated cells consisting of murine insulinomas in calcium alginate were vitrified and assessed over four days for metabolic activity and compared to a conventionally frozen group achieved by slow cooling. Vitrified and frozen groups had average post-thaw viabilities of 71, 62 and 50% for DP6_0.3S, 55PD_1M and conventionally frozen, respectively, compared to fresh controls. Viable cell numbers of the respective groups were constant over four days ($p>0.05$). Confocal microscopy images of live and dead cells assessed on days one and four showed random distributions of live and dead cells in all cases. Structural assessment of the encapsulated cell systems after vitrification and conventional freezing by compression mechanical testing showed no differences among the groups in Young's

moduli ($p>0.05$), found to be approximately 80-100 kPa. It is concluded that vitrification of an alginate-encapsulated cell system sustained cellular metabolic activity and maintained mechanical strength after thawing. This may offer an attractive approach towards the clinical long-term storage of such systems.

5.2 Introduction

Cell-based therapies are an emerging area of research and clinical practice and offer attractive approaches for treating medical conditions, such as insulin-dependent diabetes. Long-term storage is essential for any such therapeutic product to become clinically available. Cryopreservation is commonly used for cell banking and may be attractive for long-term tissue preservation as well. Despite the advantages and applications of encapsulated cell systems, there have been limited studies on their ability for long-term storage. Results in the field have been mixed with a range of cell viabilities and capsule damage after cryopreservation-thawing [88-97]. Due to the soft, hydrogel composition of these systems, they are particularly susceptible to freezing injury. Previous studies including results from our group indicate that ice formation from conventional freezing results in loss of cell viability and matrix damage [42, 91]. Hence, the avoidance of ice crystallization during cooling and thawing, accomplished by vitrification, could maintain cellular and matrix integrity. Advantages to achieving a glassy state both intra- and extracellulary by vitrification have been shown for a variety of tissues including blood vessels [37], heart valves [164], kidney [165], embryos [166] and thin articular cartilage slices [30].

To this end, initial studies using baseline vitrification solutions and cooling/warming protocols have been applied to a tissue engineered pancreatic substitute

[42] that has been extensively characterized in our lab [11, 14, 167, 168]. The substitute consists of murine insulinoma cells encapsulated in calcium alginate microspheres. Evaluating the necessary exposure times of tissue-engineered pancreatic substitutes to various cryoprotectants provides a basis for proper design of cryopreservation protocols to most effectively preserve these constructs. By knowing approximately how much time is needed for each CPA to diffuse-in and out of this system, protocols can be designed to optimize both the introduction and elution of CPAs. This will help minimize the cytotoxic and osmotic effects of the CPAs to the cells. By design necessity, bioartificial tissues relying on diffusion for cellular nourishment are significantly more permeable to solutes than natural tissues, so CPA exposure times are expected to be much lower for artificial tissues. Because tissues and tissue-based systems vary, one general protocol would not necessarily be optimal to preserve all tissues. Hence, by knowing how long is takes for CPAs to enter and exit the system of interest, protocols can be modified accordingly.

To optimize vitrification protocols, a systematic procedure was developed. In this study, CPA transport properties at the cell level [1] and through the matrix (determined in this study) were combined in a 3-D model of encapsulated insulin-secreting cells. Two vitrification solutions were characterized by thermal analysis and used to vitrify the encapsulated cell system of βTC-tet cells in calcium alginate beads. In addition to assessing cell viability, mechanical strength of the beads was measured before and after cryopreservation. Together, this study describes an approach to develop optimized cryopreservation protocols for an encapsulated cell system based on modeling and experimentally measured parameters.

5.3 Materials and Methods

5.3.1 Cell and Cell Culture

βTC-tet cells were obtained from the laboratory of Dr. Shimon Efrat, Albert Einstein College of Medicine, Bronx, NY [87]. Monolayer cultures were initiated from frozen stocks and cultured in T-flasks (Greiner Bio-One, Monroe, North Carolina USA) in complete growth medium consisting of Dulbecco's Modified Eagle's Medium (DMEM) (Sigma Chemical Co, St. Louis, MO USA) supplemented with 1% L-glutamine (Sigma Chemical Co), 10% fetal bovine serum (Triton Biologics, Durham, NC USA) and 1% penicillin/streptomycin (Fisher Scientific, Fairlawn, NJ USA). Cultures were incubated in a 37°C, 5% CO_2, humidified incubator. Cells were split at ratios of 1:5 when confluent and used between passage numbers of 40 and 45.

5.3.2 Fabrication of beads

βTC-tet cells were entrapped in calcium alginate as described previously [42]. Briefly, cells were detached from monolayer cultures by trypsinization using 0.05% trypsin-EDTA (MediaTech, Herndon, VA USA) and suspended at a density of $3x10^7$ cells/mL in 2.0% (w/v) 0.2μm-filtered sodium alginate (Pronova LVM alginate; NovaMatrix, Norway). Alginate microbeads with entrapped βTC-tet cells were made with an electrostatic droplet generator (Nisco Engineering AG, Zurich, Switzerland) by adding the cell-alginate suspension in a dropwise fashion using a syringe pump into a 1.1% (w/v) $CaCl_2$ gelling bath. Beads for the cryopreservation studies ranged in diameter from 500 to 600 μm and were incubated with culture media in T-flasks placed on an orbital shaker in a 37°C, 5% CO_2, humidified incubator.

5.3.3 Mathematical modeling and calculations

Multi-solute CPA transport within the encapsulated cell system was simulated with a two-compartment model to characterize diffusion within the hydrogel matrix as well as across the βTC-tet cell membrane.

5.3.3.1 CPA transport across cell membrane

βTC-tet membrane permeabilities for DMSO and PD were taken from previously determined values [1]. To account for solute transport across the cell membrane, a two-parameter membrane formalism with modications, was used [51].

Briefly, the water flux into a cell is given by

$$\frac{dV_w}{dt} = -L_p ART(M^e - M^i) \tag{5.1}$$

and the solute flux is given by

$$\frac{dN_i}{dt} = P_{si} A(M_i^e - M_i^i) \tag{5.2}$$

where V_w (μm^3) is the volume of water inside the cell; L_p ($\mu m/s \bullet atm$) is the water permeability; A (μm^2) is the surface area of the cell; R (($\mu m^3 \bullet atm$)/(mol•K)) is the universal gas constant; T (K) is the absolute temperature; M^e and M^i (osmoles/μm^3) are the total external and internal osmotic concentrations, respectively; M_i^e and M_i^i (osmoles/μm^3) are the external and internal osmotic concentrations, respectively of the ith solute; N_i (osmoles) is the intracellular amount of the ith solute; P_{si} ($\mu m/s$) is the ith solute permeability. M^e and M^i were determined using the osmotic virial equation extended for 1 or 2 solutes depending on the solution being modeled (2-solute equation given in

equation 5.11); M_i^e and M_i^i were determined using the osmotic virial equation for a single solute [147].

5.3.3.2 CPA transport through matrix - effective diffusivity determination

A volume of 500 μL of 2 mm alginate beads with gluteraldehyde-deactivated cells was transferred into a 10 mm Petri dish and media was removed. The deactivated cells were included for consistency in D_{eff} values as deactivation prevents cell metabolism and function, while retaining the basic elements of cell structure. Cells were deactivated through incubation with 1% glutaraldehyde for 1 minute; the glutaraldehyde was then removed through a series of four washes with PBS, and the dead cells were suspended at a density of $3x10^7$ cell/mL in sodium alginate and used to make cell-laden microbeads (general encapsulation method described above). A volume of 5.0 mL of 2 M CPA in 0.85% NaCl was added to the beads. 50 μL samples were taken at times: 15s, 30s, 45s, 60s, 90s, 120s, 240s, 600s (with replacement, to maintain a constant volume). Time 0 sample consisted of pure 2 M CPA. In order to reduce mass transfer limitations outside the beads, the Petri dish was put on an orbital shaker. Beads were stored in the incubator in a T-flask on an orbital shaker until needed. Samples were put into 5 mm glass NMR tubes (Norell, Landisville, NJ) along with 450 μL D_2O (Sigma) and 100 μL acetonitrile (Sigma), giving a total volume of 600 μL in each tube. Acetonitrile was added to each sample to serve as an external reference. Acetonitrile was chosen because it has a sharp, single peak and its resonance does not interfere with that of the CPAs investigated. CPA bulk diffusivity values were determined by using the Wilke-Chang equation [169].

Processing of Results

Samples were analyzed using ^{1}H NMR operating at 300 MHz (Varian Mercury Vx 300), pulse 32.4 degrees, relax delay 1s, 16 repetitions. Due to the high water content in the samples, water was suppressed using a standard water suppression routine. In order to analyze the spectra, the acetonitrile peak was set to 1 and the CPA peaks were measured relative to that. CPA concentrations were found by linear interpolation using a calibration curve of known CPA concentrations and their relative CPA to acetonitrile peak areas.

The CPA concentration in the bulk solution was followed over time until equilibrium was practically reached. The partial differential equations and boundary conditions for diffusion coupled with the mass balance between the beads and solution (assuming partition coefficient of 1) can be solved analytically for solute diffusing from the liquid bulk into the beads initially free of solute or for solute diffusing out of the bead into an initially solute-free bulk solution. The analytical solutions are as follows [170]:

Diffusion-In:

$$\frac{C_b}{C_{bo}} = \left(\frac{\alpha}{1+\alpha}\right)\left(1+\sum_{n=1}^{\infty} \frac{6(1+\alpha)e^{\left(\frac{-D_{eff}q_n^{\,2}t}{R^2}\right)}}{9(1+\alpha)+q_n^{\,2}\alpha^2}\right) \tag{5.3}$$

Diffusion-Out:

$$\frac{C_b}{C_o} = \left(\frac{1}{1+\alpha}\right)\left(1-\sum_{n=1}^{\infty} \frac{6\alpha(1+\alpha)e^{\left(\frac{-D_{eff}q_n^{\,2}t}{R^2}\right)}}{9(1+\alpha)+q_n^{\,2}\alpha^2}\right) \tag{5.4}$$

$$\tan q_n = \frac{3q_n}{3 + \alpha q_n} \tag{5.5}$$

where,

C_b = concentration in the liquid bulk (mol/L)
C_{bo} = initial concentration in the liquid bulk (mol/L)
C_o = initial concentration throughout the bead (mol/L)
D_{eff} = effective diffusivity (cm^2/s)
α = volume ratio of liquid to beads
q_n = n^{th} root of equation (5)
R = radius of bead (mm)
t=time (s)

q_n values were substituted into equations 3 or 4, which were solved numerically to obtain C_b vs. t. The solutions of equations 3 and 4 were fit to experimental data using regression with D_{eff} as the only adjustable parameter.

5.3.3.3 CPA transport through matrix and across cell membrane: CPA tissue equilibration

MATLAB software (MathWorks, Natick, MA) was used to couple the CPA concentration profiles from the two compartments (tissue matrix and βTC-tet intracellular compartment) as determined from above.

Model Assumptions

1. No CPA reaction or consumption by the cells or matrix.
2. Uniform cell distribution.
3. Isotropic effective diffusivities throughout tissue.
4. Isothermal experimental conditions.
5. Constant cell membrane permeabilities (independent of CPA concentration, position within the tissue and time).
6. No solute-solute interactions for multi-solute CPA transport across cell membrane or in the tissue matrix; CPA transport is driven only by its concentration gradient.

Mass transport through the alginate matrix (in spherical coordinates) can be expressed as

$$\frac{\partial C}{\partial t} = -D_{eff}\left(\frac{1}{r^2}\frac{\partial}{\partial r}(r^2\frac{\partial C}{\partial r}) + \frac{1}{r^2\sin\Theta}\frac{\partial}{\partial\Theta}(\sin\Theta\frac{\partial C}{\partial\Theta}) + \frac{1}{r^2\sin^2\Theta}\frac{\partial C^2}{\partial\Phi^2}\right) + r_A \qquad (5.6)$$

In the above equations, C=CPA concentration (mol/L); t=time (s); D_{eff}=effective diffusivity (cm^2/s); r=radial position (cm); r_A=reaction rate per unit volume (mol/L.s); Θ=zenith angle (radians); Φ= azimuthal angle (radians); R_o=radius of the bead (cm)

Assuming angular symmetry ($\frac{\partial}{\partial\Theta},\frac{\partial}{\partial\Phi} = 0$) and that the reaction rate r_A is0,

$$\frac{\partial C}{\partial t} = -D_{eff}\left(\frac{1}{r^2}\frac{\partial}{\partial r}(r^2\frac{\partial C}{\partial r})\right) \qquad (5.7)$$

The following boundary and initial conditions apply:

i) $C(r, t=0) = 0$ (no CPA initially present in the bead (5.8)

ii) $C(r=R_0,t) = C_{external}$ (5.9)

where R_o is the bead radius (CPA concentration at the spherical surface equal to that in the liquid bulk)

iii) $\frac{\partial C}{\partial r}(r=0,t) = 0$ (symmetry condition at the center of the bead) (5.10)

The resulting second-order PDE function describing Fick's Second Law was solved using MATLAB's built-in PDE solver. Addition and removal of high concentration of CPAs were simulated in step-wise manner to minimize osmotic effects; the input conditions for the PDE solver were different at each step. CPA diffusivities through the alginate matrix were assumed constant and independent of local solute concentration. Single and multi-solute intracellular solute osmolality and cell volume

excursion profiles for βTC-tet cells were simulated as a function of time at chosen points within a 500 μm diameter alginate bead containing a homogeneous distribution of βTC-tet cells. One of the positions considered was the center of the bead, as this is the limiting position for solute equilibration. In addition, a multi-solute osmotic virial equation model was used to account for the non-ideality of the high concentration solutes in predicting CPA osmolalities as described by Elliott et al. [147]. The osmolality calculations relating CPA concentrations to osmotic concentrations, M^e, M^i, M_i^e, and M_i^i, were used in cell volume and intracellular CPA concentration predictions in equations 5.1 and 5.2. The osmotic virial equation for a 2-solute system can be expressed as [147],

$$\pi = c_1 + c_2 + B_1 c_1^{\,2} + c_1 c_2 (B_1 + B_2) + B_2 c_2^{\,2} \tag{5.11}$$

where π is the osmolality (Osm), c_1 and c_2 are the molal concentrations (moles of solute per kilogram of solvent) of CPA DMSO and PD, respectively; B_1, B_2 are the second osmotic virial coefficients for DMSO and PD, respectively. The virial coefficient values for DMSO and PD were taken from [147] and are given in Table 5.3. Sucrose, a non-permeating cryoprotectant, was a component in the removal solutions and had to be accounted for in the model. A D_{eff} value of 4.39 x10^{-10} m^2/s was used in the calculations, assuming a sucrose bulk diffusivity of 5.49x10^{-10} m^2/s at 22°C [169] and a D_{eff}/D_o factor of 0.8 (based on effective diffusivity values of CPAs through alginate).

5.3.4 Thermal Characterization of Vitrification Solutions using Differential Scanning Calorimetry (DSC)

Unless otherwise stated, all chemicals were purchased from Sigma Chemical Company (St. Louis, MO USA). The solutions used for vitrification consisted of 5.5 M 1,2 propanediol (PD) + 1 M sucrose (referred to as 55PD_1S) and 3 M dimethyl sulfoxide (DMSO) + 3 M PD + 0.3 M sucrose (referred to as DP6_0.3S) in a modified Euro-Collins carrier solution (34.95 g/L dextrose, 0.84 g/L sodium bicarbonate and 1.12 g/L potassium chloride). Between 10-12 mg of each solution was put into DSC pans (Perkin-Elmer, USA) and sealed. The phase transition temperatures and heat flow of the solutions were measured during warming by differential scanning calorimetry (Diamond DSC, Perkin-Elmer, USA). Each run had a sample pan and an empty pan as reference. The samples were cooled rapidly at 100°C/min from room temperature down to -130°C. The samples were held for two minutes to allow for thermal equilibration and then warmed between 5-10°C/min. The glass transition temperature, T_g, was determined as the midpoint of a jump in heat flow; the devitrification temperature, T_d, was selected from the peak of the exothermic event of the thermogram.

5.3.5 Vitrification and Conventional Freezing: CPA Addition-Removal, Cytotoxicity and Cryopreservation

The solutions used for vitrification consisted of 5.5 M PD + 1 M sucrose and 3 M dimethyl sulfoxide DMSO + 3 M PD+0.3 M sucrose. The equilibration times and number of steps needed to safely load and remove the vitrification solutions were derived based on the two-compartment model as described above. Following these protocols, cell viability was determined. In addition, a study was done to measure the cytotoxicity of the solutions.

For vitrification, CPA solutions were added stepwise, and after addition of the final vitrification solution, encapsulated constructs were cooled in 20 mL glass scintillation vials (Kimble Glass Inc., Vineland, NJ) as follows: i) For DP6+0.3 M sucrose, samples were cooled rapidly (100°C/min) to -100°C by immersion into a pre-cooled isopentane bath (Fisher), followed by slow cooling (10°C/min) to -135°C by moving the samples out of the isopentane bath and into the vapor phase of LN_2. To monitor the temperature, a thermocouple was inserted into a separate dummy sample of the same vitrification solution and its output was tracked via a digital thermometer (Omega) in parallel. Samples were held at this temperature for 5-10 minutes and then thawed in two stages: first, a slower warming to -100°C (30°C/min) and then rapid warming (225°C/min). The slower warming rate was achieved by moving the vials higher up in the LN_2 vapor phase and the fast warming rate was generated by placing the glass vials in a 37°C water bath. ii) For 5.5 M PD + 1 M sucrose, samples were cooled rapidly (100°C/min) to -85°C, followed by slow cooling (10°C/min) to -135°C. Samples were thawed in two stages: first, a slower warming to -85°C (30°C/min) and then rapid warming (225°C/min) in a 37°C water bath. Following the last step of CPA removal, encapsulated cell constructs were incubated with culture media in T-flasks placed on an orbital shaker in a 37°C, 5% CO_2, humidified incubator. In addition, one of the solutions, 3 M DMSO+3 M PD+0.3 M sucrose, was investigated in more depth. Three sub-optimal protocols were carried out by modulating the exposure times and number of steps. Vitrified-thawed samples were cultured and assessed for cell viability over time via alamarBlue®. In these groups, i) the number of steps were reduced so that volume excursions experienced by the cells would be greater and approach their osmotic

tolerances (group called Vit DP6_0.3S Nonopt: Vol); ii) at the end of optimized, stepwise addition, the full strength solution was left for 15 minutes, the specimen vitrified-thawed, and CPA removed stepwise; thus the cells experienced CPA cytotoxic effects due to prolonged exposure (group called Vit DP6_0.3S Nonopt: Cyto); iii) the third group was a combination of i) and ii) where the cells experienced higher volume excursions and CPA cytotoxic effects (group called Vit DP6_0.3S Nonopt: Vol+Cyto) These non-optimal groups served as various negative controls and provided information on the sensitivity of an addition and removal protocol towards cell viability in fast CPA diffusing, hydrogel-based systems. The CPA addition-removal protocols used are summarized in Table 5.1.

Table 5.1 Optimized and sub-optimal cryopreservation protocols used for vitrification of encapsulated βTC-tet cells. **A**. optimized protocol used for 3 M dimethyl sulfoxide (DMSO) + 3 M 1,2 propanediol (PD) + 0.3 M sucrose; **B**. optimized protocol used for 5.5 M PD + 1 M sucrose; **C**. Sub-optimal protocol used for 3 M DMSO + 3 M PD + 0.3 M sucrose; CPA=cryoprotectant, M=molarity;

A

Step	[CPA]	[Sucrose]	Time	Temperature
	(M)	(M)	(s)	(ºC)
1	2	0	120	4
2	4	0	120	4
3	6	0.3	60	4
4	4	0.2	120	22
5	2	0.15	120	22
6	1	0.075	120	22
7	0	0	300	22

Table 5.1 (continued)

B

Step	[CPA]	[Sucrose]	Time	Temperature
	(M)	(M)	(s)	(ºC)
1	1.83	0	120	4
2	3.67	0	120	4
3	5.5	1	60	4
4	4	0.2	120	22
5	2	0.15	120	22
6	1	0.075	120	22
7	0	0	300	22

C

Step	[CPA]	[Sucrose]	Time	Temperature
	(M)	(M)	(s)	(ºC)
1	2	0	120	4
2	6	0.3	120	4
3	4	0.15	30	22
4	0	0	300	22

Conventional cryopreservation was used as the frozen control [42]. Briefly, encapsulated cell constructs were initially immersed for 5 minutes in complete growth medium containing 1.4 M DMSO at 4°C in cryovials (Nalgene, Nalge, Rotherwick, UK). Samples were then cooled at a controlled rate of 1.0°C/min to -80°C and finally transferred to liquid nitrogen for storage. Thawing was accomplished by immersing the containers in a water bath controlled at 37°C until all ice had visibly disappeared. Consequently, the DMSO was removed from the beads in a one-step removal with DMEM. Following the

last step of CPA removal, encapsulated cells were incubated with culture medium in T-flasks placed on an orbital shaker in a 37°C, 5% CO_2, humidified incubator.

For the cytotoxicity study, CPAs were added in a stepwise manner; beads were exposed to the final CPA concentration for 5, 10 or 15 minutes; and the CPAs were then removed in a stepwise manner. In a positive control, cells were exposed to 1X EuroCollins in the same stepwise addition-removal manner as the corresponding experimental group. Following CPA removal, cell viability was measured by alamarBlue®.

5.3.6 Mechanical testing of cryopreserved encapsulated cells

Uniaxial compression was performed to measure the mechanical properties of 2% calcium alginate beads with a Bose ElectroForce® 3100 (EnduraTec, Inc., Eden Prairie, MN USA) after cryopreservation. The compression of non-adhesive elastic spheres between two parallel flat platens has been described by Hertz's theory and shown to be valid for small deformations between 0-10% [171, 172]. When an elastic spherical body is subjected to an applied contact normal load (P), contact will occur on the sphere-substrate interface, described by

$$a_z = \left(\frac{3RP}{4E^*}\right)^{1/3} \tag{5.12}$$

where a_z is the radius of the contact zone, E^* is the contact modulus and R is the effective radius. For an elastic sphere in contact with a platen, the Young's modulus of the rigid flat platen tends to infinity, and the contact modulus, E*, corresponds to the plain strain modulus of the sphere, comprised of ν and E, where ν is Poisson's ratio, assumed to be 0.5 [151], and E is Young's modulus. The dimensionless approach, a^*, or compressive displacement normalized to the size of the sphere, can be expressed by

$$a^{*3/2} = \left(\frac{3P(1-\nu^2)}{4ER^2} \right)^{1/3} \tag{5.13}$$

Force (P) vs. dimensionless approach (a^*) characteristics of cryopreserved cell-free and cell-encapsulated alginate beads were determined by compression between two rigid parallel plates to calculate Young's modulus using equation 5.13. A schematic of the setup is shown in Figure 5.7A. A compression rate of 0.01 mm/s was used on 1.3 ± 0.1 mm alginate beads with a 0.5 N load cell (ULC-0.5, Interface Inc., Scottsdale, AZ). Five beads were tested for each treatment group, performed in triplicate (total of 15 beads per group) and carried out under ambient conditions, 22°C. This larger bead size was used for mechanical testing due to difficulty in loading and testing of smaller samples. Beads were vitrified and conventionally frozen as described above. Similar optimized protocols were used but with modified exposure times (four minutes per step instead of two minutes) to reflect the increased bead diameter. Cell-free beads were processed in the exact same way as those with cells. After cryopreservation, all treatment groups were transferred into culture flasks with culture medium and placed on an orbital shaker in a 37°C, 5% CO_2, humidified incubator. Compression measurements were carried out within a few hours of treatment. The average Young's modulus and standard deviation were reported for each condition.

5.3.7 Cell viability measurement

The alamarBlue® (BioSource International, Inc.) assay were used to assess the cell viability of the encapsulated beads pre- and post- cryopreservation as described previously [42]. Briefly, 100 μL of beads, 100 μL alamarBlue® and 1 mL DMEM were placed into a 24- well plate. Controls were also used in which 100 μL alamarBlue® and

1 mL DMEM were placed into the wells. After proper mixing, the 24- well plate was placed into a 37˚C/5% CO_2 incubator for 3 hours. Following incubation, 100 μL of medium from each well, including controls, were placed into a 96-well microtiter plate for reading. The plate was read with a Spectra Max Gemini Plate Reader using an excitation wavelength of 544 nm and an emission wavelength of 590 nm.

Confocal microscopy was used on days 1 and 4 post-cryopreservation to visualize the distribution of living and dead cells within the alginate beads with the LIVE/DEAD™ kit (Molecular Probes Inc). This cell viability assay uses calcein AM and ethidium homodimer, two fluorescent probes, which measure intracellular esterase activity and plasma membrane integrity, respectively, to indicate living and dead cells. The kit was used as per the manufacturer's suggested protocol. Briefly, 20μL of the supplied 2 mM ethidium homodimer stock solution and 5 μL of the supplied 4 mM calcein stock solution were mixed into 10 mL of 1x PBS. Beads were incubated with the solution for 30-45 minutes in the dark at room temperature. Following incubation the beads were rinsed twice in 1x PBS and visualized. Calcein was viewed with a fluorescein optical filter, 485 nm; ethidium homodimer was viewed with a rhodamine optical filter, 530 nm. Viable cells appeared green and dead cells red.

5.3.8 Statistical Analysis

Statistical analyses were done using ANOVA and Tukey's post-hoc (Minitab Release 14.11) to determine effects of treatments. Comparisons were considered significant at a level of $p<0.05$.

5.4 Results

5.4.1 CPA transport

Figure 5.1A shows a typical proton spectrum of PD obtained in the presence of the external reference, acetonitrile. ^{1}H NMR was used as an offline assay tool to determine the CPA concentration in the bulk at various time points with a calibration curve (inset in Figure 5.1A). Figures 5.1B and 5.1C show the bulk PD concentration during diffusion-in and out of beads, respectively. Based on the bulk concentration profiles, the effective diffusivity of the CPAs through the alginate matrix were determined, and are reported in Table 5.2. As expected of small molecular weight solutes diffusing through alginate, the diffusion of the CPAs examined was fast, equal to 76 % to 90% of that in free solution.

5.4.2 Vitrification solution thermal analysis

Figure 5.2 shows the heat flow vs. temperature profiles during the warming of the two vitrification solutions, DP6_0.3S and 55PD_1S, from -130 to -30°C. Solution DP6_0.3S was found to have a T_g of -116°C and a devitrification temperature of -58°C (Figure 5.2A). Solution 55PD_1S had a glass transition temperature of -100°C and no observable devitrification event (Figure 5.2B). Moreover, no ice formation was observed macroscopically during cooling or warming of these solutions in glass vials using the cooling/warming protocols described in the Materials and Methods section.

5.4.3 CPA transport modeling and cryopreservation experiments

Figure 5.3 shows computer simulations of volume excursions and intracellular CPA concentration using multi-step addition and removal schedules. The number and duration of each 'optimized' step was such that the volume excursions were within the

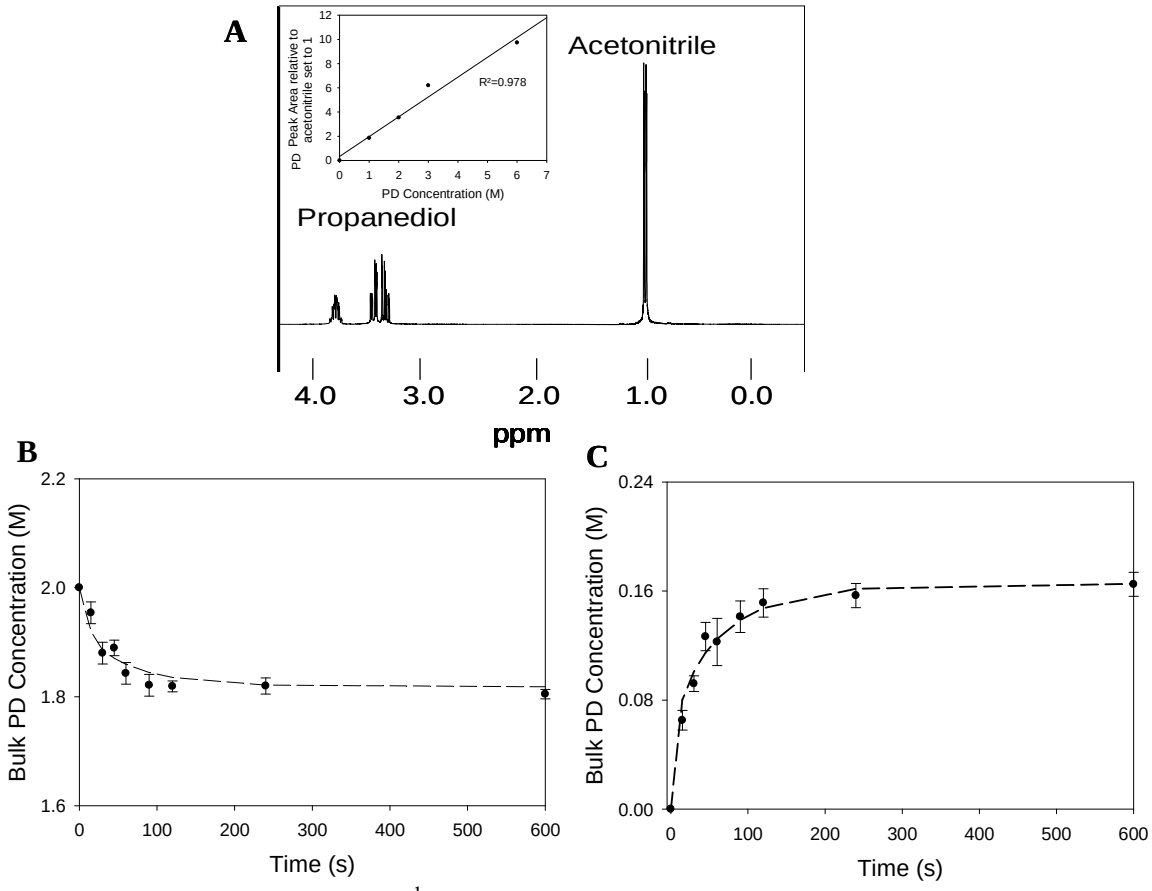

Figure 5.1 A. Typical ^{1}H NMR spectrum of CPA and acetonitrile used to determine CPA concentrations with a calibration curve (inset); representative data and modeling for **B**. diffusion-in and **C**. diffusion-out of 2 M PD at 22°C from alginate beads containing inactivated βTC-tet cells

osmotic tolerances of βTC-tet cells [1]. Using the minimum exposure time at each step to attain intracellular CPA equilibration, approximately 80% cell viability for both vitrification solutions was obtained (Figure 5.4). The cytotoxic effects of the solutions were investigated by implementing the following procedure: CPAs were added in a stepwise manner at 4°C; beads were exposed to the final CPA

Table 5.2 CPA diffusivities through alginate-encapsulated, inactivated βTC-tet cells and CPA diffusivities through cell-free alginate expressed relative to diffusivities in bulk solution (D_{eff}/D_o) at room temperature; D_{avg} is the average of 3 single fit curves through the experimental data.

		Measured Diffusivity	Bulk Diffusivity	
	CPA	**D_{avg} ± s.d.**	**D_o**	**D_{eff}/D_o**
		x10^{-5} (cm^2/s)	x10^{-5} (cm^2/s)	
Diffusion-In				
	DMSO	1.35 ± 0.18	1.62	0.83
	PD	0.926 ± 0.112	1.22	0.76
	BD	0.753 ± 0.0904	0.85	0.89
	EG	0.947 ± 0.116	1.18	0.80
Diffusion-Out				
	DMSO	1.38 ± 0.153	1.62	0.85
	PD	0.96 ± 0.125	1.22	0.79
	BD	0.692 ± 0.088	0.85	0.81
	EG	0.873 ± 0.125	1.18	0.74

Table 5.3 Values of model parameters used in this study

Parameter	Value	Units	Source
L_p (DMSO); L_p (PD) at 22°C	3.07 x 10^{-3} ; 4.45 x 10^{-3}	[μm/s.atm]	[1]
L_p (DMSO); L_p (PD) at 4°C	6.67 x 10^{-4} ; 5.0 x 10^{-4}	[μm/min.atm]	[1]
P_s (DMSO); P_s (PD) at 22°C	1.45 x 10^{-1} ; 2.32 x 10^{-1}	[μm/s]	[1]
P_s (DMSO); P_s (PD) at 4°C	4.73 x 10^{-2} ; 5.81 x 10^{-2}	[μm/s]	[1]
D_{eff} (Sucrose, 22°C)	4.39 x 10^{-10}	[m^2/s]	[169]
B (2nd virial coefficient) (DMSO)	0.0843	[mol/kg]$^{-1}$	[147]
B (2nd virial coefficient) (PD)	0.0576	[mol/kg]$^{-1}$	[147]

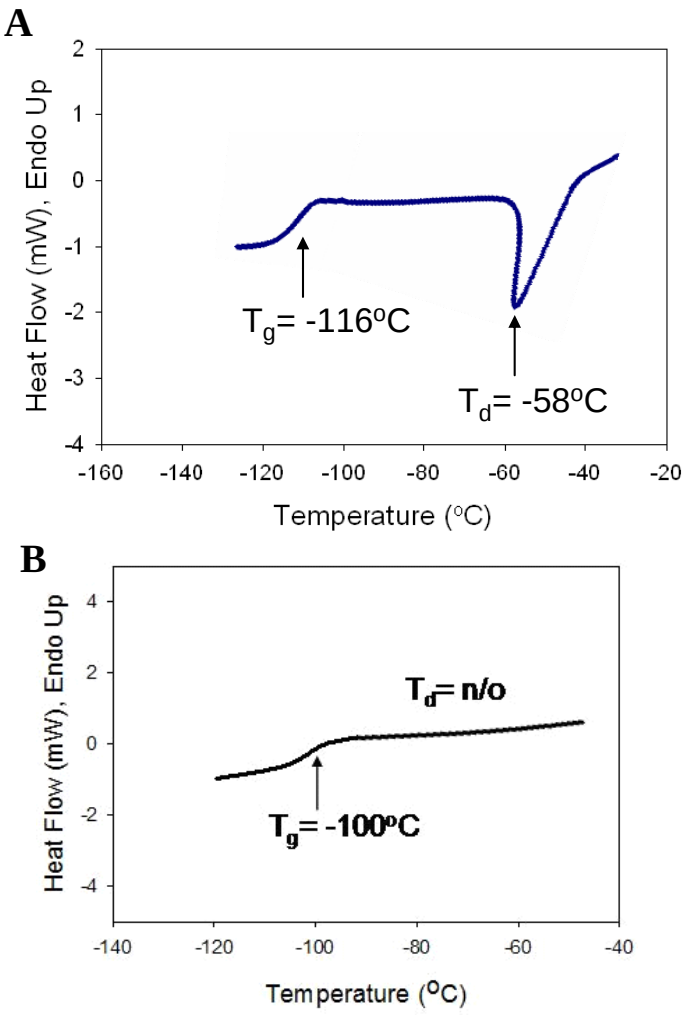

Figure 5.2 DSC thermograms during warming at 5°C/min of vitrification solutions. **A**. 3 M DMSO + 3 M PD + 0.3 M sucrose; **B**. 5.5 M PD + 1 M sucrose; T_g=glass transition temperature; T_d=devitrification temperature;

concentration for 5 or 15 minutes at 4°C; and the CPAs were then removed in a stepwise manner at 22°C. In a positive control, cells were exposed to 1X EC in the same stepwise addition-removal manner as the corresponding experimental group. Following CPA removal, cell viability was measured using alamarBlue®, a non-invasive metabolic function indicator, and normalized to fresh controls. Although there was no difference in viabilities between the two groups of solutions after 5 minutes of exposure at full

A

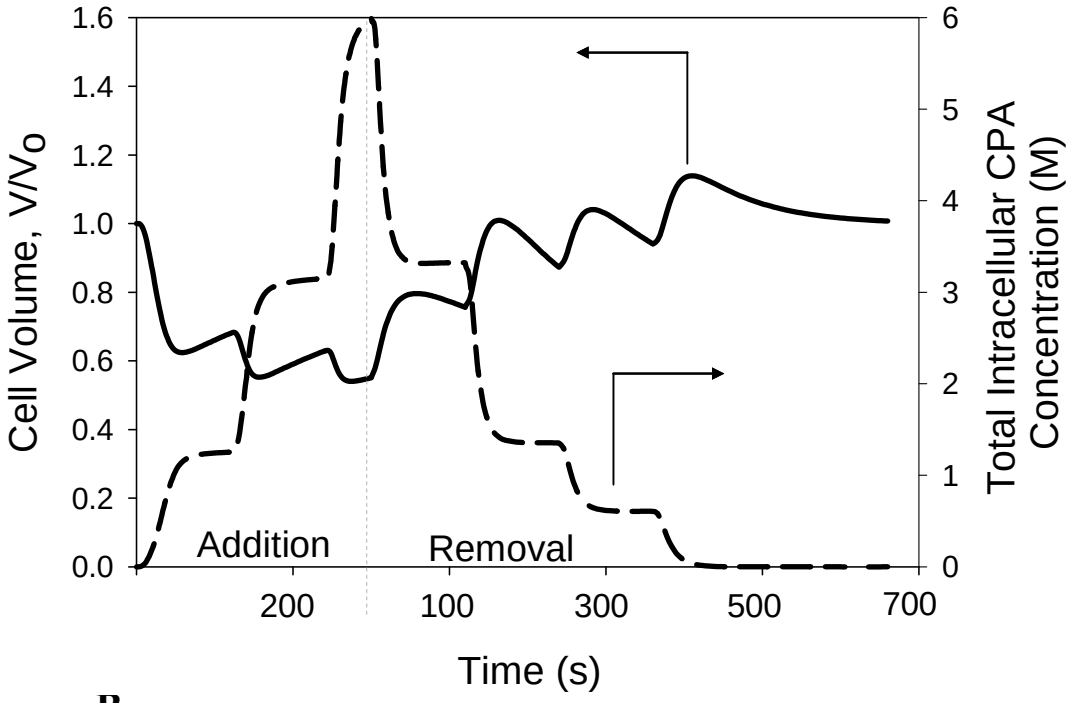
Cell Volume, V/V0
Total Intracellular CPA Concentration (M)
Addition
Removal
Time (s)

B

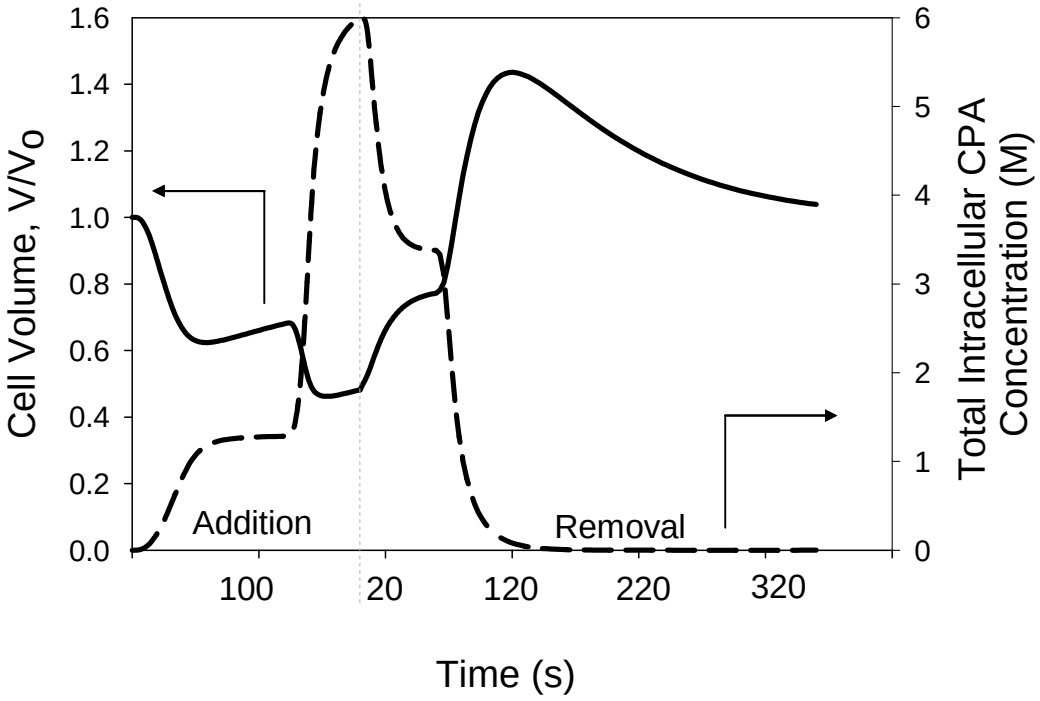
Cell Volume, V/V0
Total Intracellular CPA Concentration (M)
Addition
Removal
Time (s)

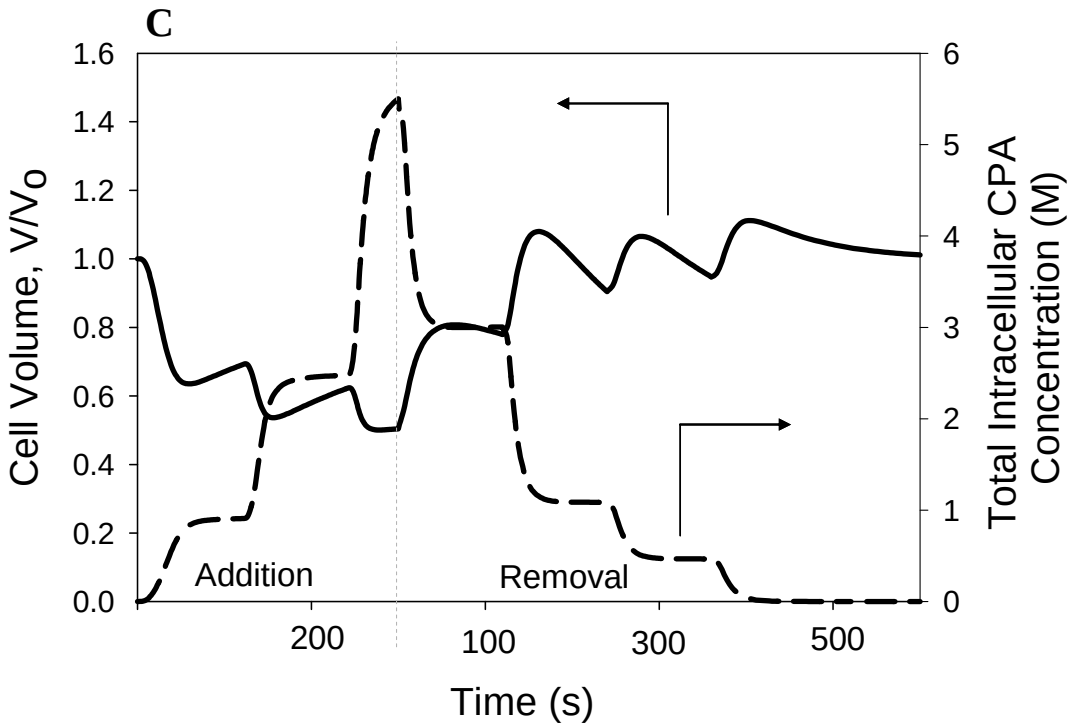

Figure 5.3 Simulated cell volume excursions and intracellular CPA concentrations at the center of 0.5 mm beads for two vitrification solutions; **A** and **B** are optimized and sub-optimal protocols used for 3 M DMSO + 3 M PD + 0.3 M sucrose, respectively; **C** is an optimized protocol used for 5.5 M PD + 1 M sucrose; osmotically tolerable limits for βTC-tet cells were 0.50 to 1.8 of V/V_o, with V_o being the isotonic, equilibrium volume (Mukherjee et al 2007).

strength, there was a difference at 15 minutes, with DP6_0.3S being more toxic to the cells than 55PD_1S.

Once it was established that the vitrification solutions could be added and removed from the beads safely, the beads were vitrified. This resulted in average post-thaw survival of 71% and 62% for DP6_0.3S and 55PD_1S, respectively, relative to fresh controls (Figure 5.5). The viability, as measured by the metabolic indicator alamarBlue®, was constant over four days of culturing post-thaw for both groups

(p>0.05). Another group of beads was also cryopreserved by conventional freezing with 10% DMSO and slow freezing. The post-thaw viability was approximately 50% after

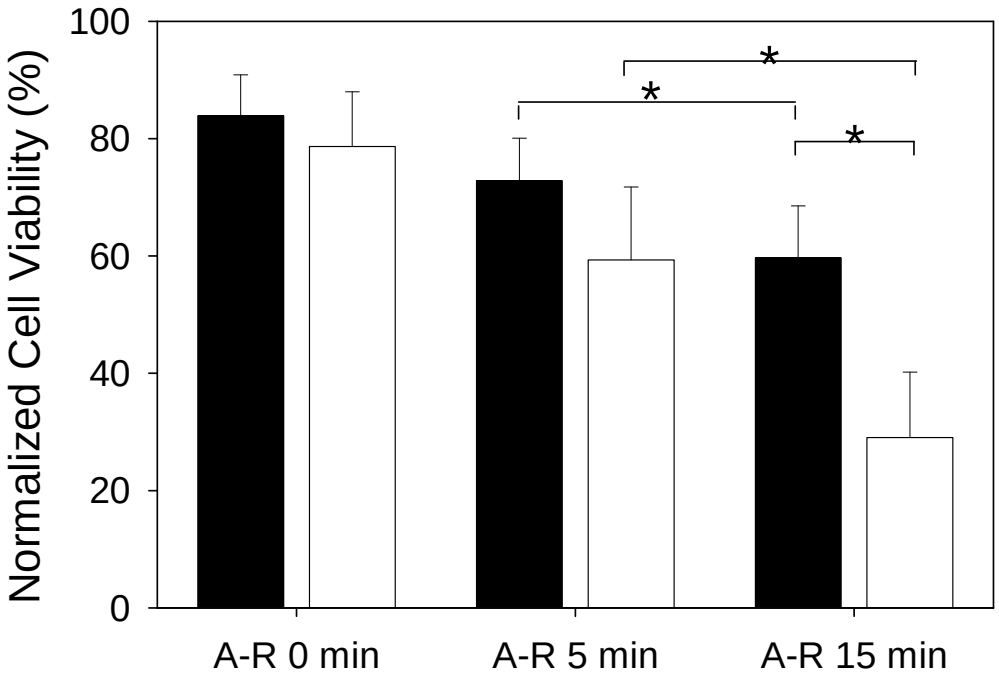

Figure 5.4 Normalized cell viability of alginate encapsulated βTC-tet cells in vitrification solutions after CPA cytotoxicity testing. CPAs were added in a stepwise manner at 4°C, exposed to the full strength solution for 5 or 15 minutes, and then removed from the beads in a stepwise manner; viabilities are reported as normalized values to fresh controls, where beads were exposed to 1X EuroCollins carrier solution using the same protocol as the corresponding experimental group; black bars are for solution 55PD_1S; white bars are for solution DP6_0.3S; bars represent avg ± s.d. from n=3; * indicates statistical difference at p<0.05.

thawing and stayed constant over culture time (p>0.05) (Figure 5.5). In addition to the optimized protocols, a set of negative control studies were done, with one of the vitrification solutions (DP6_0.3S), by intentionally employing sub-optimal vitrification protocols. In the first such protocol, 'Vit DP6_0.3S Nonopt: Vol', the number of addition and removal steps was shortened to increase cellular volume excursions; the protocol

used is in Table 5.1C and the corresponding volume excursions and intracellular solute concentration profiles are shown in Figure 5.3B. The resulting viabilities were indeed lower than the corresponding optimized protocols, but consistent around 50% over the culture period (Figure 5.5). In the next sub-optimal group, 'Vit DP6_0.3S Nonopt: Cyto', CPA was added to the beads, held for 15 minutes at full strength, the beads were vitrified and thawed, and then the CPA was removed. The resulting viabilities were 30% post-thaw and not different over culture time ($p>0.05$), shown in Figure 5.5. The last sub-optimal group ('Vit DP6_0.3S Nonopt: Vol+Cyto') was a combined protocol from the previous two, incorporating both increased volume excursions and cytotoxicity. As expected, the viability was low, at around 25%, and stayed this way over the four days of culture ($p>0.05$), as shown in Figure 5.5. The pairwise comparison between experimental groups for each day of culture are reported in Table 5.4 In addition to overall viability data, a qualitative visual assessment of live and dead cells was attained using the LIVE/DEAD® assay (Figure 5.6). The fresh controls, optimized protocols, the sub-optimal combined protocol and conventionally frozen beads were assessed. The quantitative viability data is corroborated with the confocal images of live and dead cells, with the greatest number dead cells present in the combined, sub-optimal group. Also, cell growth within the beads among all the groups is evident between day 1 and day 4 of assessment, post-thaw.

5.4.4 Mechanical testing of cryopreserved encapsulated cells

Using Hertz's theory, Young's moduli, or stiffness of alginate beads, were determined after vitrification and conventional freezing in the presence and absence of cells by compression testing using the setup shown in Figure 5.7A. Figure 5.7B shows a

typical force vs. dimensionless approach profile for a bead during compression with the measured force increasing with approach. Young's moduli were not statistically different

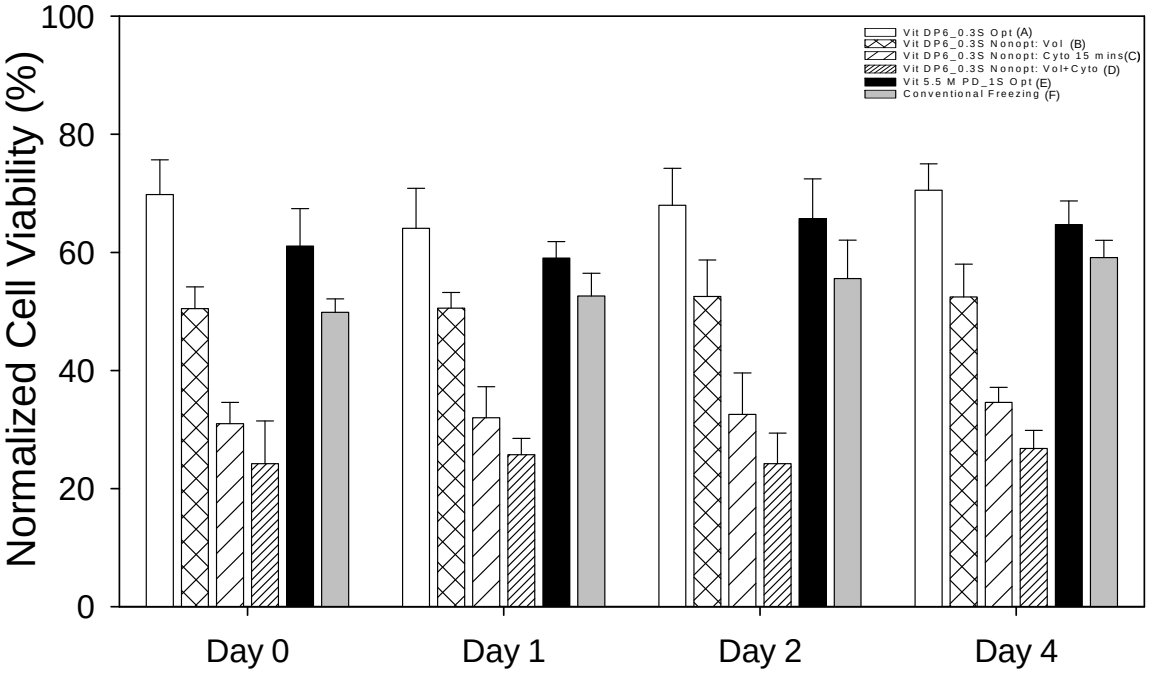

Figure 5.5 Normalized cell viability, measured by alamarBlue®, of alginate-encapsulated βTC-tet cells after cryopreservation using optimized and intentionally sub-optimal protocols; bars represent avg ± s.d. from n=4. Statistical differences are reported in Table 4. No statistical difference was found over culture time for each group ($p>0.05$)

($p>0.05$) between fresh, vitrified, and frozen alginate beads containing encapsulated cells; moduli were found to be between 70-110 kPa (Figure 5.7C). Moreover, no differences in Young's moduli were found between cell-laden and acellular beads across control and cryopreserved groups. However, there was a statistical difference between fresh and frozen acellular beads compared to 55PD_1S vitrified acellular beads

Table 5.4 Pairwise comparisons between experimental groups for each day of culture using ANOVA and Tukey's post-hoc; * denotes $p<0.05$; A=DP6_0.3S Optimized; B=Vit DP6_0.3S Nonopt: Vol; C=Vit DP6_0.3S Nonopt: Cyto; D=Vit DP6_0.3S Nonopt: Vol+Cyto; E=55PD_1S Optimized; F=Conventional freezing;

	A	B	C	D	E	F
Day 0						
A	-	*	*	*	p>0.05	*
B		-	*	*	p>0.05	p>0.05
C			-	p>0.05	*	*
D				-	*	*
E					-	p>0.05
Day 1						
A	-	*	*	*	p>0.05	*
B		-	*	*	p>0.05	p>0.05
C			-	p>0.05	*	*
D				-	*	*
E					-	p>0.05
Day 2						
A	-	*	*	*	p>0.05	*
B		-	*	*	p>0.05	p>0.05
C			-	p>0.05	*	*
D				-	*	*
E					-	p>0.05
Day 5						
A	-	*	*	*	p>0.05	*
B		-	*	*	*	p>0.05
C			-	p>0.05	*	*
D				-	*	*
E					-	p>0.05

($p<0.05$). The viabilities of the larger cell-encapsulated beads used for mechanical testing after cryopreservation were similar to values for the smaller beads reported in Figure 5 (data not shown).

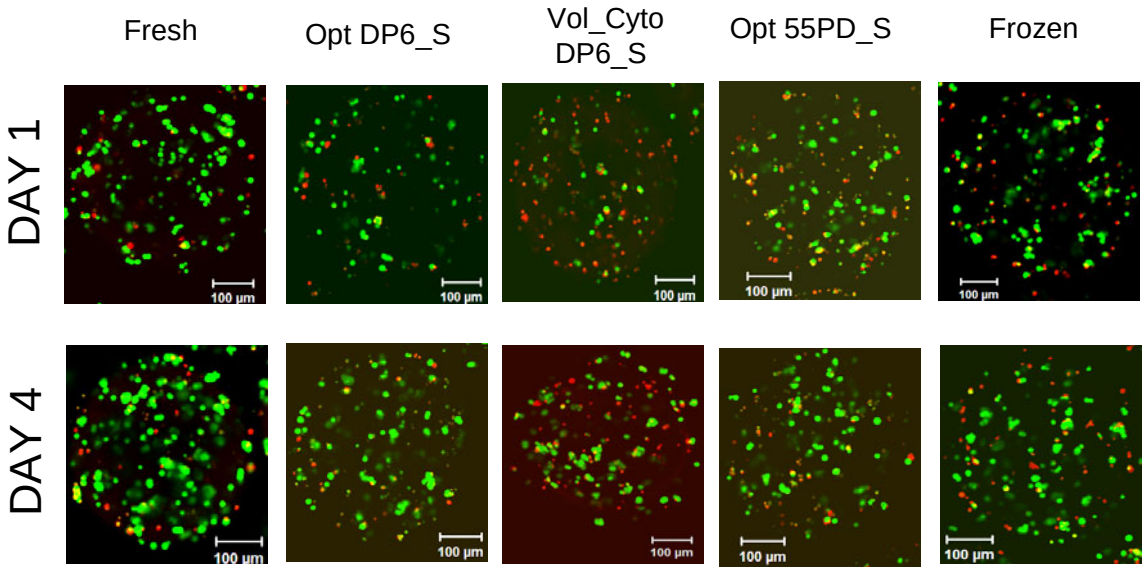

Figure 5.6 Confocal micrographs of cryopreserved-thawed alginate encapsulated βTC-tet cells at Day 1 and 4 post-preservation using the LIVE/DEAD™ assay.

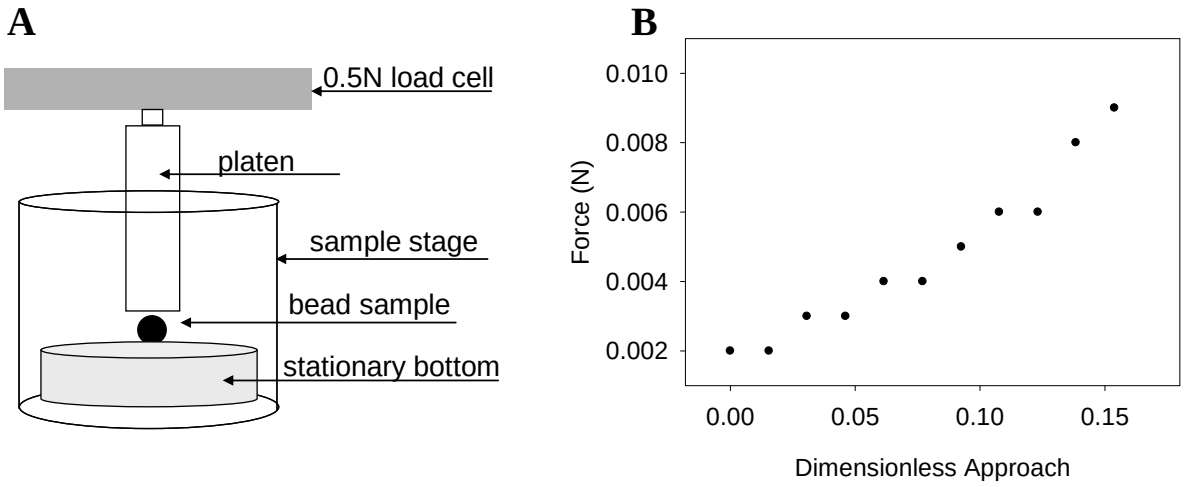

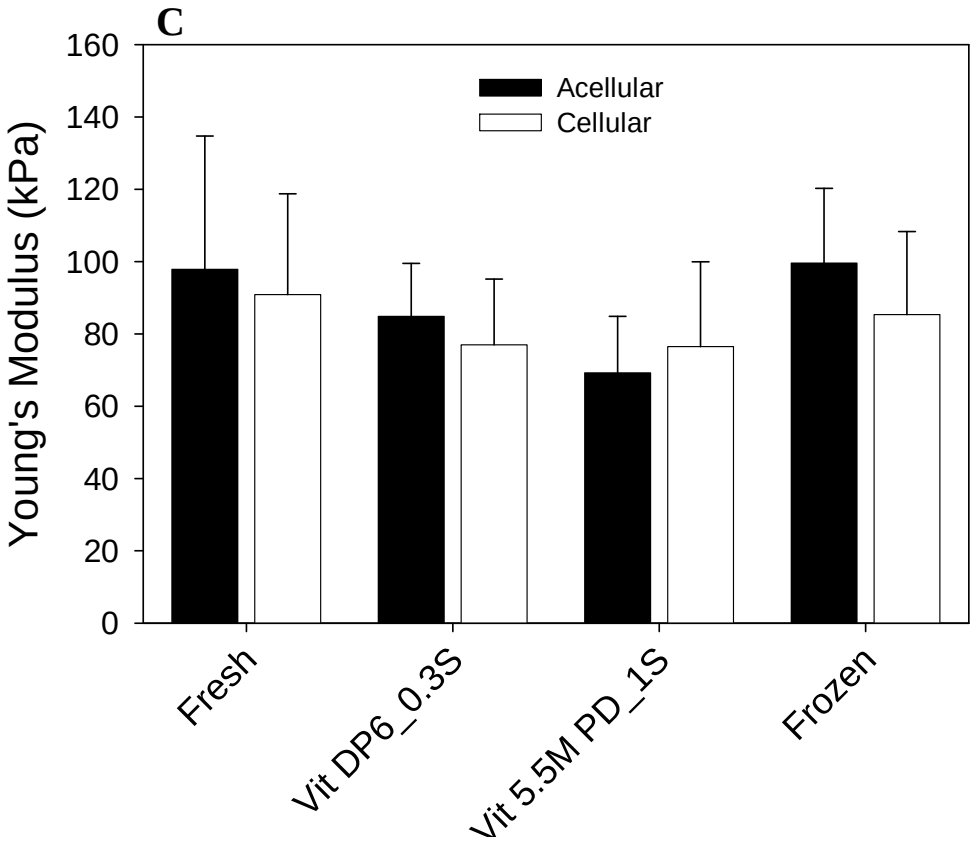

Figure 5.7 **A**. Schematic of bead mechanical testing setup; **B**. Typical force vs. dimensionless approach profile for compressing alginate beads; **C**.Young's moduli of fresh and cryopreserved alginate beads using compressive mechanical testing; bars represent avg ± s.d. from n=3, with five beads tested in each trial; no statistical difference was found between acellular and cellular for each group and across cellular bead groups ($p>0.05$); statistical difference was found between fresh-acellular, frozen-acellular vs. 55PD_1S-acellular ($p<0.05$)

5.5 Discussion

This study examined the cryopreservation of encapsulated, insulin-secreting cells by vitrification after using a 3-D CPA transport model for proper delivery and removal. NMR was used offline to evaluate diffusivities of CPAs by measuring bulk CPA concentrations. The results of this study suggest that 0.5-0.6 mm alginate-encapsulated

cells need only be exposed to a CPA for 2-3 min for equilibration during each diffusion-in or diffusion-out step. This is anticipated as the effective diffusivities of the CPAs were found to be 76 to 90% of that in free solution. This is in general agreement with others examining the diffusion of small molecular weight, nonelectrolytic molecules through alginate and other hydrogels, reported as D_{eff}/D_o: glucose (180 Da), 0.91-1.0 through 2% alginate [16, 173], 0.96 through 3% alginate [174], and 0.78 through 2% agarose [175]; sucrose (342 Da), 0.84-0.89 for 3% alginate [174]; oxygen (32 Da), 0.70 for 2% agar [176]. A few studies examining cryopreservation of 100-450μm diameter collagen-encapsulated cells used between 2-5 minutes per step for CPA addition and removal [91, 96]; however, the authors did not explain how these times were determined.

The two-compartment mathematical model used in this study is useful for rationally designing CPA addition and removal protocols for a 3-D tissue. This model accounted for transport through the extracellular matrix and across the cell membrane, multi-component CPA transport and CPA osmotic non-idealities – issues present in high concentration, vitrification solutions. After cryopreservation of encapsulated cells, spatial distribution of dead cells in beads, as assessed by confocal microscopy, were random (Fig 5.6). This is in contrast to, for example, articular cartilage where chondryocyte survival has been limited to the superficial [22, 124] or both superficial and deep zone layers, but not the intermediate zone [124]. In the cartilage case, this may be, in part, due to insufficient CPA equilibration throughout the tissue, resulting in ice formation during cooling and/or thawing and cell death. This did not seem to be the case for the hydrogel bead system studied.

Two vitrification solutions were characterized by DSC to measure the glass transition temperature (T_g) and devitrification temperature (T_d). To avoid ice formation, fast cooling was applied past T_d and then slowly through T_g to minimize cracking and thermomechanical stresses. Similar approaches have been applied for vitrifying large volumes of VS55 and/or 3 M DMSO + 3 M 1,2 propanediol (DP6) [37, 42, 177]. The determined glass transition for DP6_0.3S in this study was -116°C, a reasonable value, as DP6 without sucrose has been reported to have a T_g of -119°C [177]; and studies have shown that T_g values of CPA solutions increase in the presence of and with increasing concentrations of sugars [178-180]. Rabin and coworkers [177] as well as (unreported) results in our lab have observed crack formation during cooling with DP6. However, the addition of sucrose to the formulation used in this study augmented glass formation, a general observation supported by others [178, 181], and led to no observable cracks during cooling or devitrification during thawing. The second vitrification solution investigated, 5.5 M 1,2 propanediol + 1 M sucrose also formed glasses readily with no devitrification. T_g for this solution was found to be -100°C, a reasonable value for a PD-based CPA solution with sucrose, as T_g of PD-water solutions are around -110°C [31, 36, 182]. Similar CPA formulations, such as 5.5 M EG (ethylene glycol) + 1 M sucrose and 2.6 M EG + 2.1 M PD + 0.5 M sucrose, have been used to vitrify human oocytes [56] and bovine oocytes [57], respectively.

Compression mechanical testing was conducted on cellular and acellular beads. Average moduli values ranging from 70-110 kPa in this study agree with values reported by others for 2% sodium alginate: 105kPa [183], 89kPa [184, 185], and between 50-100 kPa [186]. Moreover, a few studies also observed that compressive moduli were not

affected by the presence of cells at concentrations of 2-4x10^6 cells/mL alginate [186, 187]. Maintaining intact beads post-cryopreservation is an important aspect to ensuring their success *in vivo* [188].

This study examined the rational design of cryopreservation protocols for hydrogel-based encapsulated cells using different vitrification solutions. Continued work in this area from our lab suggests vitrification as a potential approach to the successful cryopreservation of such systems, maintaining cellular function as well as matrix integrity. The methodology used to develop cryopreservation protocols from this study are clearly extendable to other tissue system of cells encapsulated in hydrogels of different composition and geometry.

CHAPTER 6

CRYOPRESERVATION OF ENCAPSULATED MURINE AND HUMAN EMBROYONIC STEM CELLS FOR BIOPROCESS ENGINEERING[3]

6.1 Abstract

Stem cell-based strategies for regenerative therapies are an emerging area in medicine. A key area in the development of stem cell bioprocessing to produce clinically relevant cell numbers is long-term storage, or cryopreservation. This study examined cryopreservation of alginate-encapsulated murine and human embryonic stem cells (mESCs and hESCs, respectively) in 3-D alginate beads. Freezing protocols to preserve encapsulated mESCs, though established and applied for mESC cell suspensions, have not been previously studied. Generally due to low recovery rates of suspended hESC colonies after cryopreservation, a hESC colony was entrapped in alginate to investigate any protective role encapsulation may provide during freezing. With both cell types, it is envisioned that a 3-D alginate system would be suitable for ESC expansion, EB formation and tissue-specific terminal differentiation as well as allow automation and optimization as a bioprocess. Post-thaw cell growth kinetics of slowly frozen encapsulated mESCs revealed cell numbers returning to fresh control levels after cryopreservation over several days. In addition, gene expression measured by RT-PCR revealed pluripotent cells that expressed various germ-layer markers following EB formation. However, the beads incurred structural damage to the matrix. A two-step

---

[3] Work was performed at Imperial College London in collaboration with the Biological Systems Engineering Laboratory (BSEL).

freezing protocol retained cell viability compared to fresh controls, as determined by trypan blue and fluorescence microscopy, as well as maintained matrix structural integrity. In addition, storage of beads at -80°C and liquid nitrogen were found to give similar results over a short storage period. After showing that the process of encapsulation did not affect cell viability, a slow cooling protocol used to cryopreserve an encapsulated hESC colony resulted in some viable cells. Despite expected damage to the alginate matrix and cell death due to ice formation, encapsulation of the hESC colony showed encouraging results against an unoptimized, slow cooling protocol.

6.2 Introduction

Embryonic stem cells hold great promise for cell-based therapies, regenerative medicine and fundamental research due to their self-renewal potential and ability to differentiate into any cell type [99-102]. ESCs are isolated from pluripotent cells of the developing blastocyst, and when implanted *in vivo,* they have been shown to differentiate into bone, cartilage, muscle and epithelium [103]. Despite this tremendous therapeutic potential, a major challenge to ensuring this becomes clinically available is long-term storage. Generation of clinically-relevant cell numbers and differentiation of homogenous cell populations would need to be tightly regulated, and long-term storage would be a critical aspect to this bioprocess. Successful storage would allow for the creation and sustenance of cell and tissue banks, inventory and sterility control, and shipment of samples.

The use of entrapped ESCs in 3-D alginate beads is an attractive system that can potentially promote ESC expansion, embryoid body (EB) formation and terminal differentiation. This would be valuable for tissue engineering applications, such as

skeletal engineering, for the formation of bone. Using bioreactors, this system would allow for automation and optimization of a bioprocess to yield adequate cell numbers for clinical therapies [17, 18]. For example, batches of encapsulated ESCs could be expanded up to a specific cell density and then cryopreserved. After thawing, they would be driven towards EB formation and down a specific tissue lineage. Alternatively, the beads could be cryopreserved further downstream in the bioprocess, after expansion and EB formation, and then driven towards terminal differentiation after thawing.

Cryopreservation of murine embryonic stem cells (mESCs) has been successfully achieved and well established, similar to methods used to cryopreserve commonly used cell lines [104]. This usually includes the use of low concentration cryoprotectants (1-2 M), such as dimethyl sulfoxide (DMSO) and ethylene glycol (EG), which are added to the single cell suspension and cooled in a cryovial at a slow cooling rate (1 to 5°C/min) down to -80°C and then plunged into liquid nitrogen. Samples are thawed rapidly in a 37°C water bath, CPA is then removed typically in a single-step by dilution in culture media and after centrifugation the cells are returned to culture flasks. This typically results in over 80% cell survival and the cells remain undifferentiated [104]. Unfortunately, human embryonic stem cells (hESCs) that are cryopreserved with this slow cooling, rapid thaw approach suffer from low viability and spontaneous cell differentiation. It is believed that intimate physical contact and cell-cell signaling are essential for hESC survival and pluripotency [105-108]. Due to this need for cell-cell association, it is thought that successful cryopreservation of hESCs would be as cell colonies, not single cell suspensions such as for mESCs [106]. Challenges with cryopreservation of cell aggregates include ensuring adequate CPA equilibration

throughout the cell cluster, while minimizing CPA cytotoxicity for the outermost cells; and ice formation that may occur during freezing that can damage the gap junctions and other cell-cell connections that are required for normal hESC function. Indeed studies employing slow cooling for cryopreservation of hESCs colonies have resulted in very poor post-thaw survival, generally 10-20%, with often times the cells becoming differentiated [107, 109-112]

Due to the damaging effects of ice formation, vitrification, or ice-free cryopreservation, is an attractive approach for long-term storage of hESCs. Using a combination of high concentration cryoprotectants and rapid cooling and thawing rates, ice crystallization can be avoided and instead achieve an amorphous glass. Studies applying vitrification have reported higher hESC survival, greater than 75%, than conventional slow freezing [111-113]. Moreover, these studies demonstrated that a large proportion of post-thawed cells remained undifferentiated, though colony size and growth were reduced compared to fresh controls.

In addition to vitrification, cell entrapment in gels may offer protection during cryopreservation that might otherwise be absent to naked cells. Hepatocytes that were cryopreserved in alginate hydrogels or sandwiched in between collagen had higher viabilities and metabolic function than their cryopreserved cell suspension counterparts [93, 114, 115]. In addition, tissue culture plate adherent hESC colonies that were coated in Matrigel and slowly cooled led to improved viability and less cell differentiation than hESC cryopreserved as colonies on culture plates without Matrigel ($3x10^5$ viable cells/plate vs. $0.2x10^5$ viable cells/plate).

In this study, encapsulated mESCs were cryopreserved with two different protocols with one evaluated in more detail for viability, pluripotency and EB formation potential. One cryopreservation protocol (protocol A) was found to structurally damage the integrity of the alginate matrix while the other protocol (protocol B) appeared to keep the beads intact. Also, a preliminary study was carried out in which hESCs were encapsulated in alginate and cryopreserved by slow cooling/rapid thawing. Qualitative microscopy data indicated that some cells in the colony survived, and based on the generally low recovery rates of hESC colonies after freezing, encapsulation may offer an attractive approach for hESC long-term storage.

6.3 Materials and Methods

6.3.1 Cell Culture

The murine embryonic stem cell (mESC) line, E14/Tg2α (Tg2α; ATCC, Manassas, VA), was cultured in the absence of feeder cells in tissue-culture flasks precoated with 0.1% (v/v) gelatin mixed in phosphate-buffered saline (Sigma, UK). Maintenance medium was composed of Dulbecco's Modified Eagle Medium (DMEM; Gibco, UK) supplemented with 10% (v/v) fetal bovine serum (Gibco), 1% (v/v) penicillin/streptomycin (Gibco), 1 mM L-glutamine (Gibco), 0.1 mM β-mercaptoethanol (Sigma), and 1000 U/mL of leukemia inhibitory factor (LIF; Chemicon, USA). The cultures were maintained at 37°C in a 5% CO_2 humidified incubator. The human embryonic stem cell line (hESC) SA-001 was obtained from Cellartis (Cellartis AB, Goteborg, Sweden) and cultured using their protocol. Briefly, hESCs were cultured on mouse embryonic fibroblasts (MEFs)-feeder cells seeded at 45,000 cells/cm^2 in a 6-well dish (Nunc) using VitroHES™ culture media (Vitrolife Sweden AB) supplemented with

bFGF (Invitrogen, UK). The cultures were maintained at 37°C in a 5% CO_2 humidified incubator and media were changed every 2-3 days.

6.3.2 EB formation

mESCs were trypsinized using 0.25% trypsin-EDTA (Gibco) to release the colonies. After adding serum containing media, cell colonies were very gently centrifuged at 600 rpm for 1-2 minutes and resuspended in pre-warmed alpha Minimal Essential Medium (Gibco; α-MEM) containing 15% FBS (Gibco), and 1% penicillin and 100 units/mL streptomycin (Gibco). The resuspended cells were plated onto 90 mm non-tissue- culture treated bacteriological-grade petri dishes and cultured at 37°C in a 5% CO_2 humidified incubator. The cultures were fed every 2 days by replacing spent media with fresh media. EB formation was viewed routinely using an inverted phase microscope (Olympus IX70, UK) equipped with a Nikon CoolPix 950 digital camera (Nikon, UK).

6.3.3 Cell encapsulation

mESCs were entrapped in calcium alginate beads as follows: cells were detached from monolayer cultures by trypsinization (0.25% Trypsin-EDTA) and suspended at a density of $3.1x10^6$ cells/mL alginate in a filter-sterilized solution of 1.1% low viscosity sodium alginate (Sigma, Catalog number A7003) + 0.1% gelatin (Sigma) in 1X PBS. The suspension was added in dropwise fashion by passing the suspension through a syringe and 25G needle controlled by a peristaltic pump into a 1.1% $CaCl_2$ bath. The beads were about 2.3mm in diameter and contained $2x10^4$cells/bead. Beads were incubated with maintenance media in High Aspect Rotating Vessels (HARV; Synthecon Inc, Texas) bioreactors with media completely changed daily. Approximately 500 beads

were loaded into each 55 mL HARV reactor volume. For hESCs, a similar encapsulation method was used but cell colonies, instead of single cells, were entrapped.

6.3.4 RNA extraction and reverse transcriptase polymerase chain reaction (RT-PCR)

Total RNA was extracted from cells at different time points and under different conditions using the total RNA isolation kit (Qiagen Ltd, UK) after releasing the

Table 6.1 Primer information and PCR conditions

Target	Primer	Sequence	m.w. (b.p.)	m.t. (^oC)	a.t. (^oC)	Cycle Number
Pluripotency	Oct4	(f) TGT GGA CCT CAG GTT GGACT (r) CTT CTG CAG GGC TTT CATGT	181	60	54	27
Endoderm	GATA4	(f) CTC CTA CTC CAG CCC CTACC (r) GTG GCA TTG CTG GAG TTACC	571	66	58	30
Mesoderm	Brachyury	(f) AA GGA ACC ACC GGT CATCG (r) CGT GTG CGT CAG TGG TGT GTA ATG	321	60	56	27
Ectoderm	Nestin	(f) CGG CCC ACG CAT CCC CCA TCC (r) AGC GGC CTT CCA ATC TCT GTT CC	259	74	57	30
Housekeeping	GAPDH	(f) CATCACCATCTTCCAGG AGC (r) ATGCCAGTGAGCTTCCCG TC	500	65	60	27

encapsulated cells using 50mM citrate. Single-stranded cDNA synthesis was performed with total RNA (1 μg) using a random primer and AMV reverse transcriptase (RT) with an RNase inhibitor (Promega, Madison, WI). The polymerase chain reaction (PCR) buffer consisted of 1X Amplitaq Cold Buffer, 25 mM $MgCl_2$, 10mM each dNTP, and 1.25 U/rxn of Amplitaq Gold DNA polymerase (PE Biosystems, Foster City, CA). PCR conditions were as follows: reverse transcription, 42°C, 45 min; Taq polymerase

activation, 94°C, 10 min; thermal cycling, 94°C, 30 s; specific primer annealing temperature, 30 s; 72°C, 60 s, for 30 cycles; followed by a final elongation step at 72°C, 10 min. The specific primer information along with PCR conditions are listed in Table 6.1 The RT-PCR products were analyzed by 1.5% (v/v) agarose gel electrophoresis and visualized with ethidium bromide staining. Digital images were captured using the Bio-Rad Fluor-S Multi-Imager system (Bio-Rad, UK).

6.3.5 Cryopreservation

Cryopreservation experiments were carried out at Imperial College London and Oxford University in the laboratory of Professor Z.F. Cui (Engineering Science).

I. Imperial College. Encapsulated mESCs were cultured in HARVs for 3 days prior to cryopreservation. Beads were exposed to 10% DMSO/90% FBS solution for 15 minutes at 4°C. They were then loaded into 1.8 mL cryovials (Nunc) and cooled at -1°C/min until reaching -80°C in a Nalgene "Mr. Frosty" cooler and then plunged and stored in liquind nitrogen (LN_2). After 5 days in storage, beads were thawed in a 37°C water bath until no visible ice remained. Beads were exposed to DMEM for 15 minutes at 22°C to remove CPA; medium were then removed and fresh maintenance medium was added and beads were put back into HARVs. This is henceforth referred to as freezing/thawing protocol A.

II. Oxford University. Encapsulated mESCs were cultured in HARVs for 3 days at Imperial College London. Beads were then transported to Oxford University in T-25 culture flasks filled entirely with medium (to minimize damage during transport). Beads were exposed to 10% DMSO/90% FBS solution for 15 minutes at 4°C. They were then loaded into 1.8 mL cryovials (Nunc), cooled to -40°C at -1°C/min, then down to -80°C at

-10°C/min. Some beads were stored at -80°C and others were plunged into LN_2. Cooling was achieved in a controlled rate freezer (Planar Systems Inc, UK). After storing at -80°C or in LN_2 for 24 hours, vials were thawed in a 37°C water bath until no visible ice remained. Beads were exposed to DMEM for 15 minutes at 22°C to remove CPA; medium was then removed and fresh maintenance medium was added and beads were put back into culture flasks until evaluation. In the rest of this chapter, this is referred to as freezing/thawing protocol B.

6.3.6 Viability and encapsulated cell growth kinetics assessment

Cell viability was evaluated by either trypan blue (Sigma, UK) on a haemocytometer and/or the Live/Dead kit (Invitrogen, UK). The trypan blue dye exclusion evaluates cell membrane integrity, as the dye is unable to cross intact plasma membranes labeling only dead cells. Beads were dissolved in 50mM sodium citrate to release the cells. The mixture was centrifuged gently at 800 rpm for 3 minutes to separate the slower sedimenting alginate fragments from cells. The supernatant was removed and the cell pellet was resuspended in PBS for cell counting and viability measurement. The Live/Dead kit (Molecular Probes, Eugene, OR) was used as a secondary viability assay which stained viable cells green and dead cells red. This provided spatial distribution of viable and dead cells directly in the construct. Cells in beads were washed 3 times with PBS and incubated at 37°C with a PBS solution containing calcein-AM/ethidium homodimer-1 (2 μM/4 μM, respectively) for 30 minutes in the dark. After washes with 1X PBS, specimens were imaged with either a BX-60 fluorescent microscope (Olympus, Japan) or Zeiss near-IR multiphoton microscope with a Z section thickness of 150μm (Carl Zeiss, Inc., Thornwood, NY).

6.3.7 Effect of DMSO/FBS/DMEM solutions on mESC cryopreservation outcome

mESC cell suspensions were exposed to different CPA solutions in a one step addition at 4°C for 5 minutes, cooled at -1°C/min until reaching -80°C and then plunged into LN2. After 5 days in storage, cells were thawed in a 37°C bath. CPAs were removed in one step by adding 10 volumes of media for 5 minutes at 22°C and replacing with fresh maintenance media. After thawing viability was assessed on a fraction of the cells using trypan blue and the remaining cells were plated. Six groups were tested with different percentages (% v/v) of DMSO/FBS/DMEM: Group1: 0/100/0; Group 2: 0/50/50; Group3: 5/50/45; Group 4: 5/75/20; Group 5: 10/50/40; Group 6: 10/90/0.

6.4 Results

6.4.1 Effect of DMSO solutions on mESC cryopreservation outcome

Different DMSO-based cryopreservation solutions were tested on mESC cell suspensions to evaluate the best CPA formulations for cryopreservation. As expected, cells frozen in solutions with no DMSO present (groups 1 and 2) predominantly died as viabilities were less than 10% (Figure 6.1). Cells frozen in solutions with varying compositions of DMSO (5% or 10% DMSO) and remainder FBS and DMEM, resulted in high post-thaw survival (>75%).

6.4.2 Growth kinetics and cryopreservation of encapsulated mESCs using slow cooling/rapid thawing

Freshly encapsulated mESCs were cultured in HARV bioreactors with maintenance media over time to assess their growth profile. Photomicrographs in Figure 6.2A show the expansion of the cells in the hydrogel beads over time. Cell counting via

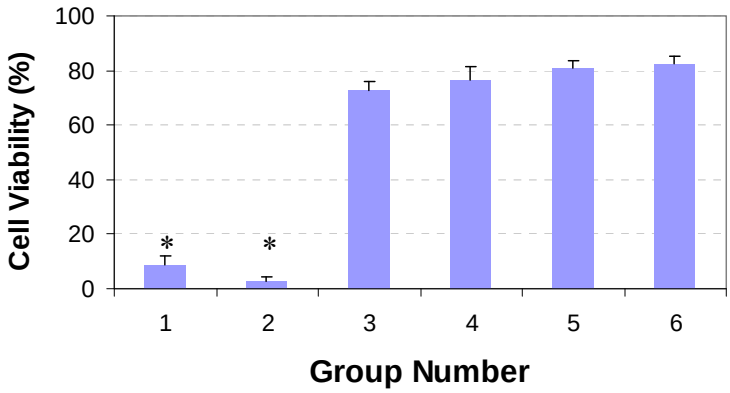

Figure 6.1 Effects of various DMSO-based cryoprotectant solutions on mESC survival; six groups were tested with different % (v/v) of DMSO/FBS/DMEM: Group1: 0/100/0; Group 2: 0/50/50; Group3: 5/50/45; Group 4: 5/75/20; Group 5: 10/50/40; Group 6: 10/90/0; cells were cooled at -1°C/min in a Nalgene Mr. Frosty™ down to -80°C and then plunged into liquid nitrogen; after storage cells were thawed in a 37°C water bath; n=3; data represents avg ± sd. * indicates a statistical difference compared to groups 3, 4, 5, 6.

trypan blue confirmed the increase in cell number within the beads over culture time with cell viability sustained over 80%, shown in Figure 7.2B.

After three days of culture in HARV bioreactors, encapsulated Tg2α cells were cryopreserved in 10% DMSO/90% FBS at -1°C/min down to -80°C and then plunged into LN_2. Beads were thawed by immersion of cryovials into a 37°C bath and CPA was removed in a single step (protocol A). Beads were then placed back into HARVs in maintenance media. Cell number and viability were assessed over time post-thaw using trypan blue after releasing the cells by dissolving the alginate matrix with sodium citrate.

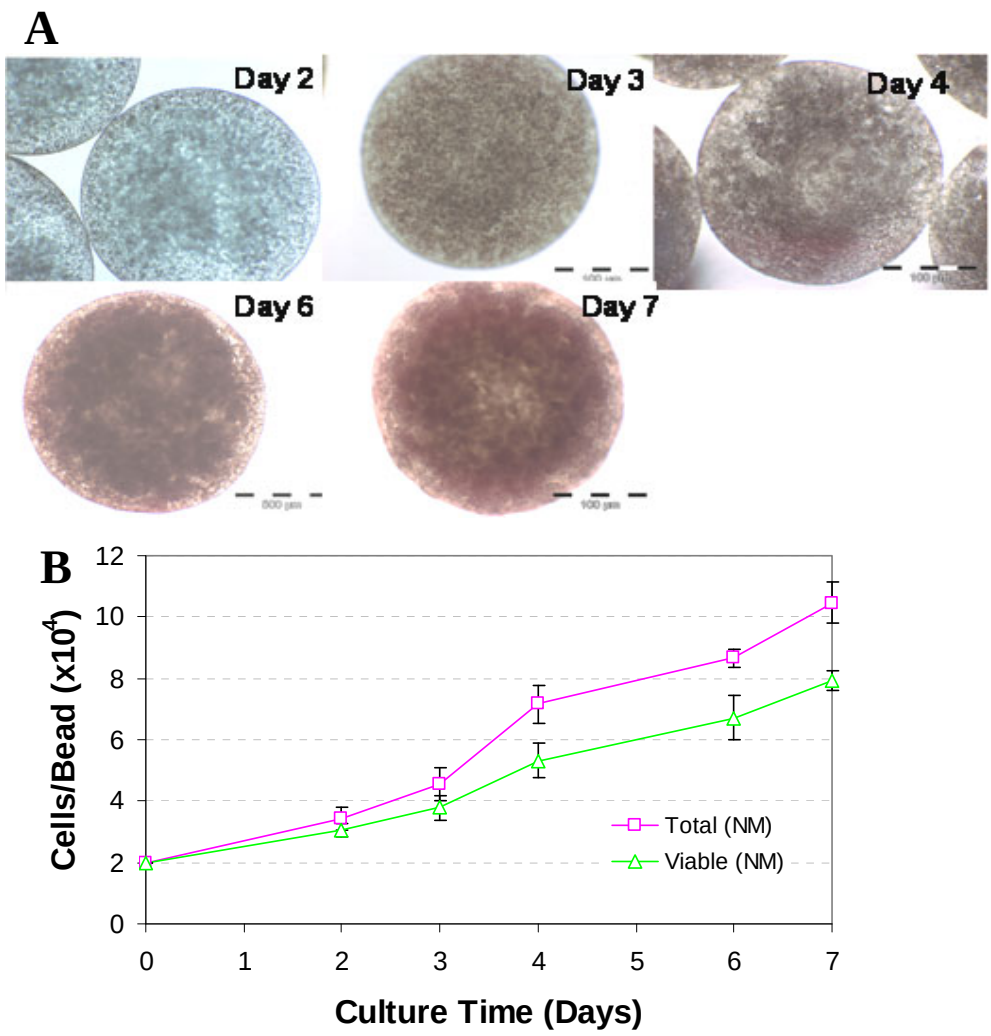

Figure 6.2 **A.** Photomicrographs of alginate-encapsulated mESCs over time cultured in a high aspect rotating vessel (HARV); initial cell density was $2x10^4$ cells/bead; **B**. Cell growth kinetics of alginate-encapsulated mESCs over time cultured in a high aspect rotating vessel (HARV); initial cell density was $2x10^4$ cells/bead; viable and total cell numbers were determined by trypan blue exclusion assay after dissolving the alginate matrix with citrate; n=3; each point is average ± s.d.

Cell number was normalized and reported as cells per bead, with an initial cell density of $2x10^4$ cells/bead. In addition, cell viability was qualitatively assessed with the Live/Dead™ assay. Due to freezing, cell survival decreased to approximately 60%, after which cell number and viability increased over culture time in bioreactors (Fig 6.3A). Three days post-thaw cell populations regained non-frozen numbers (Fig 6.2B).

Live/Dead assay indicated overall a healthy population of cells three days post-thaw, Figure 6.3B. Despite encouraging cell re-population and vitality post preservation, the freezing process had destructive effects on the alginate matrix. As indicated by light micrographs in Figure 6.3C, it was evident that the beads suffered irreversible dehydration and/or tears. Thus, this freezing protocol would not be optimal for

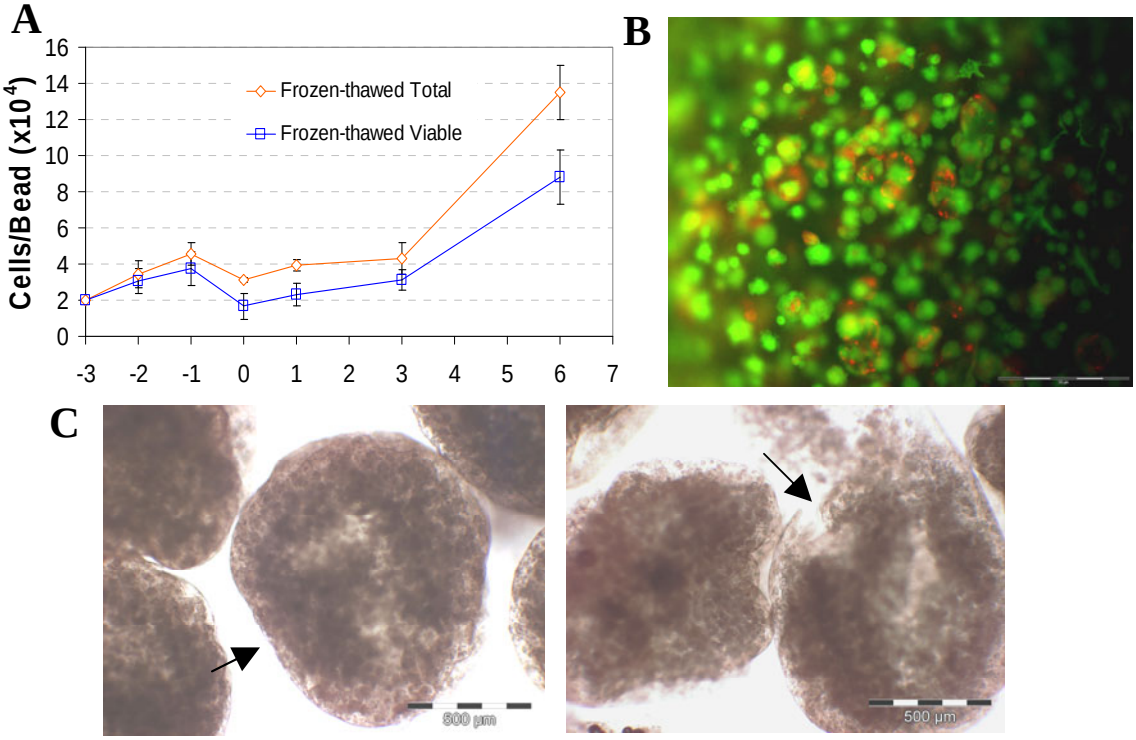

Figure 6.3 **A.** Cell growth kinetics of cryopreserved alginate-encapsulated mESCs over time cultured in a high aspect rotating vessel (HARV); beads were cultured for 3 days (indicated by -3, -2, -1 days) and then cryopreserved with 10%DMSO/90%FBS in cryovials at -1°C to -80°C and then plunged into liquid nitrogen; beads were thawed by immersion of cryovials into 37°C bath, CPA removed and cell number and viability were assessed over time post-thaw (PT), starting at day 0; initial cell density was $2x10^4$ cells/bead; viable and total cell numbers were determined by trypan blue exclusion assay after dissolving the alginate matrix with citrate; n=3; data are average ± s.d.; **B**. Viability using the Live/Dead™ kit 3 days post-thaw; green indicates live, red indicates dead cells; **C**. Photomicrographs of alginate-encapsulated mESCs after thawing. Arrows indicate evident deformations and structural damage of the beads after cryopreservation; entire scale bar represents 500µm.

6.4.3 EB formation from fresh and cryopreserved encapsulated mESCs

Cells within fresh and cryopreserved beads were released with citrate, collected, resuspended into a single cell suspension and then cultured over six to seven days to make embryoid bodies (EBs). Morphologically, cells from fresh and frozen-thawed beads were able to form EBs after one week as seen by the inner cell mass that formed as seen in Figure 6.4. Hence, cells that were cryopreserved in the beads still possessed the potential to form EBs based on morphological inspection.

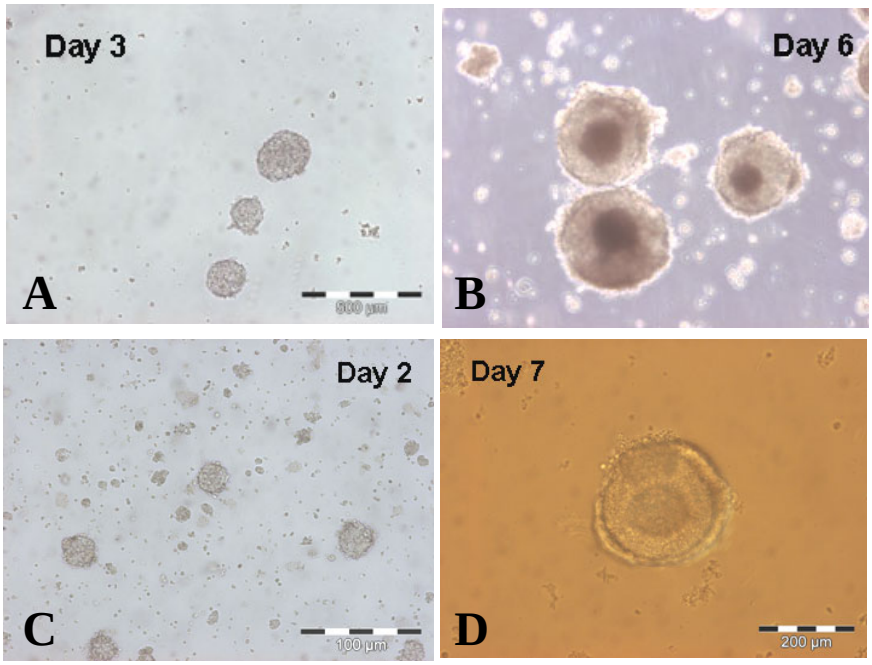

Figure 6.4 Photomicrographs of embryoid body formation over time after releasing encapsulated mESCs after 3 days in HARV culture of fresh (A-B) and after cryopreservation (C-D); Figures A and C were taken at 4X magnification; B and D were at 10X magnification

6.4.4 Gene expression of fresh and cryopreserved free and encapsulated mESCs by RT-PCR

Fresh and cryopreserved embryonic stem cells were assessed and compared for gene expression of pluripotentcy (Oct-4) and germ layer markers (endoderm, GATA-4; mesoderm, brachyury; ectoderm, nestin) via reverse-transcriptase polymerase chain

reaction (RT-PCR). The conditions included fresh monolayer cells during expansion (Figure 6.5, lane E) and EB formation (lanes F-H); fresh beads cultured in maintenance media during expansion (lanes A-C) and EB formation (lanes I, J); frozen-thawed encapsulated cells during expansion (lane D) and EB formation (lanes K, L); cells that were cultured and frozen-thawed in 3-D beads, released, cultured as monolayers in 2-D and then grown as EBs (lanes M, N).

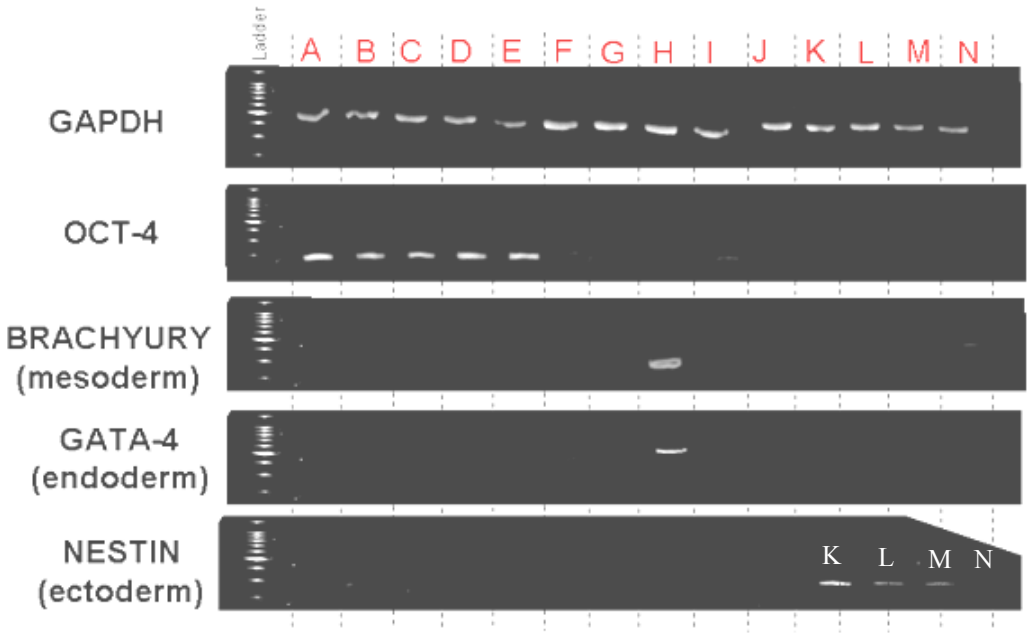

Figure 6.5 Reverse transcriptase polymerase chain reaction (RT-PCR) analysis of expression of pluripotent (Oct-4) and germ layer markers in fresh and frozen-thawed mESC Tg2α cells. Glyceraldehyde-3-phosphate dehydrogenase (GAPDH) mRNA expression was analyzed as an internal control. **A**=Expn 3-d D4;**B**=Expn 3-d D6;**C**=Exp 3-d D7;**D**=Expn F-T 3-d D5; **E**=Expn 2-d; **F**=EB 2-d D2; **G**= EB 2-d D4 ;**H**=EB 2-d D6; **I**= EB 3-d D5; **J**= EB 3-d D8; **K**= EB F-T 3-d D3; **L**= EB F-T 3-d D8; **M**=EB 3-d_2-d F-T D3; **N**=EB 3-d_2-d F-T D7; Exp=expansion; d=dimension; D=day; EB=embryoid body, F-T=frozen-thawed; 2-d=monolayers; 3-d=encapsulated cells

mESC monolayers and fresh and frozen-thawed beads (lanes A-E) cultured in maintenance media, in the presence of LIF, showed sustained expression of Oct-4 over culture time and were expected to remain pluripotent and not express any germ layer markers. EBs grown from fresh cells had no Oct-4 expression and very low germ layer

marker levels at early time points, but expressed mesoderm and endoderm markers by day 6 (lanes F-H). It is unknown why the ectoderm marker was not expressed but may have with longer culture time. Encapsulated cells cultured in EB media did not express Oct-4 or the germ layer markers at either day 5 or 8 (lanes I, J) although previous data in the lab have shown otherwise (unpublished). However, expression levels of the housekeeping gene, GAPDH, were constant throughout all samples which indicated stable cell populations. Frozen-thawed encapsulated beads in EB-forming culture conditions expressed only the ectoderm marker but not endoderm or mesoderm on both days 3 and 8 (lanes K,L). In addition, frozen-thawed encapsulated cells that were released and cultured as EBs did not express Oct-4 or germ layer markers (lanes M, N). In all EB-forming samples, Oct-4 expression was absent, as expected, but many did not express the proper germ layer markers despite being cultured for 6-8 days. This remains unclear at the time and requires further investigation.

6.4.5 Cryopreservation of encapsulated mESCs with two-step cooling/rapid thawing

Alginate encapsulated mESCs were cultured in maintenance media for three days and then transported to Oxford University for cryopreservation. In one set of experiments, beads with three different initial cell densities, $1x10^4$, $2x10^4$, $4x10^4$ cells/bead, were cryopreserved (cooled at -1°C/min to -40°C and then at -10°C/min to -80°C) and stored at -80°C for 24 hours, thawed, and the CPA removed (protocol B). Cell viability assessed with LIVE/DEAD assay using a multiphoton microscope (mpm). Figure 6.6 indicates that at the optical slice analyzed with the mpm, the post-thaw cell viability was high. Also morphological assessment of the beads post-thaw indicated

structural intactness (data not shown). However, more studies are required to confirm these initial observations.

In another set of experiments at Oxford, encapsulated cells were treated the same way as above but cryopreserved beads were stored at both -80°C and LN_2 for 24 hours (protocol B). Beads were thawed, CPA removed and the beads were taken back to Imperial College in

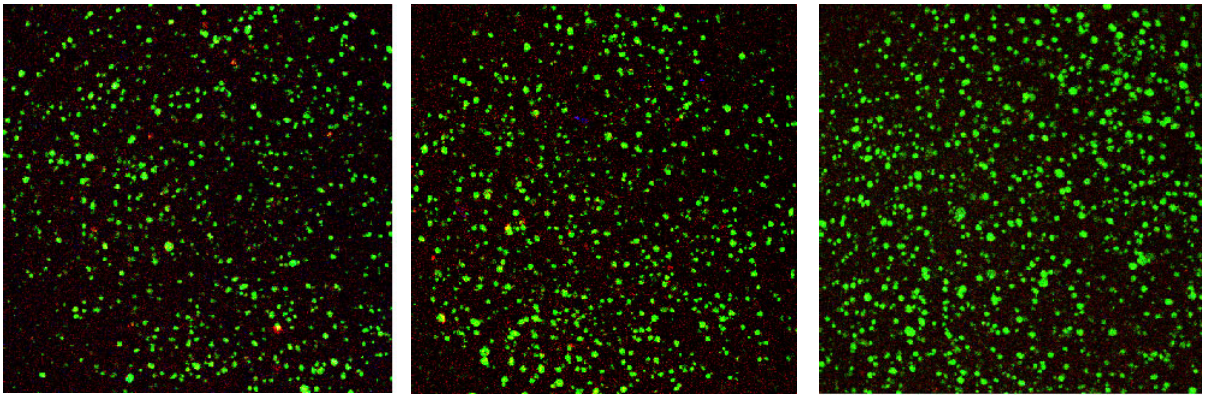

Figure 6.6 Multiphoton microscopy images of frozen-thawed encapsulated mESCs using the LIVE/DEAD™ assay with an optical slice thickness of 155 μm. Initial cell densities in the beads were $1x10^4$, $2x10^4$ and $4x10^4$ cells/bead (left to right).

maintenance media where they were then analyzed for viability with LIVE/DEAD assay using a fluorescent microscope; results are shown in Figures 6.7 A-C. Frozen-thawed beads both stored at -80°C and LN_2 appeared structurally intact and no different from the fresh controls as seen in Figure 6.7A. This is in contrast to the slow freezing experiments (-1°C/min down to -80°C) where there was damage post-thaw (Figure 6.3C). Cell viability from the different storage conditions based on trypan blue and LIVE/DEAD fluorescent image analysis indicated that viabilities after thawing from storage conditions of -80°C and LN_2 were similar to each other and to the fresh groups (Figure 6.7B). Cells

in these groups would need to be characterized for gene expression of pluripotency and three germ layers markers via RT-PCR to ensure that the mESCs did not differentiate. In addition, these experiments would need to be repeated to increase confidence and statistical significance of the data.

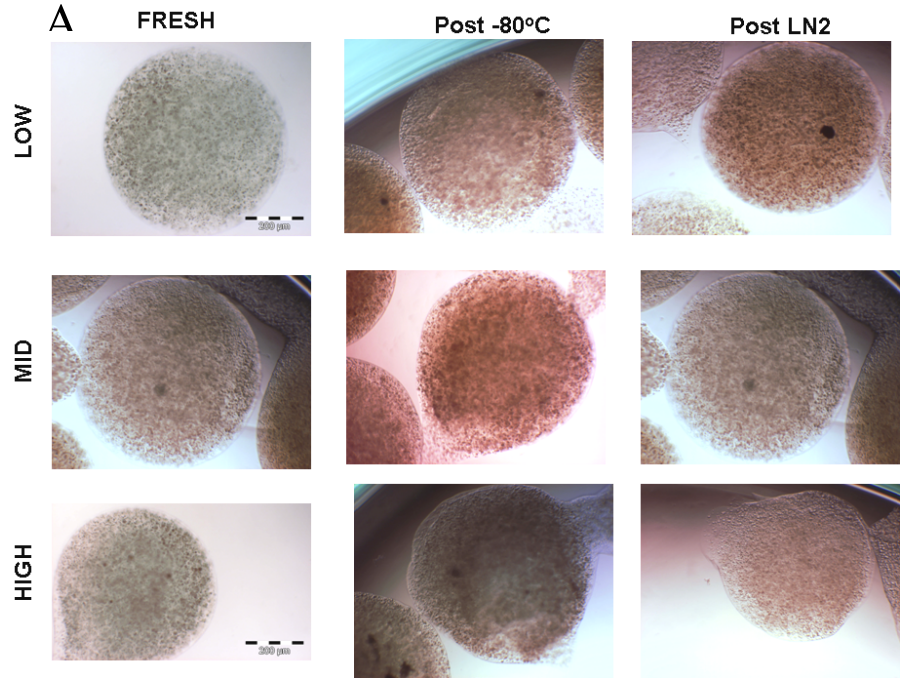

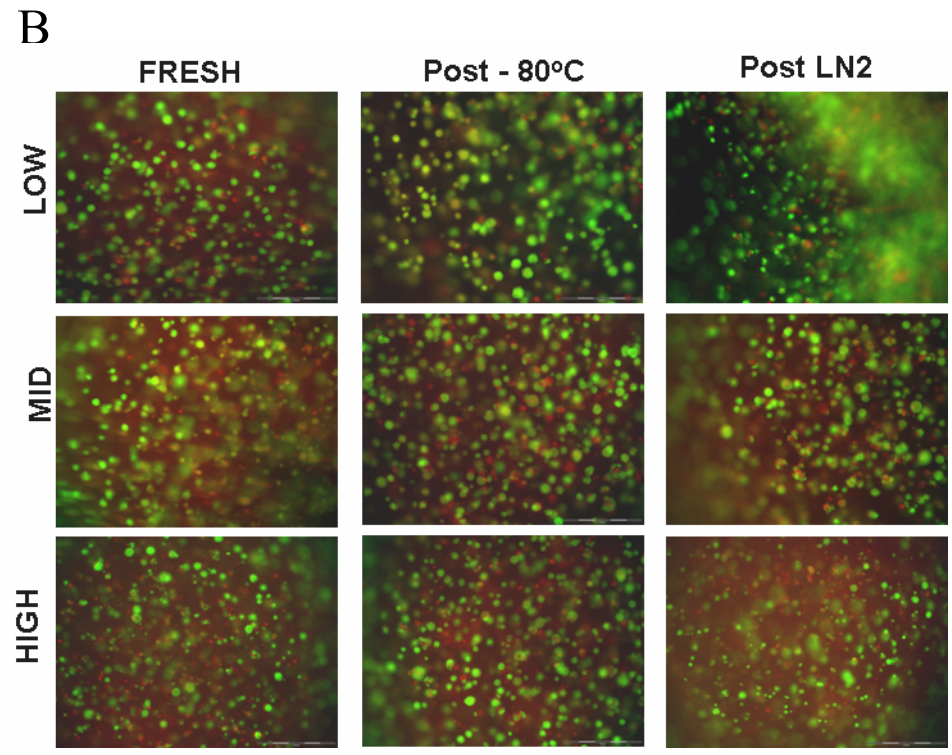

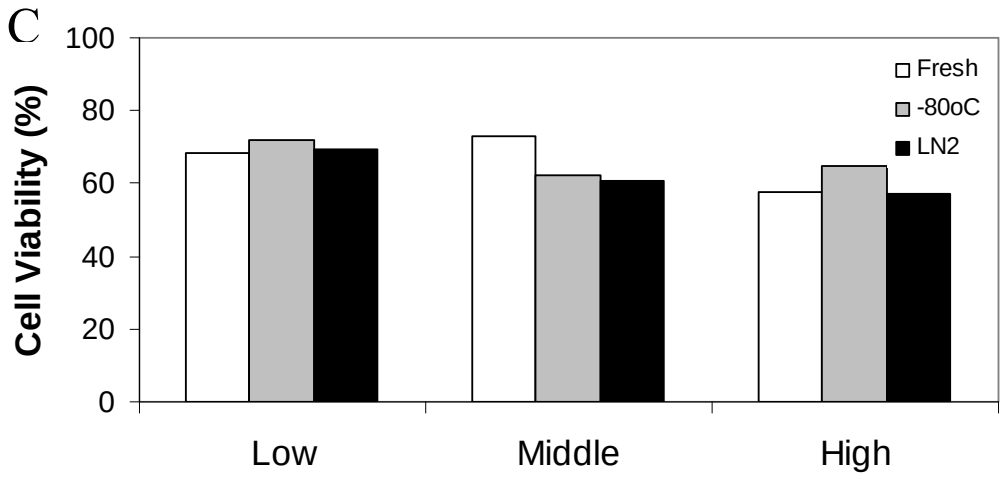

Figure 6.7 A. Photomicrographs of frozen-thawed encapsulated mESCs stored at -80°C and LN_2 to visualize macrostructural integrity of the beads. Beads had initial cell densities of $1x10^4$ (low), $2x10^4$ (mid) and $4x10^4$ (high) cells/bead (left to right). **B.** Fluorescent pictures of frozen-thawed beads using LIVE/DEAD™ assay of beads with three different cell densities, as described in A. **C**. Cell viability of cryopreserved beads described in part A using trypan blue exclusion dye, n=1

6.4.6 Encapsulation and cryopreservation of hESCs

Cellartis hESC colonies were encapsulated in 2.3 mm 1.1% alginate/0.1% gelatin beads to give one colony per bead (only two colonies were available for experiments). One bead-containing colony was examined with the Live/Dead assay to see the effects of the encapsulation process on hESC colony viability. Based on the fluorescent picture in Figure 6.8A, the encapsulation process did not cause extensive death to the colony as indicated by the green, living cells. The other encapsulated colony was cryopreserved with slow freezing (protocol A). Before freezing the alginate matrix appeared smooth and homogeneous and the colony appeared visually intact. After thawing, the colony appeared macroscopically intact but the alginate matrix underwent dehydration or matrix collapse. Visual observation of the hESC colony using the LIVE/DEAD vitality assay in

figure 7.8C after freeze-thawing showed a number of cells were alive (left panel) despite a large number of dead cells (right panel) - estimated at 15-20% by counting viable and dead cells using ImageJ. However, more cryopreserved encapsulated colonies would need to be examined and corroborated with quantitative viability analysis to draw any tentative conclusions.

A

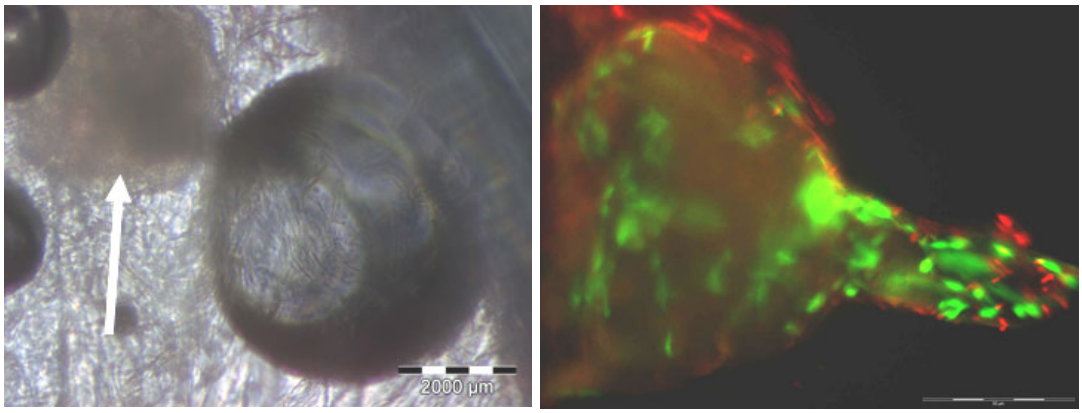

B

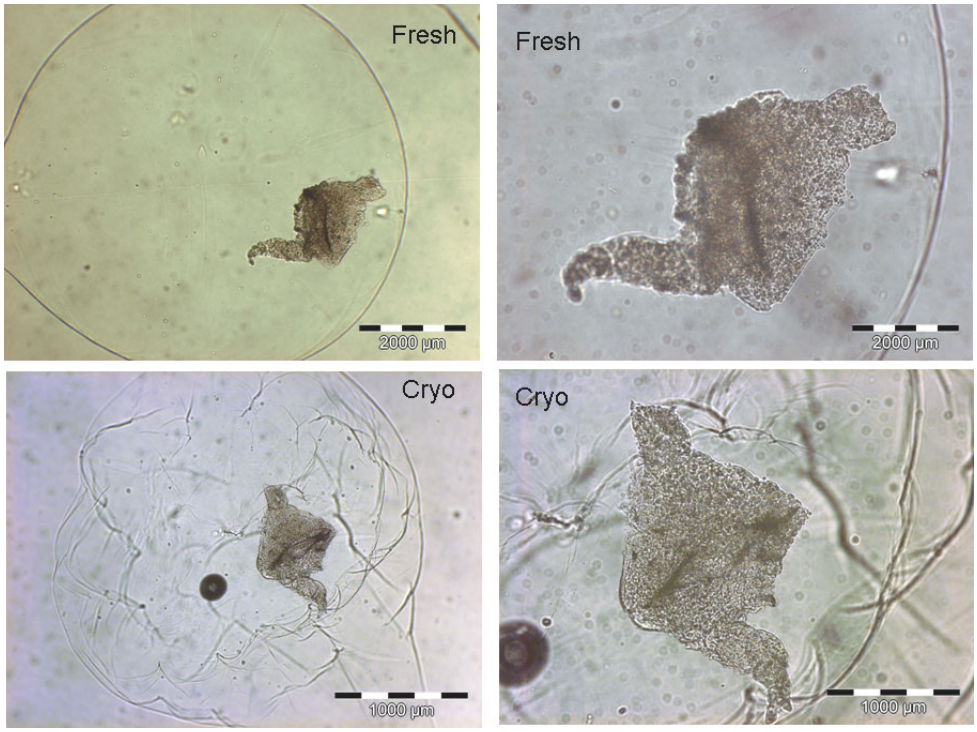

C

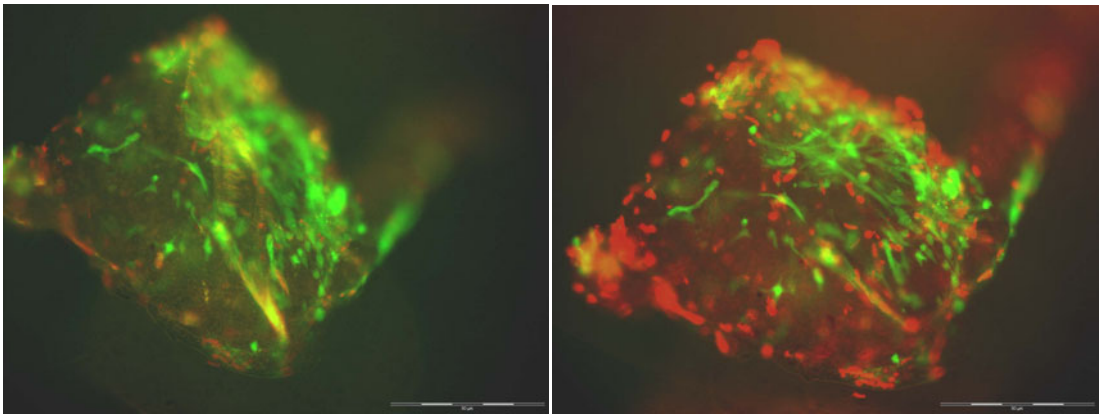

Figure 6.8 **A.** The left light micrograph shows a single Cellartis hESC colony encapsulated in an alginate bead (indicated with arrow). The right fluorescent picture shows live (green) and dead (red) cells of a colony after encapsulation using a LIVE/DEAD assay **B**. Micrographs of single encapsulated hESC colony before and after cryopreservation (left column; right column is a magnification of the left column) **C**. Panels show viability of hESC colony with LIVE/DEAD™ assay at different focusing planes

6.5 Discussion

Encapsulated ESCs offer an attractive approach for tissue engineering strategies. In an envisioned bioprocess utilizing this system for clinical therapies, long-term storage is a vital issue which this study addresses. Two different freezing protocols were used, one employing slow cooling/rapid thawing and the other using two-step cooling/rapid thawing. The former protocol resulted in damaged beads, though cell growth kinetics indicated restoration of cell numbers and gene expression analysis suggested that the cells remained pluripotent and had some EB formation potential. Structural damage of hydrogel-based microspheres due to slow freezing is not unexpected as other studies have also observed this [42, 91]. Cell numbers per bead in the frozen-thawed group reached fresh control levels, and these cells expressed the pluripotent marker, Oct-4, and some germ layer markers. The latter protocol appeared to keep the beads intact and the cells

viable, but with a lack of cell growth kinetics and gene expression data post-thaw, further studies would be needed to determine if cell numbers regained fresh control levels and whether the cells remained pluripotent and could form EBs. The increased cooling rate in the second cryopreservation protocol (10°C/min vs. constant 1°C/min in the first protocol) seemed to help maintain bead structure. A faster second-stage of cooling in the former protocol would allow less time for water dehydration and possibly less damage to the bead matrix as a result. As seen in the slow freezing experiments with encapsulated mESC and hESCs, the alginate matrix becomes irreversibly damaged due to ice formation and/or dehydration. For short storage times, beads at -80°C or LN_2 gave similar post-thaw viabilities and bead structural integrity. However, viability of samples stored over long periods at -80°C, a common practice for cell biologists, would be compromised [189]. Cells stored at these temperatures, above the glass transition temperatures of the samples, are thermodynamically unstable and would temporally deteriorate. Hence, storage in LN_2 would provide the most stable conditions and results from this study suggest that cells would be viable and bead structure would remain.

The experiment with the encapsulated hESC colony, though preliminary, offers encouragement that encapsulation may confer protection during freezing. Although a commonly used slow freezing protocol was implemented, which may certainly not be optimal for such a system, some cells within the colony survived as assessed by microscopy. However, a more detailed study would be needed to determine cell growth kinetics and gene expression levels. Due to small post-thaw viabilities of hESCs after cryopreservation, reported 0.1-15% [111, 113, 190], strategies such as encapsulation could provide a way to enhance survival after thawing. In addition, this would make it

possible to scale-up samples and create a stockpile, unlike current techniques that utilize small volume cryostraws. Encapsulated cells could then be thawed and directed, while in the matrix, towards tissue-specific terminal differentiation for regenerative medicine applications. Alternatively for cell-based uses, thawed encapsulated cells could be released from the alginate matrix by adding a chelating agent, such as sodium citrate.

This was the first study to examine cryopreservation of encapsulated mouse and human embryonic stem cells. Although slow cooling was not an ideal approach, faster cooling protocols may hold promise in preserving cell viability, pluripotency and matrix structural integrity. Successful cryopreservation would facilitate the use of novel stem cell based therapies in clinical and commercial applications.

CHAPTER 7

CRYOPROTECTANT TRANSPORT THROUGH ARTICULAR CARTILAGE FOR LONG-TERM STORAGE: EXPERIMENTAL AND MODELING STUDIES[4]

7.1 Summary

Objective: Long-term storage of articular cartilage remains challenging due to poor post-thaw viability. An initial step towards addressing this issue is characterizing cryoprotectant (CPA) transport, since ensuring adequate CPA equilibration throughout the tissue offers protection during cooling. This study takes a systematic approach in determining CPA transport rates through bovine articular cartilage and uses that information in mathematical models to determine CPA equilibration times.

Design: Diffusion of high concentration single (6.9M DMSO) and multi-component CPA solutions (VS55, 3.1M dimethyl sulfoxide (DMSO)+2.2M 1,2 propanediol+3.1M formamide) were measured through articular cartilage using ^{1}H nuclear magnetic resonance (NMR) imaging and localized spectroscopy, respectively. Using experimentally calculated effective diffusivities, diffusion models describing CPA transport through the tissue matrix and across chondrocyte membranes were combined to design a CPA addition and removal scheme for a cartilage plug of clinically relevant dimensions.

Results: ^{1}H NMR imaging and localized spectroscopy experiments suggested that the permeation of CPAs through articular cartilage (5 mm diameter, 5-10 mm in thickness)

---

[4] Modification of a manuscript that has been submitted and is currently *under review*.

took on the order of 4 hours for full equilibration at 22°C. Imaging clearly showed the permeation of DMSO into cartilage over time and localized spectroscopy was able to distinguish the permeation rates of the individual VS55 components and water. Experimentally measured diffusivity values were used in CPA addition/removal simulations with a cartilage plug of clinically relevant dimensions (5 mm diameter, 2 mm in thickness). Results suggested a multi-step approach for adding and removing high concentration CPAs, with the addition and removal each taking approximately 2 hours to complete.

Conclusions: This study provides a foundation for designing CPA addition and removal protocols for effective long-term storage of cartilage tissue using a novel approach to measure CPA permeation.

7.2 Introduction

Transplantation of fresh osteochondral allografts has proven to be effective for clinical treatment of focal articular defects. However, the limited availability of fresh allograft tissues necessitates banking for long-term storage [19-22]. Although cryopreservation by freezing is preferable for long-term tissue storage, conventional protocols result in high cell death of the chondrocytes along with the formation of ice in the matrix and/or in the chondrons [23, 191, 192]. Indeed, there exists evidence that, although extracellular ice is generally not harmful to suspensions of single cells, it poses a major hazard for natural and artificial tissues [22, 126, 193, 194] and recent studies indicate that extracellular ice forms within the chondron of cartilage causing cell damage

[23]. Therefore, improved preservation methods need to be developed as part of a successful clinical application.

Ice-free cryopreservation, or vitrification, which involves the amorphous solidification of a liquid in the absence of ice crystals, has the potential to achieve tissue preservation in terms of maintaining cellular viability and functionality, as well as integrity and function of the extracellular matrix [25, 37, 42]. Vitrification is generally accomplished through combination of high concentrations of cryoprotectants (CPAs) and rapid cooling and warming rates so that nucleation and growth of ice crystals are effectively minimized. Alternatively, recent work has shown that vitrification can be achieved by tracking the liquidus line, i.e., by gradually increasing the CPA concentration and cooling the cartilage sample [129]. In either case, vitrification of samples of clinically relevant thickness is particularly challenging. Characterizing mass transport properties of CPAs through articular cartilage is critical in addressing issues of cellular osmotic volume excursions and cytotoxicity to confer protection during cooling.

Nuclear magnetic resonance (NMR) imaging and spectroscopy are powerful, non-invasive tools that can be employed to monitor the permeation into tissues of CPAs with NMR-observable nuclei. NMR imaging can be used to obtain spatial information of CPA distribution at various times, revealing heterogeneities in CPA diffusion within the tissue. MR imaging techniques have been used to observe and quantify CPA permeation into various tissues including freeze-dried artificial dermal replacements [195], rat kidney and liver [196], zebrafish embryos [197] and human articular cartilage [198]. NMR spectroscopy can be used to determine precise solute concentrations and has been used as an offline tool to determine the permeation kinetics of CPAs into articular cartilage by

measuring the concentration in the bulk solution [199]. In all these studies, solutions containing a single CPA were used. As is often the case in vitrification, however, multi-solute solutions are used [37, 39] and acquiring simultaneously the transport rates of all components of the CPA cocktail is essential for accuracy.

In this study, we addressed the critical issue of delivering and removing in articular cartilage the high concentrations of CPAs necessary for vitrification. We first characterized CPA transport through immature bovine articular cartilage tissue; this tissue was selected because it is available, inexpensive, and can be prepared in the necessary dimensions to effectively study CPA transport. Once the methodologies are developed, applying them to human cartilage would be quite straightforward. Diffusion of a single component CPA was studied by 1H NMR imaging, whereas with a multi-component CPA solution a novel approach was implemented, which consisted of measuring by localized 1H NMR spectroscopy CPA concentrations vs. time in a volume of interest within a cartilage plug. Effective CPA diffusivities were then calculated. Equations for CPA transport through the extracellular matrix were coupled with equations for solute and water transport through cell membrane to describe multi-solute and water transport across chondrocytes throughout the tissue. This information was then used to determine equilibration times of vitrification-relevant concentrations of CPAs for cartilage tissue of clinically-relevant size. To ensure maximum tissue permeation while minimizing osmotic effects and cellular cytotoxicity, stepwise CPA addition and removal were implemented. The use of this information in designing carefully optimized cryopreservation protocols is discussed.

7.3 Materials and methods

7.3.1 Chemicals

Unless otherwise stated, all chemicals were purchased at Sigma Chemical Company (St. Louis, MO USA).

7.3.2 Tissue isolation

Full thickness articular cartilage plugs (without bone) were harvested from the femoral condyle or femoropatellar groove of 1-2 week old calves (Research 87, Marlborough, MA) using a 8 mm sterile disposable biopsy punch (Miltex, Inc., York, PA USA). Cartilage plugs isolated were 8 mm in diameter and between 5-10 mm in thickness.

7.3.3 MR Imaging Setup, Acquisition and Analysis

A sample cartilage plug was placed in a sample holder consisting of an 8 μm pore size membrane tissue culture insert (BD Biosciences, Franklin Lakes, NJ USA) placed on top of a cut Teflon® sheet with a hole of diameter slightly smaller than the diameter of the insert to ensure exposure of the membrane of the latter to the liquid solution, all contained within a 50 mL centrifuge tube (VWR International, Suwanee, GA USA) (Figure 7.1). The large pore size of the insert membrane prevented any mass transfer resistance of solute to the cartilage surface. The tube was then filled with a 6.9 M DMSO solution (50% w/w) in 1 X PBS. The conical tube was quickly placed in a 3.8 cm id quadrature birdcage resonator. Imaging was performed on a Varian/Inova spectroscopy and imaging system operating at 4.7T (200.536 MHz at 22°C). A gradient insert (11.7 cm id) was enclosed in an outer standard gradient coil. The maximum gradient amplitude was 25 gauss/cm with a rise time of 250 μs. The final tissue orientation was such that the

plane of the disk was parallel to the applied magnetic field direction. Prior to image acquisition the magnetic field was shimmed, or made homogenous. Following initial scout images to locate the imaging plane, a chemical shift selective imaging (CSSI) sequence was utilized to visualize diffusion of DMSO into the tissue over time. In the pulse sequenced utilized, the initial 90° 16 ms gaussian pulse was chemical shift

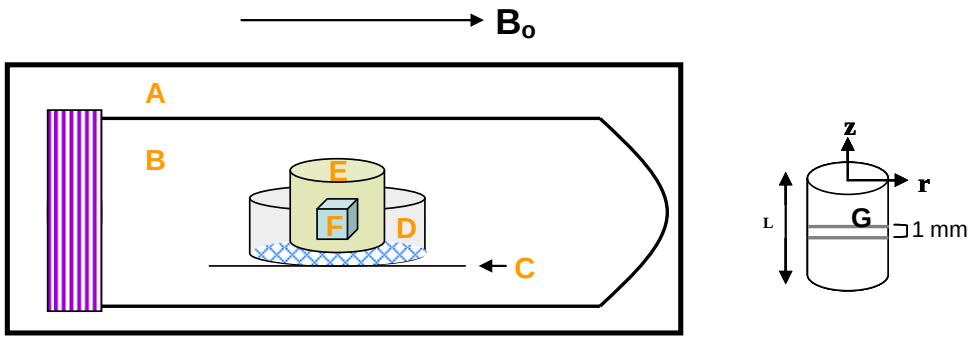

Figure 7.1 Schematic of NMR sample holder. A: field of view of the radiofrequency coil; B: 50 mL centrifuge tube; C: Teflon piece holding tissue culture insert in place; D: 10 mm diameter tissue culture insert with 8 µm pore size membrane; E: cartilage plug; F: volume of interest (VOI) for localized spectroscopy studies; G: 1.0 mm thick plane for CPA imaging studies. The Teflon piece rested on the walls of the centrifuge tube and had a hole of diameter slightly smaller than the diameter of the insert to ensure exposure of the membrane of the latter to the liquid solution. B_o=magnetic field; figure not drawn to scale.

selective, but not slice selective. Slice selection was achieved with the 180° refocusing pulse which consisted of a 2 ms sinc waveform. 256 complex points were acquired in the read direction with 128 phase encoding steps. The data matrix was zero filled to 512 x 512 before 2-D Fourier transformation. The chosen field of view (4 cm x 4 cm) gave a final in-plane displayed resolution of 78 µm x 78 µm with a slice thickness of 1 mm. Four acquisitions (NEX) were averaged for each image slice centered within the sample. The total imaging time for each scan was 51 minutes.

The extent of DMSO permeation into a piece of articular cartilage was examined by monitoring the signal intensity in the chosen slice over time. Mean brightness intensities inside the cartilage as well as in the bulk were determined for each time series image using freeware ImageJ analysis software (National Institutes of Health, USA). The mean intensities inside the tissue were normalized to the mean external solution intensity ($I_{cartilage}/I_{bulk}$), indicating the extent of CPA equilibration.

To aid in the proper choice of echo times (TE) and repetition times (TR) values during CSSI acquisition, relaxation parameters T1 (by inversion recovery) and T2 (Carr-Purcell-Meiboom-Gill, CPMG), were determined for the bulk CPA solution as well as after equilibration within a cartilage sample. Consequently, TE and TR were adjusted to reflect these relaxation times. T1 effects were assumed negligible due to long TR times used as well as T1 inside being similar to T1 outside. Apparent T2 effects were estimated by taking images at different TE values for tissue equilibrated with the DMSO solution. Images were obtained from eight TE values (23, 43, 83, 123, 143, 183, 223, 263 ms) and were fit to the equation, $M(t) = M_o \, exp(-t/T2)$, using a MR Analysis Calculator plug-in (author: Karl Schmidt) for ImageJ to yield *T2* and M_o values, where *M(t)* is the magnetization vector at time *t*, M_o is the equilibrium magnetization vector and T2 is the transverse relaxation time decay constant. Tissue and bathing solution image intensities could then be corrected for the effect of different apparent T2 values. The CPA concentration inside or outside the tissue is proportional to M_o in the respective position and the intensities are proportional to M(t) (i.e., $I^{inside}/I^{outside}=M(t)^{inside}/M(t)^{outside}$). Hence, the ratio of intensities was multiplied by a T2 factor to take into account these effects. For images acquired at TE=23 ms (assuming constant T2 inside the tissue),

$$\frac{C^{inside}}{C^{outside}} = \frac{M_o^{inside}}{M_o^{outside}} = \frac{I^{inside} e^{-\frac{TE}{T2}}}{I^{outside} e^{-\frac{TE}{T2}}} = \frac{I^{inside} e^{\frac{-23ms}{1045ms}}}{I^{outside} e^{\frac{-23ms}{116ms}}} \quad (7.1)$$

where C is the CPA concentration, M_o is the equilibrium magnetization vector, I is the intensity, $T2$ is the transverse relaxation time decay constant, TE is the echo time, *inside* refers to the cartilage sample, *outside* refers to the bulk solution

Using the value from equation 7.1, the raw intensity data inside the tissue were corrected for T2 effects by multiplying by the exponential part above which was 1.19 ($e^{-23ms/1045ms}/ e^{-23ms/116ms}$). We considered the effects of molecular translational self diffusion effects on the decay of the MR signal during both the imaging and spectroscopy sequences and determined that these are negligible under our experimental conditions.

7.3.4 MR Spectroscopy Setup, Acquisition and Analysis

A sample cartilage plug was placed in a sample holder as described above under the same magnet conditions. Standard ^{1}H NMR gradient-echo scout images were acquired to locate the imaging plane. Localized ^{1}H NMR spectra were acquired from a 1x1x1 mm^3 voxel or volume of interest (VOI), centered within the cartilage plug using a localized point resolved spectroscopy sequence (PRESS) [200]. The final tissue orientation was the same as that described for the imaging experiments. Shimming of the water signal was performed on the selected VOI using a localized PRESS sequence.

The cartilage plug was initially submerged in 1 X PBS and the initial water content in the cartilage sample was measured. Following this, the PBS was quickly and completely removed and replaced with a CPA cocktail of half strength VS55 in PBS (1.55 M dimethyl sulfoxide, 1.1 M 1,2 propanediol, 1.55 M formamide) at 22°C. VS55

is a commonly used vitrification solution for cryopreservation of various tissues [25, 37, 42]. The time from introducing the CPA-containing solution to attaining the first localized spectrum was 30 minutes. The time required to collect each spectrum was 12 minutes and data were acquired for approximately 6 hours.

Spectral data were processed using the frequency domain analysis package supplied in VNMR from Varian. Time domain data were apodized with an exponential line broadening of 5 Hz, Fourier transformed, and baseline corrected where necessary. A Lorentzian function was fit to the resulting peaks and integrated to determine the area under each peak, which is proportional to the respective solute concentration.

7.3.5 Mathematical modeling and calculations

Multi-solute CPA transport within the cartilage plug was simulated with a two-compartment model to characterize diffusion within the cartilage matrix as well as across the chondrocyte cell membrane.

Model Assumptions

1. No CPA reaction or consumption by the cells or matrix.
2. Uniform cell distribution. This is indeed a good assumption for immature cartilage where the cell distribution is relatively homogenous [201-203].
3. Isotropic effective diffusivities throughout tissue. The low molecular weight, non-electrolyte nature of the solutes used in this study makes the isotropic transport assumption reasonable.
4. Isothermal experimental conditions.
5. Constant cell membrane permeabilities (independent of CPA concentration and position within the tissue).

6. Chondrocytes *in situ* behave similarly as in cell suspensions with respect to osmotic volume excursions. The reasonableness of this assumption is corroborated by studies demonstrating that bovine chondrocytes are not restricted in their "passive" osmotic responses by the extracellular matrix, and indeed mid-zone chondrocytes behave as perfect osmometers [23, 162, 204].
7. No solute-solute interactions for multi-solute CPA transport across chondrocyte cell membrane or in the tissue matrix; CPA transport is driven only by its concentration gradient.
8. Concentration-dependence and non-ideality behavior of the solutes in the cartilage tissue similar to those in the bulk; also, D_{eff}/D_o, the ratio of effective diffusivity of CPA through cartilage to bulk solution diffusivity, assumed constant.
9. No concentration boundary layer, i.e., concentration at the surface of the tissue is the same as in the bulk solution. This is justified because diffusion of the CPAs are slow through the tissue.

7.3.6 CPA transport across cell membrane

To account for transport across the cell membrane, a multi-solute membrane transport model, extended from a two-parameter membrane formalism with modifications, was applied [51]. The fluxes of water and of the ith solute through the cell membrane are described by the following equations.

$$\frac{dV_w}{dt} = -L_p ART(M^e - M^i) \tag{7.2}$$

$$\frac{dN_i}{dt} = P_{si} A(M_i^e - M_i^i) \tag{7.3}$$

In the above equations, V_w (μm^3) is the volume of water inside the cell; L_p ($\mu m/sec \bullet atm$) is the water permeability; A (μm^2) is the surface area of the cell; R ($(\mu m^3 \bullet atm)/(mol \bullet K)$) is the universal gas constant; T (K) is the absolute temperature; M^e and M^i (osmoles/μm^3) are the total external and internal osmotic concentrations, respectively; M_i^e and M_i^i (osmoles/μm^3) are the external and internal osmotic concentrations, respectively of the ith solute; N_i (osmoles) is the intracellular amount of the ith solute; and P_{si} ($\mu m/s$) is the ith solute permeability. M^e and M^i were determined using the osmotic virial equation extended for 3 solutes (equation 7.13); M_i^e and M_i^i were determined using the osmotic virial equation for a single solute [147]. Chondrocyte CPA membrane permeabilities for DMSO and PD were taken from the literature [205] and are shown in Table 7.1. As no data are available on the formamide permeability for chondrocytes, the average of DMSO and PD permeabilities was used for this solute.

7.3.7 CPA Transport through cartilage ECM

CPA transport, for the ith solute, through a cylindrical cartilage plug is described by the following equation

$$\frac{\partial C_i}{\partial t} = -D_{eff}\left(\frac{1}{r}\frac{\partial}{\partial r}\left(r\frac{\partial C_i}{\partial r}\right) + \frac{1}{r^2}\frac{\partial^2 C_i}{\partial \Theta^2} + \frac{\partial^2 C_i}{\partial z^2}\right) + r_A \tag{7.4}$$

Assuming angular symmetry and no reaction,

$$\frac{\partial C_i}{\partial t} = -D_{eff}\left(\frac{1}{r}\frac{\partial}{\partial r}\left(r\frac{\partial C_i}{\partial r}\right) + \frac{\partial^2 C_i}{\partial z^2}\right) \tag{7.5}$$

The following boundary and initial conditions apply:

i) $C_i(r, z, t=0) = 0$ (no CPA initially present in the tissue) (7.6)

Table 7.1: Values of model parameters

Parameter	Value	Units	Source
V_b	0.414	[unitless]	[205]
L_p	0.166	[μm/min.atm]	[205]
P_s (DMSO, 22°C)	7.88 x 10^{-2}	[μm/s]	[205]
P_s (PD, 22°C)	3.716 x 10^{-2}	[μm/s]	[205]
P_s (Formamide, 22°C)	7.88 x 10^{-2}	[μm/s]	average of P_s for DMSO and PD
D_{eff} (Sucrose, 22°C)	5.49 x 10^{-10}	[m^2/s]	[169]
B (2nd virial coefficient) (DMSO)	0.0843	[mol/kg]$^{-1}$	[147]
B (2nd virial coefficient) (PD)	0.0576	[mol/kg]$^{-1}$	[147]
B (2nd virial coefficient) (Formamide)	-0.0306	[mol/kg]$^{-1}$	coefficient calculated on the basis of data from [206];

ii) $C_i(r=R_0, z, t) = C_{bulk}K$ (7.7)

(CPA concentration at the cylindrical surface equal to that in the liquid bulk times the partition coefficient, K)

iii) $\frac{\partial C_i}{\partial r}(r=0, z, t) = 0$ (symmetry condition at the cylinder axis) (7.8)

iv) $C_i(\mathrm{r},\ z = \pm\frac{L}{2}, t) = C_{bulk}K$ (7.9)

(CPA concentration at the cylindrical bases equal to that in the liquid bulk times the partition coefficient, K)

v) $\frac{\partial C_i}{\partial z}(r, z = 0, t) = 0$ (symmetry condition at the cylinder mid-plane) (7.10)

where C is the CPA concentration, D_{eff} is the effective diffusivity of the CPA through the cartilage matrix, r_A is the rate of reaction per unit volume, K is the partition coefficient, r is the radial position, R_o is the radius of the cartilage plug, z is the axial position, and t is time. It should be noted that if, instead of cartilage, an osteochondral plug with a bone segment of significant thickness is considered, boundary conditions iv and v become:

$C_i(\mathrm{r},\ z = L, t) = C_{bulk}K$ (CPA concentration at the cartilage cylindrical base equals that in the liquid bulk times the partition coefficient, K)

$\frac{\partial C_i}{\partial z}(r, z = 0, t) = 0$ (there is no CPA flux through the osteochondral interface)

where the osteochondral interface is at z=0 and the cartilage tissue extends to z=L.

7.3.8 Determination of the effective CPA diffusivity through cartilage matrix

Effective diffusivity, D_{eff}, values were calculated from imaging and spectroscopic data as follows. For the imaging experiments, average intensities were calculated from the image which represents the volume (V) from 1.0 mm thickness about the center. In the spectroscopy experiments, average concentrations ($\overline{C}_i$) came from a 1x1x1 mm^3 volume cube in the center of a cartilage plug. Average concentrations in these volumes were calculated by

$$\overline{C}_i = \frac{\int_V C_i dV}{V} \tag{7.11}$$

$\overline{C}_i / C_{bulk}$ profiles were fit using COMSOL Multiphysics™ (COMSOL, Inc, Burlington, MA) with D_{eff} as the adjustable parameter (equation 7.5) using appropriate boundary and initial conditions (equations 7.6-7.10), sample dimensions and integration volumes

corresponding to the NMR experimental volumes of interest. Least squares optimization was used to determine the best fit for D_{eff}.

7.3.8.1 Bulk solution diffusivity calculations

High concentration solutions can be thermodynamically non-ideal and have diffusion coefficients strongly dependent on concentration [207]. To account for these factors, the following equation was used to calculate CPA diffusivities in the bulk solution [208]:

$$D_{AB}^{Fick} = (\Gamma)(D_{AB}^{MS}) = \left(1 + x_A\left(\frac{\partial \ln \gamma_A}{\partial x_A}\right)\right)\left((D_{AB}^{o})^{\frac{(1+x_B-x_A)}{2}}(D_{BA}^{o})^{\frac{(1+x_A-x_B)}{2}}\right) \quad (7.12)$$

where D_{AB}^{Fick} is the Fickian diffusivity (m^2/s) of the binary pair A-B (CPA-solvent), Γ is the thermodynamic factor which accounts for non-ideality, D_{AB}^{MS} is the Maxwell-Stefan (MS) diffusivity which accounts for the concentration dependency (m^2/s), x_A is the mole fraction of solute, x_B is the mole fraction of solvent, γ_A is the activity coefficient of the solute, D_{AB}^{o} is the diffusivity at infinite-dilution of pair A-B (m^2/s) and D_{BA}^{o} is the diffusivity at infinite-dilution of pair B-A (m^2/s). Infinite dilution diffusivities were calculated based on the Wilke-Chang equation [207]. Activity coefficients were calculated using the UNIFAC activity coefficient model [209]. Equation 7.12 was used to calculate bulk solute diffusivities as a function of composition for each CPA-water pair. An average diffusivity value was used between x_A=0 and the final CPA concentration in the bulk. The ratio of diffusivities for a CPA solute between the

cartilage and bulk solution, D_{eff}/D_o, could then be computed. This ratio represents the solute transport resistance due to the cartilage tissue. As previously explained, this ratio was assumed constant for each CPA in this study.

7.3.8.2 CPA transport through matrix and across cell membrane: chondrocyte CPA equilibration

Multi-solute intracellular solute osmolality and cell volume excursion profiles for chondrocytes were simulated as a function of time at chosen points within a clinically-relevant sized cartilage tissue, taken to be of 5mm diameter and 2 mm length. This was implemented by coupling CPA concentration profiles from the two compartments (tissue matrix and intracellular), as described by equations 7.2, 7.3 and 7.5. The points for analysis were at the center and periphery (at the boundary) as these represent the extreme locations for CPA equilibration within a tissue.

Diffusivities used to determine the concentration profiles for each CPA through cartilage in the simulations were calculated as follows: D_o for each CPA was determined at the particular bulk concentration (as described in the previous section) and D_{eff} was calculated by multiplying the calculated D_o by the constant D_{eff}/D_o hindrance ratio. Using D_{eff}, COMSOL was used to generate these concentration profiles using the appropriate initial and boundary conditions at each point of analysis. The concentration profiles through the matrix (equation 7.5) at each position were coupled with equations 7.2 and 7.3, describing transport across the cell membrane, using MATLAB (Mathworks, Natick, MA, USA). Due to the high concentration of CPA (3.1 M DMSO, 3.1 M formamide, 3.1 M 1,2 propanediol), the concentration profile was simulated in a step-wise manner to minimize cell volume osmotic effects. In addition, a multi-solute osmotic

virial equation model was used to account for the non-ideality of the high concentration solutes in predicting CPA osmolalities as described by Elliott et al. [147]. The osmolality calculations relating CPA concentrations to osmotic concentrations, M^e, M^i, M_i^e, and M_i^i, were used in cell volume and intracellular CPA concentration predictions in equations 7.2 and 7.3. The osmotic virial equation was extended for the case of a 3-solute system to calculate M^e and M^i,

$$\pi = c_1 + c_2 + c_3 + B_{11}c_1^{\,2} + c_1c_2(B_{11} + B_{22}) + B_{22}c_2^{\,2} + c_1c_3(B_{11} + B_{33}) + c_2c_3(B_{22} + B_{33}) + B_{33}c_3^{\,2} \quad (7.13)$$

where π is the osmolality (Osm), c_1, c_2, c_3 are the molal concentrations (moles of solute per kilogram of solvent) for DMSO, PD and formamide, respectively; B_1 , B_2 , B_3 are the second osmotic virial coefficients for DMSO, PD and formamide, respectively. The virial coefficient values used are listed in Table 7.1.

7.4 Results

7.4.1 ^{1}H NMR Imaging and Spectroscopy

The permeation of vitrification-relevant concentrations of a single-solute and multi-solute solution was monitored over time using two different ^{1}H NMR techniques, chemical shift selective imaging (CSSI) and localized spectroscopy, respectively. For the imaging experiments, relaxation parameters, T1 and T2, were determined and are reported in Table 7.2. The time constants for DMSO and water are lower in the tissue than the bulk solution, an expected result as the tissue causes shortening of relaxation times. Results on the diffusion of DMSO from a 6.9 M solution into the tissue observed by imaging are shown in Figure 7.2A. As images tracked DMSO, the efflux of water was

not captured in this study. The brightness intensity in the cartilage sample across the images was compared to the intensity in the bulk solution, Figure 7.2B. The

Table 7.2: T1 and T2 values of 6.9 M DMSO in bulk solution and equilibrated in cartilage

		T1 (s)	T2 (s)
6.9 M DMSO	DMSO	1.99	**1.70**
	Water	1.08	**1.05**
Equilibrated Cartilage Tissue	DMSO	1.86	**0.669**
	Water	**1.07**	**0.086**

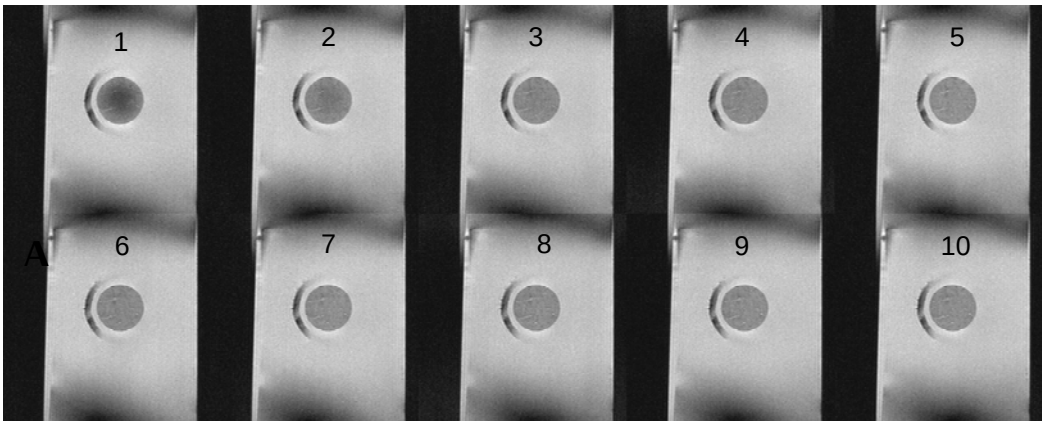

Figure 7.2 **A.** Time series montage of 1H NMR images from a 1.0 mm thick planar segment through the center of a cylindrical cartilage plug. Images are based on detection of DMSO, hence they present the permeation of this solute from a 6.9 M single-solute solution into the initially DMSO-free plug. Image 1 was acquired 81 minutes after exposing the tissue to the DMSO solution; each subsequent image was acquired 51 minutes from the preceding one. **B.** Imaging signal intensity averaged over the acquisition plane (Icartilage) normalized to the signal intensity in the surrounding solution (Ibulk). Points are experimental measurements from one imaging experiment. Dashed line is the best-fit curve, using least-squares fitting and the DMSO effective diffusivity as the only adjustable parameter, of a Fickian diffusion model through the experimental data.

B **Figure 7.2 (continued)**

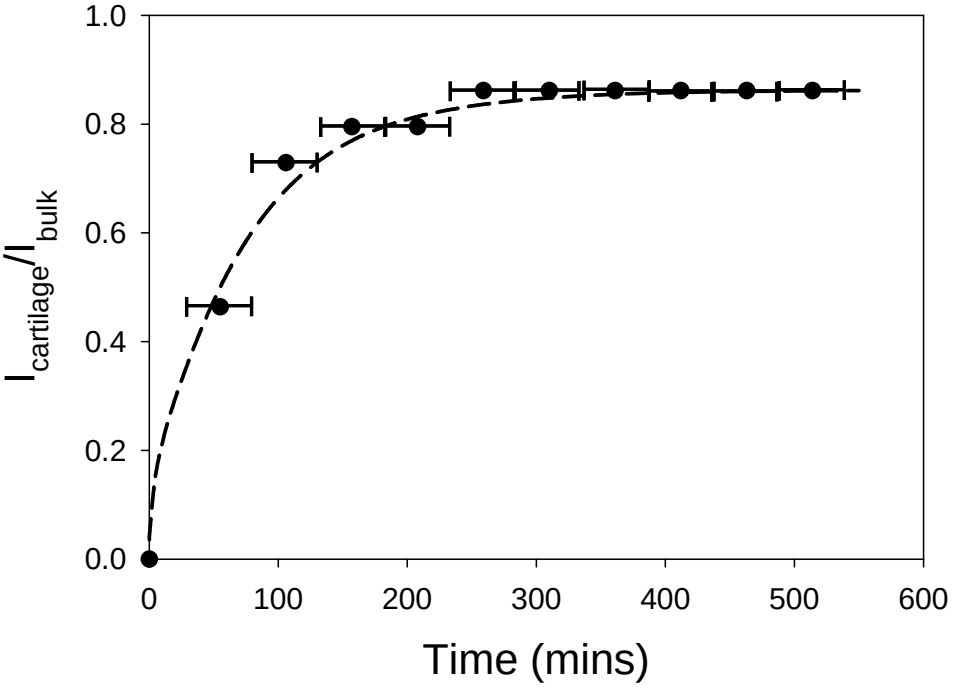

ratio of intensities, $I_{cartilage}/I_{bulk}$, proportional to the ratio of concentrations, $\overline{C}_i / C_{bulk}$, was fit to equations 7.5-7.10 with the partition coefficient, *K*, set to 0.9 (based on the last experimental data point) and D_{eff} remaining as the only adjustable parameter. With increasing time, the brightness intensity inside the tissue increased indicating an influx of DMSO. It is evident that the time for DMSO to reach equilibrium with the bulk is long, , taking of the order of 4 hours. ^{1}H NMR imaging provides a clear assessment of permeation of a single CPA solution.

Figure 7.3 shows a typical ^{1}H spectrum of a half strength vitrification cocktail, VS55, both in the bulk solution and inside cartilage tissue after solution equilibration. The individual components of the multi-component solution are easily distinguishable and the areas under the peaks correlate to their relative concentrations. Localized spectra were acquired over time of a 1 x 1 x 1 mm^3 VOI inside the cartilage sample as the

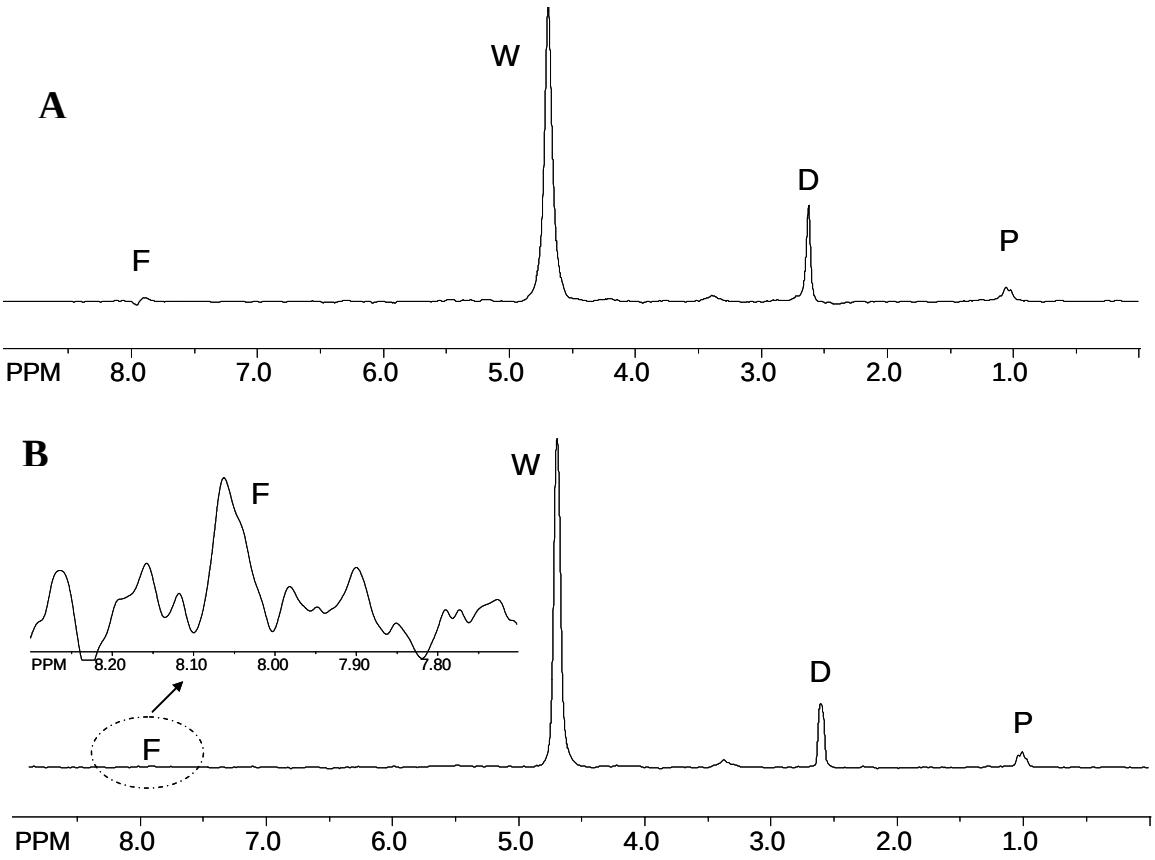

Figure 7.3 A. ^{1}H NMR spectrum of half strength VS55 cocktail (1.55 M DMSO, 1.55 M formamide, 1.05 M 1,2 propanediol) at 200MHz in a 1x1x1 mm^3 volume of interest (VOI) in articular cartilage positioned in the center after CPA equilibration; **B**. ^{1}H NMR spectra of half strength VS55 cocktail in the bulk at 200MHz in a 1x1x1 mm^3 VOI; inset in B represents a zoom-in of the formamide peak for visualization; D=dimethyl sulfoxide; F= formamide; P=1,2 propanediol; W= water

cocktail diffused into the cartilage tissue. Figure 7.4 shows the normalized concentrations (relative to the bulk concentration) of the individual CPA components over time. At equilibrium, the concentrations of all three CPAs in the tissue were equal to that in the bulk; as a result, the partition coefficient, *K*, was set equal to 1. Formamide, the smallest solute at molecular weight 45 Da, diffused the fastest. As water was clearly detected in the spectra (Figure 7.3), its concentration in the tissue was also plotted vs.

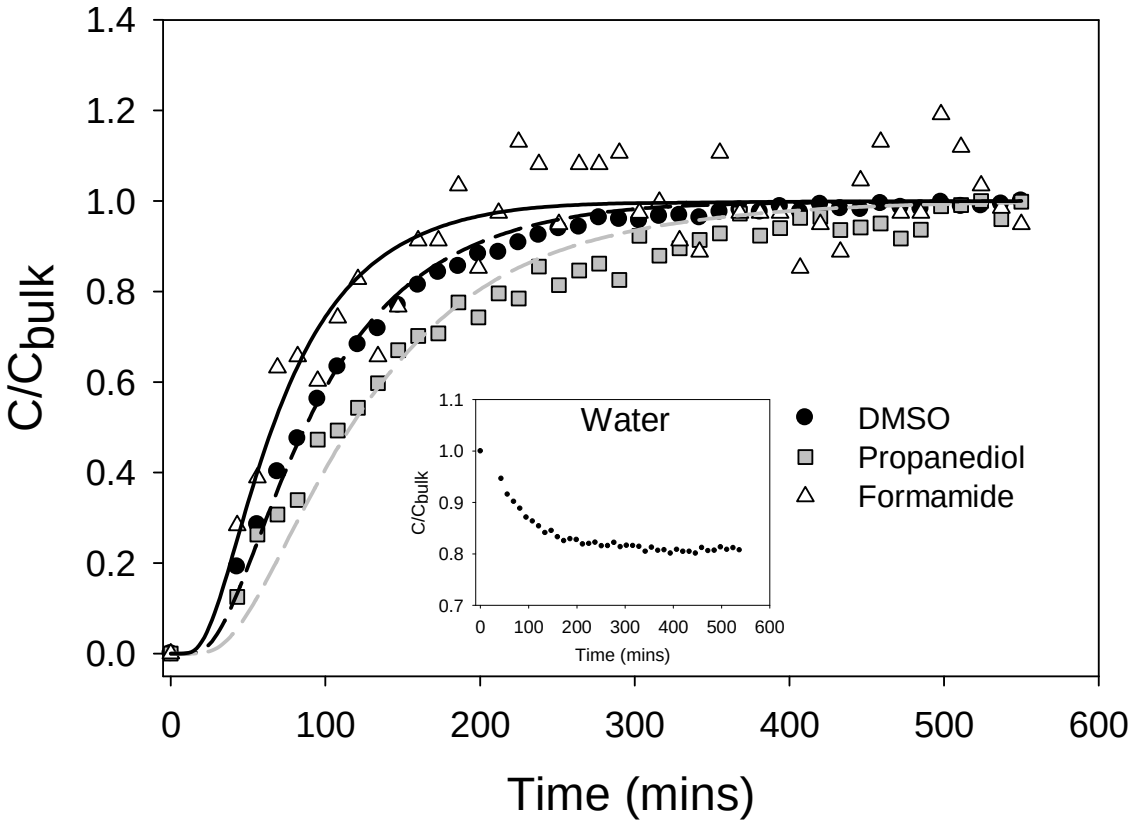

Figure 7.4 Representative concentration profiles of permeating half strength VS55 (1.55 M DMSO, 1.55 M formamide, 1.05 M 1,2 propanediol) into articular cartilage. Points are experimental measurements from localized ^{1}H NMR spectroscopy from a 1x1x1 mm^3 volume of interest (VOI) positioned in the center of the plug. Lines are best fit model simulations using the effective diffusivity of each component as the only adjustable parameter. Water was also detected in the 1H NMR spectra (Figure 7.3); the inset represents the efflux of water from the cartilage plug measured from the same VOI simultaneously as the influx of the VS55 components.

time (Figure 7.4 inset). Due to an osmotic difference between the inside and outside of the tissue, there was an efflux of water. As seen for the case of the 6.9 M DMSO, the vitrification cocktail solution took on the order of hours to equilibrate with the bulk solution. Concentration profiles generated from the localized spectroscopy experiments, tracked within a 1x1x1 mm^3 volume of interest, were fit assuming Fickian diffusion and

calculated for each CPA component (Table 7.3) using equations 7.5-7.10. As compared to the bulk, the solutes diffused 30-38% as fast through the cartilage tissue due to hindrance from the cartilage matrix.

Table 7.3A: Diffusivities through cartilage relative to bulk solution diffusivities (D_{eff}/D_o) for each component in a multi-solute vitrification solution and of DMSO in a single solute solution. D_{eff} for each component of the vitrification solution is the average from 3 independent NMR spectroscopy experiments; D_{eff} for DMSO in the single solute solution was from one MR imaging experiment.

	D_{eff} (average ± s.d) x 10^{-10} (m^2/s)	**D_{eff}/D_o**
DMSO in single-solute solution (measurement by NMR imaging)	5.8	**0.30**
VS55 cocktail (measurement by localized NMR spectroscopy)		
DMSO	4.63 ± 0.85*	**0.34**
1,2 Propanediol	3.47 ± 0.67*	**0.30**
Formamide	**6.67 ± 0.70***	**0.38**

D_{eff} = effective diffusivity; D_o = bulk diffusivity; s.d. = standard deviation; * values are averages ± s.d. from 3 independent experiments

7.4.2 Simulations of cell volume change and intracellular solute concentration

Figure 7.5 shows simulations of cell volume excursions and intracellular CPA concentrations at the center and periphery of a 5 mm diameter and 2 mm thick piece of articular cartilage after stepwise addition and removal of a vitrification cocktail of VS55 based on the contributions from all CPA solutes. CPA concentration profiles for each

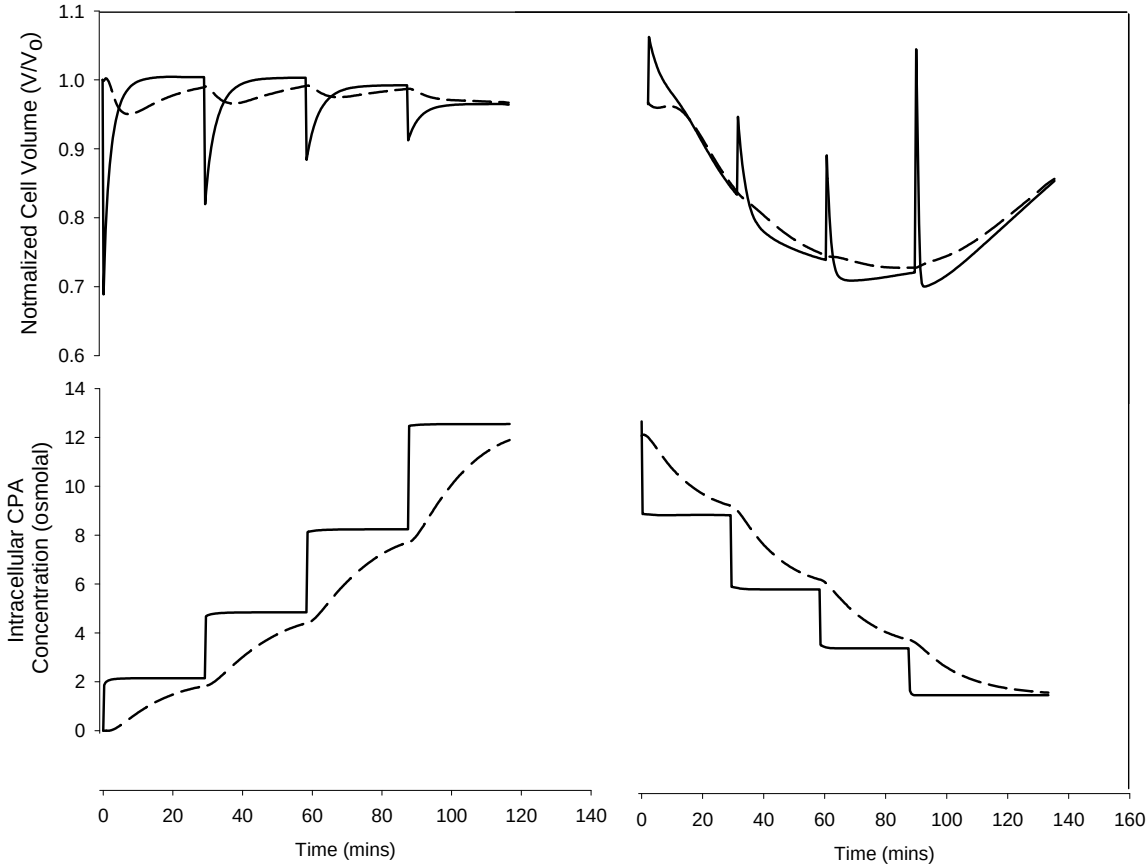

Figure 7.5 Simulated normalized cell volume and total intracellular CPA osmolality. chondrocytes at the periphery (solid lines) and the center (dashed lines) of a 5 mm diameter by 2 mm thick cartilage plug exposed to stepwise addition and removal of VS55 vitrification cocktail (3.1 M DMSO, 3.1 M formamide, 2.1 M 1,2 propanediol, 12.5 Osm).

solute through the matrix were determined using equations 7.5-7.10 and intracellular CPA concentrations were determined from equations 2-3; cell volume excursions were determined as described in [210]. In these simulations, the partition coefficient was assumed to be 1 as observed experimentally in the experiment of Figure 7.4 which employed the same CPAs. To maintain osmotic volume excursions within tolerable limits, estimated from previous studies [1], addition was carried out in 4 steps and removal also in 4 steps, in the presence of sucrose (0.35 M, 0.30 M, 0.2 M, 0.0 M,

respectively), a non-permeating solute, which aids in osmotic buffering. A D_{eff}/D_o factor of 0.34 was used with the diffusivity of sucrose through cartilage and its concentration profile was determined in the same way as with the CPA solutes using the finite element modeling solver. The duration of each addition and removal step was determined based on minimizing the exposure time but ensuring at least 90% intracellular CPA equilibration of the cells at the center with the bulk solution at each step before implementing the next step. As expected, the volume excursions at the periphery are larger than at the center, as peripheral cells experience directly the bulk CPA step concentration changes, whereas cells at the center experience smaller CPA concentration changes, attenuated by the diffusion of the solute through the thickness of the tissue. Simulated CPA and sucrose concentrations through the tissue matrix used in the cell volume and intracellular CPA concentration calculations are shown in Figure 7.6. The addition and removal of VS55 components take over 2 hours each at room temperature.

7.5 Discussion

The realization for osteochondral tissue banking relies upon successful approaches for long-term storage. Conventional freezing as well as vitrification approaches have been met with limited success and so preservation at clinically-relevant length scales still remains a challenge. One key step towards successful cryopreservation is adequate CPA penetration into the tissue for protection during cooling. Although past studies have looked into characterizing transport of CPAs through cartilage and other tissues, they have been limited to single component solutions and have primarily focused on bulk transport through the tissue matrix. Hence, this study took a systematic modeling

methodology, using experimentally determined parameter values, to describe and perform an initial design of CPA addition and removal under high concentrations and

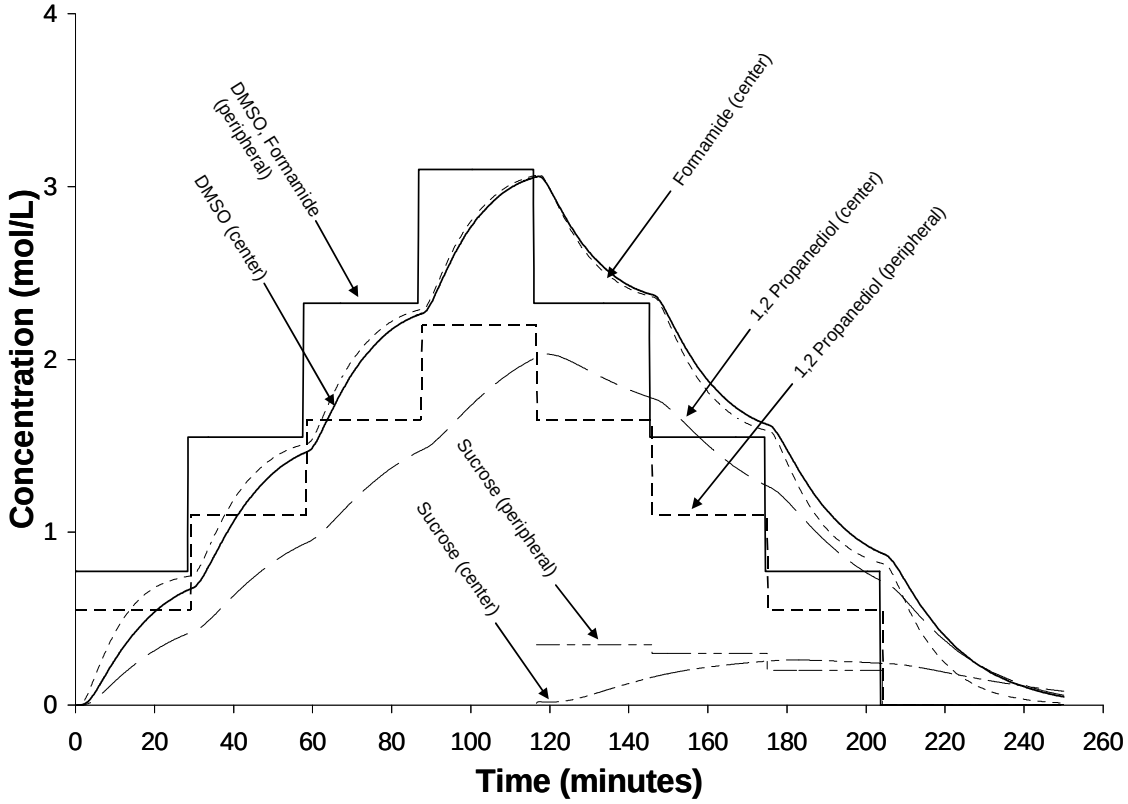

Figure 7.6 Simulated concentration profiles of VS55 components in the matrix in a 5 mm diameter by 2 mm thick cartilage plug. Concentration profiles shown for points at the center and periphery of the plug.

multi-solute conditions by using a two-compartment model. Chondrocyte cell volume excursions and intracellular CPA concentrations were examined, two important parameters in ensuring a successful preservation outcome.

A novel approach was used to measure multi-solute CPA permeation into articular cartilage using ^{1}H NMR localized spectroscopy. Moreover, NMR imaging was used to visualize permeation of a high concentration single solute CPA. The concentration profiles were fit assuming Fickian transport to determine effective diffusivities of the

CPA solutes. The partition coefficients used, based on experimental data, differed for the imaging and spectroscopy experiments. The reason for this discrepancy is not clear. It should be noted, though, that different solutions were used in the two experiments, and solute transport behavior in the presence of multiple solutes may indeed be different than transport of a single-solute system [211].

Table 7.3B: Effective diffusivities of CPAs through articular cartilage from the literature

Cartilage Source	**Dimensions**	**CPA**	**Concentration (M)**	D_{eff} **x 10^{-10} (m^2/s)**	**Temp (^oC)**	**Reference**
mature pAC	no bone: d=10 mm, z=2-4mm; with bone: d=10 mm, z=7-14 mm	DMSO	6.8	3.5 (with and without bone)	22	**[26]**
		PD	6.8	2.0 (with bone)	22	**[26]**
immature and mature hAC	d=10mm, z=2.2-3.4 mm	DMSO	1.4	17.9	37	**[198]**
immature pAC	d=5mm,z=2.9-5mm	DMSO	1	11.20	22	**[199]**
immature oAC	d=6 mm, z=1 mm	DMSO	1.4	4.06	22	**[212]**
		PD	**1.4**	**3.41**		

p=porcine; h=human; o=ovine; AC=articular cartilage

The ratios of diffusivities of the solutes through cartilage to water (D_{eff}/D_o) were found to be between 0.30-0.40. These values are similar to those found for other small, non-electrolyte solutes diffusing through articular cartilage [213-215]. The effective CPA diffusivity values through articular cartilage determined in this study (Table 2A) were similar to those reported in other studies (Table 2B), although Muldrew et al and Carsi et al [198, 199] report much higher values. Effective diffusivity values of 6.9 M DMSO through other tissues such as kidney and liver have been determined to be $180x10^{-10}$ and $50x10^{-10}$ m^2/s, respectively, under ambient conditions [196]. Clearly, diffusivity values for these tissues are significantly higher than for articular cartilage, making cartilage more difficult to preserve.

In the experiments of this study used to establish the methodology for measuring CPA diffusivities, we opted to use immature bovine articular cartilage, which can be easily obtained in thick sections, is inexpensive, and has a relatively homogeneous distribution of cells. On the other hand, it is well documented that mature articular cartilage is heterogeneous and anisotropic with respect to both cellularity and extracellular matrix properties [121]. Although studies with mature cartilage are clearly needed, there exists evidence that transport of small, uncharged molecules is similar in immature and mature tissue. For instance, Torzilli et al. reported that the biochemical changes brought on by skeletal maturation did not significantly affect the diffusion of glucose and 104 Da dextran through bovine articular cartilage, despite associated changes in the spatial distribution of interstitial water, extracellular collagen and proteoglycan content [216]. As the solutes used in this study are also small in molecular weight (45-78

Da) and uncharged, the diffusivity results as well as simulations using clinically-relevant dimensions should be potentially applicable to mature articular cartilage as well. Similarly, differences in effective diffusivities and cell membrane permeabilities are expected to exist with cartilage from other species as well, so appropriate parameter values will need to be used in each case for designing CPA addition and removal protocols. Overall, however, the time to equilibration upon stepwise addition and removal of the high CPA concentrations considered should be of the same order of magnitude for cartilage pieces of the same size, irrespective of species and age.

For the imaging experiments, T1 and T2 relaxation times were ascertained in order to use the proper acquisition parameters such as echo (TE) and repetition times (TR). This was to ensure that proper signal intensities could be determined from the images [196]. As expected, relaxation times for water and DMSO were found to be lower in equilibrated tissue than the pure bulk solution. This trend was also found by Isbell for studies with liver and kidney tissue [196].

Mathematical modeling was used to determine chondrocyte volume excursions and intracellular CPA concentrations at different spatial locations using the determined effective diffusivities through the 3-D cartilage matrix. A two compartment model to account for CPA transport through the tissue matrix and across the cell membrane is a useful approach to determine addition and removal times of CPAs for long-term storage applications. He et. al. used a similar approach to determine permeability parameters of cells within an engineered dermal replacement [217]. The model used in this study, in addition, incorporated multi-component CPAs diffusing across the cell membrane as is generally found in vitrification applications. It also incorporated non-idealities of the

CPA with respect to solute osmolality and thermodynamic activity at high concentrations for a 3-D geometry. The model developed can be used to determine the number of addition and removal steps as well as exposure time for each step required for adequate intracellular CPA equilibration for single and multiple (high concentration) CPA solutions taking into account cells at different locations within the tissue. This information coupled with cytotoxicity data (cell death as a result of CPA exposure time, concentration and temperature) could optimize exposure to CPA to maximize cell viability while still ensuring sufficient intracellular CPA concentration for vitrification. Recent work showing the impact of fixed charge density on CPA permeation into articular cartilage [212] could also be incorporated in the model structure.

The diffusivity measurements in this study were carried out at room temperature. Often times, CPAs are added and/or removed at 0-4°C to lower cellular metabolic activity and thereby reduce CPA cytotoxic effects. The results from the spectroscopy and imaging experiments presented indicate that permeation of CPAs is indeed slow through articular cartilage and thus require relatively long exposure times, on the order of two to three hours, to reach tissue equilibration. Due to the temperature dependence of CPA transport [26, 198, 199], CPAs used at lower temperatures would require longer equilibration times. The different effects of temperature on mass transport and cytotoxicity pose an optimization problem. As the temperature for CPA delivery decreases, CPA cytotoxicity is reduced but the time to equilibration is increased. Knowing the temperature dependence of these rates would allow the present model to be extended in carrying out an optimization study on delivering CPA under minimal damage to cells, by manipulating the concentrations and temperature of the bulk solution.

Cryopreservation of biological materials deals with two important transport mechanisms, namely mass transport of CPAs and heat transport during cooling and thawing. Diffusion of CPAs into cartilage tissue, as demonstrated in this study as well as others [213-215], is slow and limited. Inadequate CPA exposure and/or improper CPA addition and removal can result in poor cell viability and matrix damage due to cytotoxicity, irreparable osmotic volume excursions and possible ice formation. Consequently, chondrocyte survival has been limited to the superficial layer [20, 22, 124, 218] but not the intermediate zone [124]. Moreover, it has been shown that cell survival can be improved by enhancing CPA transport, for example by physical means of boring holes into the tissue [219]. Diffusion of CPAs, although low for natural tissue, is two to three times faster in tissue engineered cartilage [220]. This property would allow exposure times necessary for CPA equilibration to be less than native cartilage for the same dimension tissue and thereby possibly reduce cell cytotoxicity near the periphery. Preliminary data from our lab (unpublished) as well as [128] suggest that temperature equilibration times with the surrounding solution are of the order of minutes as opposed to hours for CPA equilibration (this study). Heat transport is indeed a critical issue and would therefore require further investigations characterizing its role and limitations in cartilage cryopreservation.

In conclusion, this study used experimentally measured diffusivities of CPAs through articular cartilage in mathematical models to simulate multi-step addition and removal. This study constitutes a first step toward the eventual goal of developing and optimizing models of 3-D tissue cryopreservation based on parameters that are accurately measured experimentally.

CHAPTER 8

CONCLUSIONS AND FUTURE DIRECTIONS

8.1 Conclusions

Due to the intrinsic differences among tissues, approaches for their long-term storage need to be customized. Typically, cryopreservation protocols are developed empirically; this thesis has contributed to the field by taking a rational approach of cryopreservation protocol design, using experimentally measured tissue properties, and applying it for the successful cryopreservation of model tissues. The methodology developed is generic and expected to be applicable for the long-term storage of natural and engineered tissues using measured and estimated parameters.

In the first part of the thesis, baseline vitrification solutions and cooling/thawing rates were compared against a conventional freezing protocol and applied to a model tissue engineered pancreatic substitute. Initial results, reported in Chapter 3, showed that vitrification resulted in higher cell functionality and less structural damage to the alginate matrix over conventional freezing after thawing. To optimize vitrification protocols, a systematic procedure was then developed based on a mathematical model. The first part of the model accounted for cell volume excursions and intracellular CPA concentrations for βTC-tet cells simulated on the basis of experimentally measured cell membrane water and solute permeabilities. Stepwise addition and removal protocols were developed after determining cell osmotic tolerances and CPA cytotoxicity for vitrification relevant concentrations of single and multi-solute CPA solutions. The model also accounted for osmotic non-idealities as a function of CPA concentration. Using the model- suggested protocol, optimized CPA addition and removal showed higher cellular viability against

non-optimal protocols with cells in monolayer (Chapter 4). Once CPA delivery and removal were demonstrated as safe, cryopreservation protocols were developed and applied for βTC-tet cells encapsulated in alginate using two different vitrification solutions (Chapter 5). The mathematical model was extended to incorporate experimentally measured effective CPA diffusivities through the alginate matrix extended for a 3-D geometry. Thermal properties of the vitrification solutions were determined with differential scanning calorimetry (DSC) to determine their glass transition temperatures and devitrification temperatures; this aided in cooling/warming rate protocol design. Vitrification of encapsulated cells using one of the solutions resulted in higher cellular metabolic activity post-thaw over four days compared to conventional freezing. Mechanical testing showed comparable Young's moduli for vitrified and frozen beads against fresh controls. This study suggests that vitrification is an attractive approach for the long-term storage of encapsulated cells and that a mathematical model is a valuable tool for the rational design of cryopreservation protocols.

A second tissue investigated in this thesis was alginate encapsulated murine embryonic stem cells. In these experiments, a conventional slow freezing protocol was first examined. As seen with work from the encapsulated insulinomas, slow freezing resulted in matrix damage and loss of cell viability. Frozen-thawed beads regained cell numbers three days later compared to fresh controls and gene expression analysis confirmed cell pluripotency after freezing. Due to structural damage inflicted to the beads during slow freezing, a two-step freezing protocol was tested which incorporated both slow and fast freezing. This protocol preserved structural integrity of the beads as

well as cell viability. However, further studies to confirm that the cells stayed undifferentiated upon thawing are needed, and are ongoing. This study suggests that, as in the case of the encapsulated insulinomas, avoiding ice formation is advantageous to maintaining bead integrity and cell functionality for the system of encapsulated mESCs.

With articular cartilage cryopreservation, a third tissue investigated, a key issue is the lower CPA diffusivity through the matrix. Experiments with cartilage emphasized characterizing cryoprotectant transport through the matrix. A novel method using magnetic resonance imaging (MRI) and localized spectroscopy (MRS) techniques was used to measure the diffusivities of single and multiple high concentration CPAs in the tissue (Chapter 7). MRI was used to visualize a single component CPA as it diffused into cartilage. This method has the potential to provide information on heterogeneities present within the tissue. MRS was able to track a three-component CPA solution as it permeated the tissue; it indicated that all three components equilibrated within the tissue at different rates. Calculated effective diffusivities and chondrocyte membrane permeabilities were used in a mathematical model to design addition and removal protocols of vitrification solutions for a 3-D cartilage plug. This study suggests that MRI and MRS are valuable techniques to characterize single and multi-solute transport through articular cartilage; that a mathematical model is a powerful tool to design cryopreservation protocols; and that CPA transport through articular cartilage is indeed slow and may be an underlying factor for its successful preservation at clinically-relevant thicknesses.

This thesis generated a quantitative framework for the rational design of cryopreservation protocols for three-dimensional, cell encapsulated systems and articular

cartilage. Understanding the limitations of cryopreserving such tissues with characteristicly different intrinsic properties can lead to better cryopreservation protocol design and strategies for other tissues systems.

8.2 Future Directions

8.2.1 Mathematical Model

A mathematical model has been developed in this thesis to design cryopreservation protocols for CPA addition and removal by accounting for cell volume excursions and intracellular CPA concentrations. To further improve upon this model, one next step could be to incorporate heat transfer to the existing mass transfer model. Currently, the model accounts for CPA transport through the extracellular mileu and intracellular membrane. This helps determine the time to equilibration at a given cellular position within a tissue and particular bulk CPA concentration. However, these calculations are under isothermal assumptions. Incorporating CPA diffusivities as a function of temperature and thermal diffusivities would more completely describe the conditions of a tissue being cryopreserved. For example, APPENDIX A.2 describes heat transport measurements taken for articular cartilage being cooled in different CPA solutions. From these types of measurements, the thermal diffusivity of cartilage could be calculated. Understanding and modeling heat transport is very important in vitrification applications, as uniform and specific cooling and warming rates, ensure glass and not ice formation.

In addition to incorporating heat transfer information, cell death kinetics from CPA cytotoxicity data could also be added. The current model allows the user to

determine the number and duration of each addition and removal step to ensure adequate CPA equilibration. CPA delivery and removal is an optimization problem; inadequate intracellular CPA concentrations would not confer protection (or ensure glass formation) during cooling, but overexposure would lead to cytotoxicity. Coupling cell death kinetics data would provide information on how long each step could be administrated and still have all the cells remain within a specific viability. For example, this would help avoid CPA exposure to cells in the outer layers of the tissue, especially important in a system with slow CPA permeation characteristics. The model could then be set to potentially maximize the objective function, cell viability after CPA addition and removal, by manipulating time of exposure and number of steps. Because CPA cytotoxicity is temperature, CPA and cell-type dependent, clearly this data would be needed for each specific tissue and CPA under investigation. Appendix A1.7 provides limited cytotoxicity data for encapsulated βTC-tet cells that could be fit to a first order kinetic equation and provide some initial information.

8.2.2 Encapsulated insulinomas

A natural progression of part of this work would be to evaluate the efficacy of tissue engineered pancreatic substitutes subjected to cryopreservation protocols in a diabetic mouse model. CHAPTERS 3 and 5 provide some cryopreservation formulations and protocols that could be used in future *in vivo* investigations. Viability and mechanical testing data (CHAPTERS 3 and 5) of the pancreatic substitutes suggest that several cryopreservation protocols maintain cell function and structural integrity post-thaw compared to controls. However, demonstrating *in vivo* effectiveness is clearly needed. For example, it is unclear at this time about the stability of the poly-L-lysine

(PLL) layer, which functions to provide immuno-protection against host antibodies, after cryopreservation. Preliminary data from APPENDIX A1.5 suggests that the PLL layer is not compromised post-freezing, but more extensive characterization after both freezing and vitrification would be required. Moreover, the immunogenicity of the beads after cryopreservation is unknown. It has been shown that ideal physical features of the capsule surface are required for adequate biocompatibility *in vivo* [188]. Characterization of the bead surface after cryopreservation using techniques such as atomic force microscopy (AFM) could be employed.

Another area of future work and research with encapsulated insulinomas would be to evaluate the extent of apoptosis, or programmed cell death. As discussed in CHAPTER 2, apoptosis is a form of cell death induced by cryopreservation and characterizing its levels would help in developing strategies to minimize it. Preliminary results in APPENDIX A1.1 suggest that the delivery and removal of CPAs by themselves do not induce any apoptosis, as evaluated at its early, middle and later stages, but that these levels increase in conjunction with conventional freezing for βTC-tet cell suspensions. This work would need to be extended for cells in 3-D and include characterization after vitrification.

Assessing the structural integrity of beads after cryopreservation would be another area of future work. CHAPTERS 3 and 5 showed some structural assessment techniques by ways of histology, cryosubstitution and mechanical testing. However, all of these methods required ultimate destruction of the samples; exploring non-invasive means would be a convenient and potentially faster means to assess structural integrity. NMR T2 microimaging, presented in APPENDIX A1.4, offers one such method. Structural

tears to the alginate matrix caused by freezing were clearly evident after imaging. Although light microcopy visualization provided similar information, more subtle changes to the matrix could perhaps be elucidated, such as changes to the pore size; this has been shown with the poly-L-lysine layer of alginate-poly-L-lysine-alginate beads [221]. Second harmonics generation (SHG) using multiphoton microscopy might prove to be another approach, as it has very recently been applied for comparing the effects of vitreous and frozen cryopreservation on the extracellular matrix of cardiac tissues [222].

8.2.3 Encapsulated murine embryonic stem cells

A two-step freezing protocol (protocol B, CHAPTER 6) showed some encouraging initial results in maintained cell viability and bead structural integrity. However, as discussed earlier, it is unknown at this time if the cells remained undifferentiated after thawing. Moreover, driving the cells towards a tissue-specific pathway would be important to demonstrate. Future work in this area would also include understanding the challenges and limitations in cryopreserving encapsulated mESCs at different stages of the bioprocess (for example expansion or embryoid body formation stage).

8.2.4 Articular Cartilage

Computer simulations on CPA addition and removal based on magnetic resonance localized spectroscopy experiments, reported in CHAPTER 7, suggested that CPA equilibration through articular cartilage is on the order of several hours with a sample thickness of 3 mm. CPA exposure for such long times could be toxic to chondrocytes located on the periphery; knowledge of CPA cytotoxicity kinetics would help in determining appropriate exposure times to use. If diffusion alone ends up not being

sufficient to deliver CPAs to clinically relevant samples, future work could examine strategies to enhance CPA permeation such as convection or partial enzymatic extracellular matrix degradation.

APPENDIX I

ALGINATE-ENCAPSULATED CELLS

A1.1 Apoptosis after cryopreservation of cell suspensions

Cryopreservation is an important form of long-term storage of biological materials. However, freezing methods can induce significant cell death, tissue damage, and expression of stress proteins. It has been shown that the observed cell death results not only from necrosis but also from apoptosis, a highly regulated biochemical process of programmed cell deletion. Although there have been studies on freeze-induced apoptosis, there is still a lack of information on the extent of apoptotic cell death due to the various steps of cryopreservation. The objective of this study was to investigate the extent and time course of apoptosis induced by various steps of cryopreservation using insulin-secreting βTC-tet cells. It was hypothesized that cryopreservation of βTC-tet cells would induce an apoptotic cascade

Apoptotic assays based on flow cytometry and confocal microscopy were used to examine the main hallmarks of early (caspase-8 activation), middle (externalization of phosphatidylserine – PSE), and late (DNA fragmentation) stage of apoptosis. Two groups were tested: In group one (designated as CPA-only), cells were exposed to 10% of the cryoprotectant (CPA) dimethyl sulfoxide (DMSO) for 5 min at 4°C; DMSO was then removed, and cells were either tested for apoptotic activity immediately (t=0) or plated in culture flasks for later assessment. In group 2, cells were subjected to a common cryopreservation protocol, thawed, washed free of DMSO, and evaluated in the same manner as the CPA-only group.

Results indicated that CPA-only treatment caused significantly lower activation of apoptotic markers relative to the freezing-thawing procedure. The apoptotic time course data suggest that PSE occurred along the same time scales as caspase-8 activation after freeze-thawing, whereas DNA fragmentation occurred 24-48 hours later. Moreover, the levels of caspase-8 activation did not diminish over time whereas PSE returned to basal levels by the end of the experiment; DNA fragmentation levels increased at the later time points.

This preliminary work contributes to a basic understanding of the process of apoptosis as they are induced by cryopreservation in insulin-producing cells. This knowledge can be applied to improve current cryopreservation protocols towards higher post-thaw cell viability and retention of cellular function.

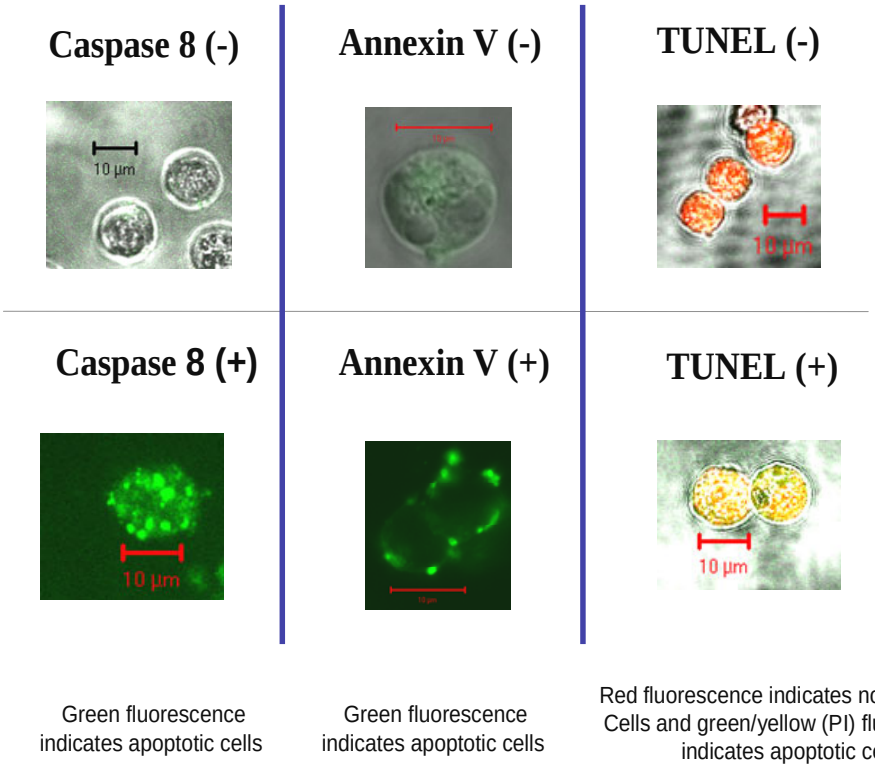

Figure A1.1 A. Confocal micrographs of control and apoptotic cells using early (caspase 8 activiation), middle (phosphatidylserine membrane externalization, Annexin V assay) and late stage (DNA fragmentation, TUNEL assay) apoptotic markers. The upper row shows fresh controls and the bottom

Figure A1.1 (cont)

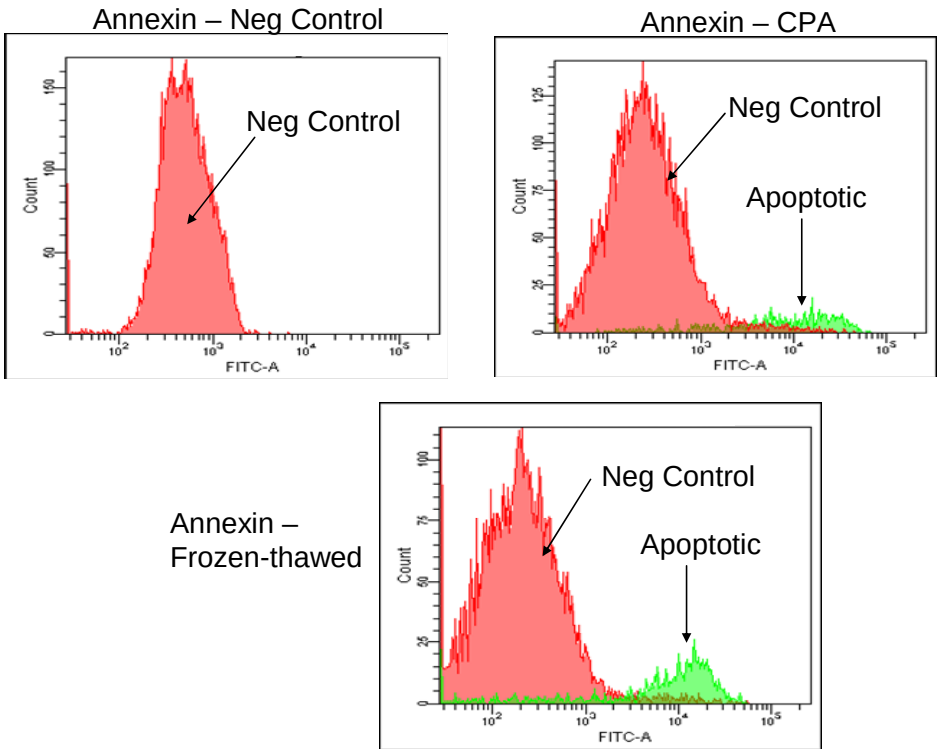

Figure A1.1 B. Typical flow cytograms of control, CPA-treated and frozen-thawed βTC-tet cells, in this case using the Annexin kit which indicates phosphatidylserine membrane externalization as a result of apoptosis with an increase in FITC signal. Red, left histogram represents autofluorescent peaks from control cells (no apoptotic activity); green, right histogram represents annexin(+) cells that are indicative of apoptotic activity

Figure A1.1 (cont)

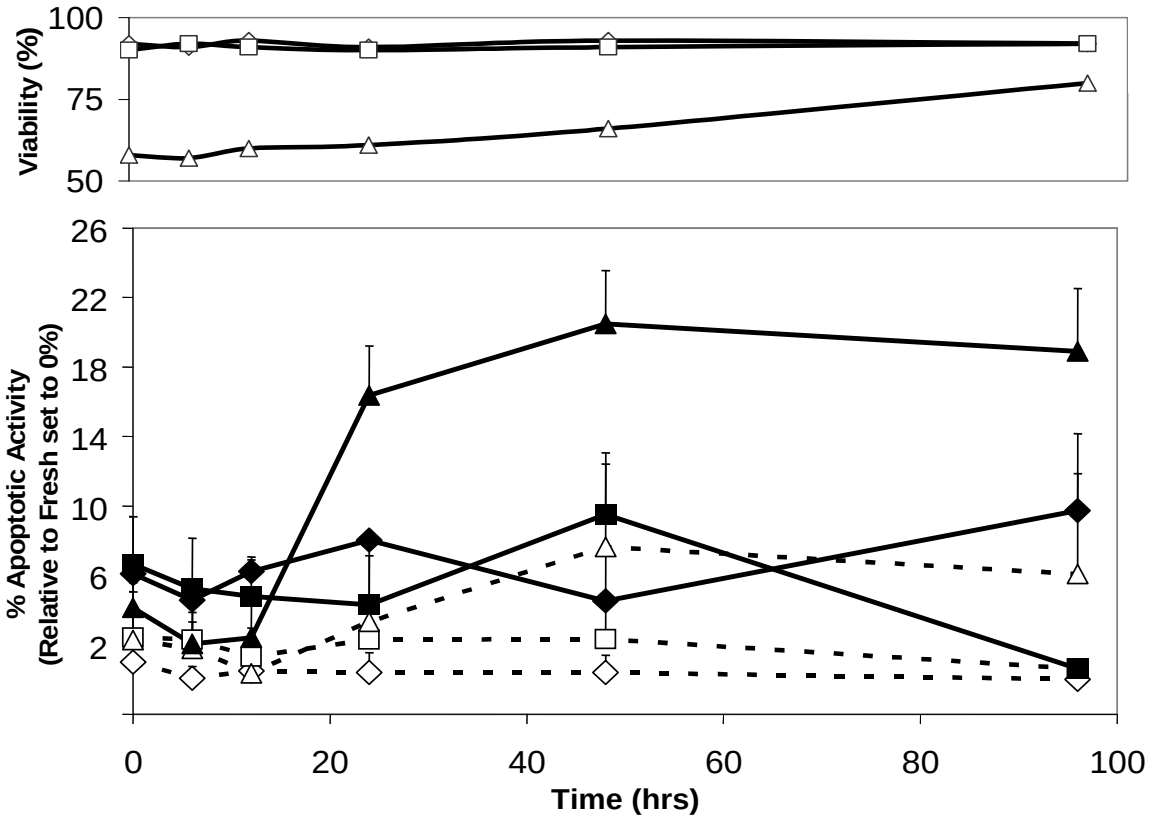

Figure A1.1 C. Apoptotic activity (%) of βTC-tet cells relative to fresh controls set to 0% after CPA-only treatment (open symbols) and freeze-thawing (closed symbols) using early (diamond), middle (square) and late (triangle) stage apoptotic markers

A1.2 Examining the role of stress proteins after cryopreservation

Stress and heat shock proteins (Hsp) play a significant role in cell physiology; hence, studying their expression under cryopreservation-relevant conditions provides insight into the influence of these processes on stress-induced changes in cell function and on the reversibility of the observed effects. Cells in one group were subjected only to addition-removal of CPA at 4°C (once again, to investigate chemical effects of CPA during implementation of cryopreservation protocols), and cells in a second group were frozen-thawed (same cryopreservation protocol as in the apoptosis studies above). Cell extracts were analyzed by western blotting to detect the expression of heat shock proteins. Briefly, samples were normalized to 25μg of protein by a BSA total protein assay (Sigma), subjected to electrophoresis on 4-20% gradient Tris-HCl polyacrylamide gels (Biorad), and transferred onto PVDF membranes (Bio-rad). Immunoreactive proteins were detected by incubating with Super Signal West Femto Kit (Fisher) and exposed to BioMax light-1 film (Kodak, Rochester, NY).

Preliminary results from an immunoblot (Figure A1.2) indicate that cryopreserved βTC-tet cells had increased levels of heat shock proteins, 72 and 90, immediately upon thawing followed by undetectable levels after 6 hours. This profile seems to be consistent with other reports [223]. The effects of the addition and removal of 10% DMSO on heat shock protein biosynthesis seemed to cause a slight increase compared to control, but not to the same extent as the effect of freeze-thawing. Further studies will include reproducing and refining the time course of Hsp expression, and investigating Hsp expression after using high concentrations of CPAs and after vitrification-thawing. Experiments will be performed with both free and encapsulated cells, and results will be compared with those obtained for apoptosis and for cellular metabolic and secretory activities following cryopreservation and

thawing. This will produce a comprehensive time profile of the cryopreservation effects on cells and on the cellular recovery post-thawing.

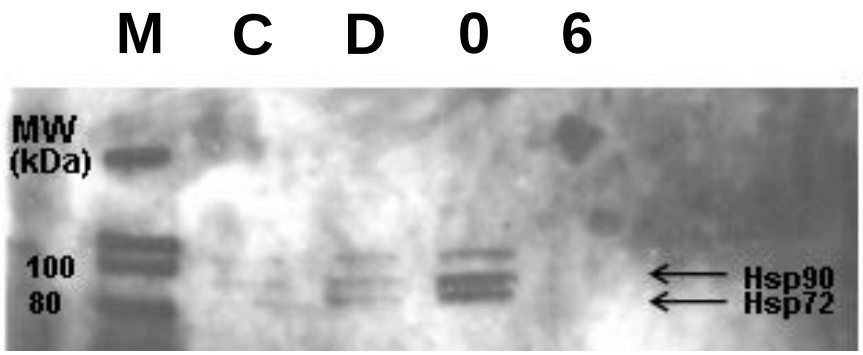

Figure A1.2 Western blot of heat shock proteins (Hsp), MW 72 and 90, synthesis (arrows) over time from βTC-tet cells; M = MagicMark^{TM} marker, molecular weight ladder; C = control, untreated βTC-tet cell lysate; D = 10% DMSO CPA addition-removal to cells only (no freezing); in a time course study cells were frozen in 10% DMSO under slow cooling, cell lysates were collected immediately after thawing (lane 0), and after 6 hours of culturing at 37°C in culture medium; all samples contained 25μg of total protein (Coomassie Blue Protein Assay). Note: isoforms of Hsp72 range from 66-78kDa (StressGen Bioreagents, manufacturer's technical specifications sheet).

A1.3 ^{13}C NMR metabolic study using PCA extraction

^{13}C nuclear magnetic resonance (NMR) spectroscopy is a powerful technique that can be used to assess cellular metabolism [224]. ^{13}C incorporation from uniformly labeled glucose was used to attain spectra that would be used to investigate specific metabolic fluxes in βTC3 cells encapsulated in alginate-based beads. Unlabelled media are removed from cell suspensions by centrifugation or from suspensions of beads, and free or encapsulated cells were washed and incubated for 1.5 hrs with a serum-free/sugar-free Dulbecco's phosphate buffered saline (DPBS) solution to normalize the initial conditions. Cells are incubated for 4 hours with a fully supplemented glucose-free DMEM medium containing 15 mM uniformly labeled ^{13}C-glucose (Cambridge Isotope Laboratories, Inc., Andover, MA). Perchloric acid extracts of free cells were performed by removing the medium by centrifugation and adding 8 mL of 0.5 N perchloric acid to the cell pellet. The cell suspension was homogenized for approximately 1 min, precipitated protein salts are allowed to settle by gravity for 1-2 minutes, and the sample is centrifuged at 4,000 g for 5 min. The supernatant was collected, neutralized with KOH, further centrifuged at 4,000 g for 10 min, and the supernatant was collected, rinsed with Chelex 100 beads (Sigma) to remove metal ions, adjusted to pH 7.4, and lyophilized. A similar protocol was used to extract the intracellular milieu from APA-encapsulated cells. Briefly, a volume of 0.5 N perchloric acid equal to the volume of beads was added, and the beads were homogenized for approximately 2 min. Bead fragments were allowed to settle for 3-4 min, after which the procedure described above for free cells was followed. To minimize biochemical changes, the entire protocol was performed at 4˚C.

Lyophilized samples were dissolved in approximately 0.5 mL of 90% H_2O/10% D_2O. In the event that precipitated salts were observed, the sample was centrifuged at 4,000 g for 5 min and the supernatant passed through a 0.2 μm filter to remove any additional particulates. Extracts were prepared from a total of 2-3 T-175 flasks (approximately $1.0x10^8$ cells) and were subjected to NMR spectroscopy. To collect the data presented below, ^{13}C NMR spectra were acquired with a 300 MHz Varian Mercury Vx 300 NMR magnet. A 5 mm broad band probe was used, and ^{1}H decoupling was applied throughout the acquisition. A coaxial insert containing a 2% dioxane solution was used as a concentration and chemical shift reference. A typical ^{13}C NMR spectra from freshly encapsulated βTC-tet cells at $3x10^7$ cells/mL alginate is shown in Figure A1.3. Some of the key acquisition parameters were: 32,768 complex points per free induction decay (FID), 6 sec relaxation delay, and 3000 transients.

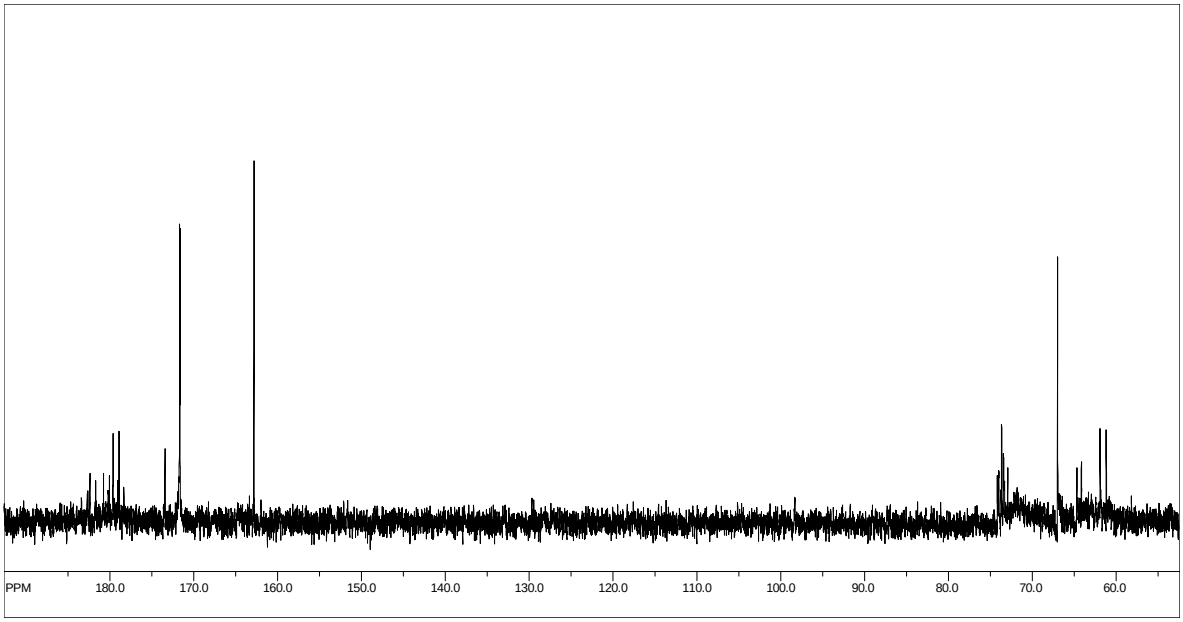

Figure A1.3 ^{13}C NMR spectrum from freshly encapsulated βTC-tet cells at $3x10^7$ cells/mL alginate after incubation in uniformly labeled ^{13}C-glucose for 4 hours and perchloric acid extraction; analysis of peak position and areas provide metabolic flux information of the Krebs (TCA) cycle

A1.4 NMR T2 microimaging of cryopreserved cell-free alginate beads

Non-invasive methods to assess tissue structural integrity after cryopreservation would provide valuable information without destroying the sample in the process. One potential way is accomplish this is by NMR imaging. For some initial studies, cell-free 2%, 0.5 mm alginate beads were imaged to detect any defects in the alginate matrix. Fresh and frozen-thawed beads were loaded into a 5 cm Teflon tube (OD 1.2mm) and inserted through a microcoil for imaging. Beads were frozen by slow cooling down to -80°C at 1°C/min in the presence of 10% DMSO and then plunged into liquid nitrogen using 1.8 mL (NUNC) cryovials. Beads were thawed by immersion into a 37°C water bath. Preliminary results were acquired on a 200 MHz NMR magnet with the following acquisition parameters: TR=2.5ms, TE = 48ms, FOV = 1 cm x 1 cm, ns=16, 256 x 256 pixels for acquired resolution of 40 μm x 40 μm x 300 μm. The images were zero-filled to 512 x 512 to give a final displayed resolution of 20 μm x 20μm x 300 μm.

Figure A1.4 shows T2 NMR microimages of fresh and frozen-thawed cell-free alginate beads (without a PLL layer). The T2 relaxation for water through the defects is the same as that in the free bulk and different from that through intact alginate matrix. The tears and defects to the alginate matrix are easily discernable. Thus, NMR microimaging proves to be a straightforward, non-invasive way to visualize defects in the bead constructs after freezing. It is interesting that the structural defects in the alginate matrix visualized by NMR form roughly what appear to be concentric circles. The underlying reason for this remains unclear and requires further investigation.

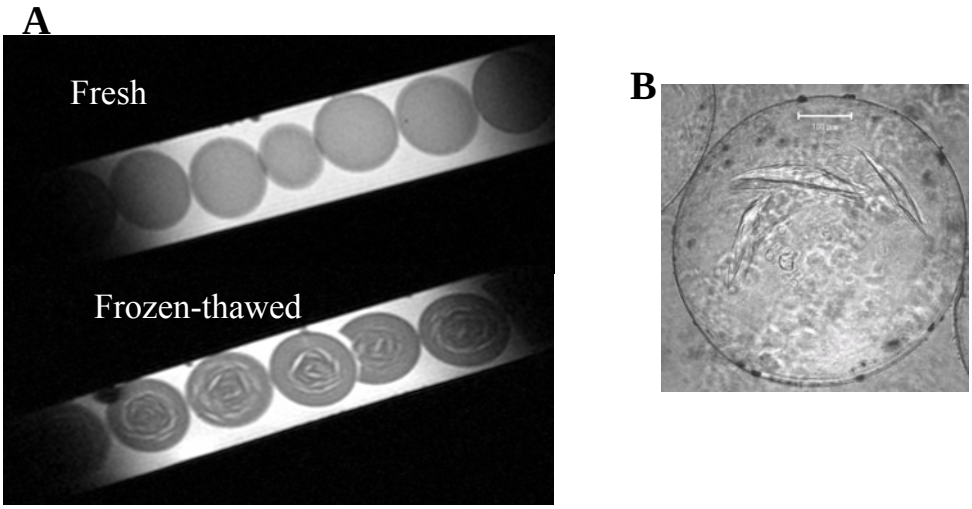

Figure A1.4 A. T2 NMR microimages of fresh and frozen-thawed, cell-free 2% alginate beads; B. Light micrograph of frozen-thawed, cell-free alginate bead- structural tears in the matrix are clearly evident in both images (scale bar represents 100μm)

A1.5 FITC Dextran PLL permeability studies

Due to the 45-60 kDa molecular weight cutoff of poly-L-lysine in the APA bead constructs, fluorescently-labeled (FITC) dextran molecules of different weights were used to assess the integrity of the PLL membrane. After cryopreservation, beads were exposed to solutions each containing a single type of FITC dextran, and the permeation of the dextran molecule in the beads were observed using confocal microscopy (Zeiss). 19kDa, 32kDa and 148kDa FITC-dextran (Sigma) solutions (dissolved in 0.9% saline at 1 mg/mL) were used to assess membrane intactness. In a construct with an intact PLL membrane, the 19 and 32kDa FITC dextrans would be able to diffuse through whereas the larger 148kDa dextran would not be able to penetrate the membrane.

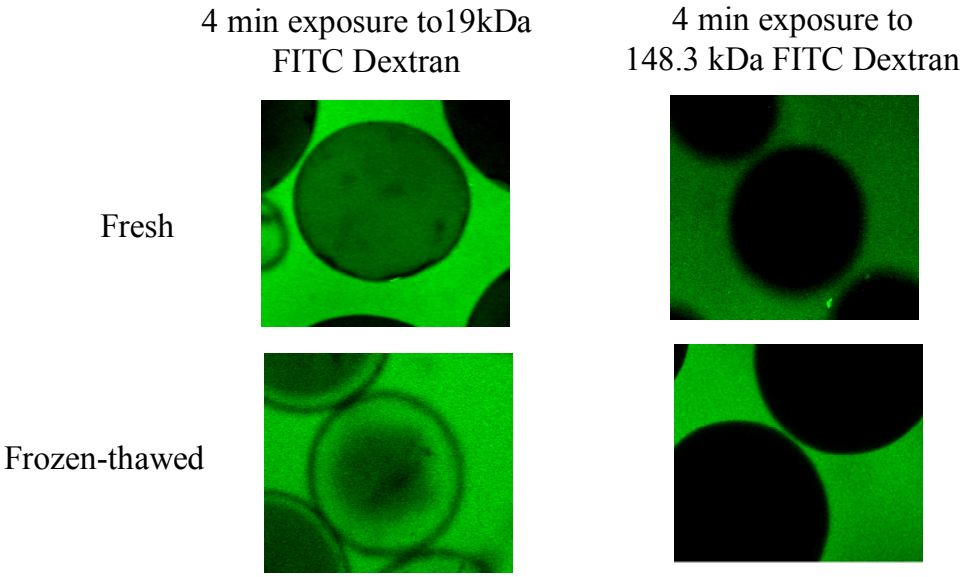

Figure A1.5 Confocal micrographs of fresh and frozen-thawed alginate-poly-L-lysine-alginate (APA) beads after 4 minutes of exposure to 19 and 148.3 kDa FITC-dextrans

A1.6 CPA addition-removal data for encapsulated insulinomas at vitrification-relevant concentrations

CPAs were added and removed in a stepwise manner using the mathematical model developed in this thesis. Negative controls consisted of single step delivery and removal. Cell viability was assessed by trypan blue – beads were exposed to sodium citrate to release the cells from the alginate matrix and then assessed with a hemocytometer. Single step vs. multi-step delivery is expectedly more pronounced at higher CPA concentrations where osmotic effects would play a considerable role in influencing cell viability. Optimized addition and removal of high concentration solutions of 3 M DMSO + 3 M PD and 6 M PD resulted in higher cell viabilites compared to 6 M DMSO.

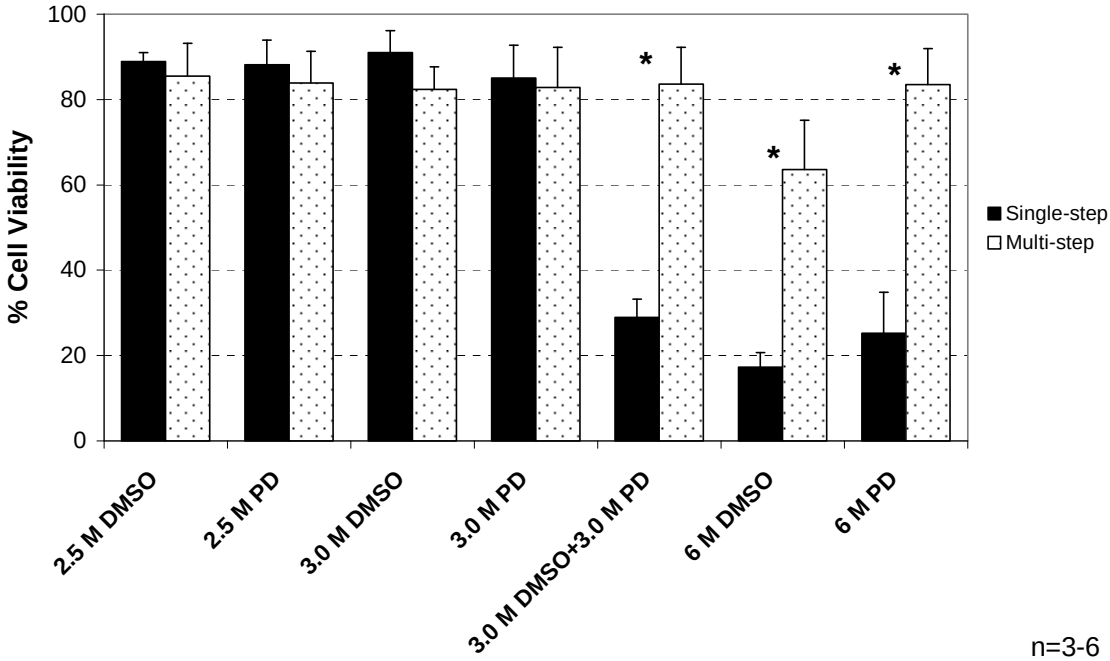

Figure A1.6 Addition-removal of low and high concentrations of single and multi-solute CPAs for alginate-encapsulated βTC-tet cells; DMSO=dimethyl sulfoxide; PD=1,2 propanediol; * represents significantly different at $p<0.05$ using Student's t-test; n=3-6

APPENDIX II

ARTICULAR CARTILAGE

A2.1 Heat transport measurements and calculations for articular cartilage

This study investigated the effects of different CPA solutions on the temperature profile during freezing. Using a Type T hypodermic thermocouple (Omega, Stamford, CT), the temperature profiles of CPA solutions as well as of a central position in cartilage tissue that had been equilibrated with the CPA solutions (overnight at 4°C) were recorded during freezing. The cryoprotectant solutions and cartilage samples were contained in cryovials (Nalgene, Rochester, NY) and cooled from approximately room temperature down to -140°C or -150°C at 99°C/min using a Cryomed® Controlled Rate Freezer (ThermoForma, Marietta, OH) (schematic of setup in Figure A2.1A). Temperature profiles, shown in Figure A2.1B indicated that with the lower concentrations of DMSO and DMSO-free phosphate-buffered saline (PBS) solutions, early release of the latent heat of fusion (H_f) followed by a steady decrease in temperature occurred. With higher concentrations of cryoprotectants, such as 6M DMSO and 8.4M VS55 shown in Figure A2.1C, H_f was smaller and was released at lower temperatures (depressed freezing point due to increased CPA concentration). These results are in agreement with the observations of Jomha et al. [128]. Experiments of this type can be performed to obtain reliable values of the heat transfer coefficient in cartilage for use in developing vitrification protocols. Overall, results indicate that the rate of heat transfer during cartilage freezing is much faster than the rate of mass transfer of CPA components (CHAPTER 7), and consequently the latter is the limiting process.

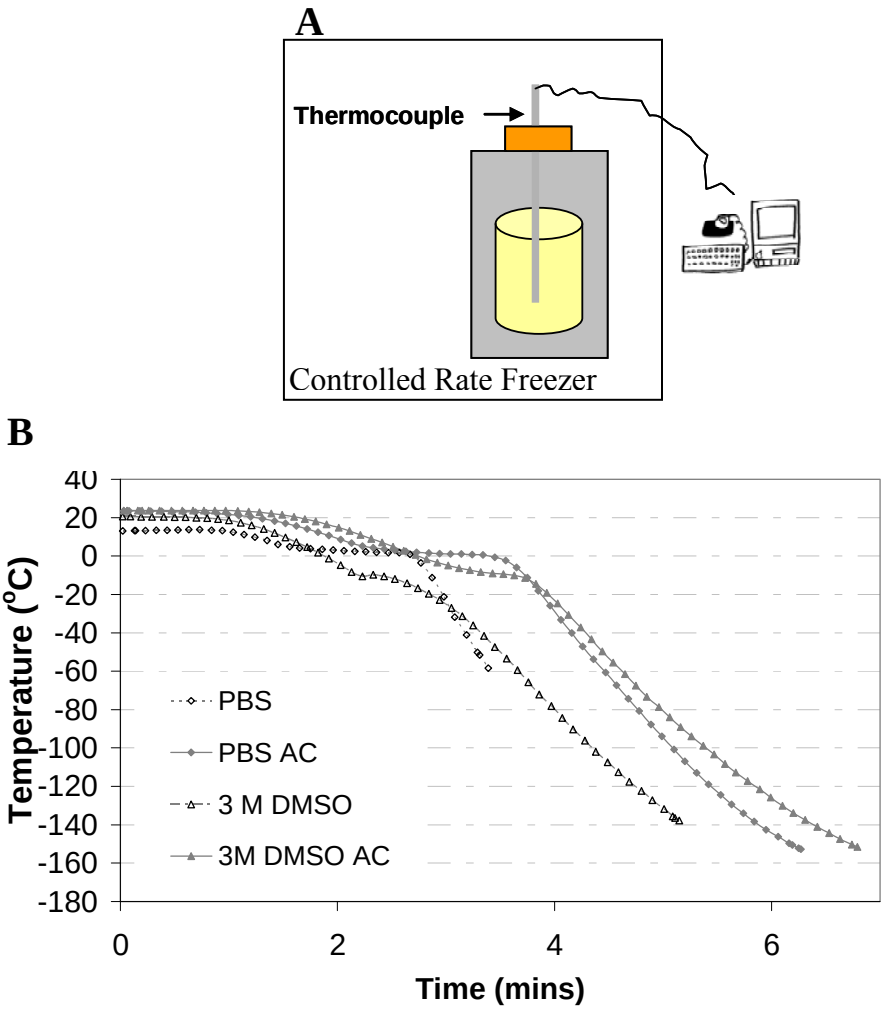

Figure A2.1 **A**. Cartilage heat measurement profile setup; **B**. Temperature profiles of CPA solutions and articular cartilage equilibrated in CPA solutions measured by a hypodermic thermocouple during cooling in a controlled-rate freezer; C. Experimental and simulation fit for determining thermal conductivity of bovine articular cartilage equilibrated in VS55

Figure A2.1 (continued)

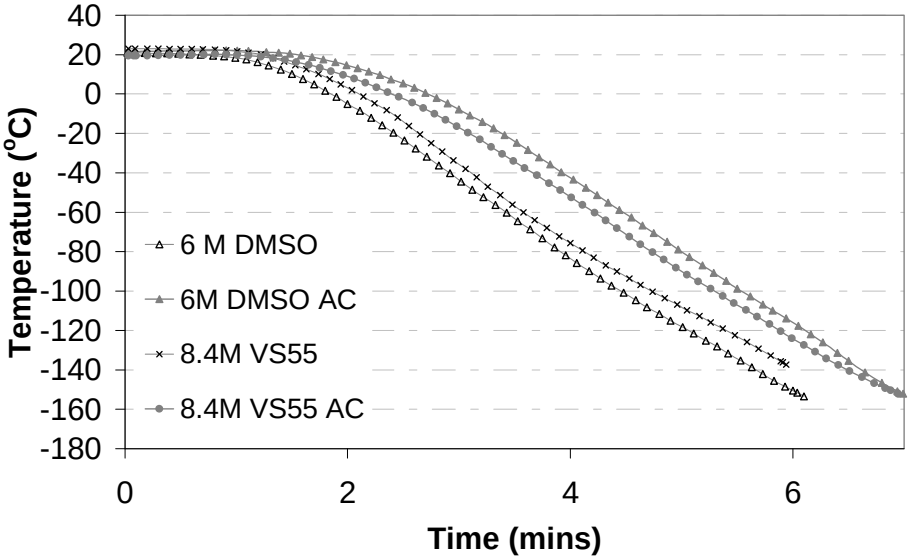

C

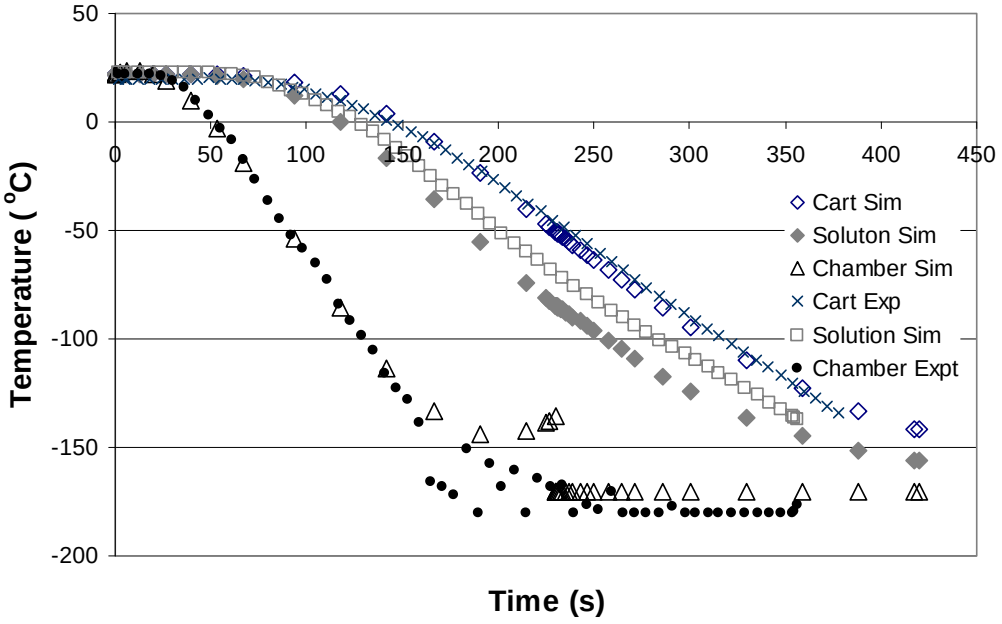

Heat Transport for cylindrical geometry:

I. Transport through the tissue:

$$\frac{\partial T}{\partial t} = \alpha\left(\frac{1}{r}\frac{\partial}{\partial r}(r\frac{\partial T}{\partial r}) + \frac{1}{r^2}\frac{\partial^2 T}{\partial \Theta^2} + \frac{\partial^2 T}{\partial z^2}\right) + \mu\Phi_v \qquad (1)$$

Assuming angular symmetry ($\frac{\partial T}{\partial \Theta} = 0$) and no dissipation ($\Phi_v = 0$),

$$\frac{\partial T}{\partial t} = \alpha\left(\frac{1}{r}\frac{\partial}{\partial r}(r\frac{\partial T}{\partial r}) + \frac{\partial^2 T}{\partial z^2}\right) \qquad (2)$$

Boundary and Initial Conditions:

i) T(all r and z, t=0) = T_o (3a)

ii) T(all r and z, t→∞) = T_f (3b)

iii) $q_{cryovial-liquid} = h(T_o - T_b(t))$ (3c)

iv) $q_{liquid-tissue} = h(T_o - T_l(t))$ (3d)

v) $\frac{\partial T}{\partial r}(r, z = 0) = 0$ (3e)

where T is the temperature (K), α is the thermal diffusivity (cm^2/s) (equivalent to $k/\rho\hat{C}_p$, where k is the thermal conductivity (W/m·K), ρ is the density and $\hat{C}_p$ is the heat capacity at constant pressure per unit mass), and t is time (s). This equation assumes that the thermal conductivity is independent of temperature and position.

The experimental temperature profiles during cooling of VS55 and cartilage equilibrated in VS55 (Figure A2.1B), recorded with a hypodermic thermocouple, were fit to determine the thermal conductivity of articular cartilage. The thermal conductivity of VS55 used is given in Table A2.1. The fit was performed using COMSOL® simulating the experimental conditions – a cartilage plug was submerged in VS55 solution in a polypropylene NUNC cryovial (k=0.12 W/m.K; C_p=1900 J/kg.K; density=900 kg/m^3) and cooled at -99°C/min to -150°C from 22°C ('Cart Sim';'Cart Expt'). Alternatively,

the temperature of just VS55 solution was measured during cooling ('Solution Sim'; 'Solution Expt'). The thermal conductivity of bovine articular cartilage based on this fitting was found to be 0.30 W/m.K. This value is close to the value of 0.478 W/m.K found for the thermal conductivity of nasal septal cartilage [225]. The experimental data and simulation fits are shown in Figure A2.1C.

Table A2.1: Thermal Properties of CPA solutions

	Density (kg/m^3)	**Cp (J/kg·K)**	**Thermal conductivity (W/m·K)**
3.1 M DMSO, 2.2 M PD, 3.1 M FM in 1X EC	1002	2971	0.36*
3 M DMSO + 3 M PD in 1X EC	1030	~2900	0.381*
5 M DMSO + 1 M PD in 1X EC	1038	~2900	0.377*

A2.2 Mechanical testing of articular cartilage after cryopreservation

To examine the mechanical properties of porcine articular cartilage following baseline freezing and vitrification protocols, 4 mm diameter and approximately 1 mm thick plugs were subjected to shear and compressive mechanical testing to determine the dynamic shear modulus and dynamic compressive modulus, respectively. The two baseline cryopreservation protocols were as follows. 1) For freezing, plugs were equilibrated with 10% DMSO and slowly cooled at -1°C/min down to -80°C, then plunged into liquid nitrogen; and 2) for vitrification, plugs were equilibrated with VS55, quickly cooled and then stored in liquid nitrogen. The plugs were thawed in a 37°C bath until all visible ice had disappeared and then transferred to DMEM culture media in which they were stored at 4°C until testing.

The dynamic shear modulus, G*, was measured using a Bohlin CVO® rheometer. The sample thickness was measured and noted. The sample was placed on the rheometer base plate and preloaded using an impermeable platen. The rheometer gap was set to 90% of the sample thickness to pre-load the sample (i.e.10% strain). A small quantity of PBS was added to the base plate of the rheometer to maintain sample hydration. After the sample was allowed to equilibrate for 15 minutes, it was subjected to the shear test. A frequency sweep of 0.01-1.0 Hz was carried out with logarithmic increase in frequency. Upon completion of the test, the measuring system was backed off and the sample was transferred back to media. This testing protocol is non-invasive, causing very little change in the fluid volume of the cartilage plugs thereby allowing for the measurement of the flow independent viscoelastic behavior of cartilage.

The dynamic compressive modulus, E*, was measured using an ELF machine (EnduraTec, Minnetonka, MN) and was carried out 30 minutes after the shear test (to allow for full sample relaxation and equilibration). The sample was moved onto an unconfined compression chamber which was filled with PBS (to prevent sample dehydration). A non-porous steel platen was placed on the cartilage sample and pre-loaded with 10% compressive strain for 15 minutes. After equilibration, a ±1.5% compressive strain was induced with a frequency sweep of 0.01-1.0 Hz with logarithmic increase in frequency. Commercially available software, DMA, was used to analyze the data and calculate the dynamic compressive modulus, E*. Like the shear test, the compressive test is also minimally invasive.

Results are shown in Figure A2.2. According to these preliminary data, the dynamic shear modulus of the fresh group was significantly higher ($p<0.05$) than either the frozen or vitrified group at 0.1 and 1.0 Hz. The shear modulus was not different between the frozen and vitrified groups ($p>0.05$). The compressive modulus of the fresh group was significantly higher than the frozen group at 0.1 and 1.0 Hz ($p<0.05$), however, the vitrified group was not significantly different than either the fresh or the frozen group ($p>0.05$). The greater effect of vitrification on the shear modulus possibly suggests more collagen than proteoglycan damage. In the proposed studies, the biomechanical properties of cartilage subjected to different preservation protocols will be thoroughly characterized *in vitro* because of the significance of tissue biomechanics in the context of this research and for insight as to the components of the tissue matrix that are damaged.

A

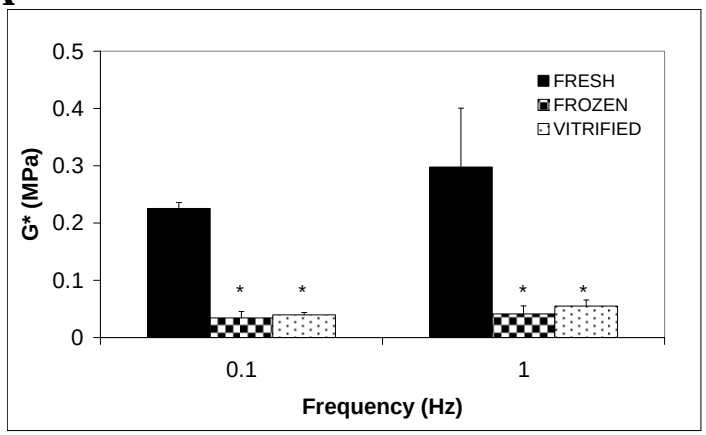

B

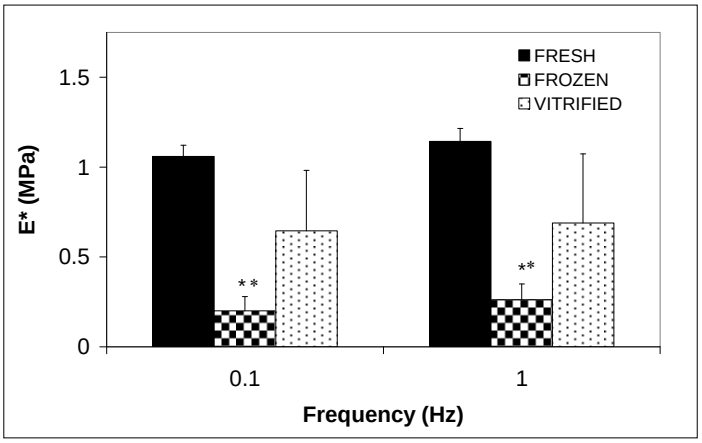

Figure A2.2: A. Dynamic shear and B. dynamic compressive moduli of cryopreserved 4 mm porcine articular cartilage; * indicates $p<0.05$, fresh vs. frozen group; fresh vs. vitrified group; n=3 for all; ** indicates $p<0.05$, fresh vs. frozen group (Student t-test)

A2.3 Chondron/Chondrocyte isolation from immature bovine articular cartilage

Chondrons were isolated as described by Lee et al [226]. Briefly, chondrons were obtained from minced bovine articular cartilage using 0.3% dispase (BD Biosciences) and 0.2% collagenase (Sigma) in Ca^{2+} and Mg^{2+}-free phosphate buffered saline (PBS) at 37°C with shaking for 5 hours. After straining through a 150µm mesh (cell strainer), chondrons were washed with PBS by centrifugation and then resuspended in Ham's F-12 tissue culture medium (CellGro) with 10% FBS (KSE Scientific). Chondrons were stained with Hoechst stain and visualized with confocal microscopy. Figure A2.3 is an optical micrograph of a typical preparation from bovine cartilage.

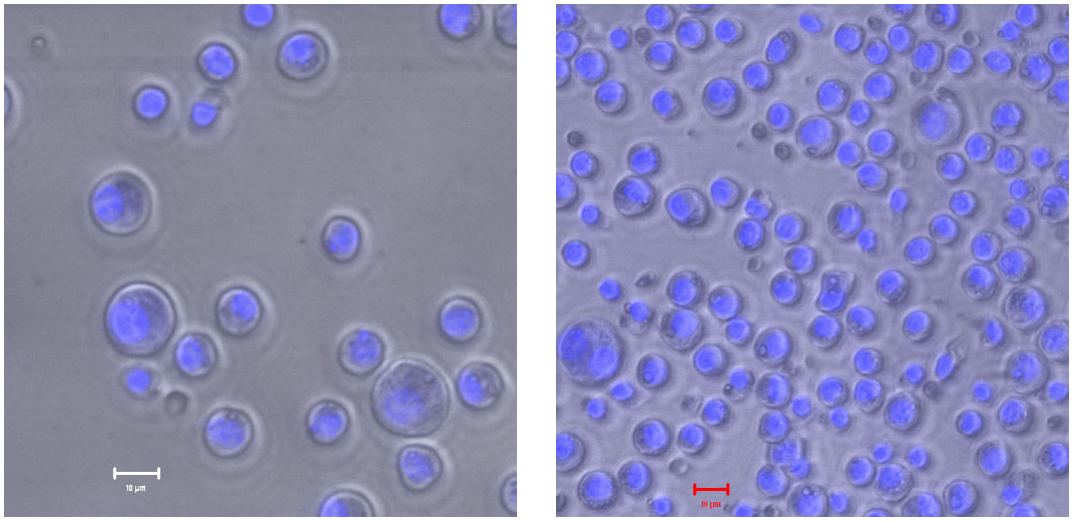

Figure A2.3 Chondrons/Chondrocytes were isolated using 0.3% dispase + 0.2% collagenase in PBS (Ca^{2+} and Mg^{2+} free) for 5 hours at 37°C; Hoechst stain was used to visualize nuclei (blue); scale bar represents 10µm

APPENDIX III

MISCELLANEOUS

A3.1 DSC runs with VS55 and DP6

Initial DSC runs were done using samples of VS55 (3.1 M DMSO + 3.1 M PD + 3.1 M FM in 1X EC) and DP6 (3 M DMSO + 3 M PD in 1X EC) as glass transition and devitrification/recrystallization temperatures have been reported for these solutions previously [136, 227]. 10-13 mg of sample was loaded into a pan with lid and ran with an empty pan with lid in the DSC.

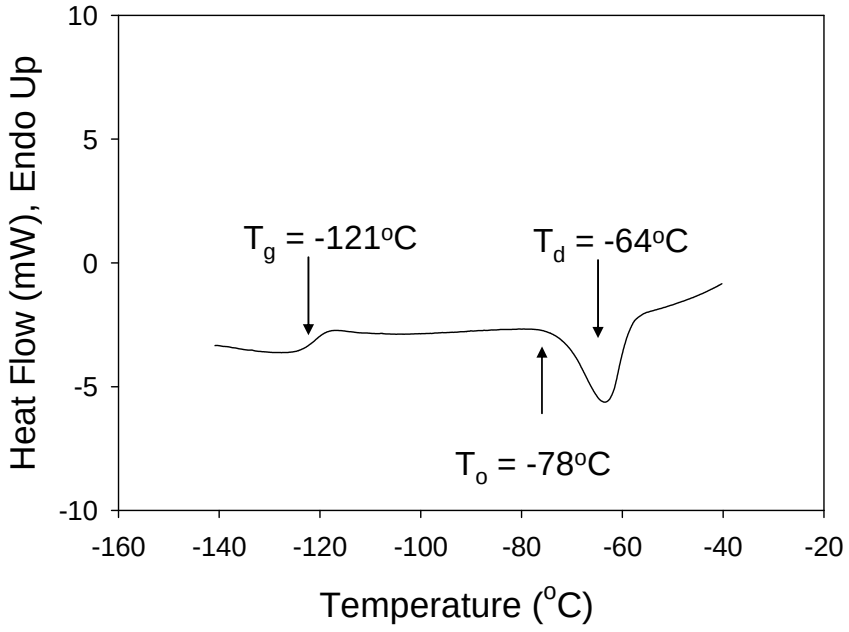

Figure A3.1 DSC heat flow thermogram of VS55 during warming at 5°C/min after sample was cooled rapidly at -150°C/min down to -150°C; T_g is the glass transition temperature; T_o is the beginning of crystallization during warming; T_d is the devitrification temperature.

Figure A3.1 shows a heat thermogram of VS55 during warming at 5°C/min after the sample was cooled rapidly at -150°C/min down to -150°C. The glass transition was found to be approximately -121°C. $T_{o.}$, the beginning of crystallization during warming, was found to be -78°C; T_d, the devitrification temperature, was -64°C. These values are in close agreement with those reported elsewhere [227] with values of T_g=-123 °C, T_o=-82 °C, and T_d=-75 °C.

Figure A3.2 shows the heat flow thermogram of DP6 during warming at 5°C/min after the sample was cooled rapidly at -150°C/min down to -150°C. The glass transition was found to be approximately -120°C. T_d, the devitrification temperature, was determined to be -90°C. The glass transition temperature is in close agreement with the value of -119°C reported by [177].

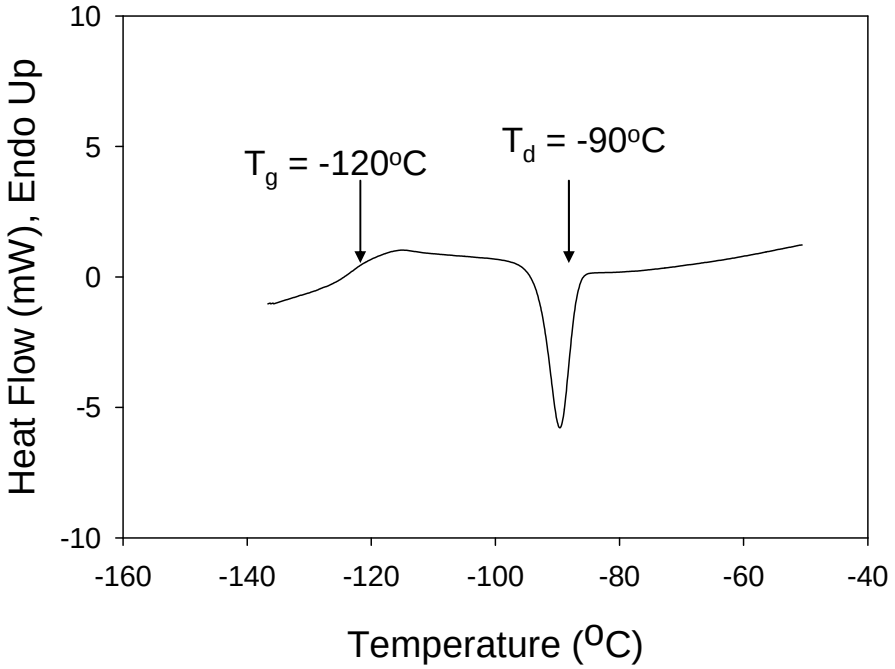

Figure A3.2 DSC heat flow thermogram of DP6 during warming at 5°C/min after sample was cooled rapidly at -150°C/min down to -150°C; T_g is the glass transition temperature; T_o is the beginning of crystallization during warming; T_d is the devitrification temperature.

Table A3.1 Thermal data for various vitrification solutions

CPA(s)	Concentration	T_g	T_d	T_{cr}	T_{wr}	Reference
(solvent)	(M)	(^oC)	(^oC)	(^oC/min)	(^oC/min)	
VS55 (EC)	3.1 M DMSO 3.1 M Formamide 2.2 M PD	-123	-75	2.5	50	[177]
DP6 (EC)	3 M DMSO 3 M PD	-119	-90	40	200	[177], T_d our lab
DP6+PEG400 (EC)	5 M PD 1 M DMSO 12% PEG MW 400	-112	?	?	?	[136]
DMSO (Water)	6 M 6.3M 7 M	-133.4 -132 -128	-82.5 n/o n/o	58 14 <2.5	$7.8x10^5$ 200-3300 10	[228]
PD (Water)	4.9 M 5.6 M 6.2 M	-119 -108 -107	-104 -87 -58	555 72 <5	$2x10^7$ 10,000 160	[229]
DP6_0.3S (EC)	3 M DMSO 3 M PD 0.3 M sucrose	-116	-59			our lab
55PD_1S (EC)	5.5 M PD 1 M sucrose	-100	n/o			our lab

DMSO=dimethyl sulfoxide; PD=1,2 propanediol; PEG=polyethylene glycol; EC=1X Euro-Collins; T_g=glass transition temperature; T_d=devitrification temperature; T_{cr}=critical cooling rate; T_{wr}=critical warming rate; n/o=not observed

REFERENCES

1. Mukherjee, I.N., Y.C. Song, and A. Sambanis, *Cryoprotectant delivery and removal from murine insulinomas at vitrification-relevant concentrations.* Cryobiology, 2007. **55**(1): p. 10-8.

2. Beere, H.M., *Death versus survival: functional interaction between the apoptotic and stress-inducible heat shock protein pathways.* J Clin Invest, 2005. **115**(10): p. 2633-9.

3. Pegg, D.E., *Principles of tissue preservation*. Progress in Transplantation - Vol 1 Transplantation of organs, tissues, etc. 1985, Edinburgh: Churchill Livingstone Inc.

4. Hunt, C.J., M.J. Taylor, and D.E. Pegg, *Freeze-substitution and isothermal freeze-fixation studies to elucidate the pattern of ice formation in smooth muscle at 252 K (-21 degrees C).* J Microsc, 1982. **125**(2): p. 177-86.

5. Song, Y.C., et al., *Ice-free cryopreservation of articular cartilage.* Tissue Engineering, 2002. **8**(6): p. 1181.

6. Taylor, M.J. and D.E. Pegg, *The effect of ice formation on the function of smooth muscle tissue stored at -21 or -60 degrees C.* Cryobiology, 1983. **20**(1): p. 36-40.

7. Mazur, P., *Principles of Cryobiology*, in *Life in the Frozen State*, F. In: Benson, B. and Lane, N. eds., Editor. 2004, Taylor and Francis Books: London. p. 3-65.

8. Black, S.P., et al., *Immune responses to an encapsulated allogeneic islet beta-cell line in diabetic NOD mice.* Biochem Biophys Res Commun, 2006. **340**(1): p. 236-43.

9. Constantinidis, I., et al., *Non-Invasive monitoring of a bioartificial pancreas in vitro and in vivo.* Ann N Y Acad Sci, 2001. **944**: p. 83-95.

10. Papas, K.K., et al., *Role of ATP and Pi in the mechanism of insulin secretion in the mouse insulinoma betaTC3 cell line.* Biochem J, 1997. **326 (Pt 3)**: p. 807-14.

11. Papas, K.K., et al., *Development of a bioartificial pancreas: I. long-term propagation and basal and induced secretion from entrapped betaTC3 cell cultures.* Biotechnol Bioeng, 1999. **66**(4): p. 219-30.

12. Sambanis, A., *Engineering challenges in the development of an encapsulated cell system for treatment of type 1 diabetes.* Diabetes Technol Ther, 2000. **2**(1): p. 81-9.

13. Stabler, C., et al., *The effects of alginate composition on encapsulated betaTC3 cells.* Biomaterials, 2001. **22**(11): p. 1301-10.

14. Stabler, C.L., A. Sambanis, and I. Constantinidis, *Effects of alginate composition on the growth and overall metabolic activity of betaTC3 cells.* Ann N Y Acad Sci, 2002. **961**: p. 130-3.

15. Tziampazis, E. and A. Sambanis, *Tissue engineering of a bioartificial pancreas: modeling the cell environment and device function.* Biotechnol Prog, 1995. **11**(2): p. 115-26.

16. Tanaka, H., M. Matsumura, and I.A. Veliky, *Diffusion Characteristics of Substrates in Ca-Alginate Gel Beads.* Biotechnology and Bioengineering, 1984. **26**(1): p. 53-58.

17. Hwang, Y.S., et al., *Enhanced derivation of osteogenic cells from murine embryonic stem cells after treatment with HepG2-conditioned medium and modulation of the embryoid body formation period: application to skeletal tissue engineering.* Tissue Eng, 2006. **12**(6): p. 1381-92.

18. Zandstra, P.W. and A. Nagy, *Stem cell bioengineering.* Annu Rev Biomed Eng, 2001. **3**: p. 275-305.

19. Bakay, A., et al., *Osteochondral resurfacing of the knee joint with allograft. Clinical analysis of 33 cases.* Int Orthop, 1998. **22**(5): p. 277-81.

20. Malinin, T.I., O.V. Martinez, and M.D. Brown, *Banking of massive osteoarticular and intercalary bone allografts--12 years' experience.* Clin Orthop Relat Res, 1985(197): p. 44-57.

21. Marco, F., et al., *Intact articular cartilage cryopreservation. In vivo evaluation.* Clin Orthop Relat Res, 1992(283): p. 11-20.

22. Ohlendorf, C., W.W. Tomford, and H.J. Mankin, *Chondrocyte survival in cryopreserved osteochondral articular cartilage.* J Orthop Res, 1996. **14**(3): p. 413-6.

23. Pegg, D.E., et al., *Cryopreservation of articular cartilage. Part 2: Mechanisms of cryoinjury.* Cryobiology, 2006.

24. Pegg, D.E., M.C. Wusteman, and L. Wang, *Cryopreservation of articular cartilage 1: Conventional cryopreservation methods.* Cryobiology, 2006. **52**(3): p. 335-346.

25. Song, Y.C., Lightfoot, F.G., Chen, Z., Taylor, M.J., Brockbank, K.G.M, *Vitreous preservation of rabbit articular cartilage.* Cell Preservation Technology, 2004. **2**(1).

26. Sharma, R., et al., *A novel method to measure cryoprotectant permeation into intact articular cartilage.* Cryobiology, 2007.

27. Karlsson, J.O. and M. Toner, *Long-term storage of tissues by cryopreservation: critical issues.* Biomaterials, 1996. **17**(3): p. 243-56.

28. Mazur, P., *Freezing of living cells: mechanisms and implications.* Am J Physiol, 1984. **247**(3 Pt 1): p. C125-42.

29. Polge, C., A.U. Smith, and A.S. Parkes, *Revival of spermatozoa after vitrification and dehydration at low temperatures.* Nature, 1949. **164**: p. 666.

30. Song, Y.C., et al., *Vitreous preservation of articular cartilage grafts.* J Invest Surg, 2004. **17**(2): p. 65-70.

31. Brockbank, K.G.M., Walsh, J.R., Song, Y.C. and Taylor, M.J., *Vitrification: Preservation of Cellular Implants*, in *Topics in Tissue Engineering*, N.A.a.P. Ferretti, Editor. 2003. p. 1-26.

32. Armitage, W.J. and S.J. Rich, *Vitrification of organized tissues.* Cryobiology, 1990. **27**(5): p. 483-91.

33. Fahy, G.M., *Vitrification*. Low Temperature Biotechnology: Emerging Applications and Engineering Contributions, ed. J.J. McGrath and K.R. Diller. 1988, New York: ASME. 113.

34. Fahy, G.M., et al., *Vitrification as an approach to cryopreservation.* Cryobiology, 1984. **21**(4): p. 407-26.

35. Franks, F., *The properties of aqueous solutions at subzero temperatures* Water: A comprehensive treatise, ed. F. Franks. Vol. 7. 1982, New York: Plenum Press.

36. MacFarlane, D.R., *Devitrification in glass-forming aqueous solutions* Cryobiology, 1986. **23**: p. 230-244.

37. Song, Y.C., et al., *Vitreous cryopreservation maintains the function of vascular grafts.* Nat Biotechnol, 2000. **18**(3): p. 296-9.

38. Taylor, M.J., et al., *Vitrification fulfills its promise as an approach to reducing freeze-induced injury in a multicellular tissue.* Advances in Heat and Mass Transfer in Biotechnology, 1999. **44**: p. 93-102.

39. Song, Y.C., et al., *Vitreous preservation of rabbit articular cartilage.* Cell Preservation Technology, 2004. **2**(1).

40. Paynter, S., et al., *Cryopreservation of multicellular embryos and reproductive tissues*, in *Reproductive Tissue Banking: Scientific Principles*, A.M. Karow and J.K. Critser, Editors. 1997, Academic Press: San Diego, CA. p. 359-397.

41. Bodziony, J., P. Schmitt, and G. Feifel, *In vitro function, morphology, and viability of cryopreserved rat pancreatic islets: comparison of vitrification and six cryopreservation protocols.* Transplant Proc, 1994. **26**(2): p. 833-4.

42. Mukherjee, N., et al., *Effects of cryopreservation on cell viability and insulin secretion in a model tissue-engineered pancreatic substitute (TEPS).* Cell Transplant, 2005. **14**(7): p. 449-56.

43. Song, Y.C., et al., *Vitrification of tissue engineered pancreatic substitute.* Transplant Proc, 2005. **37**(1): p. 253-5.

44. Rabin, Y. and B. Podbilewicz, *Temperature-controlled microscopy for imaging living cells: apparatus, thermal analysis and temperature dependency of embryonic elongation in Caenorhabditis elegans.* J Microsc, 2000. **199**(Pt 3): p. 214-23.

45. Rabin, Y., M.J. Taylor, and N. Wolmark, *Thermal expansion measurements of frozen biological tissues at cryogenic temperatures.* J Biomech Eng, 1998. **120**(2): p. 259-66.

46. Rubinsky, B., E.G. Cravalho, and B. Mikic, *Thermal stresses in frozen organs.* Cryobiology, 1980. **17**(1): p. 66-73.

47. Williams, R.J., *Four modes of nucleation in viscous solutions.* Cryobiology, 1989. **26**(6): p. 268-568.

48. Wusteman, M., M. Robinson, and D. Pegg, *Vitrification of large tissues with dielectric warming: biological problems and some approaches to their solution.* Cryobiology, 2004. **48**(2): p. 179-89.

49. de Freitas, R.C., et al., *Osmotic behavior and transport properties of human islets in a dimethyl sulfoxide solution.* Cryobiology, 1997. **35**(3): p. 230-9.

50. Zhao, G., et al., *Trapped water of human erythrocytes and its application in cryopreservation.* Biophys Chem, 2004. **107**(2): p. 189-95.

51. Kleinhans, F.W., *Membrane permeability modeling: Kedem-Katchalsky vs a two-parameter formalism.* Cryobiology, 1998. **37**(4): p. 271-89.

52. Muldrew, K. and L.E. McGann, *Mechanisms of intracellular ice formation.* Biophys J, 1990. **57**(3): p. 525-32.

53. Bhowmick, S., C.A. Khamis, and J.C. Bischof, *Response of a liver tissue slab to a hyperosmotic sucrose boundary condition: microscale cellular and vascular level effects.* Ann N Y Acad Sci, 1998. **858**: p. 147-62.

54. Mul drew, K., et al., *The Water to Ice Transition: Implications for Living Cells*, in *Life in the Frozen State*, F. In: Benson, B. and Lane, N. eds., Editor. 2004, Taylor and Francis Books: London.

55. Kuleshova, L., et al., *Birth following vitrification of a small number of human oocytes: case report.* Hum Reprod, 1999. **14**(12): p. 3077-9.

56. Yoon, T.K., et al., *Live births after vitrification of oocytes in a stimulated in vitro fertilization-embryo transfer program.* Fertil Steril, 2003. **79**(6): p. 1323-6.

57. Chian, R.C., et al., *High survival rate of bovine oocytes matured in vitro following vitrification.* J Reprod Dev, 2004. **50**(6): p. 685-96.

58. Larman, M.G., et al., *1,2-propanediol and the type of cryopreservation procedure adversely affect mouse oocyte physiology.* Hum Reprod, 2007. **22**(1): p. 250-9.

59. De Loecker, W., et al., *Effects of cell concentration on viability and metabolic activity during cryopreservation.* Cryobiology, 1998. **37**(2): p. 103-9.

60. Morris, C.B., *Cryopreservation of animal and human cell lines.* Methods Mol Biol, 1995. **38**: p. 179-87.

61. Baust, J.M., B. Van, and J.G. Baust, *Cell viability improves following inhibition of cryopreservation-induced apoptosis.* In Vitro Cell Dev Biol Anim, 2000. **36**(4): p. 262-70.

62. Baust, J.M., et al., *A molecular basis of cryopreservation failure and its modulation to improve cell survival.* Cell Transplant, 2001. **10**(7): p. 561-71.

63. Lovelock, J.E. and M.W. Bishop, *Prevention of freezing damage to living cells by dimethyl sulphoxide.* Nature, 1959. **183**(4672): p. 1394-5.

64. Mazur, P., et al., *Cryobiological preservation of Drosophila embryos.* Science, 1992. **258**(5090): p. 1932-5.

65. Martin, G., et al., *Cryopreservation induces an apoptosis-like mechanism in bull sperm.* Biol Reprod, 2004. **71**(1): p. 28-37.

66. Chinnaiyan, A.M., et al., *FADD, a novel death domain-containing protein, interacts with the death domain of Fas and initiates apoptosis.* Cell, 1995. **81**(4): p. 505-12.

67. Paasch, U., et al., *Cryopreservation and thawing is associated with varying extent of activation of apoptotic machinery in subsets of ejaculated human spermatozoa.* Biol Reprod, 2004. **71**(6): p. 1828-37.

68. Clarke, D.M., et al., *Targeted induction of apoptosis via TRAIL and cryoablation: a novel strategy for the treatment of prostate cancer.* Prostate Cancer Prostatic Dis, 2007. **10**(2): p. 175-84.

69. Baust, J.M., R. Van Buskirk, and J.G. Baust, *Modulation of the cryopreservation cap: elevated survival with reduced dimethyl sulfoxide concentration.* Cryobiology, 2002. **45**(2): p. 97-108.

70. Baust, J.M. and J.G. Baust, *The role of membrane-mediated apoptosis in cryopreservation failure.* Cryobiology, 2006. **53**(3): p. 387-388.

71. Baust, J.M., R. Van Buskirk, and J.G. Baust, *Gene activation of the apoptotic caspase cascade following cryogenic storage.* Cell Preservation Technology, 2002. **1**: p. 63-80.

72. Stroh, C., et al., *The role of caspases in cryoinjury: caspase inhibition strongly improves the recovery of cryopreserved hematopoietic and other cells.* Faseb J, 2002. **16**(12): p. 1651-3.

73. Vogel, M.J., J.M. Baust, and R. Van Buskirk, *Apoptotic caspases are activated following cryopreservation.* Cryobiology, 2000. **41**: p. 390.

74. Yagi, T., et al., *Caspase inhibition reduces apoptotic death of cryopreserved porcine hepatocytes.* Hepatology, 2001. **33**(6): p. 1432-40.

75. Sarkar, S., V. Kalia, and R.C. Montelaro, *Caspase-mediated apoptosis and cell death of rhesus macaque CD4+ T-cells due to cryopreservation of peripheral blood mononuclear cells can be rescued by cytokine treatment after thawing.* Cryobiology, 2003. **47**(1): p. 44-58.

76. *The effect of intensive treatment of diabetes on the development and progression of long-term complications in insulin-dependent diabetes mellitus. The Diabetes Control and Complications Trial Research Group.* N Engl J Med, 1993. **329**(14): p. 977-86.

77. Shapiro, A.M., et al., *Islet transplantation in seven patients with type 1 diabetes mellitus using a glucocorticoid-free immunosuppressive regimen.* N Engl J Med, 2000. **343**(4): p. 230-8.

78. Medtech Insight, L., *Tissue engineering and cell transplantation: technologies, opportunities and evolving markets.* 2000. **Analysis #A101**.

79. Lim, F. and A.M. Sun, *Microencapsulated islets as bioartificial endocrine pancreas.* Science, 1980. **210**(4472): p. 908-10.

80. Grant, G.T., Morris, E.R., Rees, D.A., Smith, P.J.C., Thom, D., *Biological interactions between polysaccharides and divalent cations: the egg-box model.* FEBS Letters, 1973. **32**(1): p. 195-198.

81. Martinsen, A., Skjak-Braek, G., Smidsred, O., *Alginate as immobilization material:I. Correlation between chemical and physical properties of alginate gel beads.* Biotechnology and Bioengineering, 1989. **33**: p. 79-89.

82. Draget, K.I., et al., *Small-angle X-ray scattering and rheological characterization of alginate gels. 3. Alginic acid gels.* Biomacromolecules, 2003. **4**(6): p. 1661-8.

83. Smidsrod, O. and G. Skjak-Braek, *Alginate as immobilization matrix for cells.* Trends Biotechnol, 1990. **8**(3): p. 71-8.

84. Efrat, S., *Cell replacement therapy for type 1 diabetes.* Trends Mol Med, 2002. **8**(7): p. 334-39.

85. Soria, B., et al., *Engineering pancreatic islets.* Pflugers Arch, 2000. **440**(1): p. 1-18.

86. Efrat, S., et al., *Beta-cell lines derived from transgenic mice expressing a hybrid insulin gene-oncogene.* Proc Natl Acad Sci U S A, 1988. **85**(23): p. 9037-41.

87. Efrat, S., et al., *Conditional transformation of a pancreatic beta-cell line derived from transgenic mice expressing a tetracycline-regulated oncogene.* Proc Natl Acad Sci U S A, 1995. **92**(8): p. 3576-80.

88. Canaple, L., et al., *Maintenance of primary murine hepatocyte functions in multicomponent polymer capsules--in vitro cryopreservation studies.* J Hepatol, 2001. **34**(1): p. 11-8.

89. Dixit, V., et al., *Cryopreserved microencapsulated hepatocytes--transplantation studies in Gunn rats.* Transplantation, 1993. **55**(3): p. 616-22.

90. Guyomard, C., et al., *Influence of alginate gel entrapment and cryopreservation on survival and xenobiotic metabolism capacity of rat hepatocytes.* Toxicol Appl Pharmacol, 1996. **141**(2): p. 349-56.

91. Heng, B.C., Y.J. Yu, and S.C. Ng, *Slow-cooling protocols for microcapsule cryopreservation.* J Microencapsul, 2004. **21**(4): p. 455-67.

92. Kuleshova, L.L., et al., *Vitrification of encapsulated hepatocytes with reduced cooling and warming rates.* Cryo Letters, 2004. **25**(4): p. 241-54.

93. Mahler, S., et al., *Hypothermic storage and cryopreservation of hepatocytes: the protective effect of alginate gel against cell damages.* Cell Transplant, 2003. **12**(6): p. 579-92.

94. Rajotte, R.V., et al., *Cryopreservation of microencapsulated canine islets.* Transplant Proc, 1995. **27**(6): p. 3389.

95. Stensvaag, V., et al., *Cryopreservation of alginate-encapsulated recombinant cells for antiangiogenic therapy.* Cell Transplant, 2004. **13**(1): p. 35-44.

96. Wu, Y., et al., *Vitreous cryopreservation of cell-biomaterial constructs involving encapsulated hepatocytes.* Tissue Eng, 2007. **13**(3): p. 649-58.

97. Zhou, D., I. Vacek, and A.M. Sun, *Cryopreservation of microencapsulated porcine pancreatic islets: in vitro and in vivo studies.* Transplantation, 1997. **64**(8): p. 1112-6.

98. Almqvist, K.F., et al., *Biological freezing of human articular chondrocytes.* Osteoarthritis Cartilage, 2001. **9**(4): p. 341-50.

99. Chen, D., R.L. Lewis, and D.S. Kaufman, *Mouse and human embryonic stem cell models of hematopoiesis: past, present, and future.* Biotechniques, 2003. **35**(6): p. 1253-61.

100. Eisenberg, L.M. and C.A. Eisenberg, *Adult stem cells and their cardiac potential.* Anat Rec A Discov Mol Cell Evol Biol, 2004. **276**(1): p. 103-12.

101. Gribaldo, L., et al., *Meeting summary: European Workshop on Stem Cells, European Centre for the Validation of Biomedical Testing Methods, Institute for Health and Consumer Protection, Joint Research Centre, Ispra, Italy, November 21-23, 2001.* Exp Hematol, 2002. **30**(7): p. 628-33.

102. Rohwedel, J., et al., *Embryonic stem cells as an in vitro model for mutagenicity, cytotoxicity and embryotoxicity studies: present state and future prospects.* Toxicol In Vitro, 2001. **15**(6): p. 741-53.

103. Thomson, J.A., et al., *Embryonic stem cell lines derived from human blastocysts.* Science, 1998. **282**(5391): p. 1145-7.

104. Robertson, E.J., *Teratocarcinomas and Embryonic Stem Cells: A Pratical Approach*, ed. E.J. Robertson. 1987, Oxford: IRL Press Ltd. 71-112.

105. Amit, M., et al., *Clonally derived human embryonic stem cell lines maintain pluripotency and proliferative potential for prolonged periods of culture.* Dev Biol, 2000. **227**(2): p. 271-8.

106. Reubinoff, B.E., et al., *Embryonic stem cell lines from human blastocysts: somatic differentiation in vitro.* Nat Biotechnol, 2000. **18**(4): p. 399-404.

107. Richards, M., et al., *The transcriptome profile of human embryonic stem cells as defined by SAGE.* Stem Cells, 2004. **22**(1): p. 51-64.

108. Sathananthan, H., M. Pera, and A. Trounson, *The fine structure of human embryonic stem cells.* Reprod Biomed Online, 2002. **4**(1): p. 56-61.

109. Bald, W.B., *On crystal size and cooling rate.* J Microsc, 1986. **143**(Pt 1): p. 89-102.

110. Kopstad, G. and A. Elgsaeter, *Theoretical analysis of the ice crystal size distribution in frozen aqueous specimens.* Biophys J, 1982. **40**(2): p. 155-61.

111. Reubinoff, B.E., et al., *Effective cryopreservation of human embryonic stem cells by the open pulled straw vitrification method.* Hum Reprod, 2001. **16**(10): p. 2187-94.

112. Zhou, C.Q., et al., *Cryopreservation of human embryonic stem cells by vitrification.* Chin Med J (Engl), 2004. **117**(7): p. 1050-5.

113. Richards, M., et al., *An efficient and safe xeno-free cryopreservation method for the storage of human embryonic stem cells.* Stem Cells, 2004. **22**(5): p. 779-89.

114. Birraux, J., et al., *Hepatocyte cryopreservation in a three-dimensional structure.* Transplant Proc, 2002. **34**(3): p. 764-7.

115. Koebe, H.G., et al., *A new approach to the cryopreservation of hepatocytes in a sandwich culture configuration.* Cryobiology, 1990. **27**(5): p. 576-84.

116. Heng, B.C., et al., *A proposed design for the cryopreservation of intact and adherent human embryonic stem cell colonies.* In Vitro Cell Dev Biol Anim, 2005. **41**(3-4): p. 77-9.

117. Mow, V.C. and A. Ratcliffe, *Structure and function of articular cartilage in meniscus*, in *Basic Orthopaedic Biomechanics*, V.C. Mow and W.C. Hayes, Editors. 1997, Lippincott-Raven: Philadelphia.

118. Stockwell, R.A., *Chondrocytes.* J Clin Pathol Suppl (R Coll Pathol), 1978. **12**: p. 7-13.

119. Cremer, M.A., E.F. Rosloniec, and A.H. Kang, *The cartilage collagens: a review of their structure, organization, and role in the pathogenesis of experimental arthritis in animals and in human rheumatic disease.* J Mol Med, 1998. **76**(3-4): p. 275-88.

120. Goldring, M.B., *The role of the chondrocyte in osteoarthritis.* Arthritis Rheum, 2000. **43**(9): p. 1916-26.

121. Hunziker, E.B., *Articular cartilage structure in humans and experimental animals*, in *Articular Cartilage and Osteoarthritis*, K.E. Kuettner, et al., Editors. 1992, Raven: New York.

122. Venn, M. and A. Maroudas, *Chemical composition and swelling of normal and osteoarthrotic femoral head cartilage. I. Chemical composition.* Ann Rheum Dis, 1977. **36**(2): p. 121-9.

123. Hunziker, E.B., *Articular cartilage repair: basic science and clinical progress. A review of the current status and prospects.* Osteoarthritis Cartilage, 2002. **10**(6): p. 432-63.

124. Muldrew, K., et al., *Localization of freezing injury in articular cartilage.* Cryobiology, 1994. **31**(1): p. 31-8.

125. Wu, F.J., T.H. Davisson, and D.E. Pegg, *Preservation of tissue-engineered articular cartilage.* Cryobiology, 1998. **37**: p. 410.

126. Stone, B.B., B.E. Defranzo, and C. Dicesare, *Cryopreservation of human articular cartilage for autologous chondrocyte transplantation.* Cryobiology, 1998. **37**(abstract): p. 445-446.

127. Studer, D., et al., *Vitrification of articular cartilage by high-pressure freezing.* J Microsc, 1995. **179 (Pt 3)**: p. 321-32.

128. Jomha, N.M., P.C. Anoop, and L.E. McGann, *Intramatrix events during cryopreservation of porcine articular cartilage using rapid cooling.* J Orthop Res, 2004. **22**(1): p. 152-7.

129. Pegg, D.E., L. Wang, and D. Vaughan, *Cryopreservation of articular cartilage. Part 3: The liquidus-tracking method.* Cryobiology, 2006.

130. Lanza, R.P., et al., *Xenotransplantation of canine, bovine, and porcine islets in diabetic rats without immunosuppression.* Proc Natl Acad Sci U S A, 1991. **88**(24): p. 11100-4.

131. Lanza, R.P., et al., *Xenotransplantation of bovine islets into dogs using biodegradable, injectable microreactors.* Transplant Proc, 1996. **28**(2): p. 820.

132. Lanza, R.P., et al., *Transplantation of islet allografts using a diffusion-based biohybrid artificial pancreas: long-term studies in diabetic, pancreatectomized dogs.* Transplant Proc, 1993. **25**(1 Pt 2): p. 978-80.

133. O'Shea, G.M., M.F. Goosen, and A.M. Sun, *Prolonged survival of transplanted islets of Langerhans encapsulated in a biocompatible membrane.* Biochim Biophys Acta, 1984. **804**(1): p. 133-6.

134. Jutte, N.H., et al., *Vitrification of mouse islets of Langerhans: comparison with a more conventional freezing method.* Cryobiology, 1987. **24**(4): p. 292-302.

135. Jutte, N.H., et al., *Vitrification of human islets of Langerhans.* Cryobiology, 1987. **24**(5): p. 403-11.

136. Brockbank, K.G.M., et al., *Vitrification: Preservation of Cellular Implants*, in *Topics in Tissue Engineering*, N. Ashammakhi and P. Ferretti, Editors. 2003. p. 1-26.

137. Papas, K.K., I. Constantinidis, and A. Sambanis, *Cultivation of recombinant, insulin-secreting AtT-20 cells as free and entrapped spheroids.* Cytotechnology, 1993. **13**(1): p. 1-12.

138. Brockbank, K.G.M., Lightfoot F.G., Song, Ying C., Taylor M.J., *Interstitial ice formation in cryopreserved homografts: a possible cause of tissue deterioration and calcification in vivo.* The Journal of Heart Valve Disease, 2000. **9**(2): p. 200-206.

139. Dahl, S.L., et al., *Feasibility of vitrification as a storage method for tissue-engineered blood vessels.* Tissue Eng, 2006. **12**(2): p. 291-300.

140. Chresand, T., B. Dale, and S. Hanson, *A Stirred Bath Technique for Diffusivity Measurements in Cell Matrices.* Biotechnol Bioeng, 1988. **32**: p. 1029-1036.

141. Lundberg, P. and P.W. Kuchel, *Diffusion of solutes in agarose and alginate gels: 1H and 23Na PFGSE and 23Na TQF NMR studies.* Magn Reson Med, 1997. **37**(1): p. 44-52.

142. Schantz, E.J. and M.A. Lauffer, *Diffusion measurements in agar gel.* Biochemistry, 1962. **1**: p. 658-63.

143. Casciari, J.J., S.V. Sotirchos, and R.M. Sutherland, *Glucose diffusivity in multicellular tumor spheroids.* Cancer Res, 1988. **48**(14): p. 3905-9.

144. Langer, S., et al., *Viability and recovery of frozen-thawed human islets and in vivo quality control by xenotransplantation.* J Mol Med, 1999. **77**(1): p. 172-4.

145. Fahy, G.M., *The relevance of cryoprotectant "toxicity" to cryobiology.* Cryobiology, 1986. **23**(1): p. 1-13.

146. Ebertz, S.L. and L.E. McGann, *Cryoprotectant permeability parameters for cells used in a bioengineered human corneal equivalent and applications for cryopreservation.* Cryobiology, 2004. **49**(2): p. 169-80.

147. Elliott, J.A., et al., *A multisolute osmotic virial equation for solutions of interest in biology.* J Phys Chem B, 2007. **111**(7): p. 1775-85.

148. Adams, S.L., et al., *Membrane permeability characteristics and osmotic tolerance limits of sea urchin (Evechinus chloroticus) eggs.* Cryobiology, 2003. **47**(1): p. 1-13.

149. Wusteman, M.C., et al., *Vitrification media: toxicity, permeability, and dielectric properties.* Cryobiology, 2002. **44**(1): p. 24-37.

150. Agca, Y., et al., *Osmotic tolerance and membrane permeability characteristics of rhesus monkey (Macaca mulatta) spermatozoa.* Cryobiology, 2005. **51**(1): p. 1-14.

151. Benson, C.T., et al., *Hydraulic conductivity (Lp) and its activation energy (Ea), cryoprotectant agent permeability (Ps) and its Ea, and reflection coefficients (sigma) for golden hamster individual pancreatic islet cell membranes.* Cryobiology, 1998. **37**(4): p. 290-9.

152. Arnaud, F.G. and D.E. Pegg, *Permeation of glycerol and propane-1,2-diol into human platelets.* Cryobiology, 1990. **27**(2): p. 107-18.

153. McGrath, J.J., *Quantitative measurement of cell membrane transport: technology and applications.* Cryobiology, 1997. **34**(4): p. 315-34.

154. Devireddy, R.V. and S.P. Leibo. *Calculated permeability coefficients for water and cryoprotective additives of ovine primordial follicles at suprazero temperatures*. in *Cryo 2006*. 2006. Hamburg, Germany.

155. Kardak, A., S.P. Leibo, and R.V. Devireddy. *Freezing characteristics of macawue and equine ovarian tissue sections in mixtures of dimethyl sulfoxide and ethylene glycol*. in *Cryo 2006*. 2006. Hamburg, Germany.

156. Balasubramanian, S.K., J.C. Bischof, and A. Hubel, *Water transport and IIF parameters for a connective tissue equivalent.* Cryobiology, 2006. **52**(1): p. 62-73.

157. Verkman, A.S., *Water permeability measurement in living cells and complex tissues.* J Membr Biol, 2000. **173**(2): p. 73-87.

158. Acker, J.P. and L.E. McGann, *Cell-cell contact affects membrane integrity after intracellular freezing.* Cryobiology, 2000. **40**(1): p. 54-63.

159. Pegg, D.E., *Cryopreservation of vascular endothelial cells as isolated cells and as monolayers.* Cryobiology, 2002. **44**(1): p. 46-53.

160. Porcshe, A.-M., C. Korber, and G. Rau, *Freeze-thaw behaviour of cultured (bovine corneal) endothelial cells: Suspension vs. monolayer.* Cryobiology, 1991. **28**: p. 545.

161. Elmoazzen, H.Y., et al., *Dimethyl sulfoxide toxicity kinetics in intact articular cartilage.* Cell Tissue Bank, 2006.

162. Bush, P.G. and A.C. Hall, *The osmotic sensitivity of isolated and in situ bovine articular chondrocytes.* J Orthop Res, 2001. **19**(5): p. 768-78.

163. Hing, W.A., et al., *An integrated environmental perfusion chamber and heating system for long-term, high resolution imaging of living cells.* J Microsc, 2000. **199 (Pt 2)**: p. 90-5.

164. Brockbank, K.G.M.a.S., Ying C., *Mechanisms of Bioprosthetic Heart Valve Calcification.* Transplantation Proceedings, 2003. **75**(8): p. 1133-1135.

165. Fahy, G.M., et al., *Cryopreservation of organs by vitrification: perspectives and recent advances.* Cryobiology, 2004. **48**(2): p. 157-78.

166. Mukaida, T., et al., *Vitrification of human embryos based on the assessment of suitable conditions for 8-cell mouse embryos.* Hum Reprod, 1998. **13**(1O): p. 2874-9.

167. Gross, J.D., I. Constantinidis, and A. Sambanis, *Modeling of encapsulated cell systems.* J Theor Biol, 2007. **244**(3): p. 500-10.

168. Stabler, C.L., et al., *Noninvasive Measurement of Viable Cell Number in Tissue-Engineered Constructs in Vitro, Using 1H Nuclear Magnetic Resonance Spectroscopy.* Tissue Eng, 2005. **11**(3-4): p. 404.

169. Aspen Technology, I., *Aspen Properties*. 1994-2006: Cambridge, MA.

170. Carslaw, H.S. and J.C. Jaeger, *Conduction of heat in solids*. 2nd ed. 1959, Oxford: Clarendon Press. 510.

171. Liu, K.K., D.R. Williams, and B.J. Briscoe, *The large deformation of a single micro-elastomeric sphere.* Journal of Physics D- Applied Physics, 1998. **31**(3): p. 294-303.

172. Hertz, H., *Uber die Beruhrung fester elastischer Korper.* J Reine Angewandte Math, 1882. **92**: p. 156-171.

173. Hannoun, B.J.M., *Diffusion Coefficients of Glucose and Ethanol in Cell-free and Cell-occupied Calcium Alginate Membranes.* Biotechnol Bioeng, 1986. **28**(June): p. 829-835.

174. Venancio, A. and J.A. Teixeira, *Characterization of sugar diffusion coefficients in alginate membranes.* Biotechnology Techniques, 1997. **11**(3): p. 183-185.

175. Stabler, C., *Development of Noninvasive Methods for Monitoring Tissue Engineered Constructs using Nuclear Magnetic Resonance*, in *Biomedical Engineering*. 2004, Georgia Institute of Technology Atlanta. p. 242.

176. Toda, K. and M. Shoda, *Sucrose inversion by immobilized yeast cells in a complete mixing reactor.* Biotechnol Bioeng, 1975. **17**(4): p. 481-497.

177. Rabin, Y., et al., *Cryomacroscopy of vitrification, Part I: A prototype and experimental observations on the cocktails VS55 and DP6.* Cell Preserv Technol, 2005. **3**(3): p. 169-183.

178. Kuleshova, L.L., et al., *Sugars exert a major influence on the vitrification properties of ethylene glycol-based solutions and have low toxicity to embryos and oocytes.* Cryobiology, 1999. **38**(2): p. 119-30.

179. Shaw, J.M., et al., *Vitrification properties of solutions of ethylene glycol in saline containing PVP, Ficoll, or dextran.* Cryobiology, 1997. **35**(3): p. 219-29.

180. Baudot, A., et al., *Effect of Saccharides on the Glass-Forming Tendency and Stability of Solutions of 2,3-Butanediol, 1,2-Propanediol, or 1,3-Butanediol in Water, Phosphate-Buffered Saline, Euro-Collins Solution, or Saint Thomas Cardioplegic Solution.* Cryobiology, 1996. **33**(3): p. 363-75.

181. Sutton, R.L., *Critical cooling rates for aqueous cryoprotectants in the presence of sugars and polysaccharides.* Cryobiology, 1992. **29**(5): p. 585-98.

182. MacFarlane, D.R. and M. Forsyth, *Recent insights on the role of cryoprotective agents in vitrification.* Cryobiology, 1990. **27**: p. 345-358.

183. Vogelsang, C., R.H. Wijffels, and K. Ostgaard, *Rheological properties and mechanical stability of new gel-entrapment systems applied in bioreactors.* Biotechnol Bioeng, 2000. **70**(3): p. 247-53.

184. LeRoux, M.A., F. Guilak, and L.A. Setton, *Compressive and shear properties of alginate gel: effects of sodium ions and alginate concentration.* J Biomed Mater Res, 1999. **47**(1): p. 46-53.

185. Nussinovitch, A., M. Peleg, and M.D. Normand, *A modified Maxwell and a nonexponential model for characterization of the stress relaxation of agar and alginate gels.* Journal of Food Science, 1989. **54**: p. 1013-1016.

186. Wong, M., et al., *Development of mechanically stable alginate/chondrocyte constructs: effects of guluronic acid content and matrix synthesis.* J Orthop Res, 2001. **19**(3): p. 493-9.

187. Ahearne, M., et al., *Characterizing the viscoelastic properties of thin hydrogel-based constructs for tissue engineering applications.* J R Soc Interface, 2005. **2**(5): p. 455-63.

188. Bunger, C.M., et al., *Biocompatibility and surface structure of chemically modified immunoisolating alginate-PLL capsules.* J Biomed Mater Res A, 2003. **67**(4): p. 1219-27.

189. Katkov, I., N. Katkova, and V. Bronshtein, *Motility and fertilization ability of boar semen frozen and stored at -80°C.* Cryobiology, 2000. **41**: p. 344-345.

190. Katkov, II, et al., *Cryopreservation by slow cooling with DMSO diminished production of Oct-4 pluripotency marker in human embryonic stem cells.* Cryobiology, 2006. **53**(2): p. 194-205.

191. Muldrew, K., et al., *Transplantation of articular cartilage following a step-cooling cryopreservation protocol.* Cryobiology, 2001. **43**(3): p. 260-7.

192. Muldrew, K., et al., *Cryobiology of articular cartilage: ice morphology and recovery of chondrocytes.* Cryobiology, 2000. **40**(2): p. 102-9.

193. Pegg, D.E., *The current status of tissue cryopreservation.* Cryo Letters, 2001. **22**(2): p. 105-14.

194. Tomford, W.W., G.R. Fredericks, and H.J. Mankin, *Studies on cryopreservation of articular cartilage chondrocytes.* J Bone Joint Surg Am, 1984. **66**(2): p. 253-9.

195. Bidault, N.P., B.E. Hammer, and A. Hubel, *Rapid MR imaging of cryoprotectant permeation in an engineered dermal replacement.* Cryobiology, 2000. **40**(1): p. 13-26.

196. Isbell, S.A., et al., *Measurement of cryoprotective solvent penetration into intact organ tissues using high-field NMR microimaging.* Cryobiology, 1997. **35**(2): p. 165-72.

197. Hagedorn, M., et al., *Magnetic resonance microscopy and spectroscopy reveal kinetics of cryoprotectant permeation in a multicompartmental biological system.* Proc Natl Acad Sci U S A, 1996. **93**(15): p. 7454-9.

198. Carsi, B., et al., *Cryoprotectant permeation through human articular cartilage.* Osteoarthritis Cartilage, 2004. **12**(10): p. 787-92.

199. Muldrew, K., et al., *Permeation Kinetics of Dimethyl Sulfoxide in Articular Cartilage.* Cryo-Letters, 1996. **17**: p. 331-340.

200. Bottomley, P.A., *Selective volume method for performing localized NMR spectroscopy* 1984, General Electric Company: USA.

201. Jadin, K.D., et al., *Depth-varying density and organization of chondrocytes in immature and mature bovine articular cartilage assessed by 3d imaging and analysis.* J Histochem Cytochem, 2005. **53**(9): p. 1109-19.

202. Williamson, A.K., et al., *Tensile mechanical properties of bovine articular cartilage: variations with growth and relationships to collagen network components.* J Orthop Res, 2003. **21**(5): p. 872-80.

203. Williamson, A.K., A.C. Chen, and R.L. Sah, *Compressive properties and function-composition relationships of developing bovine articular cartilage.* J Orthop Res, 2001. **19**(6): p. 1113-21.

204. Bush, P.G. and A.C. Hall, *Regulatory volume decrease (RVD) by isolated and in situ bovine articular chondrocytes.* J Cell Physiol, 2001. **187**(3): p. 304-14.

205. Xu, X., Z. Cui, and J.P. Urban, *Measurement of the chondrocyte membrane permeability to Me2SO, glycerol and 1,2-propanediol.* Med Eng Phys, 2003. **25**(7): p. 573-9.

206. Lilley, T.H. and R.H. Wood, *Freezing Temperatures of Aqueous Solutions Containing Formamide, Acetamide, Propionamide and N,N-Dimethylformamide.* J.C.S. Faraday I, 1980. **76**: p. 901-905.

207. Hines, A.L. and R.N. Maddox, *Mass transfer : fundamentals and applications*. 1985, Englewood Cliffs, N.J.: Prentice-Hall. xiii, 542 p.

208. Taylor, R. and R. Krishna, *Multicomponent mass transfer*. 1993, New York: Wiley.

209. Sandler, S.I., *Chemical and engineering thermodynamics*. 3rd ed. 1999, New York: Wiley. xx, 772 p.

210. Katkov, II, *A two-parameter model of cell membrane permeability for multisolute systems.* Cryobiology, 2000. **40**(1): p. 64-83.

211. Xu, X. and Z.F. Cui, *Modeling of the co-transport of cryoprotective agents in a porous medium as a model tissue.* Biotechnol Prog, 2003. **19**(3): p. 972-81.

212. Shaozhi, Z. and D.E. Pegg, *Analysis of the permeation of cryoprotectants in cartilage.* Cryobiology, 2007. **54**(2): p. 146-53.

213. Burstein, D., et al., *Diffusion of small solutes in cartilage as measured by nuclear magnetic resonance (NMR) spectroscopy and imaging.* J Orthop Res, 1993. **11**(4): p. 465-78.

214. Maroudas, A., *Distribution and diffusion of solutes in articular cartilage.* Biophys J, 1970. **10**(5): p. 365-79.

215. Urban, J.P., *Solute transport between tissue and environment*. Methods in Cartilage Research. 1990, New York: Academic Press.

216. Torzilli, P.A., et al., *Movement of interstitial water through loaded articular cartilage.* J Biomech, 1983. **16**(3): p. 169-79.

217. He, Y. and R.V. Devireddy, *An inverse approach to determine solute and solvent permeability parameters in artificial tissues.* Ann Biomed Eng, 2005. **33**(5): p. 709-18.

218. Malinin, T.I., et al., *Cryopreservation of articular cartilage. Ultrastructural observations and long-term results of experimental distal femoral transplantation.* Clin Orthop Relat Res, 1994(303): p. 18-32.

219. Kawabe, N. and M. Yoshinao, *Cryopreservation of cartilage.* Int Orthop, 1990. **14**(3): p. 231-5.

220. Leddy, H.A., H.A. Awad, and F. Guilak, *Molecular diffusion in tissue-engineered cartilage constructs: effects of scaffold material, time, and culture conditions.* J Biomed Mater Res B Appl Biomater, 2004. **70**(2): p. 397-406.

221. Grant, S.C., et al., *Alginate assessment by NMR microscopy.* J Mater Sci Mater Med, 2005. **16**(6): p. 511-4.

222. Schenke-Layland, K., et al., *Optimized preservation of extracellular matrix in cardiac tissues: implications for long-term graft durability.* Ann Thorac Surg, 2007. **83**(5): p. 1641-50.

223. Liu, K., Y. Yang, and J. Mansbridge, *Comparison of the stress response to cryopreservation in monolayer and three-dimensional human fibroblast cultures: stress proteins, MAP kinases, and growth factor gene expression.* Tissue Eng, 2000. **6**(5): p. 539-54.

224. Constantinidis, I., et al., *Towards the development of a bioartificial pancreas: a 13C NMR study on the effects of alginate/poly-L-lysine/alginate entrapment on*

glucose metabolism by beta TC3 mouse insulinoma cells. Cell Mol Biol (Noisy-le-grand), 1997. **43**(5): p. 721-9.

225. Youn, J.I., et al., *Optical and thermal properties of nasal septal cartilage.* Lasers Surg Med, 2000. **27**(2): p. 119-28.

226. Lee, G.M., et al., *Isolated chondrons: a viable alternative for studies of chondrocyte metabolism in vitro.* Osteoarthritis Cartilage, 1997. **5**(4): p. 261-74.

227. Mehl, P.M., *Nucleation and Crystal Growth in a Vitrification Solution Tested for Organ Cryopreservation by Vitrification.* Cryobiology, 1993. **30**(5): p. 509-518.

228. Baudot, A., L. Alger, and P. Boutron, *Glass-forming tendency in the system water-dimethyl sulfoxide.* Cryobiology, 2000. **40**(2): p. 151-8.

229. Wowk, B., et al., *Effects of solute methoxylation on glass-forming ability and stability of vitrification solutions.* Cryobiology, 1999. **39**(3): p. 215-27.